The shear velocity structure of the mantle from the inversion of time-domain waveform data

by

Charles Henri Mégnin

M.S. Physics (University of New Orleans) 1994
B.S. Geophysics (University of New Orleans) 1992

A dissertation submitted in partial satisfaction of the requirements for

the degree of

Doctor of Philosophy

in

Geophysics

in the

GRADUATE DIVISION

of the

UNIVERSITY of CALIFORNIA at BERKELEY

Commitee in charge:
Professor Barbara Romanowicz, Chair
Professor Mark Richards
Professor Philip Stark

1999

The dissertation of Charles Henri Mégnin is approved:

Chair	**Date**
	Date
	Date

University of California at Berkeley

1999

The shear velocity structure of the mantle from the inversion of time-domain waveform data

by

Charles Henri Mégnin

in memory of my grand mother, Félicie Mégnin

Acknowledgements

First of all, I would like to thank my advisor Barbara Romanowicz for introducing me to low frequency seismology, and for supporting me the last five years. Barbara has always been generous with her time and advice and has been for me an example of scientific integrity.

I am also endebted to Joe Murphy for triggering my interest in theoretical physics and for his kindness and attention during the course of my Master's thesis.

I have benefited considerably from the time and experience of Xiang-Dong Li who displayed much patience during the first year of my thesis. Xiang-Dong also collected most of the data used in the model, as well as crucial parts of the software.

I gratefully acknowledge Phil Stark and Mark Richards for thorough reviews of this thesis. Much of this work has been shaped by their ideas.

I also wish to thank Mark Bukowinski for always making time for discussion. T.A.'ing his classes was a particularly rewarding experience.

Many thanks to Raphaele Millot for processing the majority of the higher mode data, and to Sean Ford for collecting all the new body wave data.

I would also like to thank Fumiko Tajima for constructive advice with the writing of the last chapter of the manuscript.

It has been a pleasure to interact with the scientists and graduate students at the Berkeley seismo lab and elsewhere. Thanks to Yves le Stunff, Ludovic Bréger, Rouben Amirbekian, Catherine Thoraval, Wm Phil Richardson, Mike Pasyanos, Mike Antolik, Chaincy Kuo, Hrvoje Tkalčić, Sierra Boyd, Joe Durek, John Lynch, Peter Bunge, Uli Kastrup, Cliff Riebe, Eric Clévédé, Raphaele Millot, Sean Ford, Fred Gueydan, Fred Moulin, Andy Newman, Ed Garnero, Heiner Igel, Mike Manga, Christianne Stidham, Peg Johnson, Carolina Lithgow-Bertelloni, Cinzia Farnetani, Bob Uhrhammer, Bob Nadeau, Asya Kaverina, Daniel Chateigner, Daphné-Anne Pomméra, Nick Gregor, Yuan-Cheng Gung, Ramin Nawab, Lind Gee and Brian Savage. Thanks also to Hrvoje and Sierra for taking the place of Mike A. after his departure.

I am indebted to Doug Neuhauser for his numerous contributions to my computing skills, to Charley Paffenbarger for his patience with unreasonable requests, and to both for maintaining the computer system at a quality level that permitted the timely derivation of these results.

Nothing would run as smoothly as they do without the efforts of Eleanor Ka, Bari Burton, Rick McKenzie and Steve Fulton.

The friendship of many people has made living in Berkeley a very enriching experience. Many thanks to Doudou, Rouben & Sofia, Ludo & the real Simone, Catherine, Viejo, Séverine, Domi & Wendy, Mireille, Marie-Pierre & Benoit, Cathy & Bruno, Mike P., Mike 'the Gimp', Hrvoje, Sisi, Christhard & Utte, Jakob & Henrietta, Rod & Adriana, Andrès & Carole, Jean-Michel, Smail, Pat & Reg, Steve & Carolina.

Finally, I wouldn't have had the heart of completing this thesis without the presence of Kristine. I can't thank you enough for putting up with all this.

Table of Contents

List of Figures

Abstract

The shear velocity structure of the mantle from the inversion of time-domain waveform data

by

Charles Mégnin

Doctor of Philosophy in Geophysics

University of California at Berkeley

Professor Barbara Romanowicz, Chair

We present evidence that seismic imaging based on waveform inversion is capable of resolving the spectral signature of a convecting mantle, by computing tomographic images of a 3-D spherical convection simulation. The input model includes the thermal effects on the mantle's convection planform of 20% bottom heating, two phase transitions at 410 km and 670 km, a depth-dependent viscosity profile, and the history of plate motions starting in the mid-Mesozoic. The comparison between images of this model 'seen' by the tomography and a model of shear velocity in the mantle indicates that the part of the temperature field corresponding to cold mantle heterogeneity in the convection simulation agrees well with the fast velocities derived from tomography, but that current convection computations are lacking some key ingredients necessary to reproduce the character of upwellings correctly. After quantifying the distortive effect of the aliasing of small scale heterogeneity into long wavelength models, and of the use of the asymptotic expansion of a Born seismogram in the waveform modeling, we derive a model of 3-dimensional seismic shear velocity in the mantle by inverting a dataset consisting of body, surface, and higher mode waveforms.

Our model shows the presence of three low velocity zones continuous throughout the depth of the mantle, one under the African Plate and two in the Pacific. These 'megaplumes' connect at the surface with the mid-Indian ridge and the complex of ridges constituted by the East-Pacific Rise, the Chile Ridge and the Pacific-Antarctic Ridge, respectively. Our model suggests the presence in the upper mantle of isolated low velocity anomalies that coincide with the surface location of many hotspots, in particular in the Pacific region. No significant accumulation of low velocity anomalies is observed in the upper part of the lower

mantle, suggesting that the 670 km discontinuity does not act as a significant barrier to mantle flow. The spectral analysis of the model suggests a narrowing of the slow anomalies in the lower mantle with increasing radius. Fast anomalies coinciding with subduction regions suggest that, except for parts of the Norhtwestern Pacific, slabs penetrate into the lower mantle. This provides further evidence that the phase boundary may not impede flow between the upper and the lower mantle.

Approved:

Barbara Romanowicz, Chair Date

General introduction

The purpose of the work described in this thesis is to derive a global image of V_{SH} seismic velocity in the mantle from high quality waveform data, using a theoretical formalism both as accurate and as computationally tractable as possible.

In chapter 1, we review the theoretical foundations for the modeling of waveforms by normal mode summation as done in this thesis. In the present work, this is done by expanding asymptotically to zeroth order seismograms obtained by expressing the 3D wavefield as a first order perturbation from a seismogram derived (exactly) in a spherically symmetric mantle model. This formalism is refered to as 'nonlinear asymptotic coupling theory' (*NACT*) and was developed by [*Li & Romanowicz*, 1995]. This chapter is a compilation of results derived in several papers: [*Woodhouse*, 1983; *Tanimoto*, 1984] have developped general expressions for the Born seismogram; [*Romanowicz*, 1987; *Li & Tanimoto*, 1993; *Li & Romanowicz*, 1995] have developed the asymptotic expansions that we use to model the data. We then derive a technique to model differential travel times computed by cross-correlation in the context of the *NACT* waveform modeling formalism. We close the chapter by summarizing the inversion technique used to derive a mantle model from the waveforms.

In chapter 2, we address the issue of the resolution of tomographic models in terms of the recovery of the spectral signature of parameters characteristic of mantle dynamics. In particular, we show that the modeling technique we use allows the recovery of the footprint of a phase transition at 670 km, bottom heating, viscosity layering, and of the incidence of plate motions on the convective planform. This is achieved by imaging results from eight

3D spherical convection calculations [*Bunge et al.*, 1996; *Bunge & Richards*, 1996; *Bunge et al.*, 1997]. This chapter was published under the reference [*Mégnin et al.*, 1997].

In chapter 3, we use a refinement of the technique used in chapter 1 to quantify the incidence of mapping of small scale structure into long wavelength models. This is done by differentiating models obtained by the inversion of aliased and non-aliased synthetic datasets. The experiment shows that the distortion is modest and present mostly in the short wavelength component of the models. This chapter is currently in review [*Mégnin & Romanowicz*, 1999b].

In chapter 4, we examine the effect of the choice of data selection scheme and the use of cross-branch coupling on mantle models. This is done by inverting the same data set using both the Path average approximation (PAVA) of [*Woodhouse & Dziewonski*, 1984; *Jordan*, 1978] which is equivalent, to zeroth order, to restricting the coupling of modes along the dispersion branch, and the nonlinear asymptotic coupling theory (*NACT*) of [*Li & Romanowicz*, 1995] where across branch coupling is also taken into acount. Each of these models is derived under a waveform windowing scheme where we isolate each energy wavepacket and one where we select the entire body wavetrain. We show that although these approaches are equivalent for the imaging of uppermost mantle structure, differences appear at depths greater than 300 km. In the lowermost mantle, the use of the individual windowing is crucial as it allows to extract low amplitude S_{diff} information. In the rest of the lower mantle, the inclusion of across-branch coupling improves the image. This results from the necessity to use full mode coupling to model body waveforms. This chapter was published under the reference [*Mégnin & Romanowicz*, 1999a].

It is an unfortunate fact of computational seismology that a trade-off exists between the accuracy of the synthetic waveforms and the speed of their computation. Inaccuracies in the waveform formalism resulting from departure from an 'exact' seismogram will map into the models obtained from the inversion of data as spurious heterogeneity. In chapter 5, we examine the theoretical leakage resulting from the use of the asymptotic expansion of the first order Born approximation such as *NACT*. This is done by computing a synthetic third order Born, non-asymptotic Love wave dataset with the formalism developed by [*Lognonné & Romanowicz*, 1990] in a fictitious upper mantle model consisting of two adjacent heterogeneities, and inverting it with the [*Li & Romanowicz*, 1995] formalism. The contents of this chapter were recently submitted for publication [*Clévédé et al.*, 1999].

Finally in chapter 6, we present a model of shear velocity in the whole mantle, derived with the *NACT* formalism and expanded laterally up to degree 18 and radially in 16 unevenly spaced splines. We discuss the images in the context of the depth extent of tectonic features and analyze the depth variation of characteristic length scales in the mantle.

Chapter 1

Theoretical background

1.1 Introduction

In this chapter, we develop the expressions for a seismic waveform, modeled with the nonlinear asymptotic coupling theory [*Li & Romanowicz*, 1995]. This formalism is set in the context of first order perturbation from a spherically symmetric model developed by [*Woodhouse*, 1983; *Tanimoto*, 1984], from which several simplifications are performed. First the phase term corresponding to across-branch coupling is linearized, assuming a short span between origin time and phase arrival time. This is justified for the modeling of body waves arriving prior to the first surface wavetrain [*Woodhouse*, 1983; *Tanimoto*, 1984]. Next, the asymptotic expansions of the coupled terms allow us to replace the coupling among singlets with more computationally practical expressions which only invoke coupling among multiplets. This is obtained by first reducing the heterogeneity coupling term to an integral including a product of spherical harmonic coefficients of Earth structure, assuming the heterogeneity is smooth [*Romanowicz & Roult*, 1986]. The Legendre functions are then treated asymptotically to order zero in $\frac{1}{\ell}$, and the integrals asymptotically expanded by the method of stationary phase [*Romanowicz & Roult*, 1986; *Li & Tanimoto*, 1993].

In the second part of the chapter, we develop expressions for modeling travel time differentials computed by cross-correlating waveforms in the context of this formalism. We close the chapter by providing a synopsis of the inversion procedure used to derive our models.

1.2 Exact solution

We wish to solve the equation of motion

$$(\mathcal{H} + \rho\, \partial_t^2)\mathbf{u} \,=\, \mathbf{f} \tag{1.1}$$

for the displacement field $\mathbf{u}(\mathbf{x}, t)$, where $\mathcal{H}$ is an integro-differential tensor operator depending on Earth structure, $\rho(\mathbf{x})$ is the density distribution and $\mathbf{f}(\mathbf{x}, t)$ is the equivalent body force distribution of the source.
The solution is expanded on a complete set of basis functions $\mid i >$ such that:

$$\mathbf{u} = \sum_i a_i(t) \mid i > . \tag{1.2}$$

Using the 'bracket' notation where, for an operator Θ
$< j \mid \Theta \mid i > \equiv \int\limits_{\mathcal{V}} \mid j^* > \; \Theta \; \mid i > d\mathcal{V}$
where the '*' represents complex conjugation and $\mathcal{V}$ is the volume of the Earth.
Substituting (1.2) into (1.1), premultiplying by $\mid j^* >$ and integrating yields:

$$\sum_i \left[< j \mid H \mid i > \,+\, < j \mid \rho \mid i > \,\partial_t^2\right] a_i(t) \,=\, F_i \tag{1.3}$$

where $F_i \equiv < i \mid \mathbf{I} \mid f >$ and $\mathbf{I}$ is the identity matrix.
Equation (1.3) can be re-written in matrix notation:

$$\left[\mathbf{H} + \mathbf{P}\, \partial_t^2\right] \mathbf{a} \,=\, \mathbf{F}. \tag{1.4}$$

[*Woodhouse*, 1983] has shown that the solution to (1.4) for an initially quiescent Earth model ($\mathbf{a}(0) \,=\, \partial_t\, \mathbf{a}(0) \,=\, 0$) is given by:

$$\mathbf{a}(t) \,=\, \Re e \left(\int_0^t \mathbf{X}^{-2} \,\left(\mathbf{I} \,-\, \exp\left[i(t-\tau)\,\mathbf{X}\right]\right) \mathbf{P}^{-1}\, \partial_t\, F(\tau)\, d\tau \right) \tag{1.5}$$

where the matrix $\mathbf{X}$ is defined by the relation $\mathbf{X}^{-2} \,\equiv\, \mathbf{P}^{-1} \cdot \mathbf{H}$.
As noted in [*Woodhouse*, 1983], this solution, although exact, is nevertheless computationally impractical due to the infinite dimensional character of the matrices.

1.3 First order perturbation (Born approximation)

In the case of a step function source where $\partial_t f_i(t) = \delta(t)\, S_i$, and for an accelerogram where $u(t) = \mathbf{v} \cdot \partial_t^2 u(\mathbf{x_r}, t)$ (1.5) becomes

$$u(t) = \Re e\{\mathbf{R}\ \exp[i\,\mathbf{X}\,t]\mathbf{P^{-1}}\ \mathbf{S}\} \tag{1.6}$$

where $\mathbf{R}$ is a receiver term.

If we choose the free oscillations of the Earth as set of basis functions, the homogeneous eigenvalue equation (1.1) becomes

$$(\mathcal{H} + \rho\,\omega^2) \mid k >= 0 \tag{1.7}$$

where ω^2 is the eigenvalue and the eigenfunctions obey the orthogonality conditions:

$$\begin{aligned} P_{ij} &= \ < i \mid \rho \mid j >= \delta_{ij} && (1.8)\\ H_{ij} &= \ < i \mid \mathcal{H} \mid j >= \omega_i^2\, \delta_{ij} && (1.9)\\ X_{ij} &= \ \omega_i\, \delta_{ij}. && (1.10) \end{aligned}$$

The operators are decomposed into the sum of a reference term and a small perturbation term:

$\Theta = \Theta^{(\mathbf{0})} + \Theta^{(\mathbf{1})}$ where $\Theta_{ij}^{(0)} \gg \Theta_{ij}^{(1)}$ and $\Theta \in \{\mathbf{P}, \mathbf{H}, \mathbf{X}\}$.

Then to first order [*Woodhouse*, 1983],

$$P_{ij}^{-1} = \left(P_{ij}^{(0)} + P_{ij}^{(1)}\right)^{-1} = \left(\delta_{ij} + P_{ij}^{(1)}\right)^{-1} \approx \delta_{ij} - P_{ij}^{(1)} \tag{1.11}$$

and $\mathbf{X}^2 = \mathbf{P}^{-1}\mathbf{H} = \mathbf{H}^{(0)} - \mathbf{P}^{(1)}\mathbf{H}^{(0)} + \mathbf{H}^{(1)} = \mathbf{X}^{(0)\,2} + \mathbf{X}^{(0)}\mathbf{X}^{(1)} + \mathbf{X}^{(1)}\mathbf{X}^{(0)}$

collecting terms, using the orthogonality conditions, and defining

$$Z_{ij} \equiv H_{ij}^{(1)} - \omega_j^2 P_{ij}^{(1)}$$

and

$$X_{ij} = \omega_i \delta_{ij} + \frac{Z_{ij}}{\omega_i + \omega_j} \tag{1.12}$$

the first order of perturbation solution to (1.1) can be written (e.g. [*Li & Tanimoto*, 1993]):

$$u(t) = \Re e\{\mathbf{R}\,\Big[\exp(i\,\mathbf{X}\,t)\; - \;\exp(i\,\Omega t)\mathbf{P}^{(1)}\Big]\,\mathbf{S}\}, \tag{1.13}$$

where Ω is the column vector of eigenvalues ω_i.
This expression corresponds to the Born approximation and therefore only models the single scattering contribution of the wavefield to the seismogram: back-scattering and multiple forward scattering are negelected.

1.4 Nonlinear asymptotic coupling theory

1.4.1 Linearization of the phase term

Equation (1.13) includes a phase and an amplitude term, and the former dominates with increasing frequencies, as the effect of the density perturbations is significant mostly at the longest periods. The amplitude term is therefore neglected and (1.13) becomes:

$$u(t) = \Re e\{\mathbf{R}\;\exp(i\,\mathbf{X}\,t)\;\mathbf{S}\} \tag{1.14}$$

The phase term in equation (1.12) can be re-written:

$$X_{ij} \;=\; (\omega_i + \delta\widetilde{\omega}_i)\delta_{ij} \;+\; \frac{Z_{ij}}{\omega_i \,+\, \omega_j} \;-\; \delta\widetilde{\omega}_i\delta_{ij} \equiv \widehat{\omega}_i\delta_{ij} \;+\; \frac{\widehat{Z}_{ij}}{\omega_i \,+\, \omega_j}, \tag{1.15}$$

where $\widehat{Z}_{ij} \equiv Z_{ij} \; - \; 2\omega_i\delta\widetilde{\omega}_i\delta_{ij}$, $\widehat{\omega}_i \equiv \omega_i + \delta\widetilde{\omega}_i$ and $\delta\widetilde{\omega}_i$ is the 'path average' approximation given by:

$$\delta\widetilde{\omega}_i \;=\; \frac{1}{\widehat{SR}}\int_S^R \delta\omega^i_{local}d\phi \tag{1.16}$$

and $\delta\omega^i_{local}$ is the local frequency introduced by [*Jordan*, 1978] averaged along the epicentral distance $\widehat{SR}$ between the source and the receiver.

The contribution of the Earth's lateral heterogeneity to the seismogram can thus be expressed as the superposition of a term corresponding to the response to the average structure between the source and the receiver with a presumably smaller second term corresponding to further corrections, which we now linearize [*Li & Romanowicz*, 1995].
Following the approach of [*Woodhouse*, 1983], we linearize $\mathbf{Q}(t) \equiv \exp(i\mathbf{X}t)$ in equation (1.14).
Noting that

$$\begin{aligned} \partial_t \mathbf{Q}(t) &= i\mathbf{X}\mathbf{Q}(t) && (1.17)\\ \mathbf{Q}(0) &= 1 && (1.18) \end{aligned}$$

we let $\mathbf{Q} = \mathbf{Q}^{(0)} + \mathbf{Q}^{(1)}$.
Then, to first order, $\partial_t \mathbf{Q}(t) = \partial_t \mathbf{Q}^{(0)} + \partial_t \mathbf{Q}^{(1)} = i\mathbf{X}^{(0)}\mathbf{Q}^{(0)} + i\mathbf{X}^{(0)}\mathbf{Q}^{(1)} + i\mathbf{X}^{(1)}\mathbf{Q}^{(0)}$.
Collecting terms of the same order,

$$\begin{aligned} \partial_t \mathbf{Q}^{(0)} &= i\mathbf{X}^{(0)}\mathbf{Q}^{(0)} && (1.19)\\ \partial_t \mathbf{Q}^{(1)} &= i\mathbf{X}^{(0)}\mathbf{Q}^{(1)} + i\mathbf{X}^{(1)}\mathbf{Q}^{(0)}. && (1.20) \end{aligned}$$

The solution to equation (1.20) is given by:

$$\mathbf{Q}^{(0)} = \exp\left(i\mathbf{X}^{(0)}t\right)$$

or in index notation,

$$Q^{(0)}_{jk} = \exp\left(i\widehat{\omega}_j t\right)\delta_{jk}. \qquad (1.21)$$

For simplicity of notation, we now define the terms
$\mathbf{K} \equiv \mathbf{Q}^{(0)}; \mathbf{b} \equiv \mathbf{Q}^{(1)}; \mathbf{A} \equiv i\mathbf{X}^{(0)}; \mathbf{g} \equiv i\mathbf{X}^{(1)}\mathbf{Q}^{(0)}$.
Equation (1.20) can then be written

$$\partial_t \mathbf{b} = \mathbf{A}\mathbf{b} + \mathbf{g} \qquad (1.22)$$

and we seek a solution of the form

$$\mathbf{b}(t) = \mathbf{K}(t)\mathbf{c}(t). \qquad (1.23)$$

We can then write

$\partial_t \mathbf{b} = \partial_t \mathbf{K}\,\mathbf{c} + \mathbf{K}\partial_t c$, so $\mathbf{K}\partial_t \mathbf{c} = \mathbf{g}$ or

$\partial_t \mathbf{c} = \mathbf{K}^{-1}\mathbf{g}$.

Now,

$\mathbf{b}(t) - \mathbf{b}(0) = \mathbf{K}(t)\mathbf{c}(t) - \mathbf{K}(0)\mathbf{c}(0) = \mathbf{K}(t)\mathbf{c}(t) - \mathbf{c}(0)$.

For an initially quiescent Earth, $\mathbf{b}(0) = \mathbf{c}(0) = 0$. Thus,

$$\begin{aligned}
\mathbf{b}(t) &= \mathbf{K}(t)\,(\mathbf{c}(t) - \mathbf{c}(0)) \\
&= \mathbf{K}(t)\int_0^t \partial_\tau \mathbf{c}(\tau)\,d\tau \\
&= \mathbf{K}(t)\int_0^t \mathbf{K}^{-1}(\tau)\,\mathbf{g}(\tau)\,d\tau \\
\mathbf{Q}^{(1)}(t) &= \mathbf{Q}^{(0)}(t)\int_0^t i\,\mathbf{Q}^{(0)\,-1}(\tau)\,\mathbf{X}^{(1)}\,\mathbf{Q}^{(0)}(\tau)\,d\tau. \qquad (1.24)
\end{aligned}$$

In index notation,

$$\begin{aligned}
Q_{ij}^{(1)} &= \exp(i\widehat{\omega}_i t)\int_0^t i\,\exp(-i\widehat{\omega}_i\tau)\,X_{ij}^{(1)}\exp(i\widehat{\omega}_j\tau)\;d\tau \\
&= X_{ij}^{(1)}\,\frac{\exp(i\widehat{\omega}_j t) - \exp(i\widehat{\omega}_i t)}{\widehat{\omega}_j - \widehat{\omega}_i} \\
&= (Z_{ij} - 2\omega_i\delta\widetilde{\omega}_i\delta_{ij})\,\frac{\exp(i\widehat{\omega}_j t) - \exp(i\widehat{\omega}_i t)}{(\omega_j + \omega_i)(\widehat{\omega}_j - \widehat{\omega}_i)} \\
&= Z_{ij}\,\frac{\exp(i\widehat{\omega}_j t) - \exp(i\widehat{\omega}_i t)}{(\omega_j + \omega_i)(\widehat{\omega}_j - \widehat{\omega}_i)} - i\,t\,\delta\widetilde{\omega}_i\,\exp(i\,\widehat{\omega}_i\,t). \qquad (1.25)
\end{aligned}$$

The linearized first order phase term is therefore given by:

$$\begin{aligned}
\exp\left[it\left(\widehat{\omega}_i\delta_{ij} + \frac{\widehat{Z}_{ij}}{\omega_i + \omega_j}\right)\right] &= \exp(i\widehat{\omega}_i t)\delta_{ij} + \\
Z_{ij}\frac{\exp(i\widehat{\omega}_i t) - \exp(i\widehat{\omega}_j t)}{(\omega_i + \omega_j)(\widehat{\omega}_i - \widehat{\omega}_j)} &- i\,t\,\delta\widetilde{\omega}_i\,\exp(i\,\widehat{\omega}_i\,t). \qquad (1.26)
\end{aligned}$$

1.4.2 Asymptotic expansion of the coupled terms

Short wavelength approximation

Specifying the singlets i in terms of the azimuthal order m and an index k that incorporates the radial order number n, the angular order ℓ and the mode type, the seismogram (1.26) can thus be written:

$$u(t) \;=\; u_{pava}(t) \;+\; u_1(t) \;+\; \Re e \sum_{kk'} \frac{\exp(i\widehat{\omega}_k t) - \exp(i\widehat{\omega}_{k'} t)}{(\omega_k + \omega'_k)(\widehat{\omega}_k - \widehat{\omega}_{k'})} \times \sum_{mm'} R^k_m \, Z^{kk'}_{mm'} \, S^{k'}_{m'} \tag{1.27}$$

where $u_{pava}(t)$ is the path average seismogram $\sum_k A_k \exp(i\widehat{\omega}_k t)$ with

$$\begin{aligned} A_k \;&\equiv\; \sum_m R^m_k \, S^m_k \text{and} \\ u_1(t) \;&=\; -\sum_k i\, t\, \delta\widetilde{\omega}_k \, A_k \, \exp(i\widehat{\omega}_k t) \end{aligned}$$

The last term in equation (1.27) becomes rapidly impractical with increasing ℓ. Following [*Li & Tanimoto*, 1993], we derive its asymptotic expansion.
Noting that the coupling between distant multiplets will be small owing to the factor $(\widehat{\omega}_i \,-\, \widehat{\omega}_j)^{-1}$, we can write the frequency in $Z^{kk'}_{mm'}$ $\omega_{k'} \approx \frac{\omega_k + \omega_{k'}}{2} \equiv \omega_{kk'}$, so that

$$Z^{kk'}_{mm'} \;=\; H^{(1)\,kk'}_{mm'} \;-\; \omega^2_{kk'} \, P^{(1)\,kk'}_{mm'} \tag{1.28}$$

Under the assumption that lateral heterogeneity in the Earth varies smoothly in comparison with the wavelength of the modes ($s_{max} \ll min(\ell, \ell')$), $Z^{kk'}_{mm'}$ can be written

$$Z^{kk'}_{mm'} \;=\; 2\,\omega_{kk'} \int_\Omega \delta\omega_{kk'}(\theta,\phi)\, Y^{m\,*}_l(\theta,\phi)\, Y^{m'}_{l'}(\theta,\phi)\, d\Omega \tag{1.29}$$

where Ω is the unit sphere (e.g.[*Romanowicz*, 1987]). The Y^m_l are the fully normalized spherical harmonics defined by [*Edmonds*, 1960] and $\delta\omega_{kk'}$ is given by:

$$\delta\omega_{kk'} \;=\; \frac{1}{2\,\omega_{kk'}} \left[\int_0^{R_\oplus} \delta\mathbf{m}(r,\theta,\phi) \cdot \mathbf{M}_{kk'}(r) r^2\, dr \;-\; \sum_d r^2_d \, h_d(\theta,\phi)\, H^d_{kk'} \right] \tag{1.30}$$

where $R_\oplus$ is the radius of the Earth, $\delta\mathbf{m}$ represents the heterogeneous perturbations to Earth, h_d the perturbations in the radius r_d of the d^{th} discontinuity. The PREM kernels $\mathbf{M}_{kk'}(r)$ and $H^d_{kk'}$ are derived by [*Woodhouse*, 1980].
The source and receiver vectors can be expressed following the results of [*Woodhouse & Girnius*, 1982]:

$$R^k_m(\theta_r,\phi_r) \quad = \quad \sum_{N=-1}^{1} R_{kN}\, Y_l^{Nm}(\theta_r,\phi_r) \tag{1.31}$$

$$S^k_m(\theta_s,\phi_s) \quad = \quad \sum_{M=-2}^{2} S_{kM}\, Y_l^{Mm}(\theta_s,\phi_s), \tag{1.32}$$

where the Y_l^{Nm} are generalized spherical harmonics defined in [*Phinney & Burridge*, 1973] and the R^k_m and S^k_m are defined in Table 1 of [*Woodhouse & Girnius*, 1982].
Making use of the long wavelength approximation for $Z^{kk'}_{mm'}$ and the source-receiver terms defined above and defining $\delta\omega^2_{kk'} = 2\omega_{kk'}\delta\omega_{kk'}$, we may then write:

$$\begin{aligned}\sum_{mm'} R^k_m Z^{kk'}_{mm'} S^{k'}_{m'} \quad = \quad & \left(\frac{(2\ell+1)}{4\pi}\frac{(2\ell'+1)}{4\pi}\right)^{\frac{1}{2}} \sum_{NM} R_{kN} S_{k'M} \times \\ & \int_\Omega \delta\omega^2_{kk'}\, P^N_\ell(\cos\,\theta_{pr}) P^M_{\ell'}(\cos\,\theta_{ps}) \times \\ & \exp\left[i\,(M\phi_{ps} \, - \, N\phi_{pr})\right] d\Omega_p.\end{aligned} \tag{1.33}$$

The integral is taken over the unit sphere. P^N_ℓ are associated Legendre functions. θ_{pr} is the angular distance between scatterer and receiver. ϕ_{pr} is the azimuth of the scatterer from the receiver measured anticlockwise from the South. θ_{ps} is the angular distance between source and scatterer. ϕ_{ps} is the azimuth of the scatterer from the source. These variables are illustrated in Figure 1 of [*Li & Tanimoto*, 1993].

Great-circle approximation and stationary phase expansion

To order $\frac{1}{\ell}$, the associated Legendre function in equation (1.33) can be written (e.g. [*Romanowicz*, 1987]):

$$\left(\frac{2\ell+1}{4\pi}\right)^{\frac{1}{2}} P^N_\ell(\cos\theta) \;=\; \frac{1}{\pi\sqrt{sin\theta}}\,\cos\left(\lambda\theta \,-\, \frac{\pi}{4} \,+\, \frac{N}{2}\,\pi\right) \tag{1.34}$$

We can thus write

$$\sum_{mm'} R_m^k Z_{mm'}^{kk'} S_{m'}^{k'} \;=\; \frac{1}{2\,\pi^2} \sum_{NM} R_{kN} S_{k'M} \int_0^{2\pi} \left[I_1(\phi_p) \;+\; I_2(\phi_p) \right] d\phi_p, \tag{1.35}$$

where the integrals I_1 and I_2 are given by:

$$\begin{aligned} I_1 \;&=\; \int_0^{\pi} \frac{\delta\omega_{kk'}^2}{\sqrt{\sin\theta_{pr}\,\sin\theta_{ps}}} \cos\left[\lambda\,(\theta_{pr} \;+\; \theta_{ps}) \;+\; j\,\theta_{ps} \;+\; \frac{N+M-1}{2}\pi\right] \times \\ &\quad \exp\left[i\,(M\phi_{ps} \;-\; N\phi_{pr})\right] \sin\theta_p\, d\theta_p \end{aligned} \tag{1.36}$$

$$\begin{aligned} I_2 \;&=\; \int_0^{\pi} \frac{\delta\omega_{kk'}^2}{\sqrt{\sin\theta_{pr}\,\sin\theta_{ps}}} \cos\left[\lambda\,(\theta_{pr} \;-\; \theta_{ps}) \;-\; j\,\theta_{ps} \;+\; \frac{N-M}{2}\pi\right] \times \\ &\quad \exp\left[i\,(M\phi_{ps} \;-\; N\phi_{pr})\right] \sin\theta_p\, d\theta_p. \end{aligned} \tag{1.37}$$

Without loss of generality, the source and the receiver can be rotated to the equator such that $S(\frac{\pi}{2}, 0)$ and $R(\frac{\pi}{2}, \Delta)$ (see Figure 1).
The integrands in (1.36) and (1.37) are stationary when θ_p is in the neighborhood of the equator where $\frac{d(\theta_{pr}+\theta_{ps})}{d\theta_p} = 0$, and otherwise osillate rapidly. This allows the application of the method of stationary phase (e.g. [*Romanowicz & Roult*, 1986; *Fetter & Walecka*, 1980]) to (1.36) and (1.37). To zeroth order in $\frac{1}{\ell}$,

$$\begin{aligned} I_1 \;&=\; \delta\omega_{kk'}^2 \left(\frac{2\pi}{\lambda \mid \sin(\theta_{ps} \;+\; \theta_{pr}) \mid}\right)^{\frac{1}{2}} \exp\left[i\,(M\phi_{ps} \;-\; N\phi_{pr})\right] \times \\ &\quad \cos\left[\lambda\,(\theta_{pr} \;+\; \theta_{ps}) \;+\; j\,\theta_{ps} \;+\; \frac{N+M-1}{2}\pi \pm \frac{\pi}{4}\right] \end{aligned} \tag{1.38}$$

where the sign $\pm$ is positive or negative according to the sign of $\sin(\theta_{ps} \;+\; \theta_{pr})$, and

$$\begin{aligned} I_2 \;&=\; \delta\omega_{kk'}^2 \left(\frac{2\pi}{\lambda \mid \sin(\theta_{pr} \;-\; \theta_{ps}) \mid}\right)^{\frac{1}{2}} \exp\left[i\,(M\phi_{ps} \;-\; N\phi_{pr})\right] \times \\ &\quad \cos\left[\lambda\,(\theta_{pr} \;+\; \theta_{ps}) \;-\; j\,\theta_{ps} \;+\; \frac{N-M}{2}\pi \pm \frac{\pi}{4}\right], \end{aligned} \tag{1.39}$$

where the sign $\pm$ is positive or negative according to the sign of $\sin(\theta_{pr} \;-\; \theta_{ps})$.

To perform the ϕ integrals, we note that $I_1(\phi_p)$ oscillates rapidly with ϕ_p between the ranges $\Delta < \phi_p < \pi$ and $2\pi - \Delta < \phi_p < 2\pi$, where its integral vanishes. Similarly, the $I_2(\phi_p)$ integral vanishes in the interval $0 < \phi_p < \Delta$ and $\pi < \phi_p < 2\pi - \Delta$.
the scattering term (1.35) can thus be written:

$$\sum_{mm'} R_m^k Z_{mm'}^{kk'} S_{m'}^{k'} = \sum_{NM} T_{kk'}^{NM} \frac{1}{2\pi} \int_0^{2\pi} \delta\omega_{kk'}^2 \cos(j\phi + \lambda\Delta + \Pi_{NM}) d\phi \tag{1.40}$$

where

$$T_{kk'}^{NM} \equiv \sqrt{\frac{2}{\lambda\pi \sin\Delta}} i^{N+M} R_{KN} S_{K'M'} \tag{1.41}$$

$$\Pi_{NM} \equiv \frac{2(N+M)-1}{4}\pi. \tag{1.42}$$

Substituting 1.40 into (1.27), the $NACT$ seismogram can then be written [*Li & Romanowicz*, 1995]:

$$u(t) = u_{pava}(t) + u_1(t) + \sum_k \sum_{k' \in \Gamma_k} D_{kk'}(t) E_{kk'} \tag{1.43}$$

where Γ_k is the set of multiplets with eigenfrequencies $\omega_{k'} \geq \omega_k$ and the time dependent term is defined as:

$$D_{kk'}(t) \equiv \frac{\exp(i\widehat{\omega}_k t) - \exp(i\widehat{\omega}_{k'} t)}{(\omega_k + \omega_k')(\widehat{\omega}_k - \widehat{\omega}_{k'})}. \tag{1.44}$$

The asymptotic scattering term is given, after keeping inside the integral only the ϕ dependent terms, by

$$E_{kk'}(t) \equiv \frac{1}{2\pi} \left[Q_{kk'}^{(1)} \int_0^{2\pi} \delta\omega_{kk'}^2 \cos(j\phi) d\phi + Q_{kk'}^{(2)} \int_0^{2\pi} \delta\omega_{kk'}^2 \sin(j\phi) d\phi \right], \tag{1.45}$$

where

$$Q_{kk'}^{(i)} \equiv (-1)^{i+1} (1 - \frac{\delta_{kk'}}{2}) \left(P_{kk'}^{(i)} + P_{k'k}^{(i)} \right) \tag{1.46}$$

$$P_{kk'}^{(i)} \equiv g_l^{(1)}(\Delta)T_{kk'}^{(i)} + (-1)^i g_l^{(2)}(\Delta)T_{kk'}^{(i)} \tag{1.47}$$

$$g_l^{(1)}(\Delta) \equiv \sqrt{\frac{2}{\lambda\pi\sin\Delta}}\cos\left(\lambda\Delta - \frac{\pi}{4}\right) \tag{1.48}$$

$$g_l^{(2)}(\Delta) \equiv \sqrt{\frac{2}{\lambda\pi\sin\Delta}}\sin\left(\lambda\Delta - \frac{\pi}{4}\right) \tag{1.49}$$

$$T_{kk'}^{(1)} \equiv \sum_{NM} i^{N+M} R_{kN} S_{k'M} \cos\left(\frac{N+M}{2}\pi\right) \tag{1.50}$$

$$T_{kk'}^{(2)} \equiv \sum_{NM} i^{N+M} R_{kN} S_{k'M} \sin\left(\frac{N+M}{2}\pi\right). \tag{1.51}$$

1.5 Differential travel time kernels by cross-correlation

The major limitation of models derived from travel time tomography is the use of the infinite frequency, ray theoretic approximation combined with a parametrization in blocks. Casting the travel time formalism in terms of the waveform formalism NACT would allow to take into account finite frequency effects, thereby potentially improving models derived from travel time observables. In this section, we extend the formalism of NACT developed by [*Li & Romanowicz*, 1995] to model travel time differentials computed by cross-correlation.

Without loss of generality, the expressions developed here are for *S*-*SS* travel time differentials. We denote by $u_S(\tau)$ and $u_{SS}(\tau\,+\,\Delta\tau)$ the absolute travel times of the S and SS phase in the symmetric, non-rotating, elastic and isotropic (SNREI) Earth, and by $\delta u_S(\tau)$ and $\delta u_{SS}(\tau\,+\,\Delta\tau)$ the travel times of the scattered S and SS phases in the 3D Earth, respectively. At a time τ in the 3D Earth, a seismogram is written as the sum of an SNREI and a scattered component:

$$u(\tau) \;=\; u_S(\tau) + \delta u_S(\tau) \tag{1.52}$$

and

$$u(\tau + \Delta\tau) \;=\; u_{SS}(\tau + \Delta\tau) + \delta u_{SS}(\tau + \Delta\tau) \tag{1.53}$$

1.5.1 Cross-correlation in SNREI Earth

The cross-correlation function $C_0(\Delta t)$ is defined by

$$C_0(\Delta t) \,=\, \int_{-\infty}^{\infty} u_S^H(\tau)\, u_{SS}(\tau \,+\, \Delta t) d\tau, \tag{1.54}$$

where $u_S^H(\tau)$ is the Hilbert transform of $u_S(\tau)$ defined by

$$u_S^H(\tau) \,\equiv\, \frac{1}{\pi} \int_{-\infty}^{\infty} \frac{u(\xi)}{\xi - \tau}\, d\xi. \tag{1.55}$$

Substituting into (1.54) the expression for the SNREI seismogram

$$u(\tau) \,=\, \Re e \sum_k A_k \, \exp(i\omega_k \tau), \tag{1.56}$$

where the source-receiver vector is defined as $A_k \,\equiv\, \sum_m R_k^m S_k^m$, Δt_0 is the differential travel time in the SNREI Earth that satisfies the equality

$$\begin{aligned} \frac{\partial C_0}{\partial \Delta t}(\Delta t_0) \quad &= \quad \int_{-\infty}^{\infty} \Re e \left\{ i \sum_k A_k \, \exp\left(i\omega_k \tau\right) \right\} \times \\ & \qquad \Re e \left\{ i \sum_k A_k \, \omega_k \, \exp\left[i\omega_k(\tau + \Delta t)\right] \right\} d\tau \\ &= \quad 0. \end{aligned} \tag{1.57}$$

1.5.2 Cross-correlation in 3-D Earth

We define the cross-correlation in the 3-D Earth by

$$C_1 \,=\, C_0 \,+\, \delta C \tag{1.58}$$

where δC is given by:

$$\delta C \;=\; \int_{-\infty}^{\infty} \left[\delta u_S^H(\tau) u_{SS}(\tau \;+\; \Delta\tau) \;+\; u_S^H(\tau)\, \delta u_{SS}(\tau \;+\; \Delta\tau)\right] d\tau. \tag{1.59}$$

The differential travel time in the 3-D Earth is ϵ such that

$$\frac{\partial C_1}{\partial \Delta t}(\Delta t_0 \;+\; \epsilon) \;=\; 0. \tag{1.60}$$

Substituting yields

$$\frac{\partial C_1}{\partial \Delta t}(\Delta t_0 \;+\; \epsilon) \;=\; \frac{\partial C_0}{\partial \Delta t}(\Delta t_0 \;+\; \epsilon) \;+\; \frac{\partial \delta C}{\partial \Delta t}(\Delta t_0 \;+\; \epsilon). \tag{1.61}$$

Keeping only the first order terms of the Taylor expansion and using the identity (1.57) gives [*Romanowicz*, private communication]:

$$\frac{\partial C_1}{\partial \Delta t}(\Delta t_0 \;+\; \epsilon) \;=\; \epsilon\, \frac{\partial^2 C_0}{\partial \Delta t^2}(\Delta t_0) \;+\; \frac{\partial \delta C}{\partial \Delta t}(\Delta t_0) \;=\; 0. \tag{1.62}$$

The travel time differential ϵ is then given by

$$\epsilon \;=\; -\frac{\frac{\partial \delta C}{\partial \Delta t}}{\frac{\partial^2 C_0}{\partial \Delta t^2}}\,(\Delta t_0) \equiv \frac{N}{D}\,(\Delta t_0), \tag{1.63}$$

where

$$\begin{aligned} N \;&=\; \int_{-\infty}^{\infty} \left[\delta u_S^H(\tau) \frac{\partial u_{SS}(\tau + \Delta t)}{\partial \Delta t} \;+\; u_S^H(\tau) \frac{\partial \delta u_{SS}(\tau + \Delta t)}{\partial \Delta t}\right] d\tau \\ &=\; A + B, \end{aligned} \tag{1.64}$$

and

$$D = \int_{-\infty}^{\infty} u_S^H(\tau) \frac{\partial^2 u_{SS}(\tau + \Delta t)}{\partial \Delta t^2}. \tag{1.65}$$

The scattered field $\delta u(\tau)$ can be expressed as (*Li & Tanimoto*, 1993, *Tanimoto*, 1995)

$$\delta u(\tau) \;=\; \Re e \int_0^a \int_0^\Delta dr d\phi\, K(r,\phi,\tau)\, \delta m(r,\phi). \tag{1.66}$$

The kernel K is given by

$$K(r,\phi,t) \;=\; \sum_{kk'} g_{kk'}(t) L_{kk'}(r,\phi), \tag{1.67}$$

and the time dependent and the spatial terms are respectively:

$$g_{kk'}(t) \quad = \quad \frac{\exp(i\omega_k t) - \exp(i\omega_{k'} t)}{\omega_k^2(\omega_k^2 \,-\, \omega_{k'}^2)} \tag{1.68}$$

and

$$L_{kk'}(r,\phi) \quad = \quad \frac{i^{N+M}}{\sqrt{2\pi\lambda\sin\Delta}} R_k^N S_k^M \cos(j\phi + \lambda\Delta + \Pi_N^M) M_{kk'}(r) \tag{1.69}$$

where $\lambda \equiv \ell + \frac{1}{2}$, $j \equiv \ell' - \ell$, and $\Pi_N^M \equiv \frac{2(N+M)-1}{4}\pi$

Noting that the Hilbert transform of $g_{kk'}(\tau)$ is $i\, g_{kk'}(\tau)$, and defining

$$\gamma_{kk'}(t) \equiv \dot{g}_{kk'}(t) \;=\; i \frac{\omega_k \,\exp(i\omega_k t) - \omega_{k'} \,\exp(i\omega_{k'} t)}{\omega_k^2\,(\omega_k^2 - \omega_{k'}^2)}, \tag{1.70}$$

gives

$$\begin{aligned}
A \quad &= \quad \int_{-\infty}^{\infty} \Re e \left\{ i \sum_{kk'} g_{kk'}(\tau) \int_0^a \int_0^\Delta dr\, d\phi L_{kk'}(r,\phi) \delta m(r,\phi) \right\} \times \\
&\quad\quad \Re e \left\{ i \sum_k A_k\, \omega_k \,\exp\left[i\omega_k(\tau + \Delta t)\right] \right\} d\tau & (1.71) \\
B \quad &= \quad \int_{-\infty}^{\infty} \Re e \left\{ i \sum_k A_k \,\exp\left(i\omega_k \tau\right) \right\} \times \\
&\quad\quad \Re e \left\{ \sum_{kk'} \gamma_{kk'}(\tau + \Delta t) \int_0^a \int_0^\Delta dr\, d\phi L_{kk'}(r,\phi) \delta m(r,\phi) \right\} d\tau & (1.72) \\
D \quad &= \quad \int_{-\infty}^{\infty} \Re e \left\{ i \sum_k A_k \,\exp\left(i\omega_k \tau\right) \right\} \times \\
&\quad\quad \Re e \left\{ \sum_k A_k\, \omega_k^2 \,\exp\left[i\omega_k(\tau + \Delta t)\right] \right\} d\tau, & (1.73)
\end{aligned}$$

and the perturbed travel time is given by

$$\epsilon = \frac{A + B}{D}(\Delta t_0). \tag{1.74}$$

1.6 Inversion

We employ a stochastic formulation ([*Tarantola & Valette*, 1982; *Jackson*, 1979; *Gubbins & Bloxham*, 1985]) whereby the probability distribution of model vector $\underline{\mathbf{m}}$ for a particular choice of *a priori* constraints is given by

$$\begin{aligned} P(\underline{\mathbf{m}}) &= \exp\left[-\frac{1}{2}\left(\underline{\mathbf{u}}(\underline{\mathbf{m}}) - \underline{\mathbf{d}}\right)^T \underline{\underline{\mathbf{C}}}_d^{-1} \left(\underline{\mathbf{u}}(\underline{\mathbf{m}}) - \underline{\mathbf{d}}\right)\right] \times \\ & \exp\left[-\frac{1}{2}\left(\underline{\mathbf{m}} - \underline{\mathbf{m}}_0\right)^T \underline{\underline{\mathbf{C}}}_m^{-1} \left(\underline{\mathbf{m}} - \underline{\mathbf{m}}_0\right)\right] \end{aligned} \tag{1.75}$$

where $\underline{\mathbf{u}}(\underline{\mathbf{m}})$ is a seismogram evaluated for model $\underline{\mathbf{m}}$.
The maximum *a posteriori* probability is thus obtained by minimizing the objective function

$$\Phi\left(\underline{\mathbf{m}}\right) = \left(\underline{\mathbf{u}}(\underline{\mathbf{m}}) - \underline{\mathbf{d}}\right)^T \underline{\underline{\mathbf{C}}}_d^{-1} \left(\underline{\mathbf{u}}(\underline{\mathbf{m}}) - \underline{\mathbf{d}}\right) + \left(\underline{\mathbf{m}} - \underline{\mathbf{m}}_0\right)^T \underline{\underline{\mathbf{C}}}_m^{-1} \left(\underline{\mathbf{m}} - \underline{\mathbf{m}}_0\right). \tag{1.76}$$

If the objective function $\Phi(\underline{\mathbf{m}})$ is unimodal, the global minimum can be obtained by making use of the iterative Newton-Raphson scheme to its Fréchet derivative (e.g. [*Li*, 1990])

$$\underline{\mathbf{m}}_{\mathbf{i+1}} = \underline{\mathbf{m}}_{\mathbf{i}} + \left(\underline{\underline{\mathbf{A}}}_{\mathbf{i}}{}^T \underline{\underline{\mathbf{C}}}_{\mathbf{d}}{}^{-1} \underline{\underline{\mathbf{A}}}_{\mathbf{i}} + \underline{\underline{\mathbf{C}}}_{\mathbf{m}}{}^{-1}\right)^{-1} \times \left[\underline{\underline{\mathbf{A}}}_{\mathbf{i}}{}^T \underline{\underline{\mathbf{C}}}_{\mathbf{d}}{}^{-1} \left(\underline{\mathbf{d}} - \underline{\mathbf{u}}(\underline{\mathbf{m}}_{\mathbf{i}})\right) - \underline{\underline{\mathbf{C}}}_{\mathbf{m}}{}^{-1} \left(\underline{\mathbf{m}}_{\mathbf{i}} - \underline{\mathbf{m}}_0\right)\right], \tag{1.77}$$

where $\underline{\underline{\mathbf{A}}}_{\mathbf{i}}$ is the matrix of partial derivatives evaluated for model i

$$\underline{\underline{\mathbf{A}}}_{\mathbf{i}} \equiv \left[\frac{\partial \underline{\mathbf{u}}(\underline{\mathbf{m}})}{\partial \underline{\mathbf{m}}}\right]_{\underline{\mathbf{m}}=\underline{\mathbf{m}}_{\mathbf{i}}}. \tag{1.78}$$

1.6.1 Data covariance matrix

For each datum in vector $\underline{\mathbf{d}}$ in equation 1.77, we set the corresponding diagonal element of the matrix $\underline{\underline{\mathbf{C}}}_d^{-1}$ equal to a weight ω^2. The weighting function ω is composed of three parts: a weight associated to the error in the datum ω_e, a scaling related to the redundancy within a wavepacket ω_n, and a weight associated to the redundancy among different wavepackets ω_r, such that

$$\omega \equiv \omega_e \omega_n \omega_r. \tag{1.79}$$

Assuming that the systematic error is associated to the amplitude of the data, we set $\omega_e \equiv \frac{1}{d_{\mathrm{rms}}}$ where d_{rms} is the root mean square amplitude of the wavepacket.
For a wavepacket consisting of n data points, in the extreme case where the vector of data points can be derived from a forward operator represented by a matrix of rank n, it would have a weight of 1. In the opposite extreme case where each additional datum in the wavepacket provides no additional information on Earth structure than can be derived from the first datum (*i.e.* that the operator consists of a matrix of rank 1), we would assign it a weight $\frac{1}{n}$, where n is the number of data points in the wavepacket. Since the information contained in the data for a given wavepacket is somewhere between these two extreme cases, we associate to each wavepacket a 'compromise' weight $\omega_n = n^{-\frac{1}{2}}$.
Finally, the scaling corresponding redundancy among different two different wavepackets i and j for wavepacket i is determined by making use of a correlation function c_{ij} where $c_{ij} = 0$ for very different ray paths and $c_{ij} = 1$ for identical ones. We then set $\omega_r^i \equiv \left(\sum_j c_{ij}\right)^{-1}$. The factor c_{ij} is defined by the relation $c_{ij} \equiv p_{ij} g_{ij}$, where p_{ij} is 1 for identical phases and 0 otherwise. The coefficient g_{ij} varies between 0 (no redundancy among paths) and 1 (for g_{ii}). A detailed description of the derivation of the factor g_{ij} for a given geometry is given in [*Li & Romanowicz*, 1996], appendix A.

1.6.2 Model covariance matrix

Due to the mixed-determined nature of the inverse problem in seismology, it is not possible to derive a unique mantle model from the seismic data alone. The model covariance matrix $\underline{\underline{\mathbf{C}}}_m$ represents additional prejudice that allows to single out a particular model from the (infinite) set of possible solutions. We define the model covariance matrix through the use of the penalty function $\underline{\mathbf{m}}^T \underline{\underline{\mathbf{C}}}_m^{-1} \underline{\mathbf{m}}$ that is given the form:

$$
\begin{aligned}
\underline{\mathbf{m}}^T \underline{\underline{\mathbf{C}}}_m^{-1} \underline{\mathbf{m}} \;=\; & \int\!\!\int \eta_1 m^2 + \eta_2 \left(\frac{\partial m}{\partial r}\right)^2 + \eta_3 \left(\frac{\partial^2 m}{\partial r^2}\right)^2 + \eta_4 \left(\nabla_1 m\right)^2 dr\, d\Omega \,+ \\
& \int \eta_5 \left(m_{r=r+} - m_{r=r-}\right)^2 + \eta_6 \left(\frac{\partial m}{\partial r}|_{r=r+} - \frac{\partial m}{\partial r}|_{r=r-}\right)^2 + \\
& \eta_7 \left(\frac{\partial^2 m}{\partial r^2}|_{r=r+} - \frac{\partial^2 m}{\partial r^2}|_{r=r-}\right)^2 d\Omega \,+ \\
& \sum_{i=1}^{n_{disc}} \int d\Omega \left[\alpha_i \left(\delta r_i\right)^2 + \beta_i \left(\nabla_1 \delta r_i\right)^2\right]
\end{aligned}
\tag{1.80}
$$

where m is the model $\partial \ln(V_s)$, $r+$ and $r-$ the radii just above and just below the 670 km discontinuity respectively, δr_i the undulation of the n_{disc} mantle discontinuities, and the parameters η_1 through η_9 and α_i, β_i are damping parameters adjusted empirically. Clearly, there are many other ways this penalty function could be defined. Regularization could instead be applied explicitely, for example by incorporating constraints directly from mineralogical results.

The theoretical context being laid out, we now proceed to its application to the modeling of data.

Chapter 2

Imaging 3-D Spherical Convection Models: What Can Seismic Tomography Tell Us About Mantle Dynamics ?

2.1 Abstract

We assess whether current global seismic tomography can resolve parameters characterizing mantle dynamics, in particular 1) a viscosity increase from the upper to the lower mantle, 2) an endothermic phase transition at the 670 km discontinuity, 3) heat flux across the core-mantle boundary and 4) the effect of the motion of rigid surface plates on the convection planform. We apply a 'linear seismic filter' to numerical convection models that incorporate the desired physical parameters, assuming that the shear velocity perturbations depend only on the convectively induced temperature variations. We show that the differences between the characteristic spectral patterns of convection models are preserved by the filtering process. Comparison with actual 3D seismic mantle models indicates that the effect of rigid plates dominates the spectral characteristics of the models. We estimate the effect of spatial aliasing of higher order structure into a lower order model, and find that the structure retrieved by inversion is more distorted by the effects of the aliasing than

by those due to uneven ray coverage. This effect is strongest at shorter wavelengths and near the core-mantle boundary. We also find that the proper choice of radial smoothing parameters is crucial for detecting subtle signatures such as that of an endothermic phase transition at the 670 km discontinuity.

2.2 Introduction

Comparisons between 3-D spherical convection models and global mantle models derived from seismic tomography can help constrain physical parameters such as the heat flux from the core, the Clapeyron slope of various phase transitions, the radial viscosity profile, and the effect of rigid plate motion at the Earth's surface on the convective planform of the mantle. Numerical models of mantle convection incorporating separately the effects of each of these parameters provide example 'signatures' of the corresponding physical phenomenon. Once identified, it is possible to seek the same signatures in models obtained from the inversion of seismic data. However, geodynamic models are generally developed at much greater spatial resolution than models obtained by seismic tomography. In order to compare the spectral characteristics of the two types of models, it is necessary to bring the numerical model to the level of resolution of that of the images derived from tomography [*Tackley et al.*, 1994].

Geodynamic models resulting from a simple truncation to low order differ in three fundamental ways from the seismological representation of the Earth. First the tomography represents a snapshot in time of what is modelled in numerical convection computations. Second, the structure derived from the latter has not been subjected to the limited sampling process of tomography dictated by limited ray coverage and frequency band of the waveforms used in the inversion. Finally, simple truncation to a lower order does not take into account the aliasing caused by the mapping of small scale Earth structure into long wavelength models.

The procedure we use bridges the difference in sampling between the two types of models by the application of a 'linear tomographic filter' to the geodynamic data. We show that the resulting filtered models are suitable for comparison with tomography, thus allowing a fairly realistic evaluation of the resolving power of seismic imaging in relation to various model parameters [*Johnson et al.*, 1993]. We use spectral heterogeneity maps (SHM) representing the root mean square (rms) amplitude as a function of spherical harmonic degree and mantle depth to illustrate the models in wavenumber space. The degree of resolution is estimated by comparing radial rms amplitudes and by constructing SHMs of the difference between input and output models representing the structure unresolved by the seismic filter.

2.3 Method

We use as input models the results from eight de-meaned 3-D spherical convection calculations by [*Bunge et al.*, 1997; *Bunge & Richards*, 1996] (Figures 1 and 2, left columns). To circumvent the issue of time-dependence, we have selected models that have achieved statistical stability. We convert the temperature perturbations to shear wave velocity perturbations using a constant δT to $\delta \ln(V_s)$ scaling. We wish to compute synthetic seismograms which duplicate the set of source-receiver pairs used by [*Li & Romanowicz*, 1996] (hereafter refered to as *L&R*) to develop the SH velocity model *SAW12D* using the non-linear asymptotic coupling theory of [*Li & Romanowicz*, 1995] . The waveforms obtained can then be inverted for structure expanded to the desired spherical harmonic order. This process is nevertheless computationally intensive and it is well known that, under the assumption of linearity, the model $\underline{\mathbf{m}}_{tomo}$ resulting from the inversion of synthetics generated through an input model $\underline{\mathbf{m}}_{conv}$ are related by

$$\underline{\mathbf{m}}_{tomo} = \underline{\underline{\mathbf{R}}}\,\underline{\mathbf{m}}_{conv} \tag{2.1}$$

where $\underline{\underline{\mathbf{R}}}$ is the resolution matrix. The operator $\underline{\underline{\mathbf{R}}}$ thus acts as a 'linear tomographic filter' which, when applied to a particular model, reveals how the latter would be resolved by the tomography. The condition of linearity is however not pertinent to many waveform fitting techniques, which require inverting the data by the iterative linearization of the problem. The matrix $\underline{\underline{\mathbf{R}}}$ therefore should be model-dependent and it will accurately predict $\underline{\mathbf{m}}_{tomo}$ only in the vicinity of the model for which it was derived. In the case of *SAW12D*, convergence was obtained after only a few iterations so that application of the method described above is expected (and has been verified) to constitute a viable first order approximation to the complete tomographic process. Here, we make use of the operator $\underline{\underline{\mathbf{R}}}$ derived in the last iteration of the computation of *SAW12D* to simulate the ray sampling by the transverse components of $9,626$ body wave seismograms low-pass filtered at 32 seconds from 716 events and of $7,919$ first and second orbit surface wave traces from 687 events low-pass filtered at 80 seconds, and the inversion of the resulting synthetic traces for structure up to spherical harmonic degree 12.

We parametrize input and output models laterally using spherical harmonics up to degree 12, and radially in Legendre polynomials up to degree 5 in the upper mantle and up to degree 7 in the lower mantle, with a discontinuity at 670 km, as in model *SAW12D*. The convection models [*Bunge et al.*, 1997; *Bunge & Richards*, 1996] in the left column of Figure 1 correspond to an isoviscous mantle with a Rayleigh number of $1.1 * 10^8$ for the reference model (Figure 1 (a)). Those in the left column of Figure 2 result from the introduction of a thirty-fold viscosity contrast in the lower mantle. The models at the top (Figures 1 & 2 (a)) represent compressible flow and are purely internally heated. In the second row (Figures 1 & 2 (b)), a strong endothermic phase transition with Clapeyron slope $\gamma = -4MPa/K$ is introduced. In the third row (Figures 1 & 2 (c)), heat flux from the core is added to Figures 1 & 2 (a), by imposing a constant temperature of T=3,450K at the core-mantle boundary (CMB), corresponding to 38% and 17% bottom heating for the isoviscous and the layered viscosity models, respectively. Finally, the bottom models (Figures 1 & 2 (d)) are incompressible, internally heated, and incorporate the effects of the current motion of rigid plates at the surface. It has been shown by *Bunge & Richards (1996)* that the layered viscosity version of this model (Figure 2 (d)) matches rather well the predominantly red heterogeneity spectrum inferred from the geoid [*Richards et al.*, 1988] and observed in current tomographic models [*Su & Dziewonski*, 1991].

In the center columns of Figures 1 and 2, we show the results of applying relation (2.1) to the models in the left columns. The general spectral characteristics of the input models have been preserved despite moderate damping of the rms amplitudes which results from the size penalty in the computation of *SAW12D*. The strong 'reddening' effect caused by the viscosity layering shown in Figure 2 remains prominent in the tomographic models, as do the signatures of bottom heating above the CMB in the layered viscosity case (Figure

2 (g)) and in the short wavelength planform of the isoviscous case (Figure 1 (g)). On the other hand, the distinct spectral peaks present at degrees two and higher above the 670 km discontinuity for the layered viscosity model with a phase transition (Figure 2 (b)) are more attenuated, especially at high degrees (Figure 2 (f) & (j)). Figures 1 & 2 (i) - (l) further illustrate the attenuation of prominent short wavelength features in all models, resulting from the choice of penalties favoring smooth features, in particular the transition from the upper to the lower mantle as discussed below. It is also interesting to note that the phase transition is better resolved in the isoviscous case (Figure 1 (f)), reflecting the fact that, in the model of Figure 2, the seismic signal at that depth is dominated by the effect of the viscosity contrast across the phase boundary. Finally, the comparison between Figures 1 & 2 (d) and (h) shows that, apart from a slight amplitude attenuation, the spectral characteristics of the presence of surface plates are for the most part recovered by the tomographic filter.

2.3.1 Aliasing

To investigate how short wavelength heterogeneity is 'seen' by long wavelength tomography, we generate synthetics through the layered viscosity convection model with a phase transition expanded up to degree 12 (Figure 3 (a)) and invert the traces for structure up to degree 6 (Figure 3 (b)) and up to degree 12 (Figure 3 (c)). The difference between the first 6 degrees of both models thus constitutes the amount of aliasing of degrees 7-12 into the long wavelength model (degrees 0-6) (Figure 3 (d)). The aliasing increases with depth and peaks at the CMB where small structure contaminates all degrees up to and including the degree 0 term. The amplitude of the contamination exceeds that of the unresolved structure (Figure 3 (e)), in particular at higher degrees and increasingly with depth. Nevertheless, the dominant characteristics of the spectrum remain preserved in both inversions in spite of the fact that much of the power in the model is at degrees 7 and above (see Figure 2 (b)).

2.3.2 Effects of the regularization

We now test the hypothesis that the relative lack of resolution at the bottom of the upper mantle for the layered viscosity model with a phase transition is due to the a priori size penalty imposed in the original inversion. We do this by relaxing the continuity constraint at 670 km and drastically reducing the damping on the radial curvature of the model. The SHM resulting from the waveform inversion with the set of reduced damping parameters is shown in Figure 4 (a). We see that the peaks at all degrees are now recovered with an attenuation similar to that of the other models. For consistency, we verify that the signature of the phase transition is not an artifact of the new set of damping parameters. Figure 4 (b) represents the linear filter corresponding to the new penalty applied to the two-layered, internally heated model (Figure 2 (a)). The inverted structure is seen to be largely unaffected by the new conditions (compare with Figures 2 (e) & (l)), and in particular does not spuriously produce the signature of a phase change. This experiment suggests that imposing a strong roughness penalty between the upper and the lower mantle may impede the ability to image the effects of the phase change.

2.4 Discussion

Our results indicate that tomography can resolve characteristic signatures of input convection models. There is substantial loss in rms amplitudes in particular for the layered viscosity model in the presence of a phase transition due to the imposition of a strong penalty on discontinuity across the 670 km boundary. The input structure is nevertheless recovered when that condition is relaxed.

The spectral characteristics of the whole mantle seismic model *SAW12D* (figure 5 a) & b)) most closely resemble those of figures 1 (d) and 2 (d), indicating that the effect of the stiff plates is dominant. There is not much evidence for the presence of a phase transition or bottom heating, but we have shown that the choice of smoothing parameters is critical for the recovery of such signatures. Inasmuch as the convection calculations are valid, this suggests that the somewhat *ad hoc* choice of *a priori* smoothing conditions used in inversions of whole mantle structure could be guided using experiments such as those presented here to gain further insight into the nature of mantle convection.

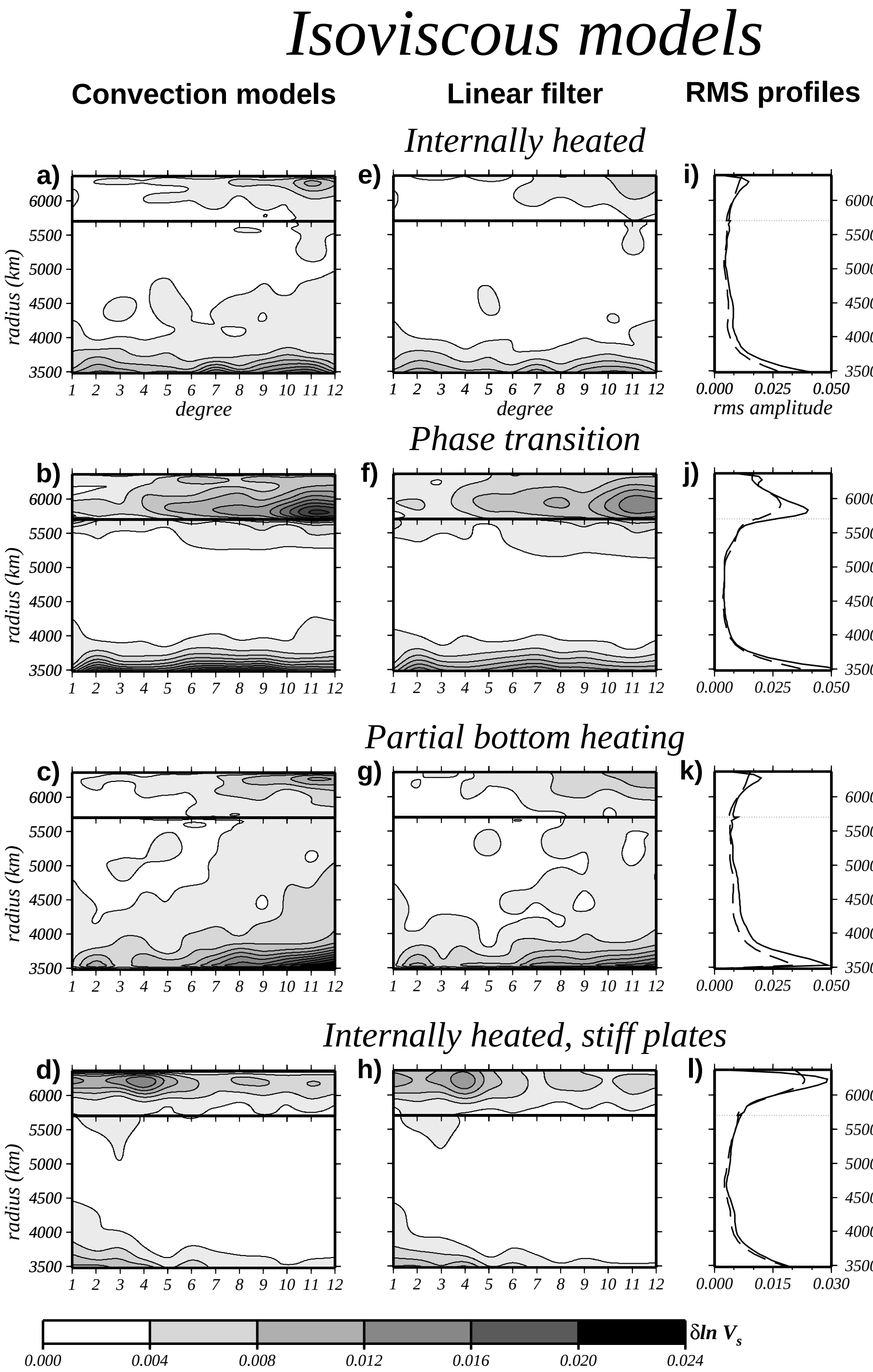

Figure 2.1. Isoviscous convection models (left) and the corresponding linear filters (middle). The isocontours represent the rms amplitude for each spherical harmonic degree (horizontal scale) at each radius (vertical scale). The 670km discontinuity is represented by a horizontal line. The corresponding radial rms profiles are given in the right column where the solid lines represent the input models and the dashed lines the inversion results.

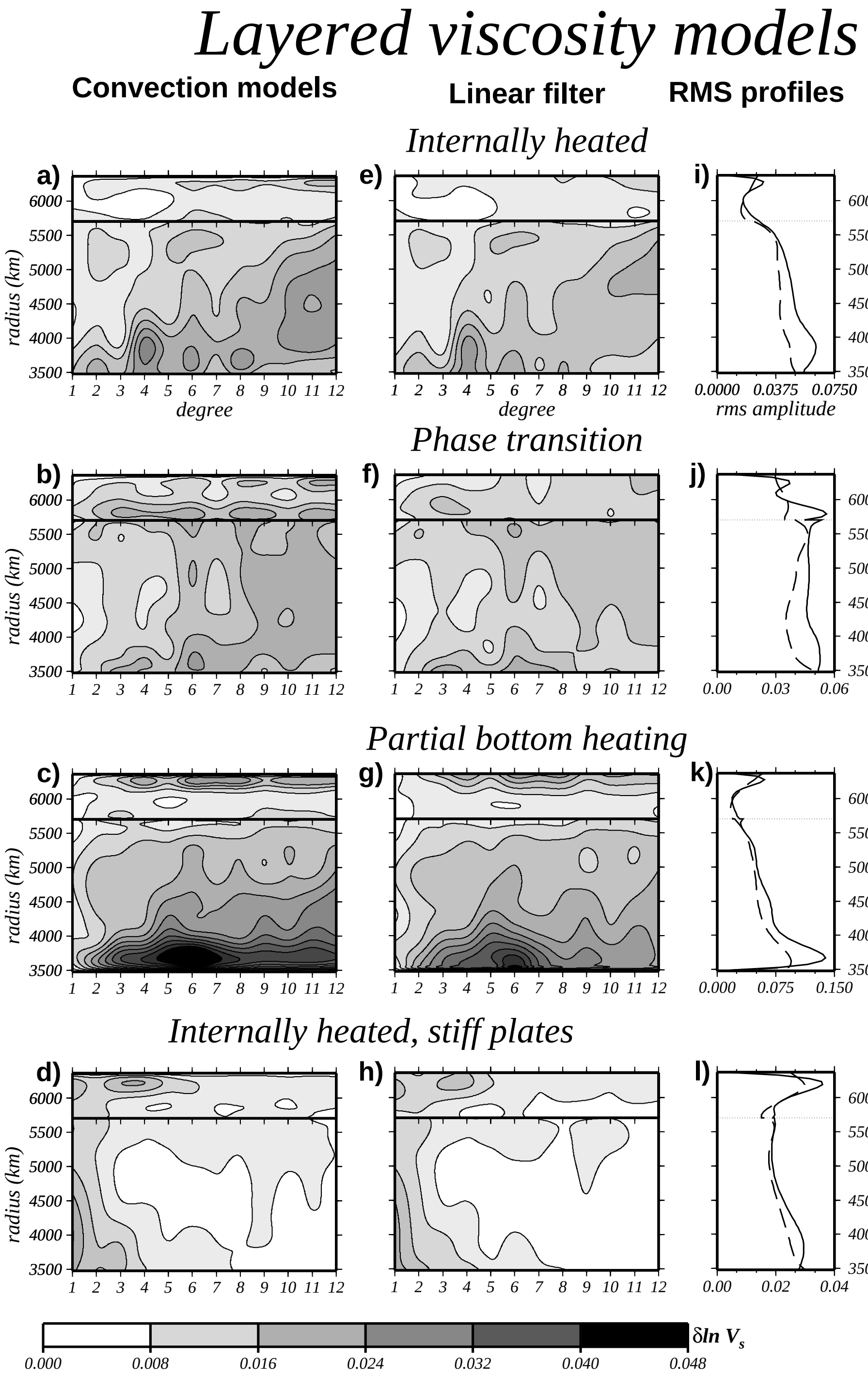

Figure 2.2. Same as Figure 1 for layered viscosity convection models.

Figure 2.3. a) Layered viscosity model with a phase transition (first 6 of 12 degrees) ; b) Inversion for up to degree 6 of degree 12 model synthetics ; c) Inversion for up to degree 12 of degree 12 model synthetics ; d) difference between b) and c) giving a measure of the aliasing of high degree structure (degrees 7-12) into long wavelength models (degrees 0-6) ; e) difference between a) and c) giving a measure of the structure unresolved by the waveform inversion.

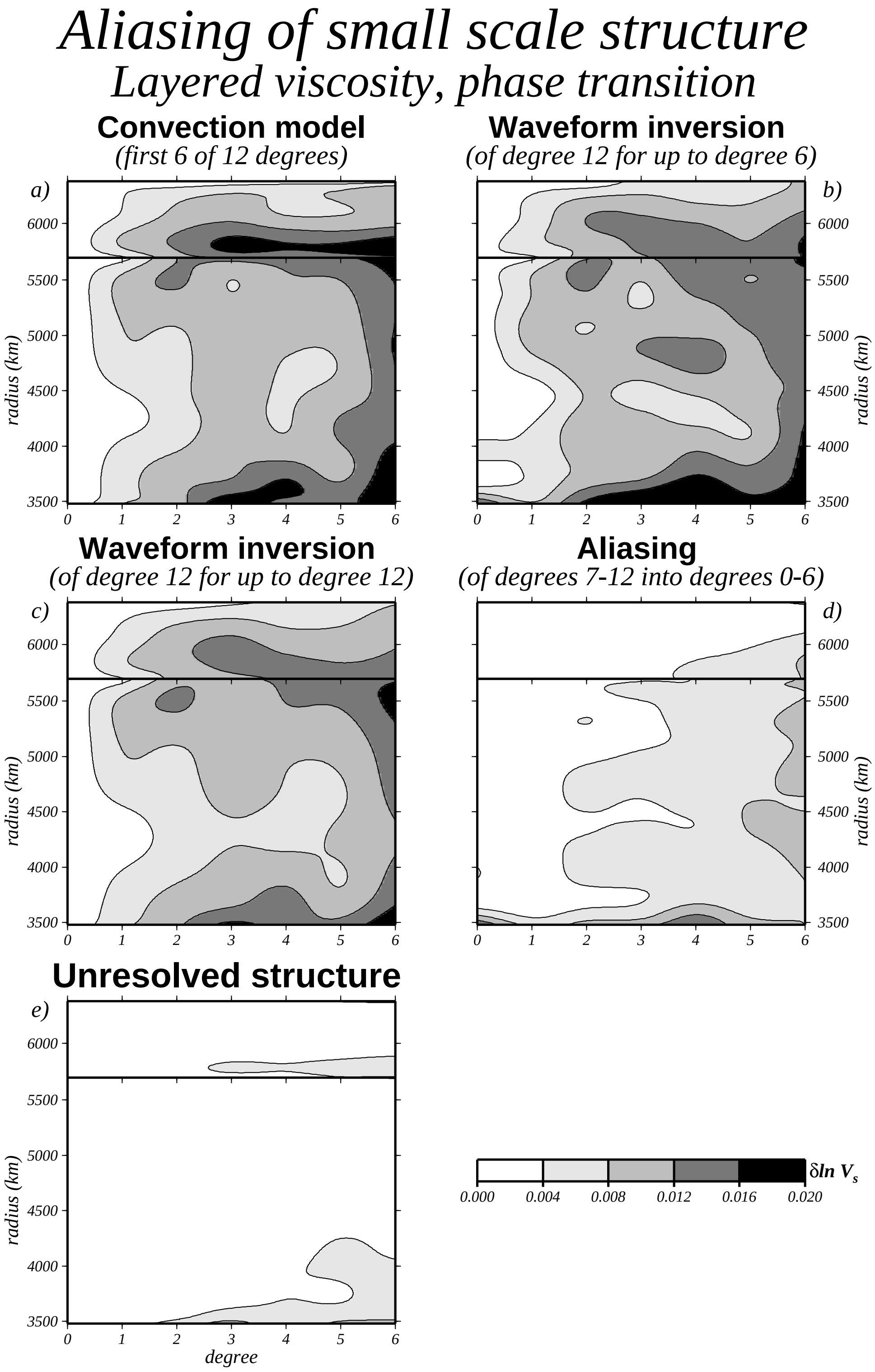
Aliasing of small scale structure
Layered viscosity, phase transition
Convection model
(first 6 of 12 degrees)
Waveform inversion
(of degree 12 for up to degree 6)
Waveform inversion
(of degree 12 for up to degree 12)
Aliasing
(of degrees 7-12 into degrees 0-6)
Unresolved structure
a)
b)
c)
d)
e)
radius (km)
degree
δln V_s
0.000
0.004
0.008
0.012
0.016
0.020

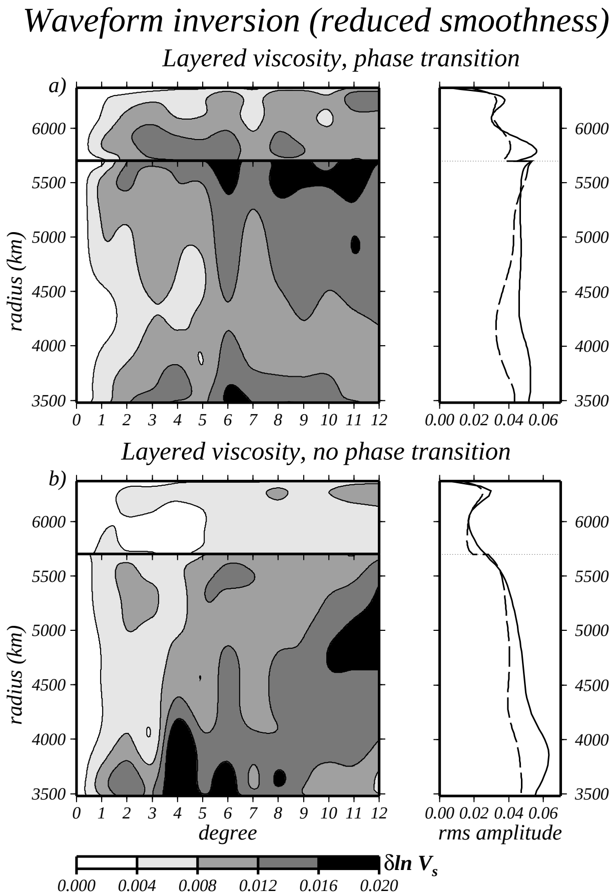

Figure 2.4. a) Inversion results for the layered viscosity model with a phase transition, with weak smoothness constraints across the 670 km discontinuity. In the right part of the figure, the solid line represents the rms of the input convection model and the dashed line that of the inverted model b) Same as a) but with the internally heated-layered viscosity model. No spurious phase change signature is seen in this case.

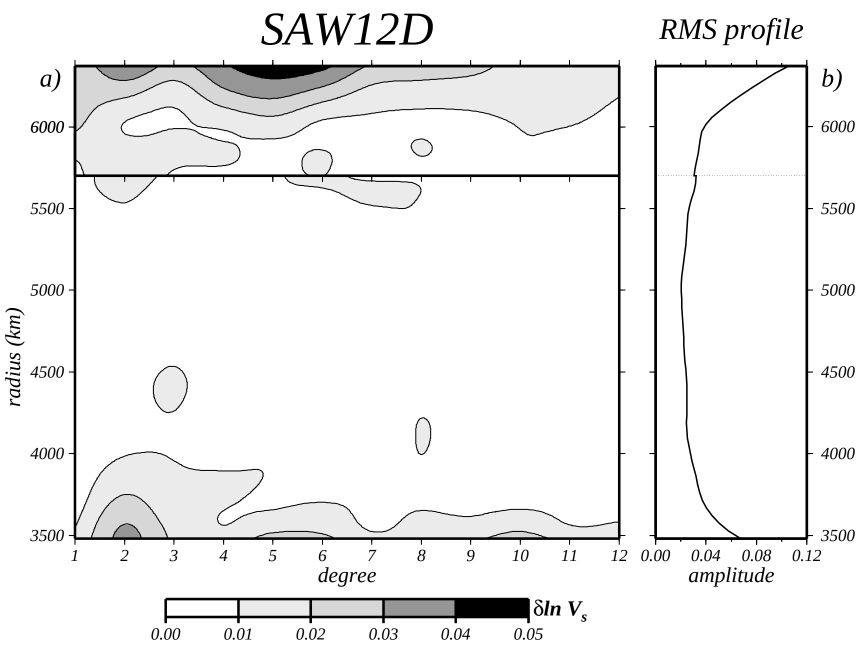

Figure 2.5. a) Spectral heterogeneity map of the seismic model *SAW12D* [*Li & Romanowicz*, 1996]; b) Radial profile of the rms velocity fluctuations in *SAW12D*.

Chapter 3

A comparison between tomographic and geodynamic models of the Earth's mantle

Abstract

We compute tomographic images of the short and long wavelength expansions of a 3-D spherical convection simulation to a resolution comparable to that of current global seismic models of the mantle. The simulation incorporates realistic thermal effects associated with convection in the mantle, namely, 20% bottom heating and phase transitions at 410 km and 670 km. A depth-dependent viscosity profile, and the history of plate motions starting in the mid-Mesozoic are also imposed. We show that tomography recovers the image of the convection simulation well, making it a useful tool to investigate physical parameters characteristic of mantle convection, in conjunction with geodynamic modeling. Our results indicate that the part of the temperature field corresponding to cold mantle heterogeneity in the convection simulation agrees relatively well with the fast velocities derived from tomography, but that current convection computations are lacking some key ingredients necessary to reproduce the character of upwellings correctly. Contingent upon the accuracy of the time dependence of the plate reconstruction, we place an upper bound of -4 $MPa.K^{-1}$ on the Clapeyron slope of the phase transition at 670 km.

Comparisons between the images of the short and long wavelength model (developed up to degrees 32 and 12, respectively) provide insight into the spectral leakage in waveform inversions of actual data. We show that contamination of long-wavelength models by small-scale structure is present at all depths, increases with spherical harmonic degree, and has a peak magnitude of the order of 1% perturbation from *PREM*. Although this effect is small in absolute terms, it is significant on the scale of the models and casts doubts on the reliability of the smallest amplitude component of the heterogeneity pattern in long wavelength seismic images of the whole mantle, particularly in the bulk of the lower mantle.

3.1 Introduction

Three-dimensional images of the Earth's deep mantle obtained by seismic tomography provide us with increasingly accurate constraints on the large scale dynamics that drive plate motions. Since the earliest global tomographic models of the upper mantle [*Woodhouse & Dziewonski*, 1984; *Nataf et al.*, 1986], and even earlier regionalized models (e.g. [*Lévêque*, 1980; *Okal et al.*, 1983]), it has been shown that the velocity structure in the uppermost mantle correlates with surface tectonics and that this correlation breaks down below about 250 km, with, in particular, a strong "degree 2" pattern in the transition zone [*Masters et al.*, 1982; *Souriau & Souriau*, 1983]. This pattern is shifted to the west with respect to the shallower signature at degree 2 of plate tectonics, and is correlated with a degree 2 pattern in seismic attenuation [*Romanowicz et al.*, 1987; *Romanowicz*, 1990; *Montagner & Romanowicz*, 1993]. In the lowermost mantle, a large scale degree 2 pattern of geodynamical significance, correlated with that of the geoid, has also been found in the earliest studies [*Dziewonski et al.*, 1977; *Hager et al.*, 1985].

Over the years, as resolution in tomographic models has improved, greater details concerning the large scale flow in the mantle have been obtained. In particular, recent models with high resolution around subduction zones have allowed seismologists to trace the fate of subducted lithospheric slabs through the upper mantle transition zone and into the lower mantle, and have shown a variety of situations, with slabs appearing to be lying flat at the upper-mantle/lower-mantle transition in some regions, and penetrating to large depths in the lower mantle in others. This has been shown both in regional studies (e.g. [*Spakman et al.*, 1989; *Zhou & Clayton*, 1990; *van der Hilst et al.*, 1991; *Fukao et al*, 1992; *van der Hilst & Seno*, 1993; *van der Hilst*, 1995]), and in whole mantle models (e.g. [*van der Hilst et al.*, 1997; *Grand*, 1994]). Because of a less favorable geometry in mid-oceanic areas, regions of upwellings, as expressed by low velocities in tomographic regions, are less well resolved, and, in particular, this has given rise to a vigorous debate regarding the continuity at depth of low velocities associated with mid-ocean ridges ([*Zhang & Tanimoto*, 1992; *Su et al.*, 1992]).

While high resolution images increasingly will become available on a regional scale, global models of the whole mantle, in which the structure is typically expressed as a truncated spherical harmonic expansion in the horizontal dimension, provide useful constraints on the long wavelength characteristics of mantle circulation and how it relates to surface tectonics. Until recently, such models were limited to degree 12 (e.g. [*Su et al.*, 1994; *Li & Romanowicz*, 1996]), and are now progressively reaching higher degrees [*Masters et al.*, 1996; *Mégnin & Romanowicz*, 1997; *Liu & Dziewonski*, 1998; *Mégnin & Romanowicz*, 1999c], with the newest models showing good agreement in their low degrees (up to degree 8-12) with the previous generation. A common feature of these models is their strong low degree component, with peaks at degree 2 in the transition zone and lowermost mantle, and predominance of degrees 1-8 in the upper mantle. These features provide strong constraints for numerical modeling of convection in the mantle, in that a variety of ingredients, such as level of heating from the bottom of the mantle, nature of the 670 km discontinuity, viscosity stratification, and boundary conditions at the top of the mantle, contribute to the spectral characteristics of the synthetic velocity models derived from numerical computations, which ultimately need to match the seismological results.

While good agreement between mantle models resulting from convection calculations and seismic tomography would go a long way towards improving our understanding of mantle dynamics, geodynamicists and seismologists have traditionally failed to produce compatible images, particularly the characteristic length scale of heterogeneity. Simple fluid dynamic models predict dominant wavelengths of the order of mantle depth [*Busse & Whitehead*, 1971]. This is in contradiction with both geoid observations(e.g. [*Lerch et al.*, 1982]) and images derived from seismic tomography (e.g. [*Tanimoto*, 1990; *Su et al.*, 1994; *Li & Romanowicz*, 1996; *Grand et al.*, 1997]) which find, as mentioned above, that the spectrum of heterogeneity in the mantle peaks at scales of 10,000 to 20,000 km. The disagreement remains with spherical axisymmetric convection simulations which predict a pattern of heterogeneity with a much broader spectrum (e.g. [*Machetel*, 1990]). The discrepancy was attributed to the presence of a filtering effect in the tomography and to computational limitations that did not permit the imaging of very fine scale mantle structure.
More recently, it was shown that, by introducing a depth dependent viscosity profile in the convection simulations [*Bunge et al.*, 1996], and more importantly by imposing plate

motions [*Davies*, 1988; *Bunge & Richards*, 1996], a convective planform could be generated, characterized by the predominance of long wavelength circulation, which considerably improved the spectral agreement between geodynamic calculations and seismological models. Although differences between seismic images of the mantle and convection calculations remain, the similarities now allow direct comparisons. In particular, the thermal effect of phase transitions on the convection planform in a realistic geometry produces spectrally localized features at transition zone depths. It is possible to use the convection models in conjunction with a realistic distribution of seismic data to estimate whether such features, if they exist, would be recovered in the inversion of real seismic data.

The spatial resolution of tomographic models and models resulting from convection calculations, however, are very different. Resolution in geodynamic models is controlled by the numerical mesh, (in the case of the convection model in this study, 10 million finite elements were used, corresponding to heterogeneity of the order of 50 km). In contrast, the resolution achieved by seismological models is limited by the filtering that the uneven data sampling, the regularization and the parametrization introduce in the inversion. For the purpose of comparison between seismological and numerical modelling, the recent "high resolution" models, as mentioned earlier, are accurate mostly in regions around subduction zones, so that long wavelength, global models are better suited for such comparisons. However, contamination of long wavelength seismic images by unmodeled small scale heterogeneity may result in a distorted model. Therefore, predicted seismic images of convection models must be computed by applying the same filtering process as has been applied to the real earth in the inversion of actual data. Such an approach allows to assess how a particular convection model would be "seen" through the blurred glass of global seismic tomography, and therefore to perform meaningful comparisons.

The issue of contamination of long wavelength tomographic models by small scale heterogeneity is central to the interpretation of seismic images in terms of mantle dynamics. By analyzing frequency shifts in the normal mode ${}_0S_{40}$, [*Snieder et al.*, 1991] have suggested that the presence of fine scale subduction zones and spreading ridge structures introduces appreciable spectral leakage into the even-degree expansion of the local frequency perturbation, up to spherical harmonic degree 6. However, the local frequency perturbations only represent the effects of the radially integrated earth structure. In the present study, we analyze how aliasing impacts the velocity models in different depth ranges using synthetic computations based on the combination of a recent numerical convection model [*Bunge et al.*, 1998] and the seismic sampling provided by a recent global tomographic study [*Li & Romanowicz*, 1996].

3.2 Method

The resolution of seismic models is generally tested by constructing synthetic input patterns such as 'checkerboards' and evaluating their recovery. In regional and global studies, more realistic synthetic structures, such as slabs, are also commonly evaluated (e.g. [*Spakman et al.*, 1989; *Fukao et al*, 1992; *van der Hilst et al.*, 1997]). [*Pulliam & Stark*, 1994] have also assessed the overall reliablility of images from travel time tomography. Realistic numerical convection models provide the advantage of allowing to assess the resolution by seismic tomography of both large scale global features and localized heterogeneity, specific for example to subduction zones or hot upwellings, and to determine whether such effects as the strength of phase transitions can be detected.

Several studies have used tomographic sampling of convection simulations as an effective way to explore similarities between geodynamic and tomographic mantle models. [*Johnson et al.*, 1993] used the global distribution of available $SS-S$ and $ScS-S$ travel times to image spherical convection simulations of [*Tackley et al.*, 1993] and found general agreement between the spectra of the convection simulations and of the seismic models derived from these synthetic travel time data. [*Mégnin et al.*, 1997] argued that waveform tomography can successfully reproduce the spectral signature of various convection scenarii, each characteristic of a particular aspect of the physics of mantle convection. The method consisted in applying the resolution matrix derived in the computation of the tomographic model *SAW12D* [*Li & Romanowicz*, 1996] to image eight convection calculations by [*Bunge et al.*, 1997]. Although convenient, this method involves strong linear approximations and is not suitable for the analysis of short-wavelength contamination. An analysis of the aliasing of degrees 7-12 into a degree 6 model was attempted but the results proved strongly dependent on the choice of roughness penalty used in the modeling. It is important to note that such studies of convection calculations have so far focused on particular physical parameters corresponding to a dynamical mantle possibly very different from the actual earth. A new generation of 3-D spherical convection simulations of [*Bunge et al.*, 1998] that includes the principal thermal effects expected to be present in the mantle allows to make somewhat more meaningful comparisons between geodynamic and tomographic models, even though the currently available convection simulations only represent one step further towards a more realistic dynamic Earth.

In this study, we consider the source-receiver distribution used in computating the whole mantle model *SAW12D*, consisting of 9,000 SH body wave seismograms low-passed at 32s and 7,500 first and second orbit Love wavetrains, low-passed at 80s. The body wave seismograms correspond to a collection of over 28,000 body phases, corresponding to S, SS, S_3, S_4, ScS, ScS_2, ScS_3, S_{diff} and the corresponding depth phases (sS, etc...). They are catalogued in Table 3.1. Modeling of waveforms with accurate body wave kernels [*Li & Tanimoto*, 1993; *Li & Romanowicz*, 1995] gives access to information contained in many phases, including those that arrive close together in time, thus providing improved sampling compared to single phase travel time delays.

We compute synthetic waveforms corresponding to the actual source-station configuration, in a predefined geodynamic model and invert them for up to spherical harmonic degree 12. The synthetic waveform dataset and its subsequent inversion are computed using the 'non-linear asymptotic coupling theory' (*NACT*) developed by [*Li & Romanowicz*, 1995]. This formalism takes into account the coupling of multiplets along and across mode branches, a prerequisite for the correct modeling of body waveforms [*Li & Tanimoto*, 1993]. Because of the zeroth order asymptotic expansion of the coupling terms, the sensitivity of the waveforms is restricted to the two-dimensional structure along the great-circle path [*Romanowicz*, 1987]. Resolution in the lowermost mantle is improved by a data selection scheme that isolates the different energy wavepackets of a given seismic trace [*Li & Romanowicz*, 1996]. This enhances the low amplitude phases, in particular the S diffracted along the core-mantle boundary (S_{diff}) which constitutes the primary source of information on lowermost mantle heterogeneity [*Mégnin & Romanowicz*, 1999a].
All the models in this study are parametrized radially in Legendre polynomials up to degree 5 in the upper mantle and 7 in the lower mantle, and laterally in spherical harmonics, up to degree 12 for *SAW12D*, and up to degree 32 for the convection model.

3.2.1 Temperature to velocity scaling

In the absence of chemical heterogeneity, the shear velocity perturbation $\delta \ln V_s$ is obtained from the temperature field δT from *GEMLAB 1* through the relation:

$$\delta \ln V_s = \frac{\alpha}{2}\,(1 - g)\,\delta T \tag{3.1}$$

where α is the thermal expansivity $-\frac{\partial \ln \rho}{\partial T}|_P$, g is the second Grüneisen parameter $\frac{\partial \ln \mu}{\partial \ln \rho}|_P$, μ the shear modulus, P the pressure field, and all the variables are computed in the 3-D Earth.

In this study, we use as reference the thermal expansivity profiles of the spherically symmetric model *PREM* [*Dziewonski & Anderson*, 1981]. The parameter g is poorly constrained and we assign it the constant value of 4 throughout the mantle, which is within the range of estimates of [*Anderson*, 1989, p. 120]. Equation 3.1 thus reduces to

$$\delta \ln\, V_s(r,\theta,\phi) = \frac{\alpha(r)}{2}\,(1 - g)\,\delta T(r,\theta,\phi) \tag{3.2}$$

3.2.2 Aliasing of small-scale structure into long wavelength models

We compute a set of seismograms for the input model truncated at degree 12 and invert for shear velocity perturbations from *PREM* up to degree 12. The resulting model is 'unaliased' in the sense that it is not contaminated by small scale heterogeneity (*i.e.* by structure at shorter wavelengths than degree 12). The difference between the unaliased and the input models results from the combination of several effects: 1) Gaps in spatial coverage; 2) Varying degree of sensitivity of the waveforms to the wavelength of structure (for instance very long period surface waves aren't sensitive to very small scale heterogeneity); 3) Inappropriate choice of tuning parameters and regularization in the inversion; 4) Possible artefacts due to separate vertical parametrization of the upper and lower mantle; 5) Parametrization. In the present study, the same theory is used in the forward and the inverse problem. This analysis therefore cannot provide insight into the distortion caused by approximations in the formalism. The effect of modeling the waveforms with an asymptotic formalism is discussed in [*Clévédé et al.*, 1999] in the context of upper mantle tomography.

We compute a second set of synthetic seismograms with the same source-receiver distribution as the former, but this time through the short wavelength expansion of the model (degrees 0-32) and invert again for heterogeneity up to degree 12. In this respect, the procedure is analogous to the inversion of actual data as it allows us to examine possible aliasing of degree 13-32 structure into the degree 0-12 model. Hereafter, we refer to that model as the 'aliased' model.

We refer to the difference between the unaliased and the input model as the 'inherent' error in the model. In the absence of error arising from misjudgement in the selection of roughness penalty, the unaliased model is indeed the best possible model that can be derived with our methodology, given the data distribution, its frequency band and the model parametrization.

Although the effect of spectral leakage is clearly present on a given seismogram, its impact on velocity models may be modest because data averaging tends to remove incoherent structure. We estimate the amount of aliasing in tomographic images by subtracting the heterogeneity of the unaliased model from that of the aliased model. The resulting 3-D image then represents the spectral leakage of degrees 13-32 into the aliased model. This measure only represents an approximation of the aliasing in inversions of actual data, since the mantle clearly contains heterogeneity of finer scale than used for the purpose of this study. The truncation to degree 32 is motivated by computational limitations. Although *GEMLAB 1* was developed up to degree 400, we truncated it to degree 32 due to computational limitations. The spectrum of *GEMLAB 1* is nevertheless dominated by the long wavelengths, allowing us to model the first order effect of the contamination of the image from small-scale heterogeneity.

3.2.3 Inversion procedure: tuning the regularization

We use the same inversion procedure as that of [*Li & Romanowicz*, 1996]. A detailed description is given in that paper and we present here only the aspects relevant to this study:
The inverse problem is solved by making use of a stochastic formulation [*Jackson*, 1979] and the finite-dimensional model is obtained by the recursive application of the following Newton scheme to the Fréchet derivatives of the L^2-norm objective function [*Tarantola & Valette*, 1982]:

$$m_{i+1} = m_i + \left(\mathbf{A}_i^T \mathbf{C_d}^{-1} \mathbf{A}_i + \mathbf{C_m}^{-1}\right)^{-1} \left(\mathbf{A}_i^T \mathbf{C_d}^{-1} \left(\mathbf{d} - \mathbf{u}(m_i)\right) - \mathbf{C_m}^{-1} m_i\right) \tag{3.3}$$

Where $\mathbf{d}$ is the data, $\mathbf{u}(m_i)$ the synthetic seismogram evaluated for model m_i and $\mathbf{A}_i$, the matrix of partial derivatives with respect to the parameters of model m_i.
The component of the model covariance matrix $\mathbf{C}_\mathbf{m}^{\mathbf{het}}$ corresponding to perturbations in lateral heterogeneity $dlnV_s$ is constructed according to:

$$\mathbf{m}^T \left(\mathbf{C}_\mathbf{m}^{\mathbf{het}}\right)^{-1} \mathbf{m} = \int_{\oplus} \eta_1 m^2 + \eta_2 \left(\frac{\partial m}{\partial r}\right)^2 + \eta_3 \left(\frac{\partial^2 m}{\partial r^2}\right)^2 + \eta_4 \mid \nabla_1 m \mid^2 d\oplus \tag{3.4}$$

where $\oplus$ is the volume of the mantle, and ∇_1 the surface gradient operator. Similar expressions apply to perturbations in the topography of mantle discontinuities. The selection of damping parameters η_i is arbitrary. In this study, the problem of the determining the optimal set of damping parameters is posed as an inverse problem in which we seek to identify the η_i that will minimize the Euclidian distance between the output model m_{i+1} and the target input geodynamic model. To minimize the number of iterations, we use as starting model m_i the target model truncated to degree 8. The optimal set of model norm, lateral derivative, and first and second radial derivatives is computed with a simulated annealing algorithm coupled with a downhill simplex method [*Press et al.*, 1994].

3.3 Convection model *GEMLAB 1*

We use as input model the time-dependent 3-D spherical convection calculation 'Geodynamical Model of Los Alamos and Berkeley' (*GEMLAB 1*) derived by [*Bunge et al.*, 1998] and characterized by:

- Imposition of the plate motion history starting in the mid-Mesozoic (119 Ma).
- An exothermic phase transition at 410 km with Clapeyron slope of $2MPa.K^{-1}$.
- An endothermic phase transition at 670 km with Clapeyron slope of $-4MPa.K^{-1}$.
- A rheology whereby the lithosphere and the lower mantle are 40 times more viscous than the upper mantle.
- 20% heating from the core.

This model is arguably one of the most realistic numerical models available to date, in that it predicts a spectrum of heterogeneity peaked at low degrees. However, we must keep in mind that it is, for the purpose of our study, only a convenient proxy for the real Earth.

3.3.1 Resolution analysis

Two sets of synthetic seismograms are computed from *GEMLAB 1*: using its degree 32 expansion (Figure 3.1) and using its degree 12 expansion (Figure 3.2). The resulting 'data sets' are inverted for heterogeneity up to degree 12, producing an aliased (Figure 3.3) and unaliased (Figure 3.4) model, respectively. Although a damping of amplitude is observed, maps at given depths do not display noticeable spatial distortion of the input structure. Spectral heterogeneity maps (*SHM*s) of the models are shown in Figure 3.5. The plots represent the rms amplitude of each model as a function of wavelength (horizontal axis) and depth (vertical axis). Horizontal lines are traced at 410, 670 and 2600 km depths. Since amplitudes in the mantle are dominated by the top and bottom boundary layers, little can be seen at other mantle depths. In Figure 3.6, we normalize the amplitudes of Figure 3.5 by the rms at each depth. Figures 3.5 & 3.6 (a) show the first 12 degrees of the input model *GEMLAB 1* and correspond to Figure 3.2. The uppermost mantle is characterized by a white spectrum dominated by spectral peaks at degrees 1 and 4 to 6 which are most prominent between 100 km and 150 km depth. The signature of the phase transitions is observed at degrees 2 to 5, 7 and 10 between 400 km and 700 km depth. The heterogeneity pattern in most of the lower mantle is dominated by the long wavelengths. The D" region displays a broad spectrum, peaking at degrees 2-3 and showing energy up to degree 10.

Figures 3.5 & 3.6 (b) are the spectral representation of the aliased model in Figure 3.3, resulting from the inversion for up to degree 12 of the synthetics traced through the degree 32 model. In the uppermost mantle, the low degree spectral peaks are well recovered although a slight loss of amplitude and radial smearing of the degree 6 heterogeneity is observed. In the bottom of the mantle, the spectral peaks at degrees higher than 6 in the input model are noticeably attenuated.

Figures 3.5 & 3.6 (c) correspond to the model of Figure 3.4 and represent the unaliased model resulting from the inversion for up to degree 12 of the synthetics traced through the long wavelength (degree 12) model. Here again, a modest amount of radial smearing is observed in the amplitude peaks of the upper mantle. The spectral character of the input model is nonetheless well preserved.

Radial smearing in the upper mantle is also apparent in the rms profiles of Figure 3.5 (d). The radial character of the rapid amplitude excursions associated with the plates and the phase transitions in the input model (solid line) cannot be resolved perfectly with 32s body waves: vertical averaging is present in both the aliased (dotted line) and the unaliased (dashed line) models.

Figures 3.5 & 3.6 (e) and 3.7 represent the inherent error obtained by subtracting the model in Figure 3.2 (*GEMLAB 1*, expanded up to degree 12) from the model in Figure 3.4 (its unaliased version). The contamination appears strongest in the uppermost mantle and the transition zone where the strength of the amplitude peaks is underpredicted and the peaks are spread radially. The amplitude of the error is nonetheless modest when compared to the scale of the models: the spurious heterogeneity introduced never exceeds 1%. An interesting effect is the presence of inherent error at degrees 5 and 10 in D". At 2,800 km, Figure 3.7 shows features that resemble the global tectonic pattern in the Southern hemisphere (note the presence of low velocities under the East Pacific Rise and the Southern Mid-Atlantic Ridge, as well as the fast anomaly under South Africa). We have shown in a recent study [*Mégnin & Romanowicz*, 1999a] that this effect is associated with the quality of lowermost mantle coverage. With the available global data distribution, coverage in the Southern Hemisphere is indeed sparse compared to that in the Northern hemisphere. This is a common problem for all tomographic studies, not just *SAW12D*. Figure 3.9 (top) shows the reflection points of ScS, ScS_2 and ScS_3 phases and diffraction paths on D" of the S_{diff} in our dataset. At the bottom of the figure, we show the corresponding ray density coverage $\rho = \log(1+n)$ for each $15^o \times 15^o$ cell (the spatial resolution corresponding to degree 12). Here, n represents the number of one degree length segments of the S_{diff} phase and the number of bounce points of the ScS, ScS_2 and ScS_3 phases on the CMB. The figure shows that the number of hit counts per unit cell exceeds 100 everywhere except in the South Atlantic and the Southwest Pacific, where it is 10.

In Figure 3.10 (top), we plotted the degree by degree euclidian distance between the unaliased and the long wavelength input models, relative to the former. The distance for spherical harmonic degree s between two models m and p, expanded radially in polynomials up to degree kmax is defined as:

$$D_s \equiv 100 \times \left(\frac{\sum_{k=0}^{kmax} \sum_{t=0}^{2*s+1} \left(m_k^{st} - p_k^{st}\right)^2}{\sum_{k=0}^{kmax} \sum_{t=0}^{2*s+1} (m_k^{st})^2} \right)^{\frac{1}{2}} \tag{3.5}$$

In Figure 3.10, the thick line corresponds to upper mantle depths and the thin line to lower mantle depths. The horizontal bars represent the total distance between the models. As expected, the relative error is greater in the lower mantle and increases with decreasing wavelength. The peak distance occurs at degree 12 where it represents 25% of the model amplitude in the upper mantle and 50% in the lower mantle. The average distance is 17% in the upper mantle and 32% in the lower mantle.

Figures 3.8 and 3.5 & 3.6 (f) represent the spectral leakage in the degree 12 model, obtained by subtracting the model in Figure 3.3 from the model in Figure 3.4. The small scale structure component of the model (degrees 13-32) maps preferentially at high degrees and in the transition zone. We also note that the effect of spectral leakage on the model exceeds that of the inherent error. The maps at different depths show spurious heterogeneity that exceeds 1% in the transition zone. Figure 3.10 (middle) shows the dependence on wavelength of the spectral leakage, computed by taking the distance (3.5) between aliased and unaliased models. Here again, the peak distance occurs at degree 12, and is significantly stronger than the inherent error, representing 55% of model amplitude in the upper mantle and 70% in the lower mantle. The average distance is 28% in the upper mantle and 45% in the lower mantle.

Finally, Figures 3.5 & 3.6 (g) represent, in the absence of noise, the effects of the total error in the models, computed by subtracting model 3.1 from model 3.3. Radial smearing is noticeable at the surface and the amplitude of the error at high degrees near the 670 km discontinuity is comparable to that of the input structure (compare the peak at degree 10 in the transition zone in Figures 3.6 (a) and 3.6 (g)). Figure 3.10 (bottom) shows a distance between input and aliased models of 35% in the upper mantle and 50% in the lower mantle. As expected, the total error peaks at high degrees, where it represents 60% and 70% of model amplitude in the upper and the lower mantle respectively.

3.3.2 Comparison with tomography

While *GEMLAB 1* only represents the current status of "realistic" convection computations, it is interesting to discuss how well its "aliased" version compares to a tomographic model obtained with real seismic data and the same geometry of paths and waveforms as used in the previous synthetic experiments. As mentioned earlier, the damping parameters used for the inversion of the aliased model are optimized for our source-receiver distribution and for waveforms that have sampled a mantle model containing short wavelengths. The prejudice they impose on the inversion is indeed that which best recovers degrees 0 through 12 of the synthetic input structure and therefore also represents the best we can do for the inversion of actual data for heterogeneity up to degree 12, under the assumption that recovering a model as close as possible to the convection model *GEMLAB 1* is a desirable goal.

Since model *SAW12D* was originally obtained using a different set of damping parameters, in order to compare more effectively the inversion results using actual data to the synthetic inversions performed here, we compute a new tomographic model based on our actual dataset, using the optimized set of damping parameters determined in the calculation of the aliased *GEMLAB 1*. In this manner, we cannot completely confirm the reality of the features of the *GEMLAB 1* model that can be recovered through seismic tomography, but we can assess those features in the tomographic models that are significantly different from the predictions of the convection computation. An element of circularity is also present in calibrating smoothness constraints based on convection calculations made to match the tomography. To check whether this method could introduce features of the reference model where they do not exist, [*Mégnin et al.*, 1997] computed a set of synthetic seismograms in a convection model including a phase transition at 670 km, and derived a set of damping parameters adjusted to optimize the recovery of the input model. The inversion of this data set showed good restitution of the spectral footprint of the phase transition. A second set of synthetics was traced in another convection model which did not include the phase transition and was inverted with the same tuning parameters. The inversion of this new set of synthetics did not introduce the pattern associated with the phase transition in the control model, and hence indicates that there is no systematic circularity in our methodology.

Figure 3.11 is a mantle model derived with damping parameters that best allow the recovery of the heterogeneity pattern of *GEMLAB 1*; it is readily compared to the aliased convection calculation of Figure 3.3. The models show both similarities and differences across the mantle. Notable differences are slab structures, which display more continuity in the convection simulation. Clearly, this discrepancy is not due to the tomography since continuity of slab structure is observed in the 'aliased' calculation. Large differences are also observed in D", where the convection calculation fails to reproduce the slow anomalies in the regions beneath the Central Pacific and Africa, probably due to the presence of chemical heterogeneity at the base of the mantle.

In Figure 3.12, we show a spectral comparison between the aliased model (left) and the image resulting from the optimized inversion of real data (center). The right of the plot shows the rms profiles for *SAW12* modified (solid line) and *GEMLAB 1* aliased (dashed line). The SHMs have been truncated at a minimum depth of 200 km because the convection model was not constructed with a realistic lithosphere.

An important similarity between the two models is in the transition zone where the spectral signature of the phase transitions in *GEMLAB 1*, although somewhat attenuated, is well reproduced in the tomographic pattern, up to degree 5. In both models, the heterogeneity at degrees 2 and 3 is largely unaffected by the phase transition and penetrates into the lower mantle down to 800 km depth. Convection simulations by [*Bunge et al.*, 1997; *Tackley et al.*, 1993] show that the introduction of a phase transition in the convection simulation increase the long wavelength amplitudes of the heterogeneity pattern in the transition zone. Based on the comparison between the two models, the convection calculation seems to overpredict the Clapeyron slope of the phase transition. Contingent upon the correct modeling of the time dependence of the subduction history, this observation places an upper bound of $-4MPa.K^{-1}$ on the strength of the phase transition.

Both models predict a strong pattern in the lower mantle at degrees 2 and 3. The tomography nonetheless shows considerably more complexity with heterogeneity at higher degrees. In the lower mantle, the convection calculation shows a spectral peak at degree one which is absent from the seismic image. Another important difference is the absence of the two large upwellings under Africa and the Pacific. This difference may be due to the presence of effects such as partial melting or other chemical anomalies in the lowermost mantle that have not been modeled in the convection simulation. It thus appears that, while current generation convection models seem to be relatively successful in modeling downwellings, future calculations must deal better with the characteristics of the upwellings as shown by tomography. This might require introducing rheological and chemical stratification and the effects of partial melting.

3.4 Discussion and conclusion

In the present study, we used convection simulations to calibrate the recovery of heterogeneity characteristic of the mantle's convective pattern by seismic imaging techniques. We have applied a tomographic filter to results from 3-D spherical convection calculations that incorporate the history of plate motions starting in the Mid-Mesozoic, a viscosity contrast between upper and lower mantle, phase transitions at 410 km and 670 km, and 20% heating from the core. This model represents one of the most realistic convection computations currently available, in that it predicts a spectrum of heterogeneity peaked at low degrees in the lower mantle. The filtered convection model is compared to results derived from the inversion of actual waveform data, using an optimized set of damping parameters. A comparison between the two models allows to make the following inferences regarding the *GEMLAB 1* model:

1) The spectral peak at the low degrees in the pattern of heterogeneity is continuous from the transition zone to depths of about 800 km, across the 670 km discontinuity in both models.

2) In the lower mantle, the tomography shows a broader spectrum than is predicted by the convection simulation.

3) The large difference between the convection calculation and the tomography in the lowermost mantle indicates that the former must lack an important ingredient for correctly predicting the character of major upwellings. Part of the difference may be due to poor constraints on the position of fossil slabs in the Mesozoic, but the thermal and chemical boundary conditions in the lowermost mantle do not yet seem to be well understood, and they must play an important role in the global dynamics.

4) Given that the convection calculations were made under assumption of a uniform mantle rheology across the 670 km discontinuity, the images of transition zone structure are inconsistent with a Clapeyron slope larger than 4 $MPa.K^{-1}$. This conclusion is contingent upon the quality of the historical plate reconstruction.

The upper bound on the strength of the phase transition is also contingent on the choice of the second Grüneisen parameter g (equation 3.2) that we use to convert the temperature field of the convection model into shear velocity perturbations. The pressure dependence of this parameter is poorly constrained experimentally. Nevertheless, for the radial thermal expansivity profile of $PREM$, the value of $4.0K^{-1}$ chosen here for g produces a thermal field converted to velocity whose rms is in general agreement with that of of the tomography (see Figure 3.12, right).

Taking the difference between images of the long and short-wavelength expansions of the convection simulation, we quantify the effect of aliasing of small scale structure into long wavelength seismic images. We find that the amplitude of the spurious structure rarely exceeds 1% but is present at all depths, particularly at the shorter wavelengths. This effect is small when compared to the amplitude of the models in the upper mantle. It is nevertheless closer to the amplitude of the heterogeneity in most of the lower mantle (D" excepted) as seen in tomographic models.

Body phase	Number of occurences
S & sS	5,330
SS & sSS	6,578
$S3$ & $sS3$	4,466
$S4$ & $sS4$	2,354
ScS & $sScS$	4,226
$ScS2$ & $sScS2$	3,098
$ScS3$ & $sScS3$	132
S_{diff} & sS_{diff}	1,039
Unidentified phases	854
Total	**28,077**

Table 3.1. Body wave phases

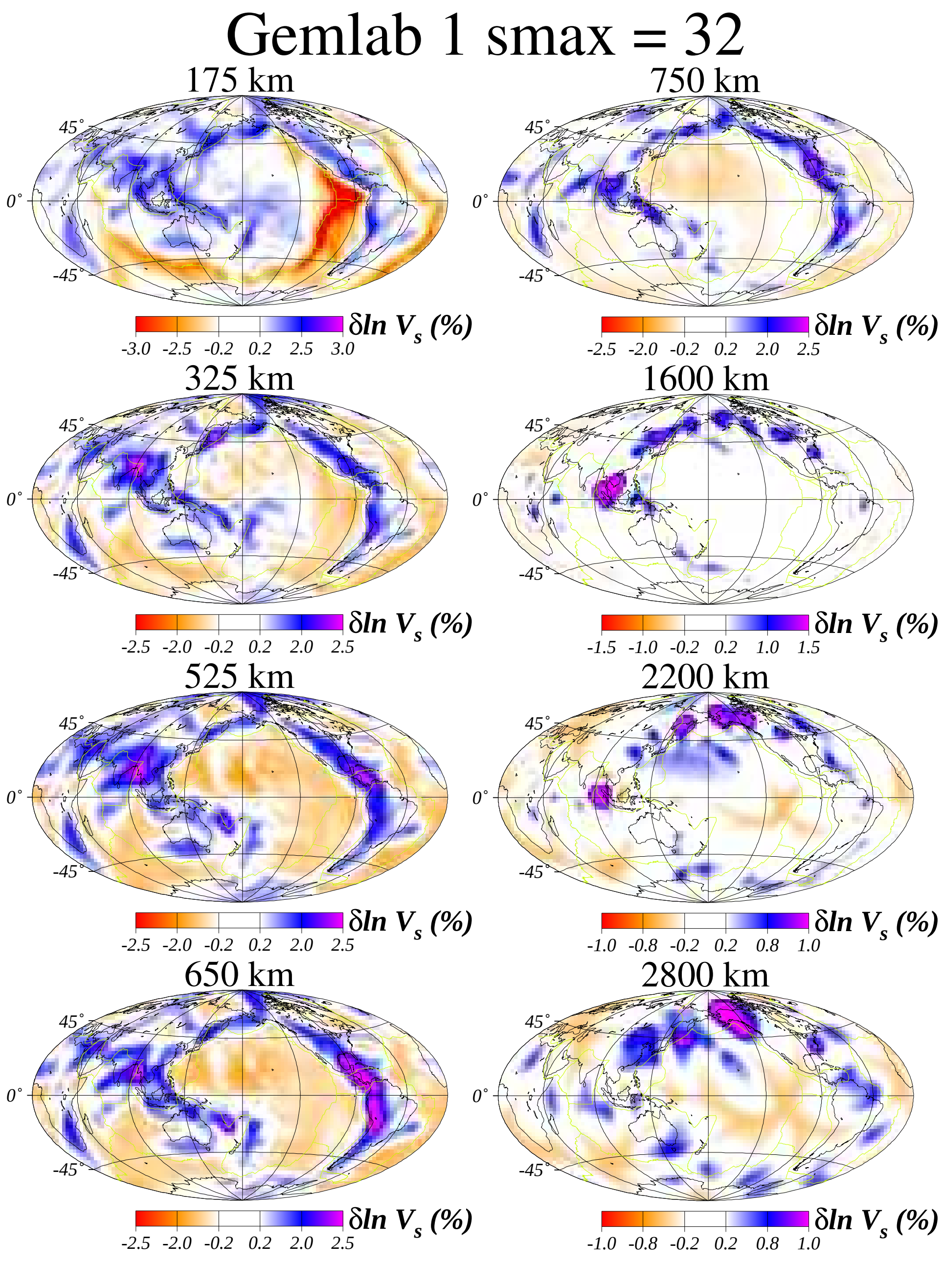

Figure 3.1. Convection model *GEMLAB 1* [*Bunge et al.*, 1998] expanded up to spherical harmonic degree 32

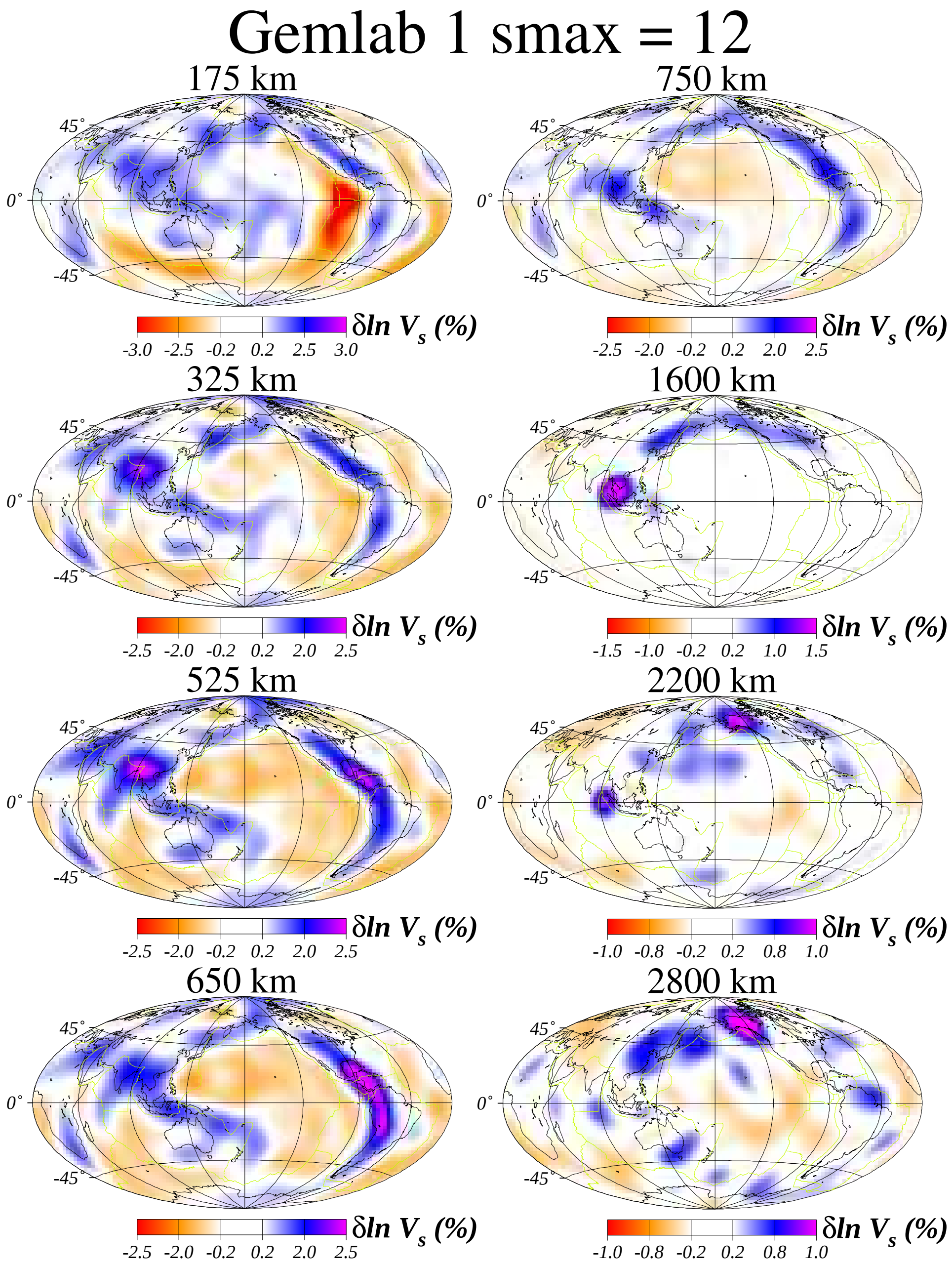

Figure 3.2. Convection model *GEMLAB 1* expanded up to spherical harmonic degree 12

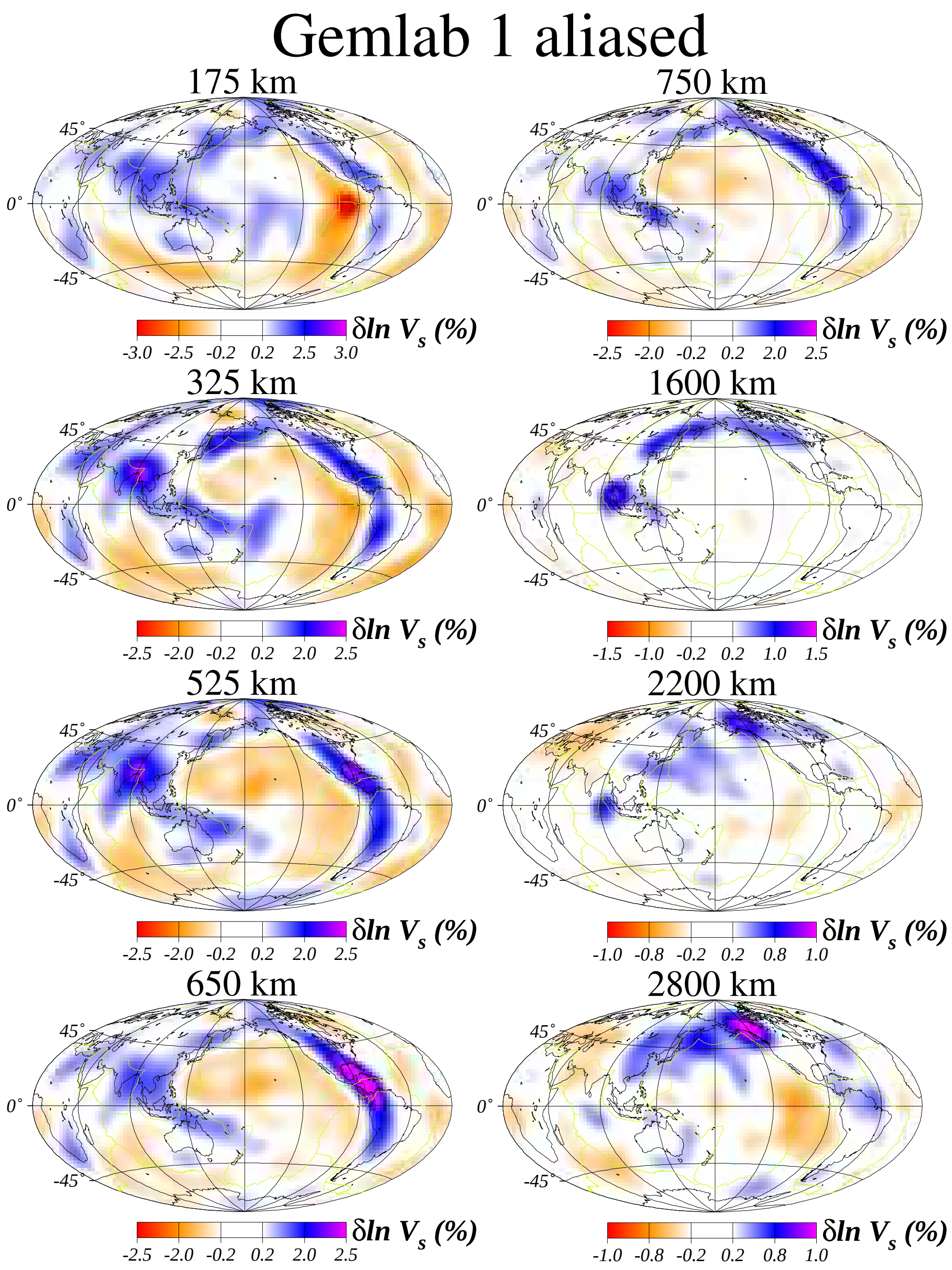

Figure 3.3. *GEMLAB 1* aliased: Inversion of synthetics traced through the model in figure 3.1 for lateral heterogeneity up to degree 12

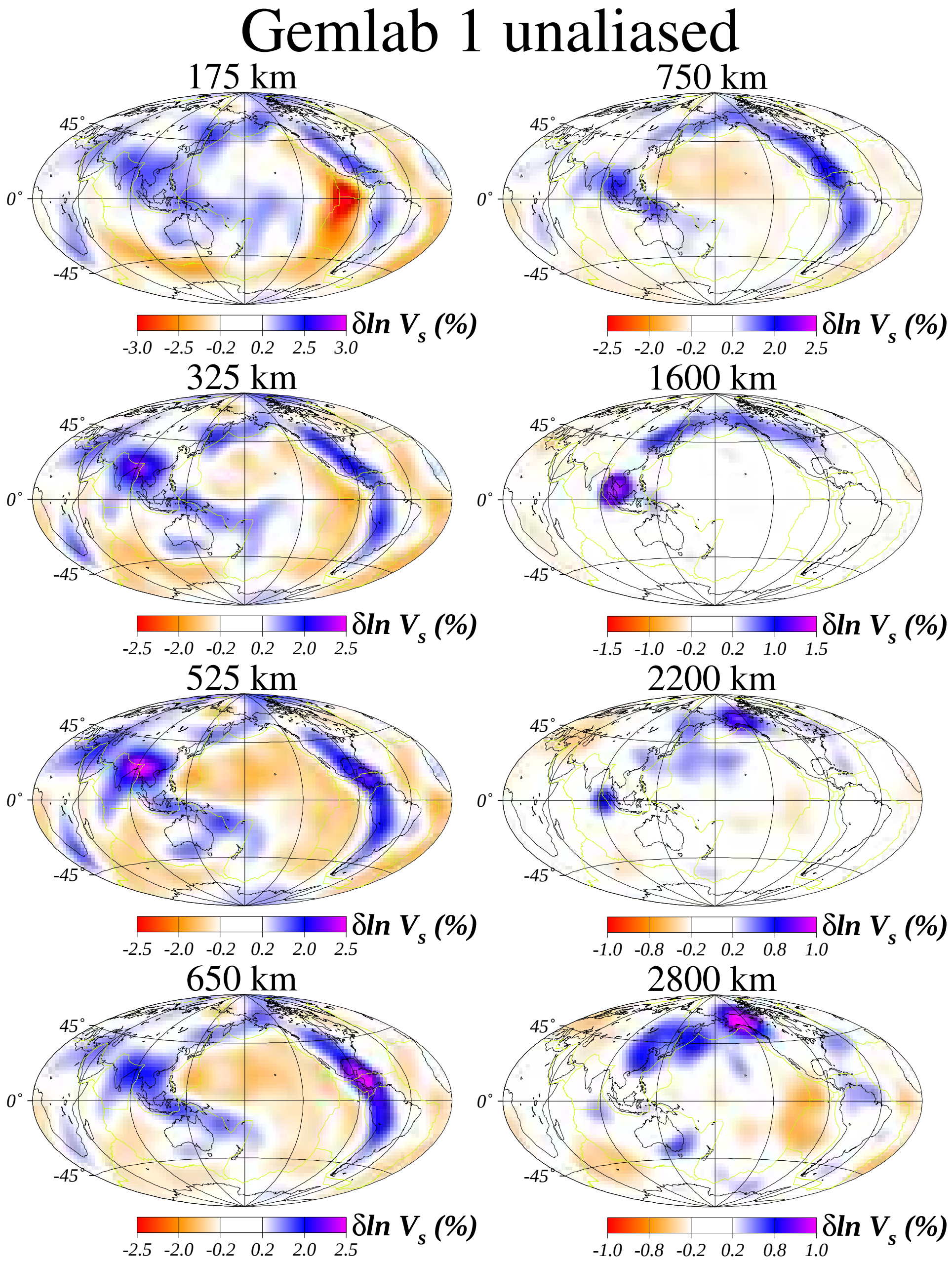

Figure 3.4. *GEMLAB 1* unaliased: Inversion of synthetics traced through the model in figure 3.2 for lateral heterogeneity up to degree 12

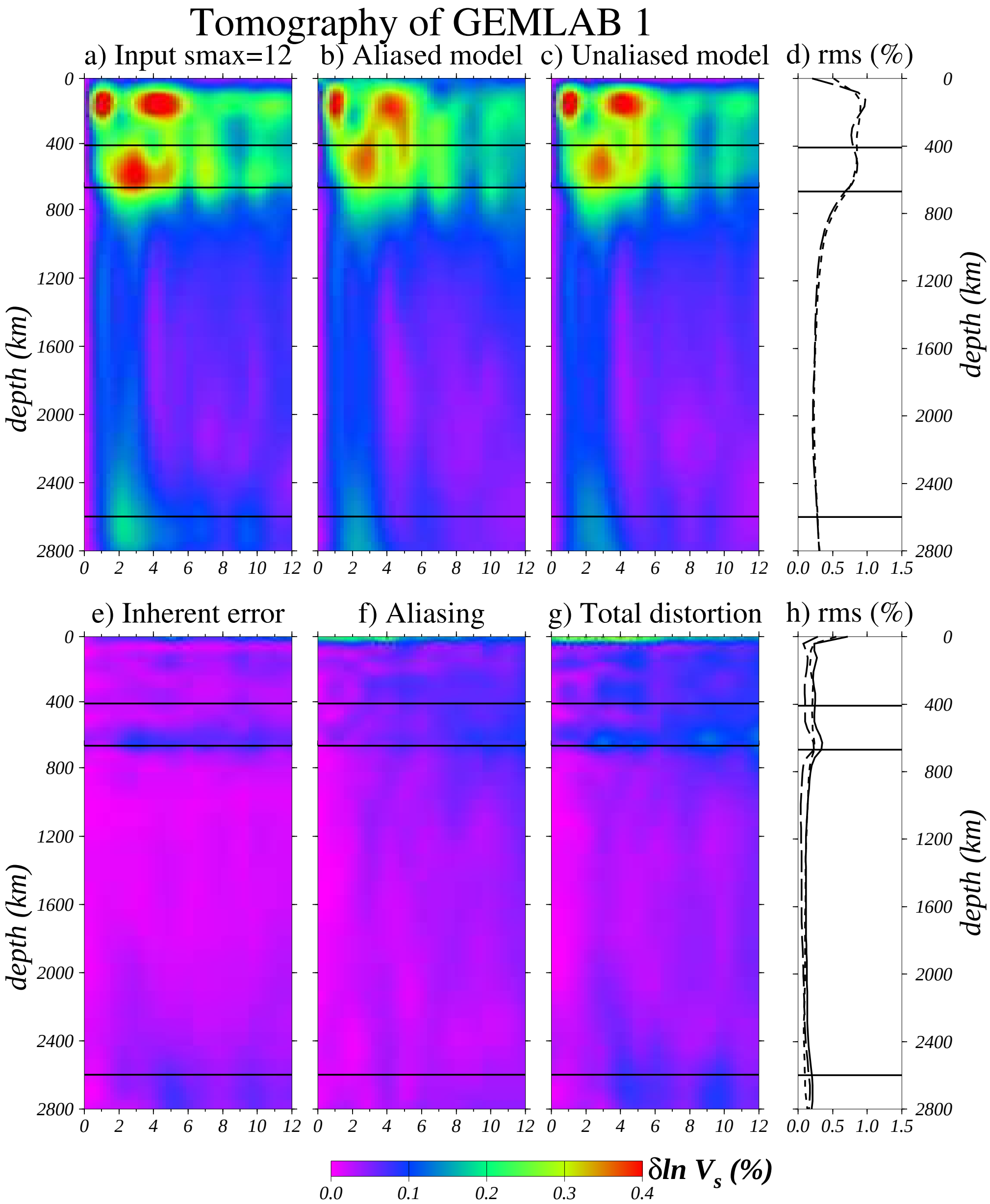

Figure 3.5. Spectral analysis of aliasing: a) Input model *GEMLAB 1* (degrees 0-12). b) Inversion of synthetic data through *GEMLAB 1* expanded up to degree 32. c) Inversion of synthetic data through *GEMLAB 1* truncated at degree 12. d) rms profiles for the models in a) solid line, b) dotted line, c) dashed line. e) Inherent error: difference between c) and a). f) Aliasing of degrees 13-32: difference between c) and b). g) Total distortion: difference between b) and a). h) rms profiles for the models in g) solid line, f) dotted line, e) dashed line.

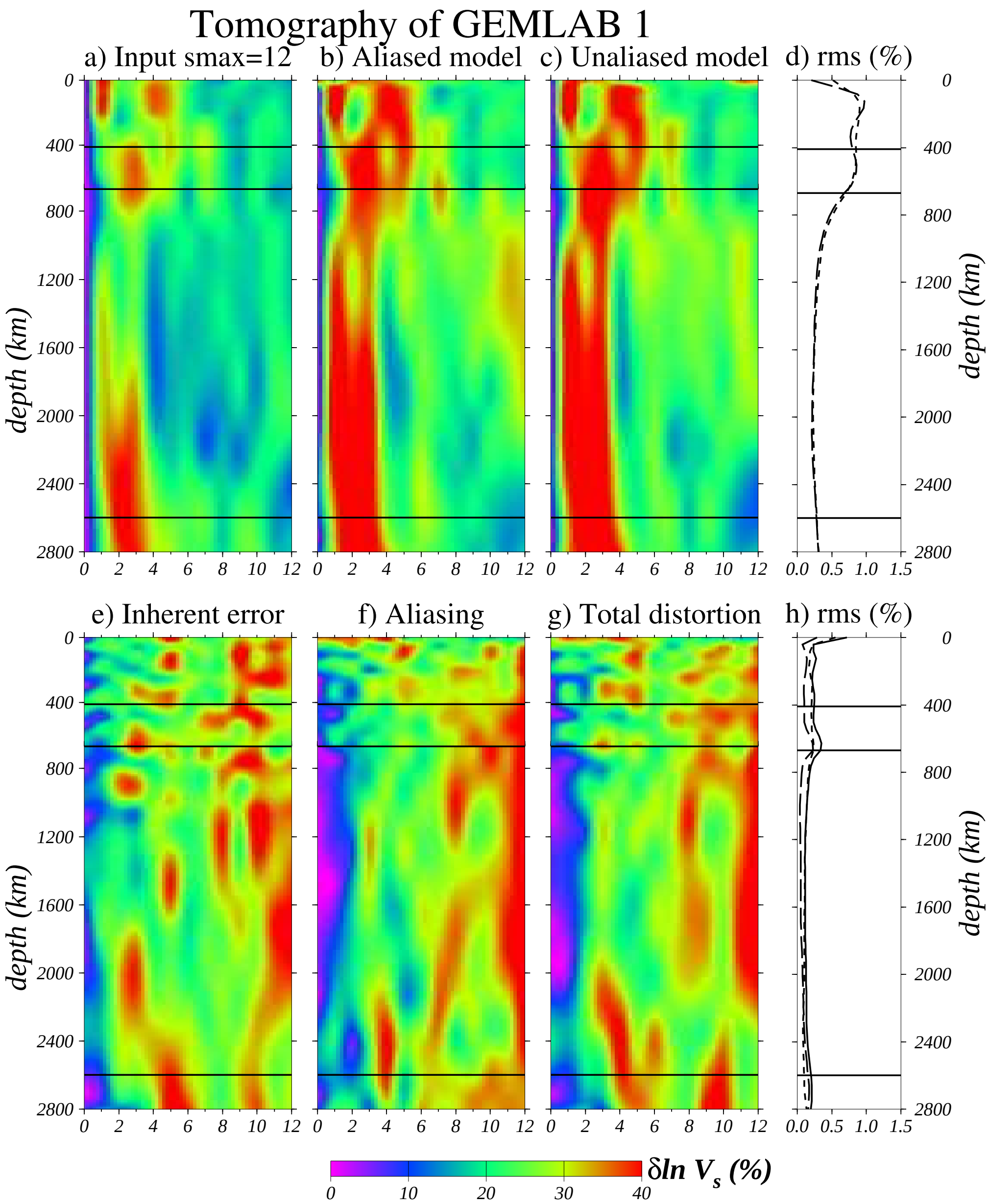

Figure 3.6. Same as figure 3.5 but the maps are normalized by the rms amplitude at each depth.

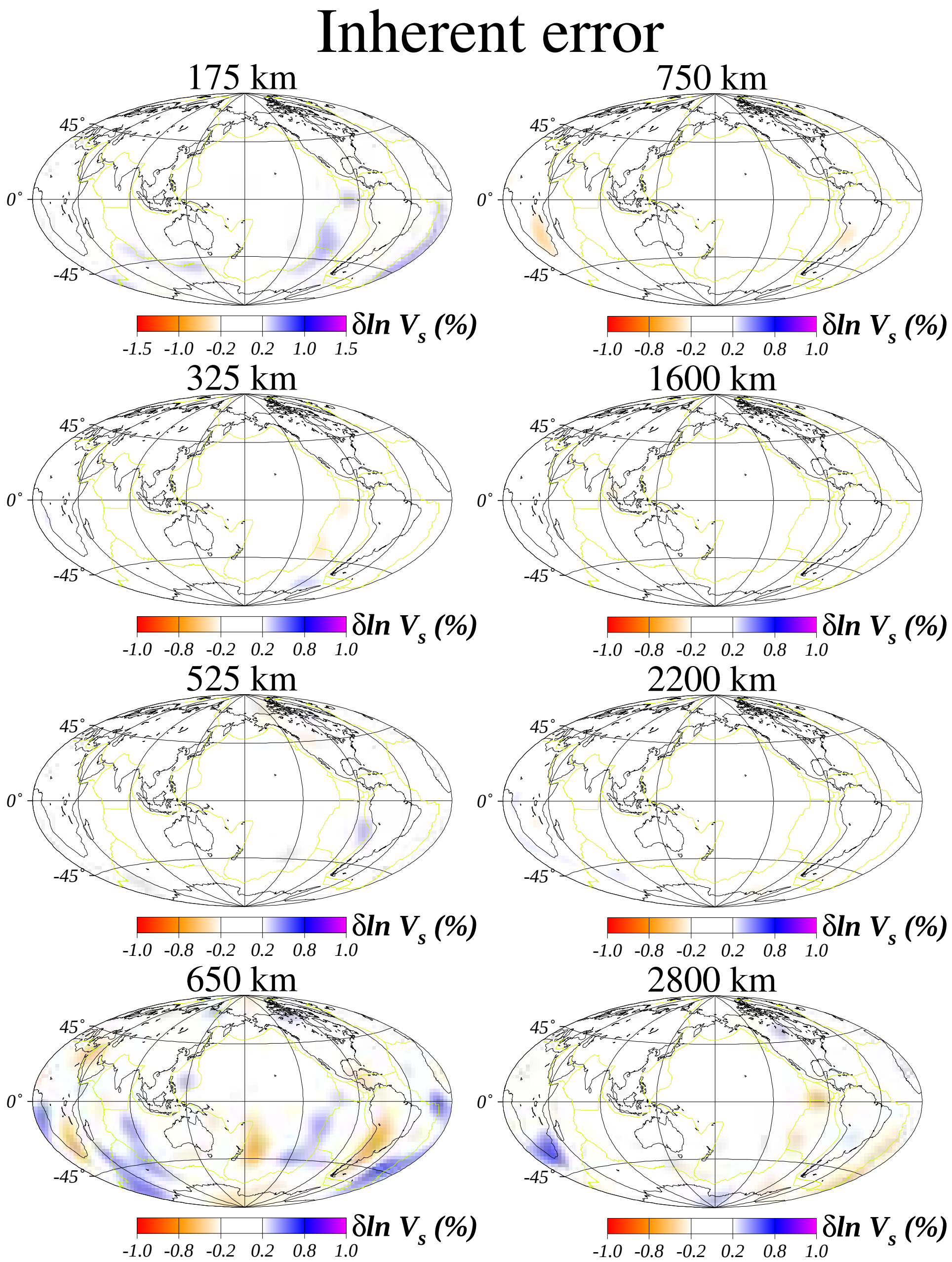

Figure 3.7. Spurious structure in the models caused by inherent error: difference between input model truncated at degree 12 and the unaliased model (figures 3.5 & 3.6 e)).

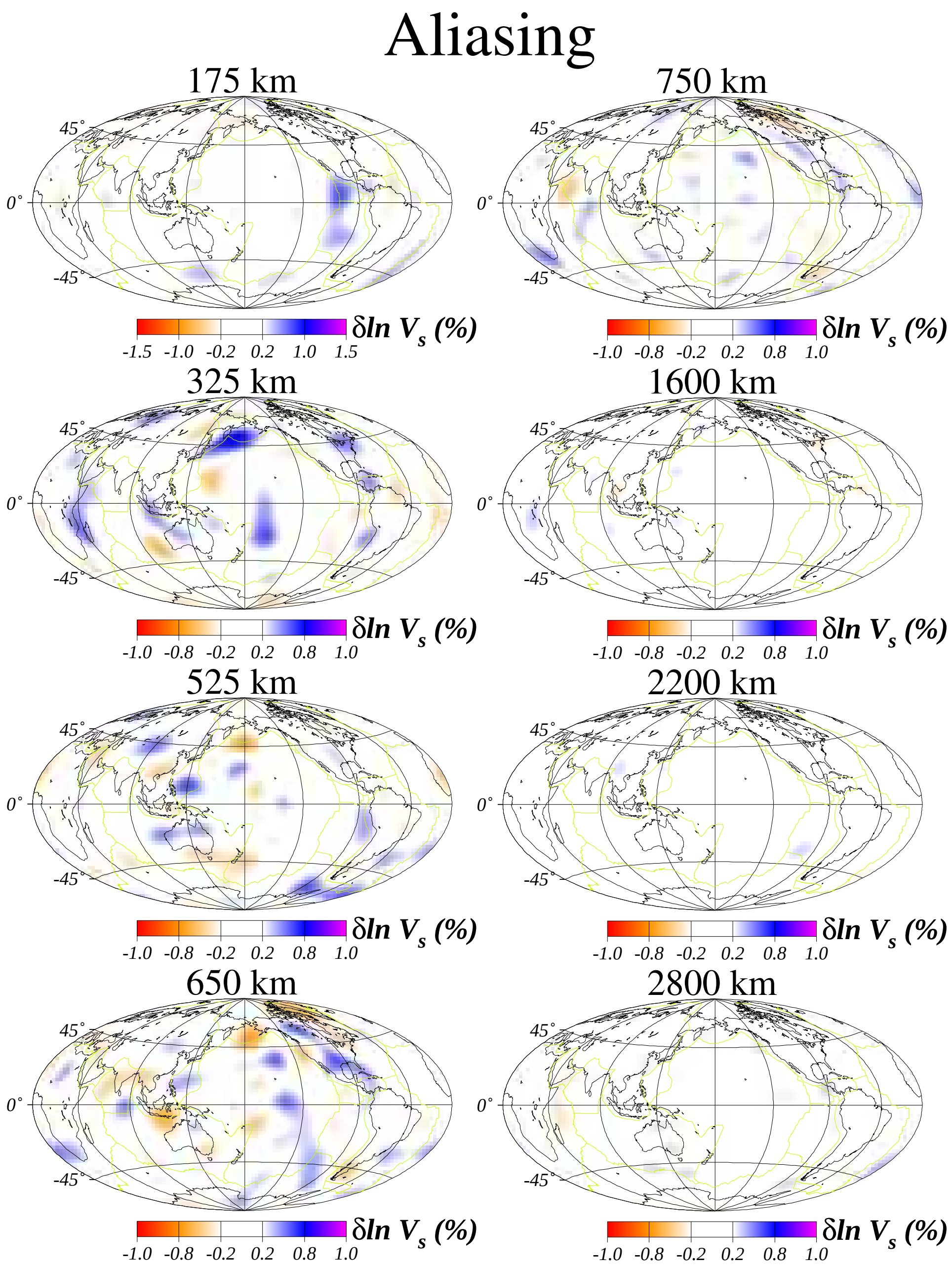

Figure 3.8. Spurious structure in the models caused by aliasing: difference between aliased and unaliased models (figures 3.5 & 3.6 f))

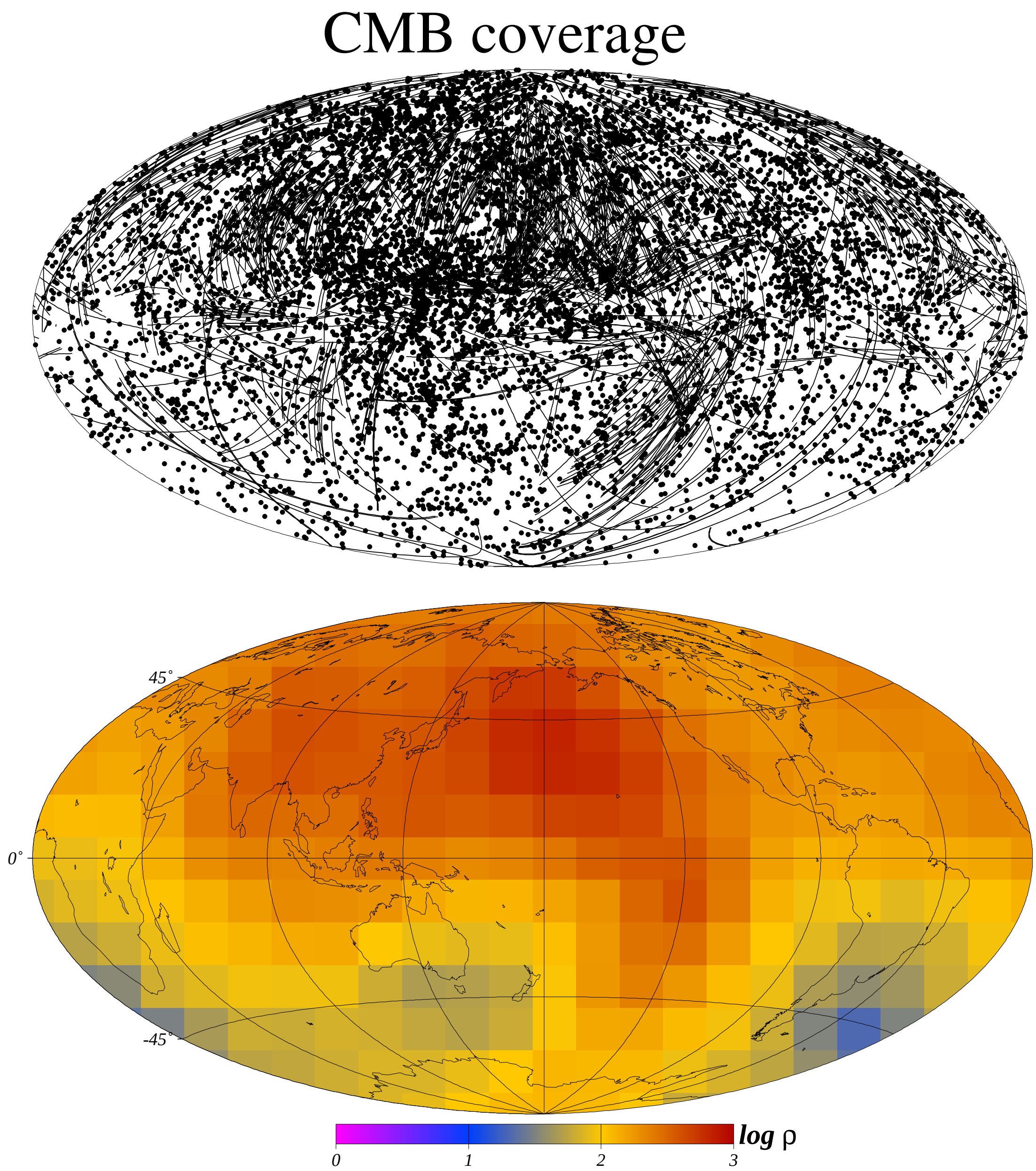

Figure 3.9. Top: Coverage at the core-mantle boundary. The linear features represent the paths on the CMB sampled by the S_{diff} phases. The circles correspond to the CMB reflections of the ScS, ScS_2 and ScS_3. Bottom: Density of coverage at the CMB for each $15^o \times 15^o$ cell.

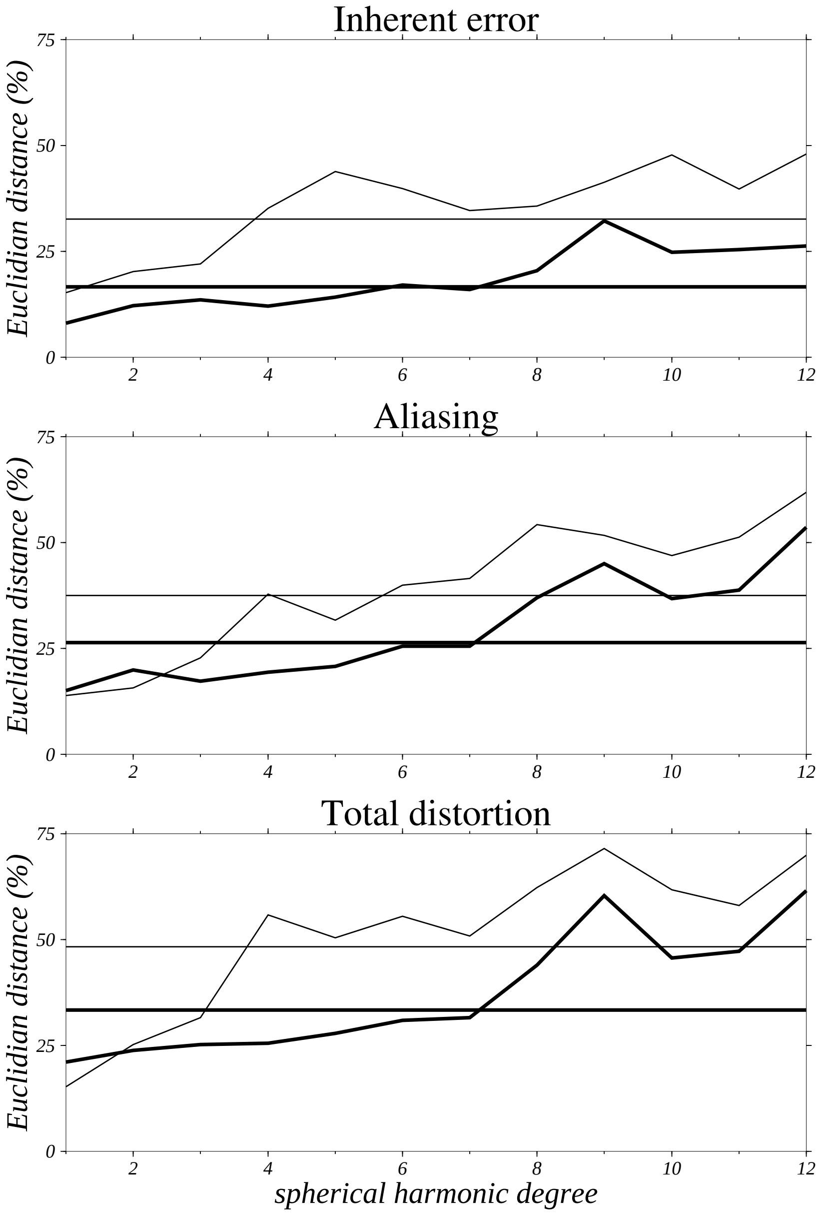

Figure 3.10. Top: Degree by degree euclidian distance between unaliased and input model, relative to the unaliased model coefficients. Thick lines: upper mantle, thin lines: lower mantle. The horizontal lines represent the distance for all degrees. Middle: same as top figure but for the difference between aliased and unaliased models. Bottom: Same but for the difference between aliased and input model.

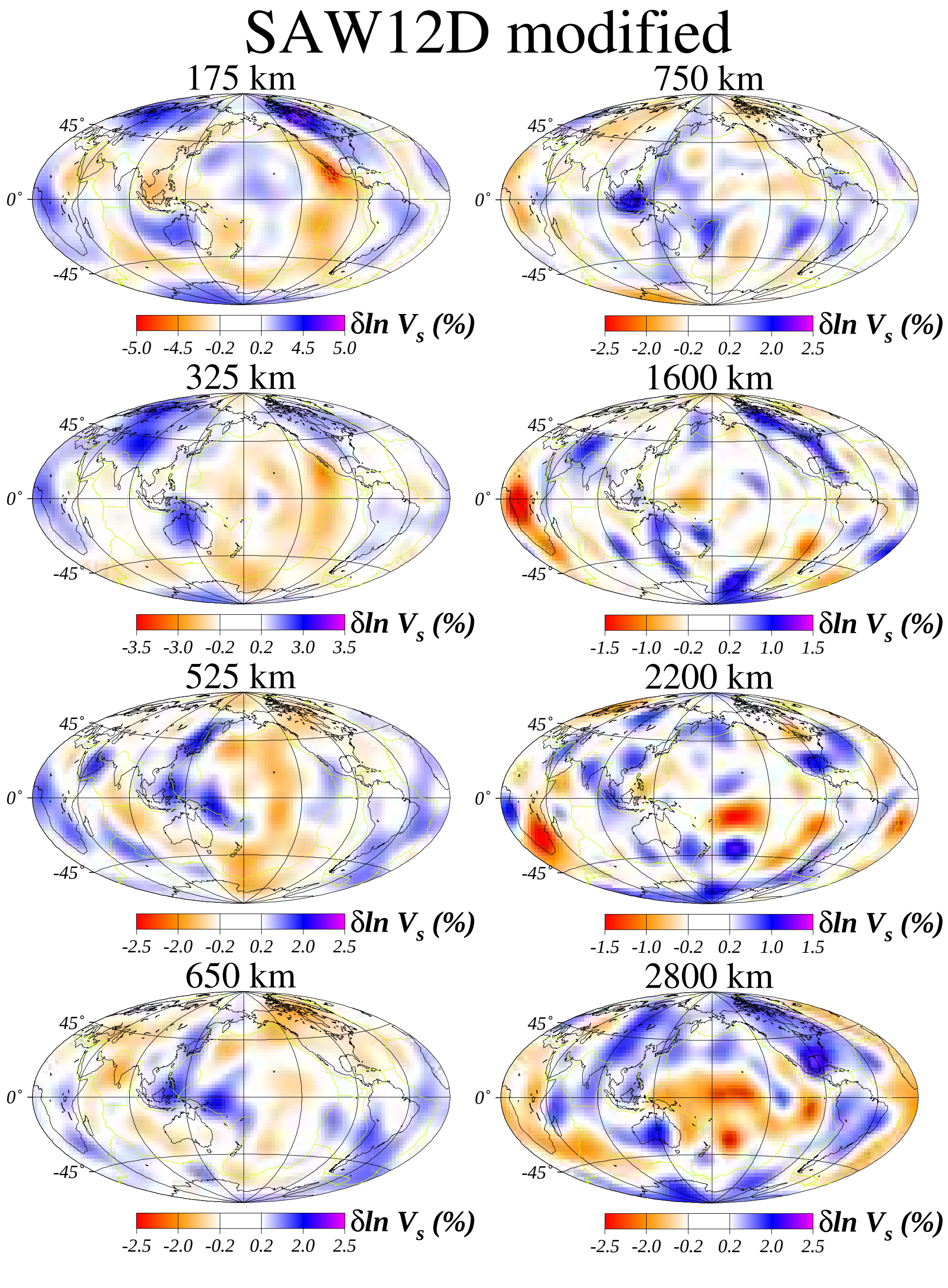

Figure 3.11. Tomographic model *SAW12* modified, as described in the section 'Comparison with tomography'.

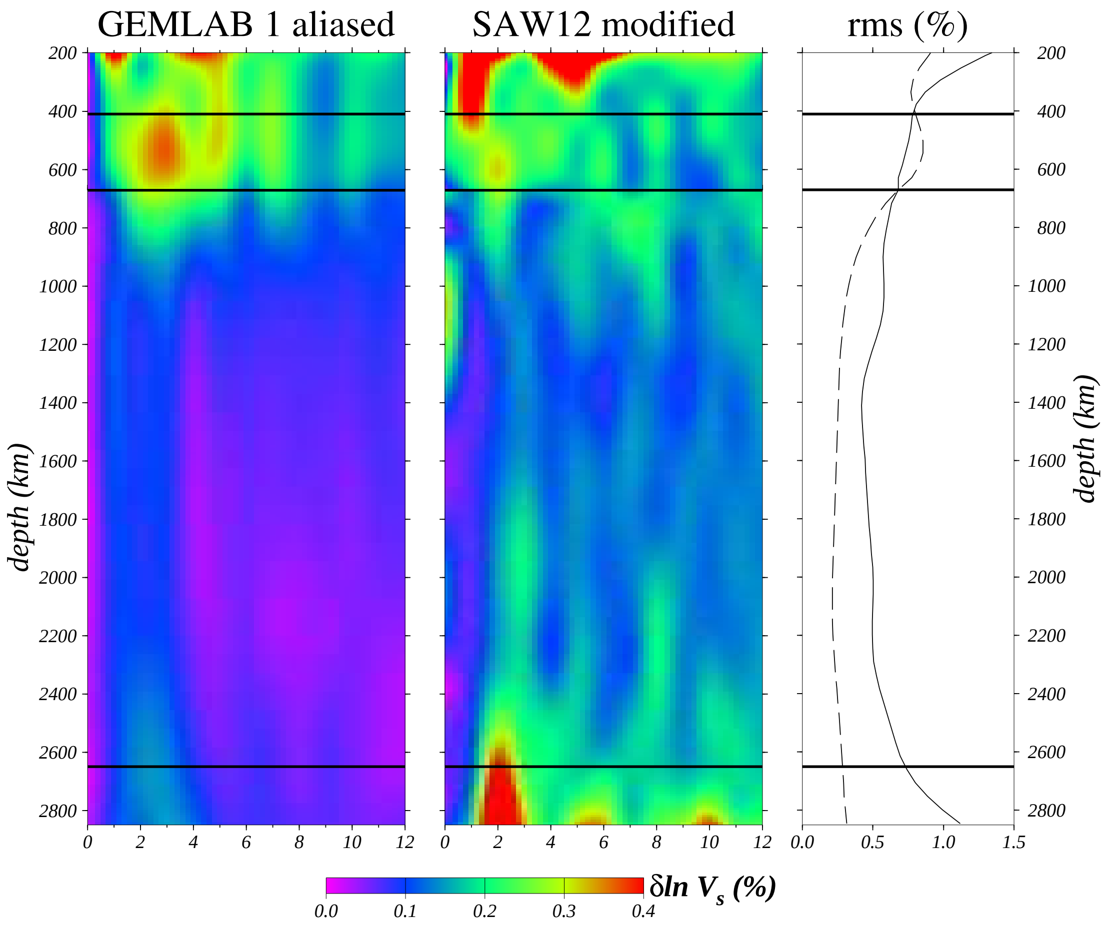

Figure 3.12. Spectral comparison between left: *GEMLAB 1* aliased, and right: tomographic model *SAW12* modified, as described in the section 'Comparison with tomography'.

Chapter 4

The effects of the theoretical formalism and data selection on mantle models derived from waveform tomography

4.1 Abstract

Most global tomographic models have been derived using a combination of surface wave (or normal mode) data and body wave travel time data. The travel time approach limits the number of phases available for inversion by requiring them to be isolated on the seismogram. This ultimately may result in limiting the resolution of 3D structure, at least in some depth ranges in the mantle. In previous work, we successfully derived a degree 12 whole mantle SH velocity tomographic model (*SAW12D*) using exclusively waveform data. In that inversion, a normal mode formalism suitable for body waveforms, the nonlinear asymptotic coupling theory (*NACT*), was combined with a bodywave windowing scheme, referred to as the 'individual wavepacket' (*IW*) technique, which allows to assign individual weights to different body-wave energy packets. We here compare the relative merits of this choice of theoretical formalism and windowing, in different depth ranges in the mantle. Choosing for reference a model obtained using 7,500 transverse component body wave and

8,000 surface wave seismograms and the *NACT* and *IW* approaches, we discuss the relative performance of the path average approximation (*PAVA*), a zeroth order theoretical approximation appropriate for single mode surface waves, relative to *NACT*, and compare the *IW* windowing scheme with a more standard 'full window' (*FW*) approach, in which a single time window is considered from the first body wave arrival to the fundamental mode surface waves. The combination *PAVA*/*FW* is often used in global tomography to supplement the travel time data.

We show that although the quality of the image derived under *PAVA*/*FW* formalism is very similar to that derived under *NACT*/*IW* in the first 300 km of the upper-mantle, where the resolution is dominated by surface waves, it deteriorates at greater depths. Images of the lower mantle are shown to be strongly sensitive to the theoretical formalism. In contrast, the resolution of structure near the core-mantle boundary depends mostly on the windowing scheme. This is because this resolution is controlled by low amplitude phases such as S_{diff}, which are downweighted in the *FW* scheme. While the image obtained in D" using the combination *NACT*/*IW* agrees well with images obtained by other authors using both waveforms and travel times, we show that, when using *FW*, uppermost mantle structure can be mapped into D". This result is confirmed by synthetic tests performed on a composite of the upper mantle geodynamic model 3SMAC. Using synthetic tests, we also show that, for structures in the upper mantle with sharp boundaries, differences are observed between *NACT* and *PAVA*. While a combination of travel times and surface wave data is adequate for resolving relatively smooth features in the mantle, our results show that, by potentially increasing the achievable sampling, the waveform approach shows great promise for future high-resolution tomographic modeling of mantle structure, if cast in appropriate theoretical framework.

Keywords: Tomography, mode coupling, synthetic waveforms, global seismology, Earth's interior, mantle

4.2 Introduction

Waveform tomography holds promise to resolve detailed structure in Earth's mantle in that it provides a way to use the entire information in the seismogram, rather than being limited to isolated phases as is the case in travel time tomography.

Synthetic seismogram computations are generally performed in a normal mode framework. The theoretical formalism required to model a waveform propagating through an arbitrarily heterogeneous medium exactly is complex, and the computation time is prohibitive in the context of most computational environments (e.g. [*Lognonné & Romanowicz*, 1990; *Geller & Takeuchi*, 1995]). Various simplifications thus need to be made to render the problem tractable. In the last fifteen years, several seismic waveform modeling techniques have been developed to compute three-dimensional models of seismic wave velocity in the Earth at a reasonable computational cost. The nature of the approximation used, as well as the way in which the individual phases are weighted, can significantly impact the ability to image heterogeneity.

Most global waveform tomographic studies rely on a zeroth order asymptotic expansion, the 'Path Average Approximation' (*PAVA*) [*Jordan*, 1978 ; *Woodhouse & Dziewonski*, 1984]. Under *PAVA*, sensitivity of the waveform is restricted to the horizontally averaged structure between the source and the receiver in the vertical plane containing the great-circle path. The path average phase perturbation is expressed as the average along the raypath of the local frequencies $\delta\omega^k_{local}$ as defined by Jordan (1978). To zeroth order in ℓ (where ℓ is the angular degree of the mode), *PAVA* is equivalent to taking into account the coupling of multiplets along a dispersion branch [*Mochizuki*, 1986, *Park*, 1987, *Romanowicz*, 1987], an approximation that is reasonably accurate for surface waves. Because it offers the important advantage of being relatively fast computationally, *PAVA* has also been applied to model body waves, although it is not able to reproduce the "ray" character of the path. In tomographic applications, it has been used to compute several mantle models [e.g. *Woodhouse & Dziewonski*, 1984, *Tanimoto*, 1990] and has been augmented with travel time data in more recent models, under the infinite frequency, ray theory approximation [e.g. *Su et al.*, 1994, *Liu & Dziewonski*, 1994] in order to improve resolution in the lower mantle.

To correctly account for the sensitivity of broadband body waves to the three-dimensional structure along the raypath it is necessary to include the effect of coupling across mode branches in the mode summation [*Li & Tanimoto*, 1993]. In the Nonlinear Asymptotic Coupling Theory formalism (*NACT*) [*Li & Romanowicz*, 1995], only the term corresponding to across-branch coupling is linearized under the assumption of smoothness of heterogeneity. The path average contribution to the seismogram remains nonlinear, which improves the validity of the approach beyond the strictly short-time approximation of Li & Tanimoto (1993). To order zero in the asymptotic formalism, off-plane effects, i.e. focusing and defocusing of energy affecting wave amplitudes [*Romanowicz*, 1987], are not accounted for. Inclusion of such effects has been discussed for example by [*Clévédé and Lognonné*, 1996a; *Marquering et al.*, 1998].

The whole-mantle shear velocity model *SAW12D* [*Li & Romanowicz*, 1996] was developed in the *NACT* framework. Comparisons of 'checkerboard' tests have shown increased resolution in lower mantle versus models derived under *PAVA* formalism [*Li & Romanowicz*, 1995]. *SAW12D* also presents good agreement with the results of local modeling of heterogeneity in the lowermost mantle [*Bréger & Romanowicz*, 1998].

In addition to an improved theoretical formalism, *SAW12D* was developed using a windowing scheme which we call the 'individual wavepacket' technique (*IW*), designed to allow relative weighting of individual energy wavepackets. The *IW* windowing consists in extracting separately the individual body wave energy packets in each seismic trace (figure 4.1, bottom). A data weighting scheme that normalizes the individual wavepacket amplitudes brings out the signal from the low-amplitude arrivals, and simultaneously allows each waveform to be fit independently. This method contrasts with the traditional approach where a single wavepacket consisting of a continuous train of phases starting with the first energy arrival above the noise level (figure 4.1, top) is extracted. We refer here to this windowing scheme as the 'full waveform' (*FW*) technique. This procedure is widespread [e.g. *Tanimoto*, 1990, *Su et al.*, 1994] and has the advantage of allowing the rapid aquisition of a large quantity of data. However, the resulting models are influenced mostly by the information contained in the high amplitude phases, at the detriment of low-energy wavepackets such as, for example, the $S_{\rm diff}$ diffracted along the core-mantle boundary. This is because, in minimizing the difference between the data and the corresponding synthetics, the inversion will preferentially fit the high amplitude part of the wavepacket.

The *IW* method requires considerably more processing effort than the *FW* approach but it is crucial for the extraction of information related to the structure located in the lowermost part of the mantle, as the low amplitude S_{diff} phase is arguably the most valuable source of information relative to D" heterogeneity in a transverse component seismogram. Since low amplitude signal is enhanced in this method, it has the potential of increasing the effect of noise. However, our data selection is entirely manual. For each deconvolved and filtered seismogram, we compute the corresponding synthetic in the reference *PREM* model and compare it to the observed one, both visually and using a variance reduction criterion for each wavepacket considered. In this fashion, noisy data can be rejected together with records affected by timing errors and errors in instrument corrections.

The issue we wish to address here is the relative benefit of the theoretical improvements of *NACT* over *PAVA* and the windowing of individual energy wavepackets versus using the body wave part of the seismogram as a whole. To quantify these benefits, we compare four tomographic models resulting from the inversion of a dataset under *PAVA* and *NACT* formalisms with the *FW* and IW windowing schemes. Ideally, one would want to use as reference a model obtained with a more exact theoretical formalism (*i.e.* [*Friederich*, 1998; *Lognonné & Romanowicz*, 1990; *Geller & Takeuchi*, 1995]). However, computations for a degree 12 whole mantle model with the number of paths considered in our study and the necessary bandwidth (down to periods of 32 seconds) are currently beyond reach. We therefore use as reference the *NACT-IW* model, as it is the one derived with the more 'exact' theoretical formalism and the most sophisticated procedure that we can currently afford. We then observe and quantify how the image changes as a result of the use of a different windowing scheme (*FW*), a less accurate theoretical formalism (*PAVA*), and both. While we cannot prove rigorously that the *NACT-IW* approach is the 'best' possible one, differences in the models can give insight into the relative importance of various inversion ingredients in different depth ranges in the mantle. In addition, resolution tests for up to degree 8 (*Li & Romanowicz*, 1995, figures 5 & 6) and 12 (*Li & Romanowicz*, 1995, figure 6) constitute further evidence that *NACT* resolves the lower mantle better than *PAVA*.

4.2.1 Inversion

We use the inversion procedure used by [*Li & Romanowicz*, 1996]. A detailed description is given in that paper and we present here a synopsis of its most relevant aspects.
The inverse problem is solved by making use of a stochastic formulation [e.g. *Jackson*, 1979 ; *Tarantola & Valette*, 1982] and the finite-dimensional model is obtained by the recursive application of a Newton scheme to the Fréchet derivatives of the ℓ^2-norm objective function. The penalties imposed through the model covariance matrix have been kept identical in the derivation of each of the four solutions. The models are expressed as relative perturbations in shear wave velocity $\delta\ln(V_{SH})$ from the spherically symmetric model *PREM* [*Dziewonski & Anderson*, 1981] and are parametrized laterally in spherical harmonics up to degree 12 and radially in Legendre polynomials up to degree 5 in the upper mantle and up to degree 7 in the lower mantle.
The data are weighted by three factors ω_e, ω_n and ω_r. Each wavepacket is scaled by $\omega \equiv \omega_e\omega_n\omega_r$. The weight ω_e corresponds to systematic error (uncertainty in source parameters, off-great circle effects, small scale heterogeneity, etc...) which is scaled to the amplitude of the wavepacket such that $\omega_e = \frac{1}{\epsilon}$ where ϵ is the rms of the wavepacket. The weight ω_n accounts for the redundancy in the data that constitutes a given wavepacket and is computed as the geometric average of the two extremes: for no redundancy in the wavepacket, ω_n should be set to unity. In contrast, for totally redundant data, ω_n should be $\frac{1}{n}$ where n is the number of data points in the wavepacket. We thus set $\omega_n \equiv n^{-\frac{1}{2}}$. Finally, a factor ω_r accounts for the redundancy among wavepackets. A full description of its computation is given in [*Li & Romanowicz*, 1996, Appendix A].
Hereafter, we use the nomenclature given in Table 4.1 to refer to the four combinations of models derived. Horizontal comparisons (*i.e.* between models 1 and 2 or 3 and 4) provide information about the effect of the theoretical formalism on the models. In contrast, vertical comparisons (*i.e.* between models 1 and 3 or 2 and 4) bring out the impact of the windowing scheme.

4.2.2 Dataset

We use a set of transverse component accelerograms, consisting of 7,527 body wave traces low-pass filtered at 32 seconds, and 7,919 first and second orbit Love wavetrains low-passed at 80 seconds, collected from GSN, GDSN and GEOSCOPE networks between 1977 and 1992. The same dataset was used in computing models 1 through 4.

4.3 Results

In figure 4.2, we present the correlation as a function of depth of model 1 with the models resulting from each of the other three inversions. The solid line (labeled 2) represents the correlation between the *NACT* and the *PAVA* formalism. In contrast, the dashed line (labeled 3) shows the correlation between *IW* and *FW*-derived models under *NACT* formalism. The dotted line (labeled 4) shows the decorrelation due to the combined use of the *PAVA* formalism with the *FW* scheme.

4.3.1 Uppermost mantle

In the first 300 km of the mantle, models 2 and 3 remain very similar to *NACT-IW* (Figure 4.2). The comparison between the heterogeneity pattern at 150 km (Figure 4.3 (top) and Table 4.2 (a)) shows nearly perfect correlation among models at that depth: in all cases, the major global tectonic features are recovered well. The first 300 km of the mantle are predominantly sampled by the Love wavetrains for which the *PAVA* approximation works well, as discussed above. Since *IW* and *FW* differ predominantly for body waveforms, the windowing scheme has little impact on the tomographic image of the uppermost mantle. The similarity among these four images also indicates that the sets of damping parameters used in each inversion have been comparably calibrated. Except for smoothness across the 670 km discontinuity, the differences among the models at depths other than the uppermost mantle are unlikely to be caused by inconsistencies in the regularization. We address the issue of the continuity across the 670 km discontinuity below.

4.3.2 Transition zone

The similarity among the models decreases continuously below a depth of 300 km. In the lower part of the upper mantle, models 2 and 3 remain correlated with model 1 at the 0.90 level but the effect of *PAVA* combined with *FW* brings the correlation between models 1 and 4 below 0.80 at the bottom of the transition zone (Figure 4.2). The near overlap between the correlation profiles of models 2 and 3 indicates that the theoretical formalism and windowing scheme in the upper mantle contribute equally to the quality of the tomographic image. In Figure 4.3 (bottom) and Table 4.2 (b), we compare the models at 600 km depth. Important features such as the westward shift with depth of low velocities in the Central Pacific (*e.g.* [*Romanowicz*, 1987]) is present in all four models. However, the model details are somewhat displaced in the *PAVA* images, in particular under the Southern Pacific and the South-American craton and the amplitudes are decreased in the *FW*-derived models. The issue of model amplitude is closely related to damping in the inversion. Our experience is that slight adjustment of damping to obtain a closer match of the amplitudes in different models is always possible. However, it will not affect to first order the geographical distribution of model heterogeneity.

4.3.3 Lower mantle

In the lower mantle, the progressive decorrelation between models 1 and 2 (Figure 4.2) illustrates the importance of an accurate theoretical formalism in a region sampled predominantly by large amplitude body wave phases such as S and its multiples, down to 2,500 km depth. Figure 4.4 (top) shows maps of heterogeneity at a depth of 1,500 km where models 1 and 2 are least similar. Differences in amplitudes are observed under the Asian continent and the models differ most in pattern under the Arctic, the Central and North Eastern Pacific, the South Western Atlantic and the North and South American cratons. The same discrepancies persist in the comparison between the *FW* models 3 and 4, providing further evidence that the theory controls the resolution of structure in the lower mantle. Comparison between the end member models 1 and 4 shows disagreement in most regions of the globe, with correlation falling to 0.50 at 2,300 km. In most of the lower mantle the choice of windowing has a minor importance, (see the similarity in correlation level between models 2 and 4 between 1,000 km and 2,500 km depth). The decorrelation from *IW-NACT* to *FW-NACT* (or *IW-PAVA* to *FW-PAVA*) is indeed small compared to that resulting from the passage from *IW-NACT* to *IW-PAVA* (see table 4.2 (c)).

4.3.4 D" region

In the lowermost mantle, the resolution is driven by the fit to the ScS phase and its multiples reflected on the core-mantle boundary, and the low amplitude S_{diff} phase. In figure 4.5, we present a projection on the CMB of the coverage by 954 S_{diff}, 3,766 ScS, 1,539 ScS_2 and 125 ScS_3 phases. The linear features represent the sampling by S_{diff} and the circles correspond to the CMB reflections of ScS and its multiples. This projection is calculated in the ray theoretic approximation (no Fresnel zone is computed) and thus represents a lower bound of our D" coverage. Due to inhomogeneous sampling, the northern hemisphere is expected to be better resolved than the southern hemisphere.

As discussed above, resolution at these depths is expected to be highly sensitive to the windowing scheme because of the relatively low amplitude of S_{diff}. Figure 4.4 (bottom) shows considerable differences between models obtained using the two different windowing schemes, with the correlation coefficient falling below 0.70 (see table 4.2 (d)). A noticeable distortion arising from the use of *FW* is the change in sign of the anomaly under the Southern African craton both in *NACT* and *PAVA* models. More importantly, the D" structure in the models derived with *FW* is found to be correlated at up to the 0.85 level with that of the heterogeneity at 150 km depth in the *NACT-IW* model. Table 4.2 (d) also shows that the *FW* models in the D" region correlate better with the heterogeneity at 150 km (correlation coefficient of 0.80) than with their *IW* counterparts in the D" (correlation coefficient of 0.70). This effect is absent in the models derived with the *IW* scheme where little correlation is observed between the uppermost mantle and the D" (correlation coefficient of 0.33). In figure 4.6, we present the spherical harmonic degree-by-degree correlation between uppermost mantle and D" heterogeneity for all models. Models derived with the *IW* scheme in the *NACT* (solid line-diamonds) and *PAVA* (dashed line-circles) formalisms are poorly correlated with the surface at all degrees (correlation coefficient between 0 and 0.60), except at degree 1. Conversely, the models derived with the *FW* scheme (dotted line-squares for *NACT* and long dashed line-triangle for *PAVA*) correlate strongly except at degrees 2 and 3 and are strongest at degrees 4 to 6 which correspond to the spectral signature of tectonics.

Our results show that upper mantle structure is mapped into the lower mantle at degrees higher than 3 when the *FW* formalism is used. This effect can be understood in the following way: lateral heterogeneity is strongest in the uppermost 200 km of the mantle, and the least squares inversion procedure (ℓ^2 norm minimization in the inversion) will have a tendency to map the unexplained part of the signal into the least sampled regions of the model. This is possible because, although the parametrization is split across the 670 km discontinuity, imposition of a smoothness constraint between upper and lower mantle is necessary to maintain continuity in the model rms. We indeed observe wide fluctuations in the transition zone and uppermost lower mantle amplitudes in the absence of roughness penalty at the discontinuity. A similar trade-off would of course also be observed for a 'whole mantle' radial parametrization, using either local or global basis functions, in the presence of radial damping.

It thus appears that, in the absence of S_{diff} coverage, the lowermost mantle is poorly sampled and acts as repository for model nullspace. To verify that this is indeed the case, we conduct an *IW-PAVA* inversion where we exclude from the data set the wavepackets corresponding to S_{diff} and ScS phase arrivals. Figure 4.7 shows the result of this experiment. The top left figure shows model 2 at 2,800 km depth where all the data have been included and the correlation with the structure at 150 km is weak (correlation coefficient of 0.36). The top right figure shows the D" structure after inverting the data set without the S_{diff} phases. The correlation with the uppermost mantle increases to 0.57. In the bottom left figure, the S_{diff} and the ScS phases have been taken out of the data set and the correlation reaches with upper mantle 0.88. We show in the bottom right part of the figure model 2 at 150 km depth for comparison. This test demonstrates that the absence of sampling in the lowermost mantle produces the transfer of heterogeneity from the uppermost mantle in the inversion. This effect is seen to become more prominent as the sampling of D" diminishes. This is precisely what is observed in the *PAVA-FW* inversion of the full dataset, an indication that, because it fails to take the S_{diff} into account, this methodology misses to a large extent information about the lowermost mantle. This is one of the reasons why studies that rely on *PAVA-FW* formalism augment their dataset with travel time data of phases sensitive to the lowermost mantle.

4.4 Synthetic tests

4.4.1 Mapping of upper mantle heterogeneity in the D"

So far our analysis has relied on the postulate that of all the formalisms presented, the *NACT-IW* best images the structure sampled. Although plausible, this remains an assumption. A less biased approach to measuring the distortion resulting from the use of either formalism is to perform a synthetic test on a model with realistic upper mantle and no lower mantle 3D structure. Ideally, this test would be performed by tracing 'exact' (*i.e.* non-asymptotic) synthetics through the input model and by inverting them using each of the four methods. As indicated above, there does not exist any method that allows the computation of a synthetic data set of the size used in the present study in a reasonnable amount of time. An element of circularity is currently unavoidable in the models derived from synthetic tests preformed with *NACT*. It is nevertheless instructive to examine the differences between models obtained using various approaches.

We compute synthetic seismograms for the paths used in the inversions described above using as input the geodynamic model *3SMAC* [*Nataf & Ricard*, 1996] between 50 km and 600 km depths and spherically symmetric model PREM [*Dziewonski & Anderson*, 1981] in the rest of the mantle. The input model model is parametrized radially in Legendre polynomials up to degree 5 in the upper mantle. *NACT* synthetics are traced through the composite model expanded laterally up to spherical harmonic degree 32 (Figure 4.8) and inverted in *NACT-IW* and *PAVA-FW* formalisms for up to degree 12, thus allowing aliasing of small-scale heterogeneity into the long-wavelength model (*e.g.* [*Mégnin et al.*, 1997]). In the upper mantle, we compare the input model truncated to degree 12 (Figure 4.8) to the result of the *NACT-IW* (Figure 4.9) and the *PAVA-FW* (Figure 4.10) inversions. In the lower mantle (Figures 4.9 and 4.10), the heterogeneity recovered is spurious.

At 100 and 200 km depths (Figures 4.9 and 4.10), the heterogeneity pattern of the input model is largely recovered by both inversion schemes, although the amplitudes are slightly depressed, in general agreement with a similar test made with phase velocities by [*Ricard et al.*, 1996]. In agreement with the observations from the inversion of the 'real' dataset, the models exhibit little dependence on the formalism, owing to the dominance of surface waves well modeled by *PAVA* theory.

Radial smearing of the heterogeneity is observed between 300 and 400 km depths. This region corresponds to a sharp drop in coverage owing to the diminishing Love wave sampling, which causes a downward transfer of heterogeneity. This effect is compensated at 500 km (and 600 km with *PAVA-FW*) by the appearance of 'negative tectonic features', in particular over the Asian, North American and South American shields. We note nevertheless that the amplitude of this effect is modest (not exceeding $\pm 1\%$) compared with amplitudes recovered from real datasets and may be further diminished by the adoption of local basis functions such as splines (*e.g.* [*Masters et al.*, 1996; *Su & Dziewonski*, 1996]) to parametrize the model.

In the lower mantle, (Figures 4.9 and 4.10) the *PAVA-FW* models show more heterogeneity than the *NACT-IW* at nearly all depths. In particular at 2,800 km, heterogeneity resulting from the projection of the uppermost mantle structure is observed, with amplitude peaks nearing 2%, an effect largely absent in the *NACT-IW* inversion. The *PAVA-FW* image is indeed characterized by amplitudes larger than 1%, coinciding with the surface location of the African Craton and the North and South American shields. Negative peaks exceeding -1% are also observed below the East Pacific Rise, the Southeast Indian Ridge and the southernmost part of the Mid-Atlantic Ridge. In contrast, the *NACT-IW* amplitudes are almost everywhere less than the smallest contour gradation (1%) and nowhere related to uppermost mantle structure. This agrees with the conclusions from the inversion of real data and thus confirms the predominance of this effect with *PAVA-FW* tomography.

4.4.2 Surface wave tomography: *NACT* vs *PAVA*

The results for the upper mantle show that, although comparable, *PAVA* and *NACT* models differ somewhat in the depth range sampled mostly by Love waves. Discrepancies between the two formalisms result from the absence of coupling across mode branches in *PAVA* that may affect wavepackets that include higher mode energy in addition to the fundamental mode. To assess the impact of these differences on upper mantle structure, we trace 7,919 *NACT* Love wave synthetics through a model consisting of a fast and a slow heterogeneity of identical dimensions buried between 200 and 600 km depth and latitudes 0^o and 45^o. The fast heterogeneity covers longitudes from 135^o to 180^o and the slow heterogeneity from 180^o

to 225^o (Figure 4.11). The model is expanded laterally up to spherical harmonic degree 12 and radially in Legendre polynomials up to degree 5. We then invert the synthetic dataset using *NACT* and *PAVA* formalisms for heterogeneity up to degree 12. For computational reasons, the low-pass cutoff frequency has been decreased from 12.5 mHz to 8 mHz (80 to 125 seconds). In Figure 4.11 (center), we show the result of the *NACT* inversion. Although some radial smearing is observed, (compare with the input model at 650 km), the lateral pattern is almost perfectly recovered: even the Gibbs oscillations resulting from the truncation of the spherical harmonics expansion have been preserved in the *NACT* inversion. The *PAVA* inversion on the other hand results in significant loss of the input signal: the shape of the heterogeneity has been distorted and projected southward after an inversion of polarity (note the appearance of the mirror image of the heterogeneity pattern between 250 km and 400 km between latitudes 0^o and 45^o south).

A different view of that difference is seen in the spectral heterogeneity maps of figure 4.12 (top) where the amplitude of the heterogeneity for each model is plotted as a function of wavelength (horizontal axis) depth in the upper mantle (vertical axis). The left figure shows the input model (the spectral equivalent of Figure 4.11) which displays a strong signal between degrees 1 and 7 and above degree 10, with an amplitude peak at degree 4. In the middle figure, the model resulting from the *NACT* inversion is presented (equivalent to Figure 4.11, center), displaying some radial smearing of the low degrees but an overall good reconstruction of the input image. To the right, the *PAVA* inversion is plotted (equivalent to Figure 4.11, right), showing leakage across heterogeneity of different wavelengths (note for example that the strong degree 9 signal between 200 and 400 km depth is entirely absent from the input model). At the far right of the figure, the rms amplitude of the input model (solid line), the *NACT* (dashed line) and the *PAVA* inversions (dotted line) is plotted as a function of depth. The radial agreement between input and *NACT* models is quite good. On the other hand, the overshoot of the *PAVA* model in the uppermost mantle is compensated at depth, in particular at 300 km and 500 km.

We finally investigate the transfer of heterogeneity across wavelengths, observed above when using the *PAVA* formalism, by tracing the same set of *NACT* Love wave synthetics through the synthetic model, expanded this time up to spherical harmonic degree 6, and inverting it for up to degree 12 in *NACT* and *PAVA* formalisms. The result is shown in figure 4.12 (bottom). At the left, the input model is plotted. The middle figure shows the result of the *NACT* inversion. No leakage of heterogeneity is detected across wavelengths. At the right the *PAVA* inversion show significant transfer of heterogeneity from the long into the short wavelengths, representing on average 25% of the input structure and peaking at 50% (*e.g.* at degree 11 between 200 km and 300 km depth). This is a direct consequence of the difference between the two theoretical formalisms in the context of surface waves: the *PAVA* inversion compensates for the inability to fit the *NACT* synthetics by introducing ghost structure at high degrees.

4.5 Discussion and conclusions

We have shown that two improvements to the common path average-'full window' data selection inversion procedure have a significant effect on the tomographic image: a more accurate theoretical formalism such as the nonlinear asymptotic coupling theory (*NACT*), which allows the modeling of the two-dimensional sensitivity along the great circle ray path, and a windowing scheme that extracts separately the energy wavepackets in a seismic trace. However, these improvements have different effects on the resolution of the tomographic image at different mantle depths. The uppermost regions of the mantle, sampled predominantly by surface waves, are not affected much by the choice of theoretical formalism or the windowing scheme applied to the body waveforms. Images of the mid-mantle, sampled by large amplitude body waves, are strongly dependent on the choice of theoretical formalism, as illustrated by the differences resulting from the passage from *NACT* to *PAVA* formalism. In contrast, in the lowermost mantle, sampled to a large extent by low energy phases, the choice of a windowing scheme that enhances the contribution of these phases is critical in order to avoid mapping upper mantle structure into this part of the Earth. In the models shown, the combination of *PAVA* with *FW* (and, to a similar extent, of *NACT* with *FW*) projects tectonic features into the D" region. This effect is not present when the *NACT* formalism is used in conjunction with an 'individual wavepacket' windowing scheme. This result is independently confirmed by a synthetic test using the geodynamic model *3SMAC*. By conducting another synthetic test with Love waves on a simple heterogeneity pattern in the upper mantle, we observed noticeable differences between *NACT* and PAVA-derived models. This is likely due to the coupling between the fundamental and the harmonic branches in *NACT*, for surface wavepackets with group velocity windows which contain higher mode energy.

We note that other global mantle tomographic models that have been derived using, in particular, body waveforms under the *PAVA* approximation [e.g. *Su et al.*, 1994] fortunately do not show the pervasive mapping of uppermost mantle structure into D". This is because these studies combine the waveform dataset with a large dataset of travel times of isolated bodywave phases, such as multiple S and ScS, which provide them with resolution in the lower mantle. This is arguably a valid approach when the focus is long wavelength structure such as currently recovered ([*Su et al.*, 1994; *Masters et al.*, 1996; *Liu & Dziewonski*, 1998]). Nevertheless, the poor performance of the *PAVA-FW* approach in the recovery of lowermost mantle heterogeneity casts doubt on the appropriateness of supplementing the travel time data set with body waveforms fit under a formalism designed for surface wave tomography. As more and more attention is given to smaller scale detail, the accuracy of the theoretical formalism will become critical in recovering the distribution of lateral heterogeneity in the deep mantle without bias.

We have shown in this paper that, with appropriate methodology, a data set of well-distributed waveforms alone can be used to recover structure in the deep mantle. The use of travel-times in combination with waveforms has several limitations. The necessity of using isolated seismic phases limits the sampling of the mantle that can be achieved. Moreover, travel times, as currently used, are inverted using kernels appropriate for infinite frequency ray theory, which assumes that the sensitivity to structure is 1) limited to the infinitely narrow raypath, 2) distributed uniformly along the raypath. For broadband bodywaves, these assumptions are inaccurate [e.g. *Stark & Nikolayev*, 1993, *Tanimoto*, 1995] and may lead to further biases in the recovered lower mantle structure. We are presently investigating this issue.

The set of experiments presented in this paper is limited in that the reference framework for forward and inverse modeling is that of the approximate *NACT* theory, rather than an exact computation of seismograms in the 3D earth. Computing exact bodywave seismograms for a realistic path coverage in a degree 12 earth model down to periods of 30 seconds still represents a formidable computational task. In a related study, we are addressing the performance of *NACT* and *PAVA* versus more exact computations in the upper mantle, using surface wave data down to periods of 80 sec [*Clévédé et al.*, 1999].

Although the combination of *NACT* with *IW* does much to enhance the resolution in the lower mantle, seismic tomography can still greatly benefit from a variety of improvements in the waveform inversion techniques. The modeling of sensitivity to heterogeneity off the great circle plane can bring another level of improvement to the modelisation of waveforms, as it allows to take into account elastic effects on wave amplitudes. This can be achieved by using higher order asymptotics [e.g. *Romanowicz*, 1987, *Marquering et al.*, 1998] and, eventually, accurate higher order perturbation theory [e.g. *Lognonné & Clévédé*, 1997].

Data selection scheme / Theory	$NACT$	$PAVA$
Individual wavepacket (IW)	1	2
Full waveform (FW)	3	4

Table 4.1. Nomenclature of the four models computed in this study.

Table 4.2. a) Correlation between models at 150 km depth. As seen in the corresponding figure (4.3, top) the models do not depend on which theoretical formalism and data selection scheme is used. b) Correlation between models at 600 km depth. Theory and windowing contribute equally to the image quality. This table corresponds to figure 4.3, bottom. c) Correlation between models at 1500 km depth. The decorrelation due to the use of *PAVA* exceeds that due to *FW*. This table corresponds to figure 4.4, top. d) Correlation between models at 2800 km depth. Although the windowing is the more important factor, the theoretical framework contributes significantly to the image quality. The models are also correlated with the structure at 150 km depth. The *FW* models at the CMB correlate better with the surface heterogeneity than they do with their *IW* counterparts at the CMB. This table corresponds to figure 4.4, bottom.

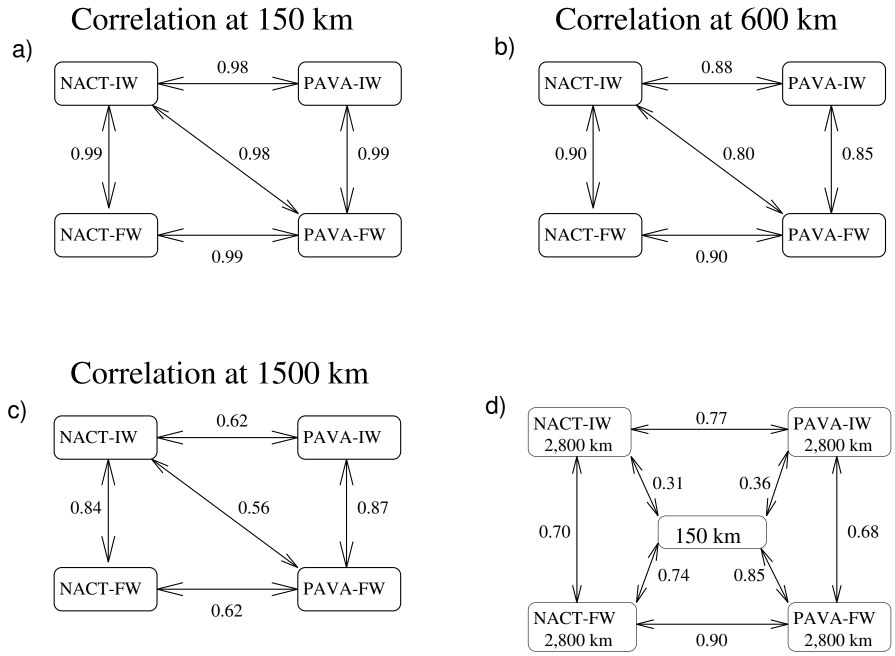

Correlation at 150 km
a)
NACT-IW
PAVA-IW
NACT-FW
PAVA-FW
0.98
0.99
0.98
0.99
0.99
Correlation at 600 km
b)
NACT-IW
PAVA-IW
NACT-FW
PAVA-FW
0.88
0.90
0.80
0.85
0.90
Correlation at 1500 km
c)
NACT-IW
PAVA-IW
NACT-FW
PAVA-FW
0.62
0.84
0.56
0.87
0.62
d)
NACT-IW 2,800 km
PAVA-IW 2,800 km
NACT-FW 2,800 km
PAVA-FW 2,800 km
150 km
0.77
0.31
0.36
0.70
0.68
0.74
0.85
0.90

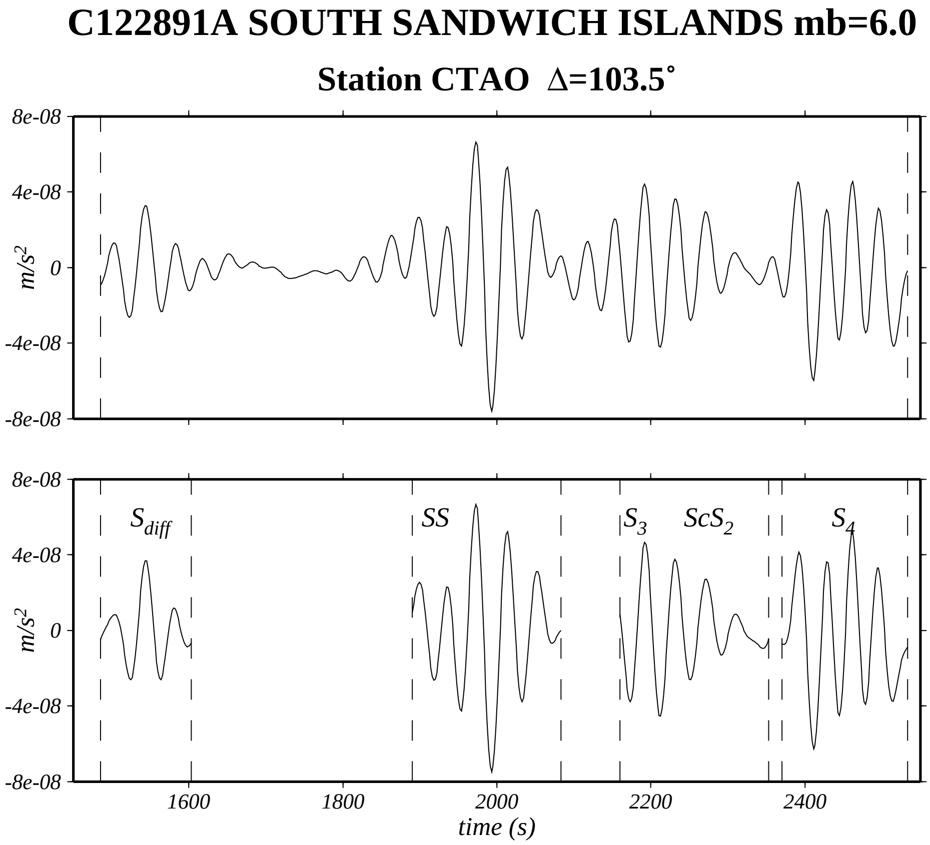

Figure 4.1. Top trace: Full waveform selection scheme (FW). The entire body wavetrain is selected. High amplitude phases are preferentially fit in the inversion. Bottom trace: Individual wavepacket selection scheme (IW). The different energy wavepackets are selected and fit separately. The body waveforms selected for the inversion are the energy arrivals between the dashed vertical lines. The assignment of phase names to the extracted window is not required by the theory but is used in the weighting scheme to penalize redundant paths.

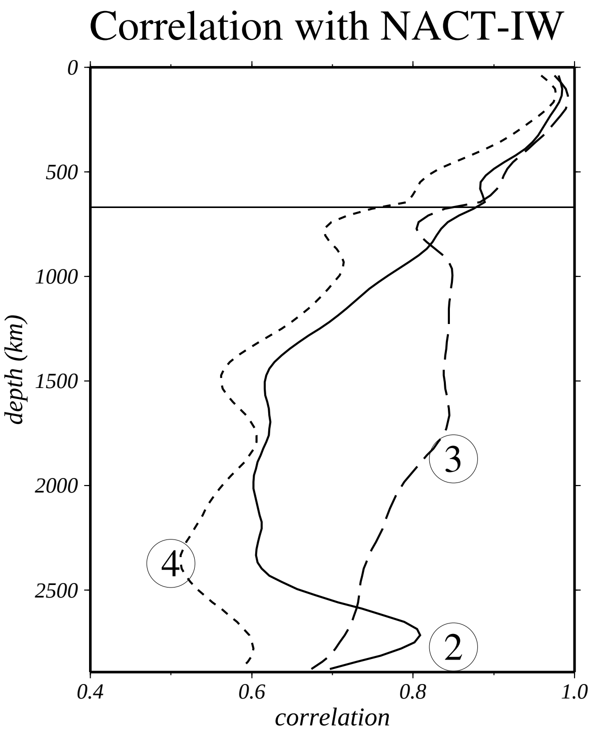

Figure 4.2. Correlation of the *NACT-IW* model with *PAVA-IW* (solid line) *NACT-FW* (dashed line) and *PAVA-FW* (dotted line). The model numbers correspond to those of Table 4.1.

Figure 4.3. top: Heterogeneity at 150 km depth derived from each waveform inversion technique. The structure is sampled predominantly by surface waves, and no significant difference is observed among the various models. bottom: Heterogeneity at 600 km depth derived from each waveform inversion technique.

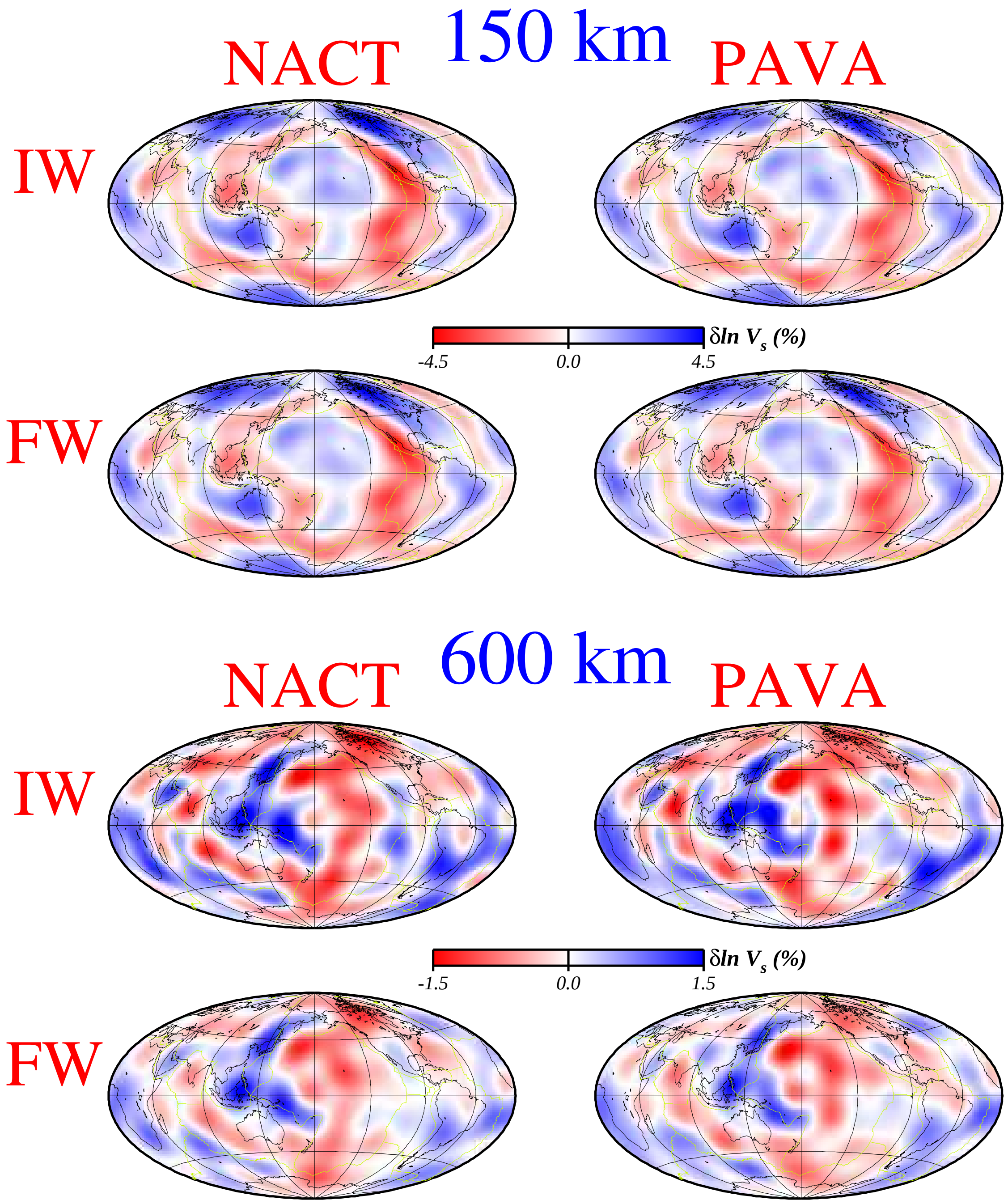
150 km
NACT
PAVA
IW
δln V_s (%)
-4.5
0.0
4.5
FW
600 km
NACT
PAVA
IW
δln V_s (%)
-1.5
0.0
1.5
FW

Figure 4.4. top: Heterogeneity at 1,500 km depth derived from each waveform inversion technique. This region is predominantly sampled by large amplitude body waves (S, SS, ...). The quality of the image at that depth depends strongly on the accuracy of the waveform modeling and weakly on the windowing scheme. bottom: Heterogeneity at 2,800 km depth derived from each waveform inversion technique. The use of a non-selective windowing scheme (bottom graphs) causes the mapping of surface heterogeneity to the CMB.

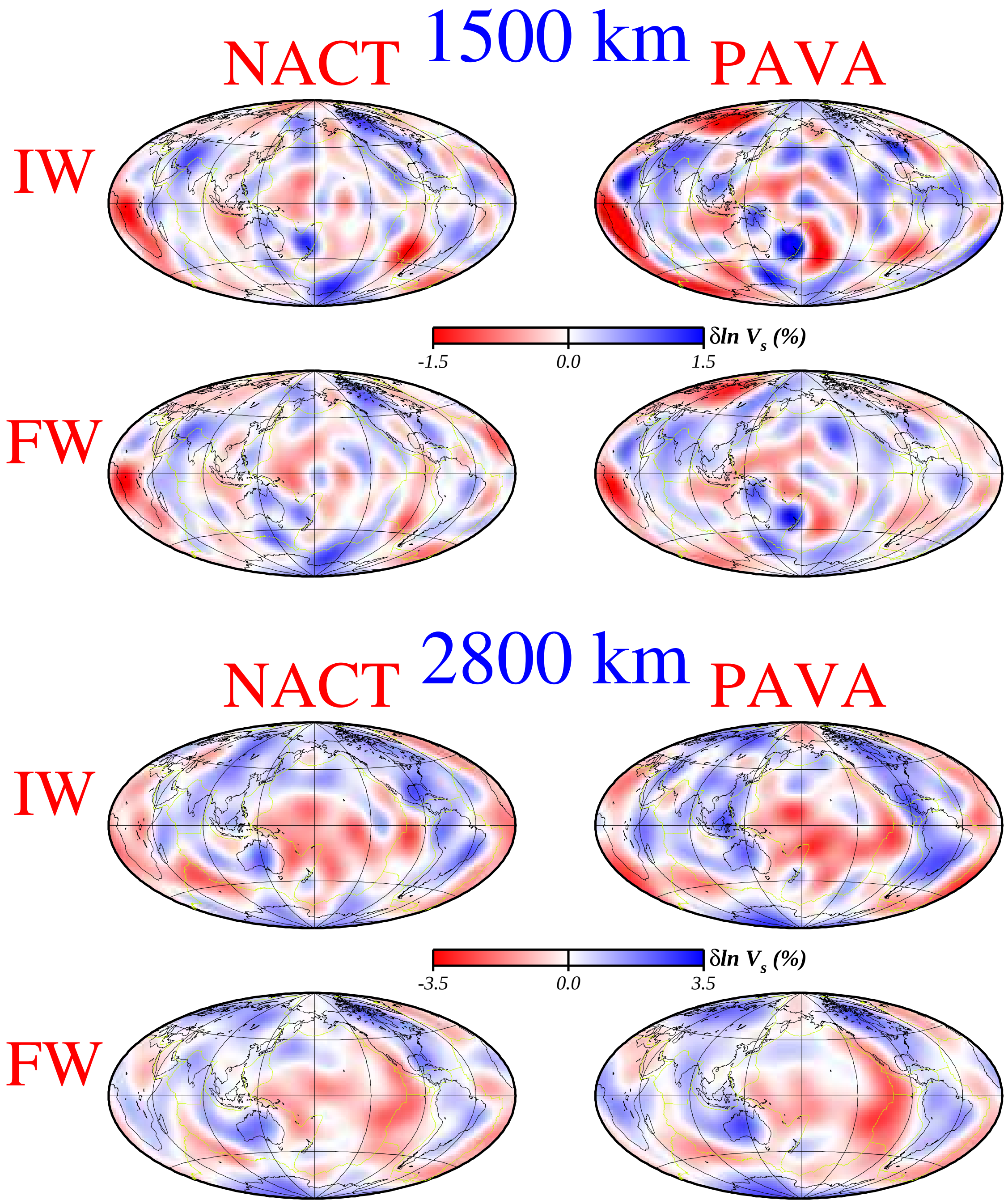
1500 km
NACT
PAVA
IW
FW
δln V_s (%)
-1.5
0.0
1.5
2800 km
NACT
PAVA
IW
FW
δln V_s (%)
-3.5
0.0
3.5

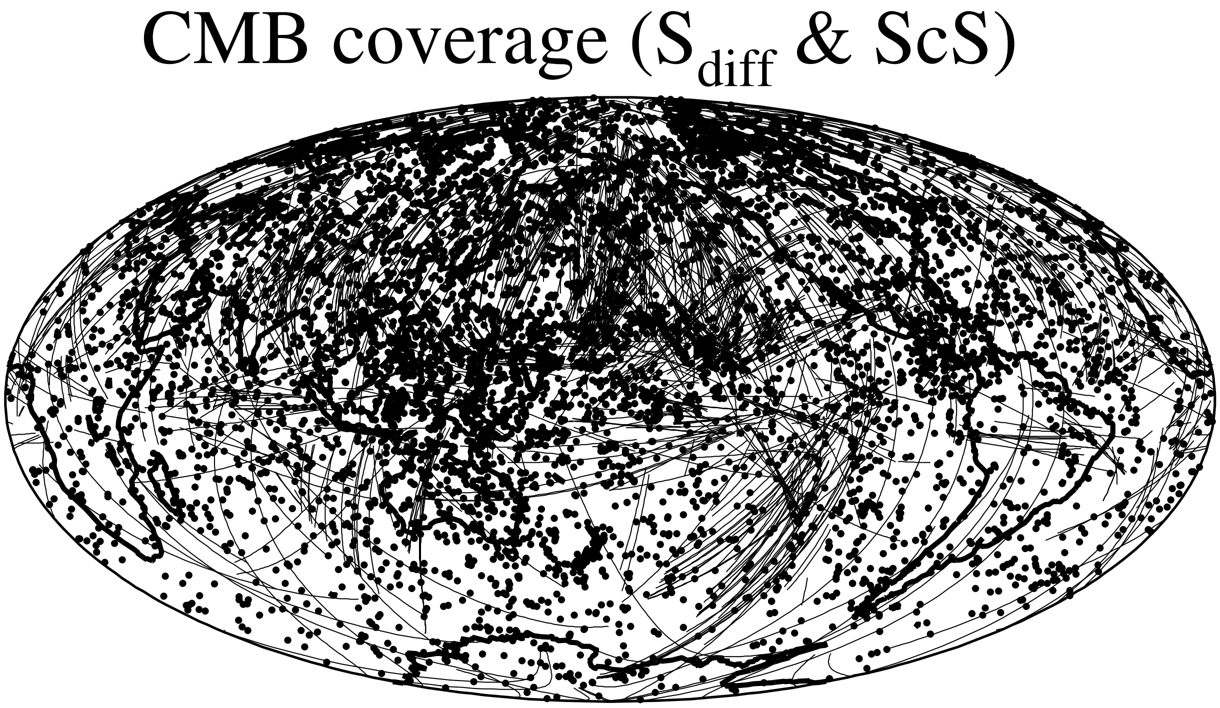

Figure 4.5. Coverage at the core-mantle boundary. The linear features represent the regions sampled by the 950 S_{diff} phases. The circles correspond to the 7,200 CMB reflections of the ScS, ScS_2 and ScS_3 phases.

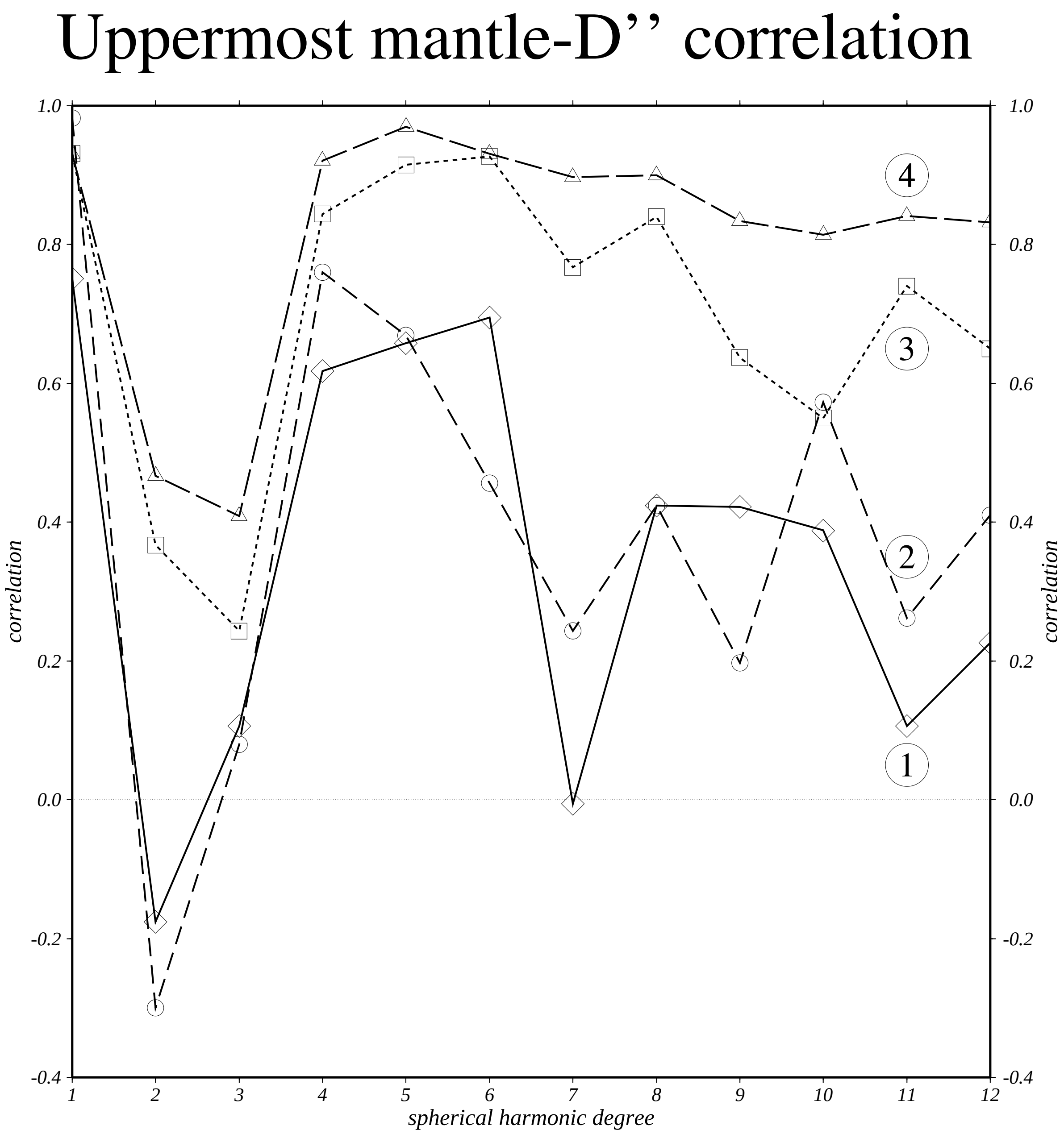

Figure 4.6. Degree-by-degree correlation between surface (150 km) and D" (2,800 km) heterogeneity at each spherical harmonic degree for *NACT-IW* (solid lines-diamonds), *PAVA-IW* (dashed lines-circles), *NACT-FW* (dotted lines-squares) and *PAVA-FW* (long dashed lines-triangles)

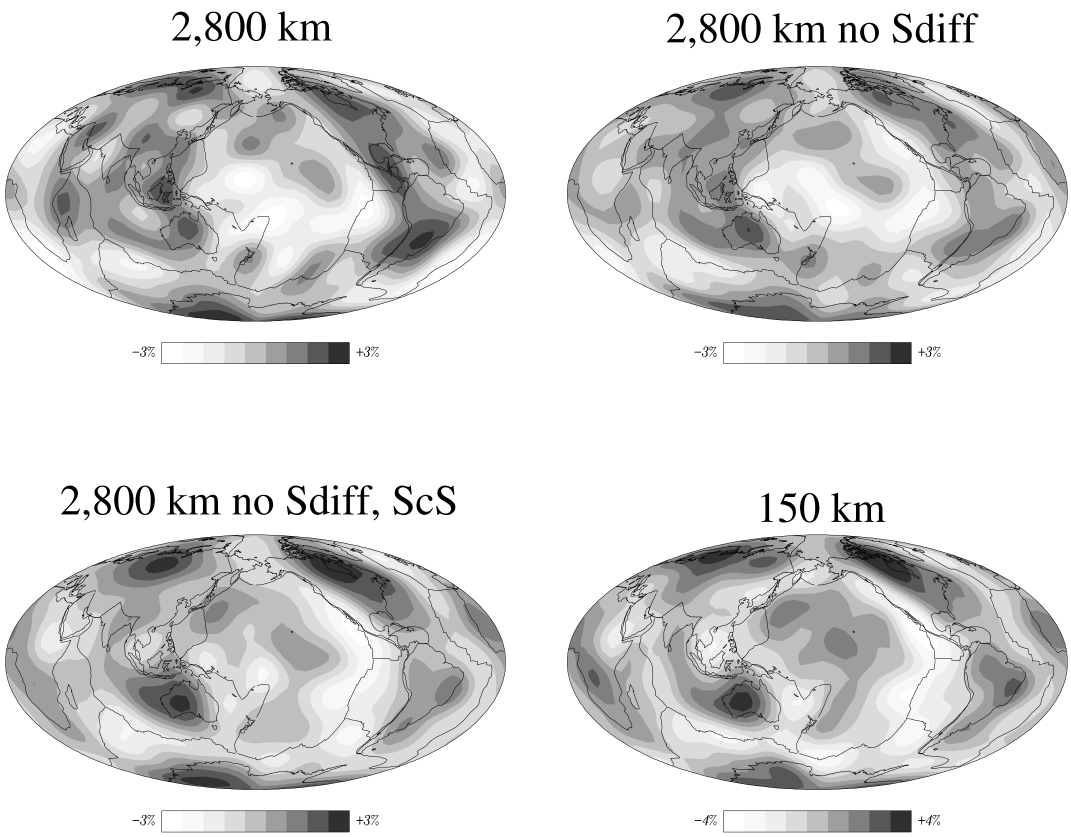

Figure 4.7. Top left: Model 2 (*PAVA-IW*) at 2,800 km (same as [Figure 4.4, bottom] top right). Top right: *PAVA-IW* inversion of the data set without the S_{diff} phases. Bottom left *PAVA-IW* inversion of the data set without the S_{diff} and the ScS phases. Bottom right: Model 2 (*PAVA-IW*) at 150 km (same as Figure [4.3, top] top right).

Figure 4.8. Left: Input model *3SMAC* expanded laterally up to spherical harmonic degree 32 and radially in Legendre polynomials up to degree 5. In the lower mantle, the input model is the spherically symmetric model *PREM*. Right: *3SMAC* truncated at spherical harmonic degree 12.

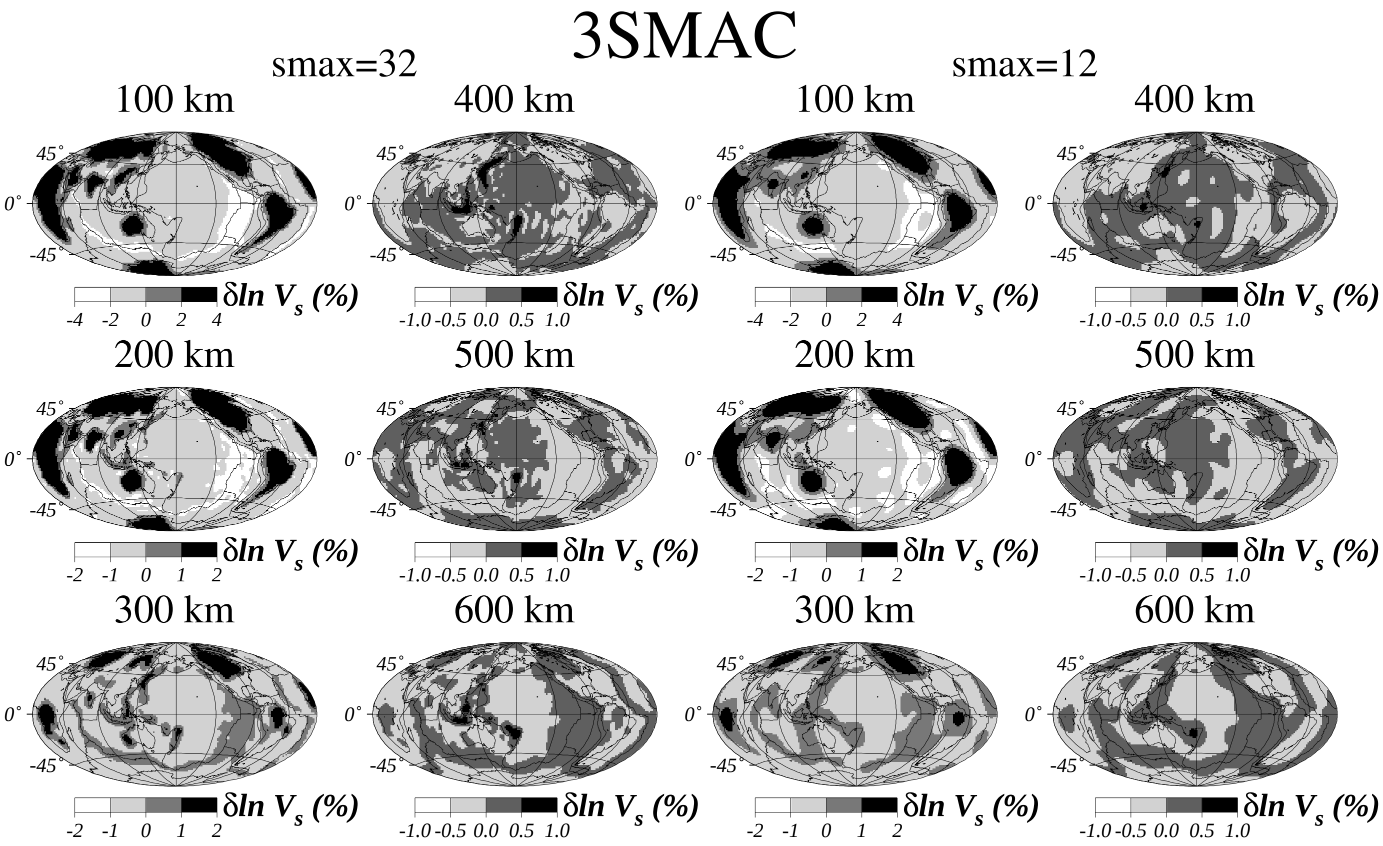
3SMAC
smax=32
smax=12
100 km
400 km
100 km
400 km
200 km
500 km
200 km
500 km
300 km
600 km
300 km
600 km
45°
0°
-45°
δln V_s (%)
-4 -2 0 2 4
-2 -1 0 1 2
-1.0 -0.5 0.0 0.5 1.0

Figure 4.9. *NACT-IW* inversion for up to spherical harmonic degree 12 of synthetics computed for the (degree 32) model in Figure 4.8.

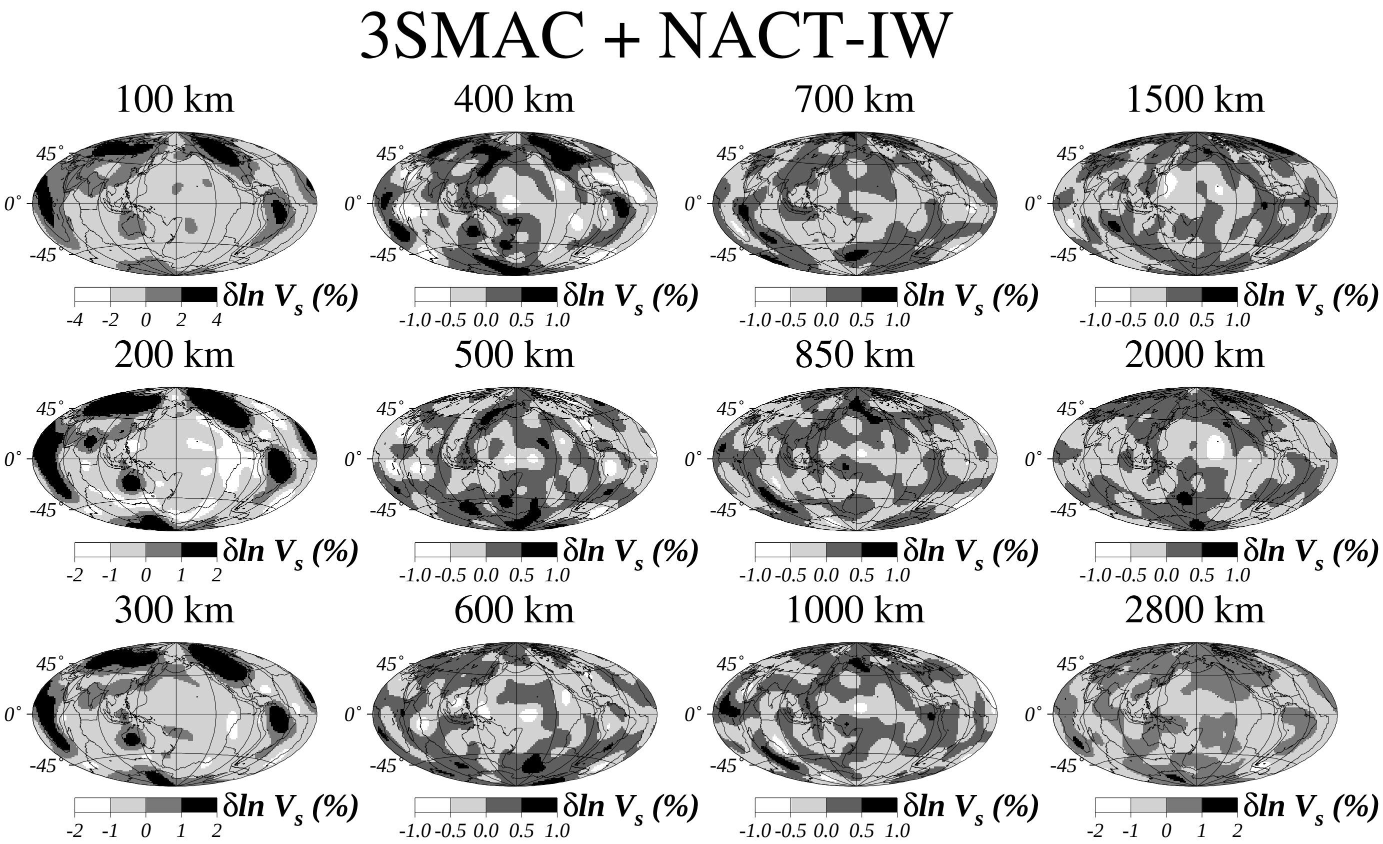
3SMAC + NACT-IW
100 km
400 km
700 km
1500 km
200 km
500 km
850 km
2000 km
300 km
600 km
1000 km
2800 km
45°
0°
-45°
δln V_s (%)
-4 -2 0 2 4
-2 -1 0 1 2
-1.0 -0.5 0.0 0.5 1.0

Figure 4.10. *PAVA-FW* inversion for up to spherical harmonic degree 12 of synthetics computed for the (degree 32) model in Figure 4.8.

3SMAC + PAVA-FW

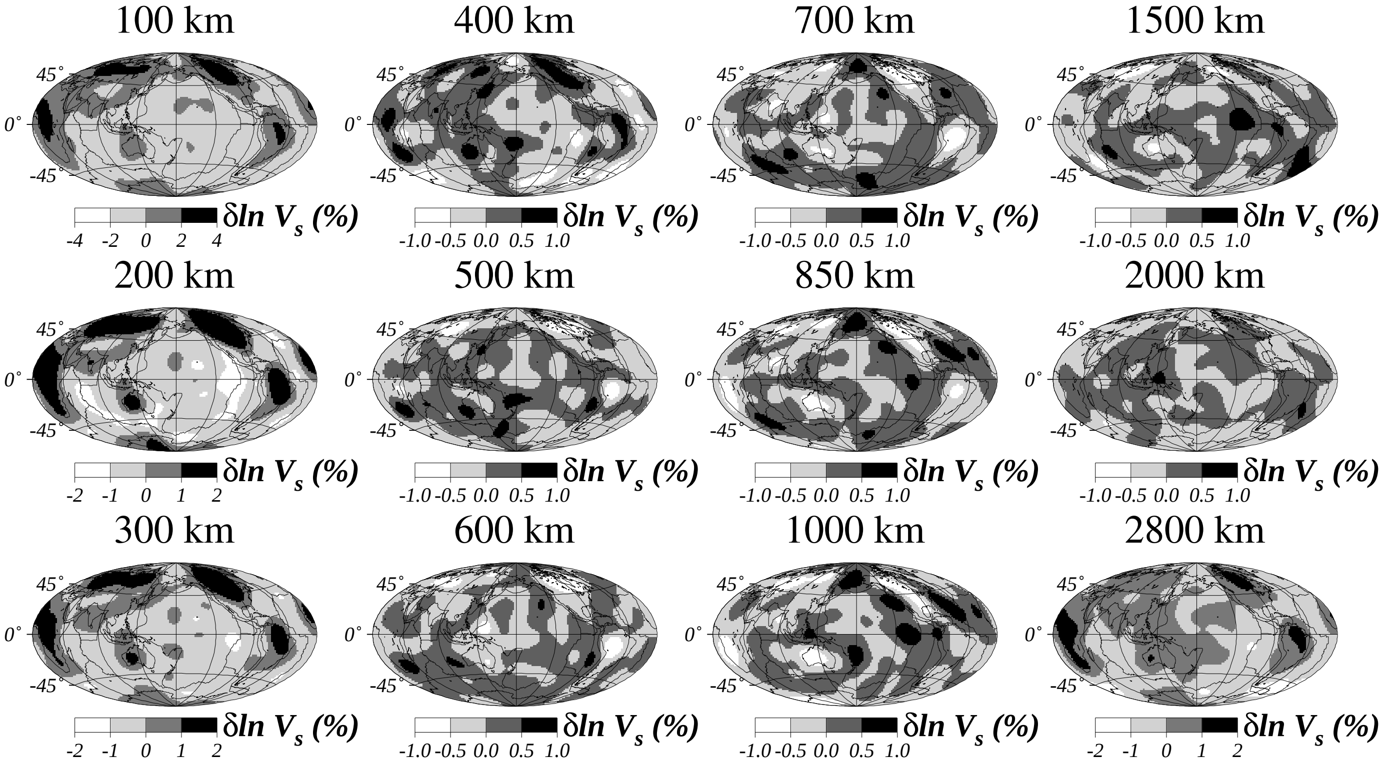

Figure 4.11. Left: Synthetic model used in the surface wave experiment. The heterogeneities are distributed radially between 200 and 600 km depth and laterally between latitudes 0^o and 45^o and longitudes from 135^o to 180^o (fast heterogeneity) and from 180^o to 225^o (slow heterogeneity). The model is expanded laterally in spherical harmonics up to degree 12 and radially in Legendre polynomials up to degree 5. Center: $NACT$ inversion of synthetics through the synthetic model. Right: $PAVA$ inversion of synthetics through the synthetic model.

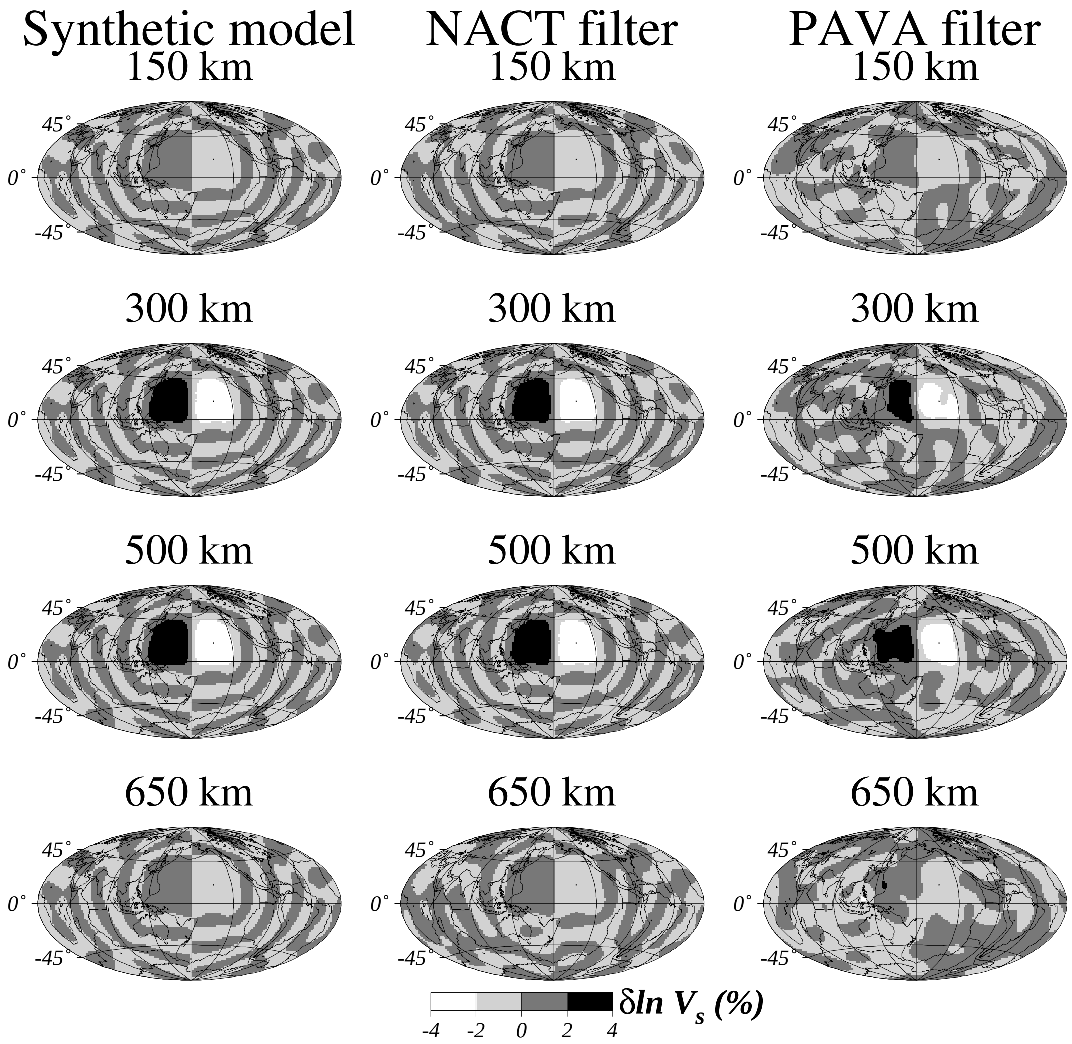

Synthetic model
NACT filter
PAVA filter
150 km
300 km
500 km
650 km
45°
0°
-45°
$\delta ln\ V_s$ (%)
-4
-2
0
2
4

Figure 4.12. Spectral representation of the synthetic experiments. Amplitudes are plotted for each model as function of spherical harmonic degree (horizontal axis) and depth (vertical axis). Top: left: input synthetic model (Figure 4.11, left). Center: *NACT* inversion (Figure 4.11, center). Right: *PAVA* inversion (Figure 4.11, right). Far right: rms amplitudes for -solid line- the input model, -dashed line- the *NACT* model, and -dotted line- the *PAVA* model. Bottom: left: input synthetic model (smax=6). Center: *NACT* inversion for up to degree 12. Right: *PAVA* inversion for up to degree 12. Far right: rms amplitudes for -solid line- the input model, -dashed line- the *NACT* model, and -dotted line- the *PAVA* model.

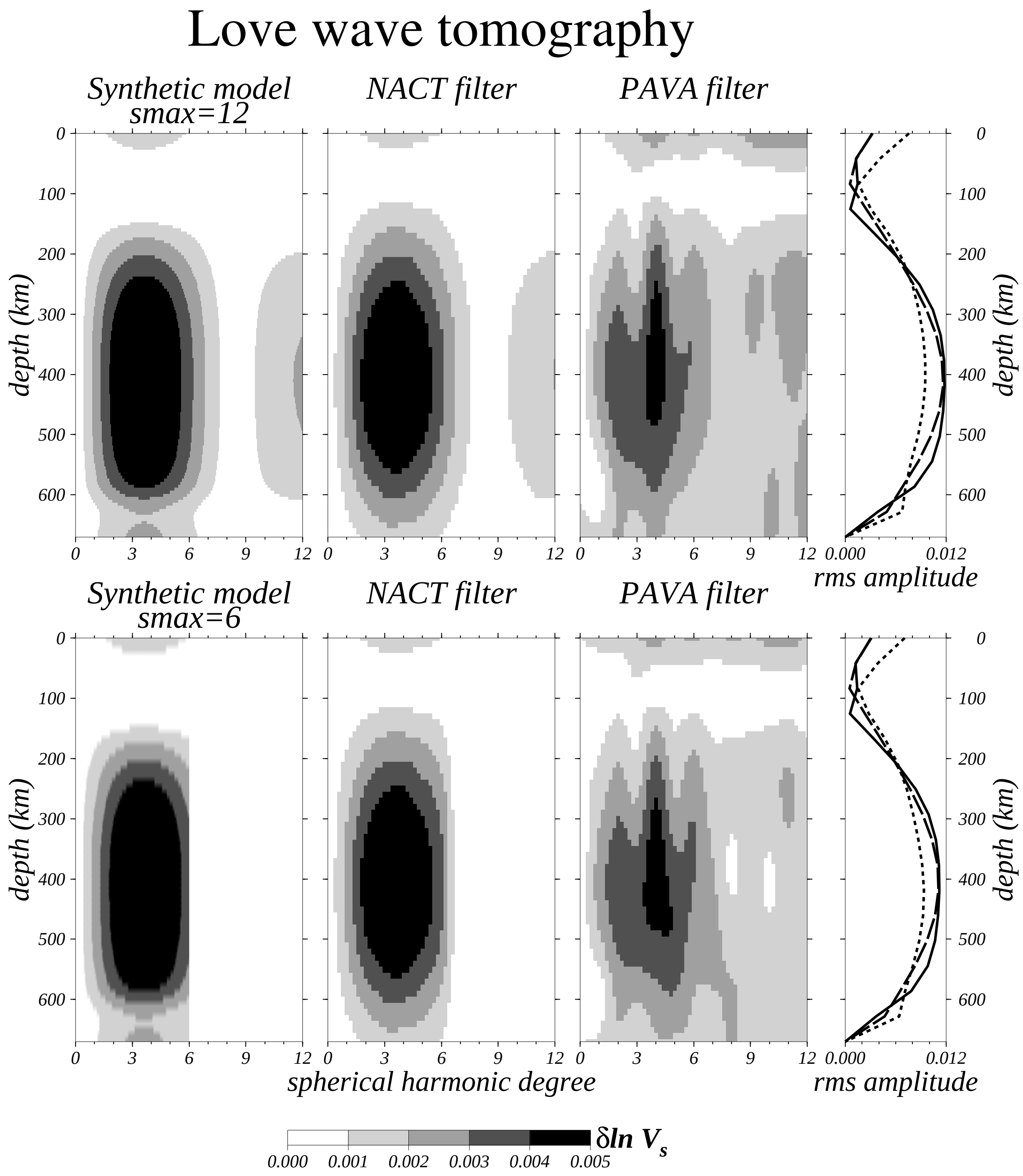
Love wave tomography
Synthetic model
smax=12
NACT filter
PAVA filter
Synthetic model
smax=6
NACT filter
PAVA filter
depth (km)
0
100
200
300
400
500
600
0 3 6 9 12
rms amplitude
0.000 0.012
spherical harmonic degree
δln Vs
0.000 0.001 0.002 0.003 0.004 0.005

Chapter 5

Seismic waveform modeling and surface wave tomography in a three-dimensional Earth: asymptotic and non-asymptotic approaches

5.1 Abstract

We investigate the impact of the theoretical limitations brought by asymptotic methods on upper-mantle tomographic models deduced from long-period surface wave data (period > $80s$), by performing a synthetic test using a non-asymptotic formalism. This methodology incorporates the effects of back scattering and multiple forward scattering on the wave field by summing modes computed using third order perturbation theory directly in the 3-D Earth, and models the sensitivity to scatterers away from the great-circle path. We present results from 7,849 synthetic Love waveforms in an upper mantle model consisting of two heterogeneities with power up to spherical harmonic degree 12. The waveforms are subsequently inverted using a zeroth order asymptotic formalism (equivalent to a path-average approximation in the surface waves domain). We show that the main structures are retrieved, but that the theoretical noise in the output model is of the same order as the noise due to the path-coverage and regularization.

5.2 Introduction

Since the early 1980s global seismic tomography has provided images of the large scale variation of the seismic velocities in the mantle [*Woodhouse & Dziewonski*, 1984]. These models are widely used to infer thermal and mineralogic heterogeneities in the mantle, making tomography a popular and powerful tool. The uppermost mantle images rely essentially on the inversion of surface wave data, because the body waves give poor resolution in this part of the mantle, due to the distribution of seismic sources and receivers. All the global tomographic models agree reasonably well on the long wavelength structure (*i.e.* the first 12 degrees in spherical harmonics, corresponding to a resolution of about 1500 km at the surface) between 100 km and 600 km depth: the upper mantle is usually considered well resolved on the global scale (*e.g.* [*Dziewonski*, 1995; *Ritzwoller & Lavely*, 1995]).
Tomographic imaging can be decomposed into three elements: the data selection, the forward modeling and the inversion scheme. Concerning the first element, tomographers have now access to abundant high quality digital data (*e.g.* from the GEOSCOPE and IRIS networks), ensuring that the coverage does not introduce significant bias in the inversion (at least for global surface wave data). The algorithms used to perform the inversion assume that the problem is essentially linear, which, in the case of the large scale structure of the mantle is considered to be correct. The data coverage and the inversion algorithms differ from one study to another, but the theories employed to model the surface wave seismograms are essentially equivalent. Hence, the differences between the upper mantle tomographic models do not depend on the theory. The impact of the theory on the models obtained has never been fully assessed: the resolution tests performed use the same theory to compute synthetic data, giving only information on the quality of the data coverage, the selection scheme and the choice of regularization.
The theory used for surface wave inversion in global tomography finds its modern formulation and first applications in the late 70s and early 80s ([*Jordan*, 1978; *Woodhouse & Girnius*, 1982; *Woodhouse*, 1983; *Tanimoto*, 1984; *Woodhouse & Dziewonski*, 1984]). It relies on two assumptions: the lateral variation of the seismic velocities is small in amplitude (a few percent with respect to a global average), and varies smoothly (the lateral velocity gradients are small). This implies in theoretical terms that the actual wave field

in the mantle is a small perturbation to a spherically symmetric Earth, and that the wave propagation is well explained by the laws of geometrical optics. In other words, the wave equation in the Earth is simplified by two approximations: the first order Born approximation (the heterogeneities are considered as secondary sources in an unperturbed reference wave field), and the zeroth-order asymptotic approximation (or high frequency approximation: the wavenumber of the seismic signal is higher than the wavenumber of the anomalies, so the wave path can be modeled by an 'optical' ray laterally). These choices were necessary for computational purposes, as a global inversion of surface wave data requires the computation of several thousands of seismograms and their partial derivatives with respect to the seismic parameters, which is still a huge task in terms of computation time and storage.

In the past ten years, numerous efforts have been directed towards improving the theoretical framework of surface wave propagation in a three-dimensional Earth (*e.g.* [*Woodhouse & Wong*, 1986; *Park*, 1987; *Romanowicz*, 1987; *Dahlen*, 1987; *Snieder & Nolet*, 1987; *Snieder & Romanowicz*, 1988; *Lognonné & Romanowicz*, 1990; *Park*, 1990; *Lognonné*, 1991; *Tromp & Dahlen*, 1992; *Friederich et al.*, 1993; *Tromp & Dahlen*, 1993; *Pollitz*, 1994; *Wang & Dahlen*, 1994; *Cummins et al.*, 1997]. However, most global tomography applications assume that the first-order Born approximation is valid and, in general, use it in its zeroth-order asymptotic approximation. Most efforts beyond that have so far focused on regional applications, in studies of crustal and lithospheric structure (e.g. [*Alsina & Snieder*, 1996; *Alsina et al.*, 1996; *Meier et al.*, 1997; *Friederich*, 1998]), where lateral variations are known to be large and strong effects on waveforms have been often documented.

Only one attempt has been made to introduce more accurate waveform modeling in global mantle imaging: [*Hara et al.*, 1993] used a non-asymptotic fully-coupled modes method [*Geller et al.*, 1990; *Geller & Hara*, 1993] to infer S-wave velocity in the upper mantle in a long wavelength (degree-8 laterally) model, and compared *a posteriori* the results with the M84A model [*Woodhouse & Dziewonski*, 1984]. Even at this large scale they found significantly different results. However, no one has ever tried to estimate experimentally the actual theoretical noise in the inversion scheme and the resulting models.

In this paper we try to test directly the theoretical noise induced by using first order Born and asymptotic approximations in global upper mantle tomography using long-period surface wave data. To do so, we compute long-period seismic waveforms using the method developed by [*Lognonné & Romanowicz*, 1990] and [*Lognonné*, 1991] (referred to as *HOPT*, for Higher Order Perturbation Theory), where normal modes of a given aspherical model are computed using higher order perturbation theory, and where no asymptotic approximation is used.

In the first section we review the main features of the non-asymptotic method methods used in this study. In the second section, we introduce our test model and draw some comparisons in the time domain and about phase velocity observations. The third section presents the inversion test on the synthetic data, computed with the HOPT method, using first order Born and asymptotic approximations. The number of seismograms and the coverage are realistic, corresponding to the surface waveform data used in the whole mantle shear velocity model *SAW12D* by [*Li & Romanowicz*, 1996] consisting in 7849 *SH* accelerograms of first and second orbit Love waves.

5.3 Non-asymptotic theory

The non-asymptotic higher order perturbation theory (*HOPT*) has been developed by [*Lognonné & Romanowicz*, 1990] and [*Lognonné*, 1991]. We summarize the principal points of the method.

We start from the normal modes of a spherical non-rotating anelastic isotropic Earth model (SNRAI). The eigenmodes and eigenfrequencies of the three-dimensional Earth model are expressed using perturbation theory. The eigenmodes $|u_k\rangle$ and associated complex eigenfrequencies σ_k, with $\sigma_k = \omega_k + i\alpha_k$, are solutions of:

$$-\sigma_k^2 \mathbf{K}|u_k\rangle + \sigma_k \mathbf{B}|u_k\rangle + \mathbf{A}(\sigma_k)|u_k\rangle = 0\,, \tag{5.1}$$

where $\mathbf{A}$ is the elasto-dynamic operator and $\mathbf{B}$ the Coriolis operator. Note that now the problem lies in the complex plane. Here the model can include laterally heterogeneous anelastic and anisotropic structure.

Let us define the Hamiltonian $\mathbf{H}$:

$$\mathbf{H}^2 = \mathbf{K}^{-1}\left(\sigma\mathbf{B} + \mathbf{A}(\sigma)\right)\,. \tag{5.2}$$

The n^{th} order approximation of the problem (5.1), in the sense of the perturbation theory, where $|u_k\rangle$ and σ_k are developed in terms of a power series of a small parameter ϵ related to the perturbation of the operator $\mathbf{A}$, is:

$$\sigma_k^{(n)}|u_k^{(n)}\rangle = \mathbf{H}^{(n)}|u_k^{(n)}\rangle + o(\epsilon^{(n+1)})\,, \tag{5.3}$$

To avoid a convergence problem occurring in the perturbation procedure due to the instability of the interaction terms within a multiplet, the perturbation path is constrained in order to cancel the first secular terms of the perturbation series. Then $\mathbf{H}^{(n)} = \left[\mathbf{H}_{kk'}^{(n)}\right]$, with $\mathbf{H}_{kk'}^{(n)} = \langle u_{k'}|\mathbf{H}^{(n)}|u_k\rangle$, can be diagonalized

$$\mathbf{H}_{kk'}^{(n)} = \sigma_k^{(n+1)}\delta_{kk'} + o(\epsilon^{(n+1)})\,. \tag{5.4}$$

A seismogram corresponding to a source $|\mathbf{S}\rangle$ and a receiver $\langle\mathbf{R}|$ can be written:

$$s^{(n)}(t) = \Re e\left[\sum_k \exp(it\sigma_k^{(n+1)})\langle\mathbf{R}|u_k^{(n)}\rangle\langle v_k^{(n)}|\mathbf{S}\rangle\right] + o(t\epsilon^{(n+1)})\,, \tag{5.5}$$

or

$$s^{(n)}(t) = \Re e\left[\sum_K \exp(it\sigma_K^{(0)})A_K^{(n)}(t)\right] + o(t\epsilon^{(n+1)})\,, \tag{5.6}$$

where σ_K^0 is the SNRAI complex frequency associated with the multiplet K, and the modulation function $A_K^{(n)}(t)$, a time-dependent function, which slowly modulates the oscillations of the spherical mode:

$$A_K^{(n)}(t) = \sum_{k\in K} \exp\left[it(\sigma_k^{(n+1)} - \sigma_K^{(0)})\right]\langle\mathbf{R}|u_k^{(n)}\rangle\langle v_k^{(n)}|\mathbf{S}\rangle\,. \tag{5.7}$$

In the absence of lateral heterogeneity, this function is constant in time, and simply represents the initial amplitude of the mode at the receiver.

The first order perturbation, in $t\epsilon$, corresponding to the 0^{th} order in eigenfunction and first order in eigenfrequency, is equivalent to the isolated multiplet hypothesis, for which only coupling between singlets in a same multiplet occurs, and this term is only sensitive to the symmetric part of the lateral heterogeneities. The higher order perturbations, in $t\epsilon^n$, correspond to the $(n-1)^{th}$ order in eigenfunction and n^{th} order in eigenfrequency, implying multiplet-multiplet coupling, and are both sensitive to symmetric and anti-symmetric lateral heterogeneities. A detailed analysis of the perturbation procedure is given by [*Lognonné*, 1991].

[*Lognonné & Romanowicz*, 1990] have shown that, in the elastic case (using the model M84 of [*Woodhouse & Dziewonski*, 1984]), the second order approximation of the eigenmodes and third order of the eigenfrequencies compares with the solutions obtained with the variational method within a relative error lower than the observation error. We assume that in the following cases this order of perturbation is sufficient (the extension of the computation to higher orders is straightforward, but the gain in accuracy is outweighted by the computational cost).

5.4 Numerical experiment: forward problem

As this paper focuses on the difference between asymptotic and non-asymptotic approaches, we need to design a test such that expressions (5.5) and (1.43) are both in their domain of validity, so that we can compare the resulting seismograms. This supposes a smooth test model, and "short-time" seismograms, which in this case consist of the first direct and indirect surface-wave trains. In order to perform a detailed analysis of the seismograms, we choose to consider a very simple structure. The model we designed consists of two adjacent anomalies, one negative and one positive, with respect to the spherically symmetric PREM model [*Dziewonski & Anderson*, 1981]. The heterogeneities extend from 200 km to 600 km in depth, and 45° by 45° laterally. They are located between the North Pole and the latitude 45° North. The spectral content of the model is strong up to spherical harmonic degree 12. We expand the model in spherical harmonics up to degree 12 laterally, and radially to 5^{th} order Legendre polynomials in the upper mantle (Figures 5.1 and 5.2). The resulting model is used both for forward modeling and inversion.

All the seismograms presented in this section are transverse component and include all toroidal modes (fundamentals and harmonics) in the frequency band 0.3 mHz-8.0 mHz (3300s-125s). They are band-pass filtered with a cosine taper with corner frequencies 4.0 mHz and 7.15 mHz (250s-140s). The position of the sources and receivers is shown in figure (5.3). The epicentral distance varies between 106° and 110°, the 27 receivers (and traces) are labeled clockwise. As expected, for this particular window in the seismic signal, $NACT$ and $PAVA$ give equivalent results. In the rest of this paper we will refer to $HOPT$ seismograms as non-asymptotic seismograms, and to $NACT$ and $PAVA$ seismograms as asymptotic seismograms.

We first ensure that the sidelobes due to the truncation of the spherical harmonic expansion do not produce significant signal in the seismograms : paths far away from the main heterogeneities show variations of about 0.1%. However, the closest sidelobe, with a sign opposite to that of the heterogeneity, gives detectable signal and can be identified clearly, as we will see, on the phase velocity measurement obtained by cross-correlation with the reference seismograms.

Considering a clockwise sweep of the heterogeneities (figures 5.3 and 5.4), the asymptotic seismograms start to record visible signal from the structure at station *07*, located at longitude $-155°$, the signal disappearing after station *19* (longitude $155°$). Trace *13*, corresponding to the great-circle path between the heterogeneities is, as expected, unaffected. Note that for these seismograms, only the phase is perturbed. The apparent phase velocity perturbation, shown on figure (5.5), gives more precise information on the structure: the asymptotic approximation forces the same behavior for each frequency by collapsing the sensitivity to the structure on the great-circle path associated to the trace. The differences in amplitude reflect the location at depth of the heterogeneities. The location and relative strength of the structural side-lobes also appears (traces *03* to *05* and *21* to *23*).

The corresponding results for the non-asymptotic seismograms (figure 5.6 for the comparison with the reference seismograms, and figure (5.7) for the comparison with the asymptotic seismograms) are shown in figure (5.8). The effect of the finiteness of the frequency manifesting itself through a Fresnel zone appears clearly. The wavelength corresponding to the frequencies shown on figure (5.8) are about 1300 km at 4 mHz, 1000 km at 5 mHz, 825 km at 6 mHz and 685 km at 7 mHz. Due to the frequency dependence of the Fresnel zone width, the signal appears to be difficult to interpret in the time domain, even for such a simple input model. For example traces *05* to *07* have evidently mixed information coming from both the main negative structure and the positive side-lobe. But it is also the case for all the traces at the shorter frequencies, for which the Fresnel zone is wide enough to sample regions with a heterogeneity sign different from the one seen by the great-circle path.

It is interesting that depending on their relative sign, regions are sampled differently by the energy traveling from the source to the station. Relatively positive regions tend to have more influence on the signal than relatively negative ones. If we consider the asymptotic results (figure 5.5) as a reference to determine the dominating region of influence along the great-circle path, we can see on figure (5.8) that the relatively positive regions tend to have a more persistent effect along our East to West sweep of the structure. This can be interpreted as some guiding effects deforming the Fresnel zone toward the fastest region sampled.

5.5 Numerical experiment : inverse problem

We use our input model in the inversion procedure used by [*Li & Romanowicz*, 1996] based on the *NACT* method. Synthetic data are computed using the non-asymptotic method. The data set consists of 7849 seismograms corresponding to the actual surface-wave data coverage used in the *SAW12D* model [*Li & Romanowicz*, 1996], in the frequency window 2.5mHz-12.5mHz (400s-80s) band-passed with a cosine taper with corner frequencies 4mHz-10mHz (250s-100s), and time windows corresponding to Love waves trains G1 and G2 are selected.

We use in the inversion experiment the same synthetic pattern as in the forward problem: the scatterers represent less than 5% of the volume of the model, which allows for most of the distortion effect to be directly mapped as heterogeneity. This methodology thus brings focus on the theoretical noise due to the use of the asymptotic formalism and tends to enhance that error.

Since we wish to isolate the effects of the distortion of the input structure due to the choice of the theoretical formalism from those of the subjective choice of *a priori* constraints, we compute the set of damping parameters that will minimize the Euclidian distance between input and output models. Using a simulated annealing algorithm [*Press et al.*, 1994], we compute two optimal sets of damping parameters: one for the asymptotic data, one for the non-asymptotic data, which we use to regulate each of the two inversions.

The output model for the non-asymptotic input data is shown in figure (5.9). The main component of the heterogeneity field is recovered, but spatially smeared. The maximum amplitudes at depth are given in table (5.1). Spurious structure with maximum amplitude around 1% is found at every depth. However, these inaccuracies are also a feature of the so-called "circular test" where the same theory is used in the forward modeling and in the inversion. We performed such a test by using asymptotic input data generated with the *NACT* method. The same problems arise, but with much smaller effects on the model (5.10): the maximum amplitudes are well retrieved, and the heterogeneities are more localized, with a better contrast with the background velocities. Theses problems are, of course, well known: the radial smearing can be partially attributed to the use of surface waves only; an other factor contributing to the spatial smearing and underestimation of the real amplitudes is the use of damping parameters to stabilize the inversion procedure; errors in the estimation of the spherical harmonic coefficients cause global spurious structure. But the comparison between the models obtained in the "non-circular test" and the "circular test" shows that the theoretical noise is of the same order as the noise induced by the factors described above: off-path propagation effects have a significant contribution on the surface waveform.

This can be clearly seen in the spectral domain. The spectral content of the models for the input model, the "non-circular test" and the "circular test" are shown on figure (5.11). Figure (5.12) shows the spectral difference between the two output models. Both figures represent rms amplitude of the heterogeneity as a function of spherical harmonic degree (horizontal axis) and depth (vertical axis). The angular smearing appears clearly at all depths corresponding to the location of the input heterogeneities.

5.6 Conclusion

We have presented a comparison between long-period surface-wave synthetic seismograms computed with and without asymptotic approximation. Both forward modeling and upper-mantle tomography have been addressed.

We applied a standard surface-wave inversion procedure, built on the asymptotic approximation, using non-asymptotic waveform as input data. This test is, to our knowledge, the first attempt at assessing experimentally the shortcomings of the asymptotic hypothesis in global mantle surface-wave tomography through an actual inversion. The output model shows that neglecting the lateral sensitivity of the surface waves to the structure leads to the underestimation of the amplitudes of the anomalies and to generation of spurious structure, adding a theoretical factor to the numerical noise. We did not address the issue of noise in the data on purpose: adding noise to the synthetic data is, of course, a relevant test, but our goal is to isolate the problem of the choice of the theory.

This test is extreme for the asymptotic methods: only long-period surface-waves are involved, and the input model has a significant spectral content up to degree 12. We can still, of course, consider that the up-to-date tomographic models representing large spatial wavelengths of the upper mantle are reliable when considering the detection and location of the main structures and the result of this test must be considered in the context of the many successes of asymptotic tomography.

Extension of global mantle tomographic models using surface waves data to higher spatial resolution faces the problem of the theoretical background. [*Park*, 1991; *Um et al.*, 1991] show that the asymptotic approximation breaks down rapidly for a spectral content in the structure beyond angular degree 10, when using long-period surface wave data (period $> 150s$), even with a realistic roughness of the model. This suggests that, even with shorter period data ($> 80s$), the presence of rough structures in the upper mantle (such as slabs and plumes) may significantly bias inversions based on asymptotic approximations.

On the other hand, for the deeper mantle, where body waveform data are necessary to achieve any level of resolution, the more exact theoretical formalism $HOPT$ is still computationally prohibitive. While computational enhancements are being sought for $HOPT$, asymptotic approximations such as $NACT$ represent a significant theoretical improvement over *PAVA*, by allowing more correct expressions of the sensitivity of body waves to structure along the ray path ([*Li & Tanimoto*, 1993; *Li & Romanowicz*, 1995]). An intermediate step beyond *NACT*, both for surface waves and for body waves, is to use higher order asymptotic approximations as described by [*Woodhouse & Wong*, 1986; *Romanowicz*, 1987]. These methods take into account asymptotically the influence of the off-path structure on the signal. Although still limited by the high frequency approximation, this alternative should be considered in the generation of long wavelength models, especially if we wish to retreive information on anelasticity.

5.7 Tables

Depth	Input model	Asymptotic data	Non-asymptotic data	Difference
150 km	-0.44%/0.45%	-1.55%/1.50%	-0.81%/0.77%	-0.76%/0.82%
250 km	-3.92%/3.98%	-3.39%/3.49%	-1.74%/1.76%	-1.76%/1.75%
300 km	-5.04%/5.12%	-4.13%/4.31%	-2.33%/2.44%	-1.91%/1.91%
400 km	-5.82%/5.91%	-4.92%/5.23%	-3.24%/3.56%	-1.88%/2.13%
450 km	-5.79%/5.88%	-4.89%/5.21%	-3.22%/3.59%	-1.88%/2.19%
500 km	-5.61%/5.70%	-4.55%/4.83%	-2.77%/3.14%	-1.96%/2.24%
600 km	-3.64%/3.69%	-3.07%/3.16%	-0.97%/1.16%	-2.11%/2.16%
650 km	-0.15%/0.15%	-2.09%/2.08%	-0.24%/0.32%	-1.80%/1.87%

Table 5.1. Maximum amplitudes at depth

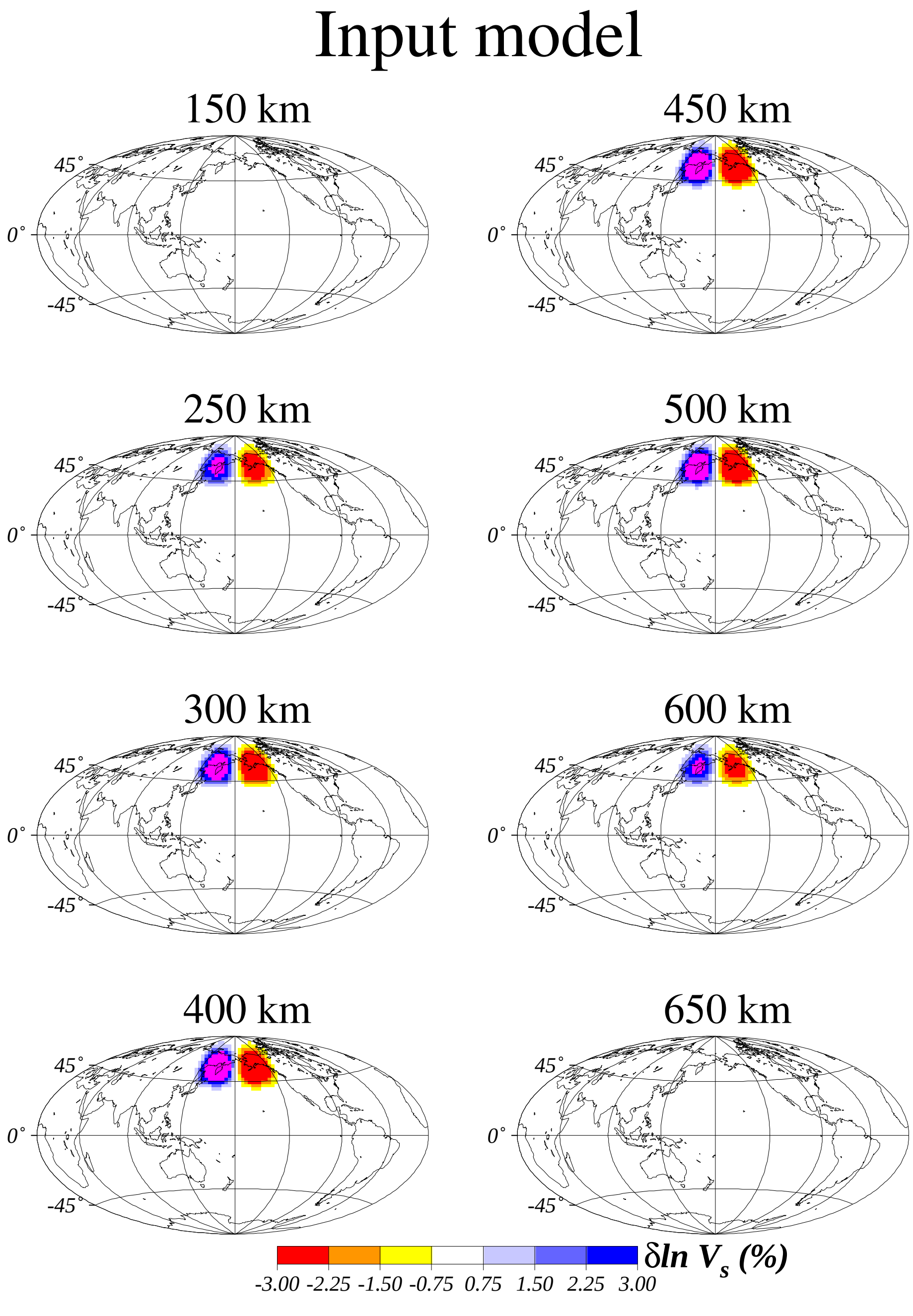

Figure 5.1. Input model: The heterogeneities are located in the upper mantle and expanded up to spherical harmonic degree 12 laterally and 5^{th} order Legendre polynomials radially (see figure 5.2).

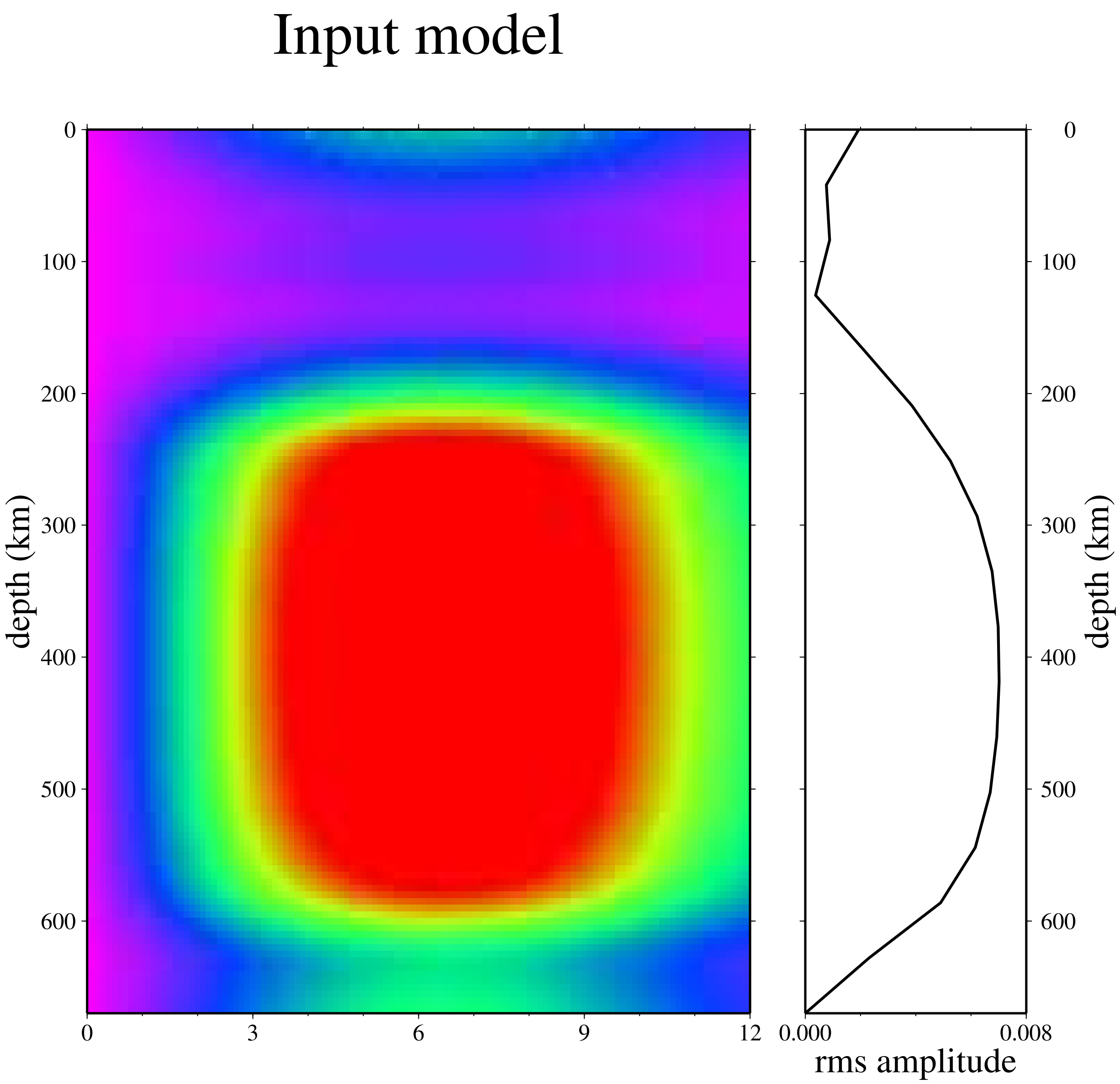

Figure 5.2. Spectral content and rms profile of the input model. The left plot shows the amplitude spectrum (spherical harmonic degrees in abscissa) at each depth in the upper mantle.

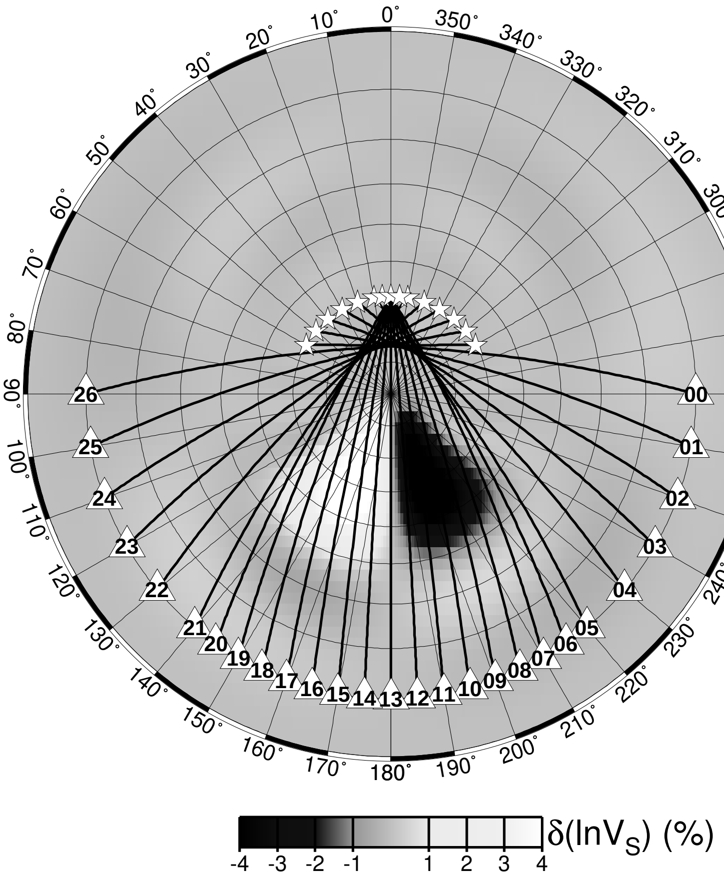

Figure 5.3. Source-receiver paths used in the forward modeling experiment: the sources are represented by the stars and the receivers, labeled clockwise, by the triangles. The epicentral distance is 110° for all the paths.

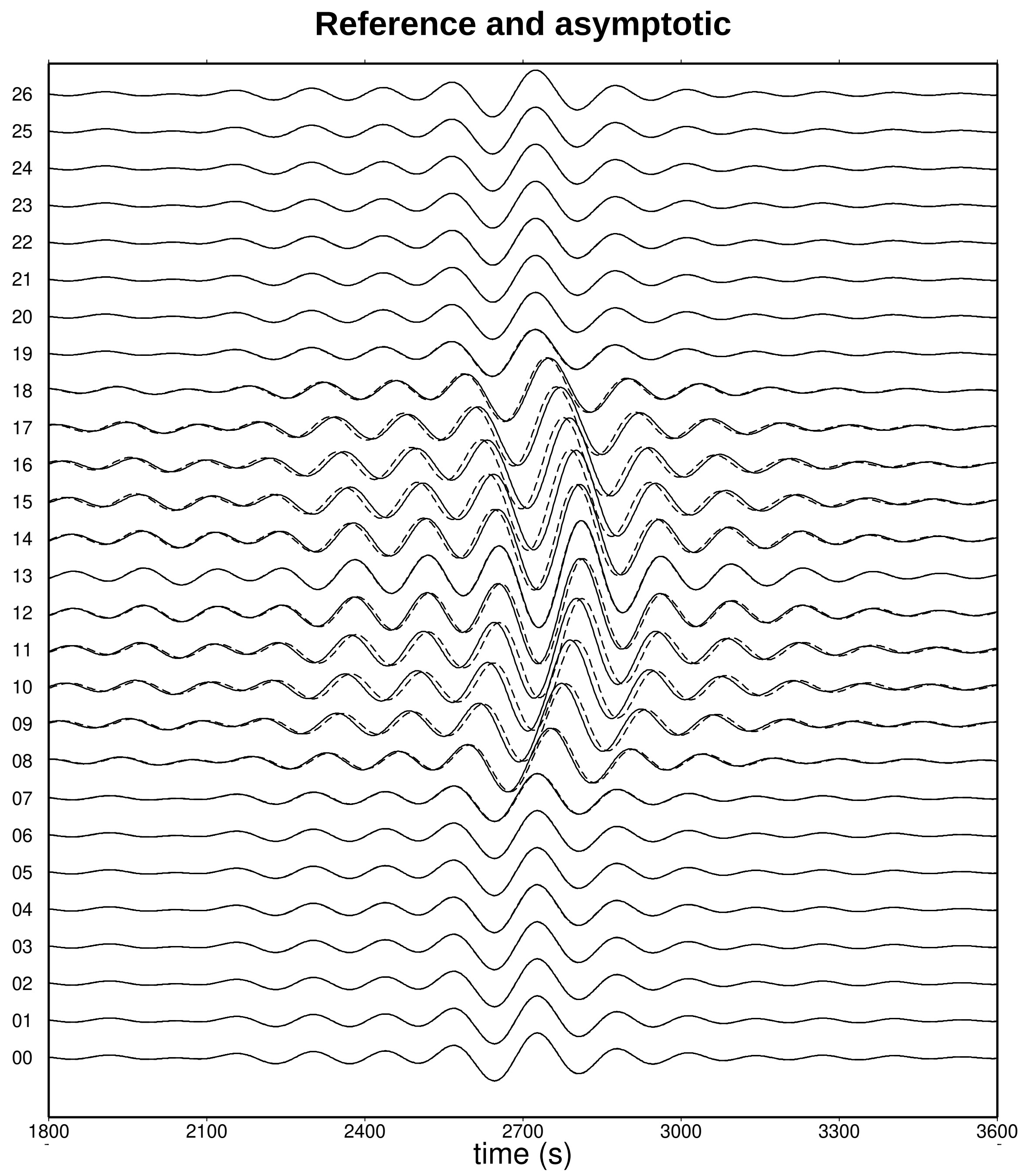

Figure 5.4. Asymptotic (solid lines) and reference (dashed lines) seismograms. The seismograms are the transverse component with maximum frequency 8.0 mHz. The reference model is *PREM* [*Dziewonski & Anderson*, 1981].

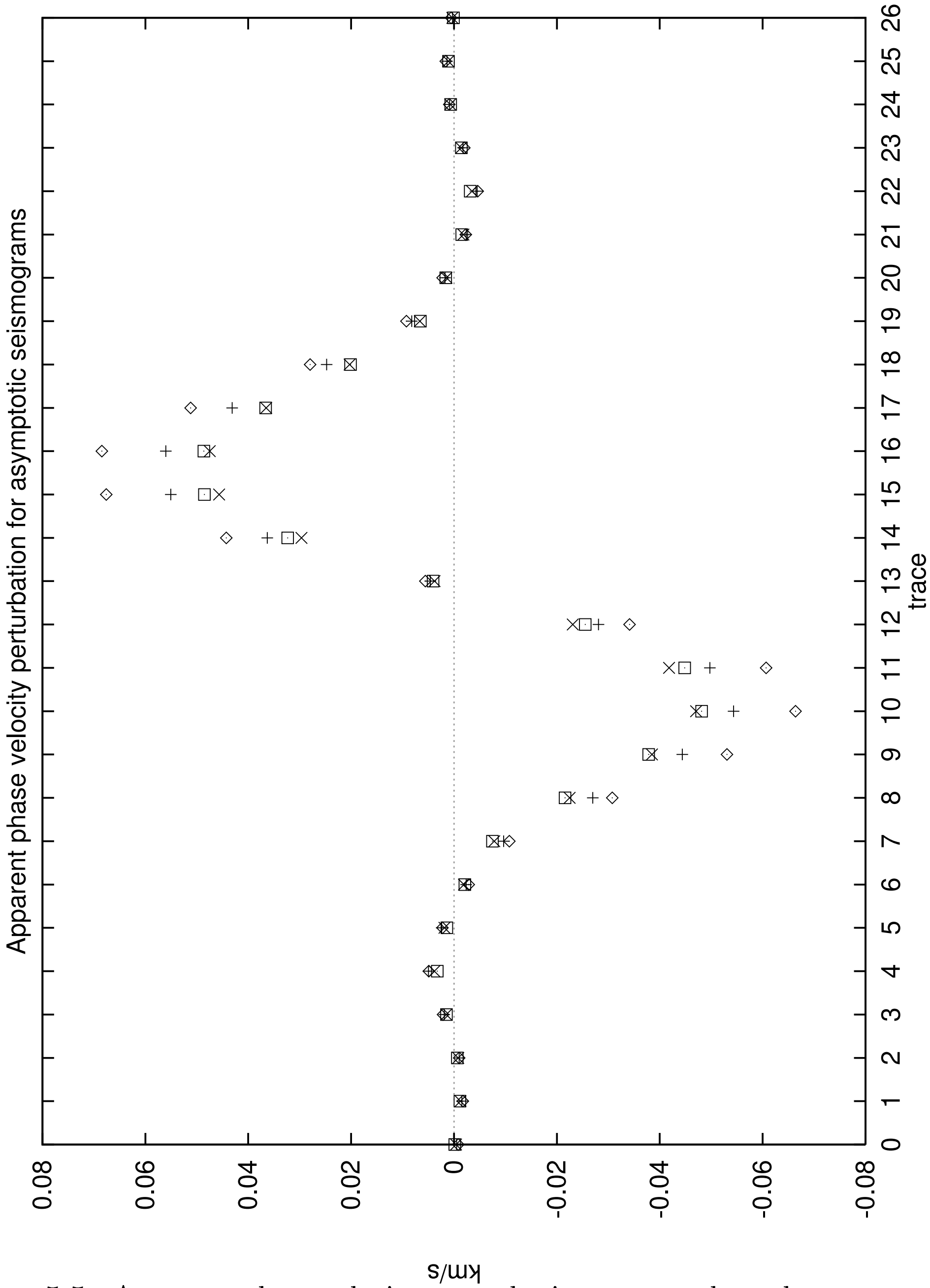

Figure 5.5. Apparent phase velocity perturbation measured on the asymptotic seismograms represented on figure (5.4) at four different frequencies: 4 mHz (diamonds), 5 mHz (pluses), 6 mHz (squares) and 7mHz (crosses).

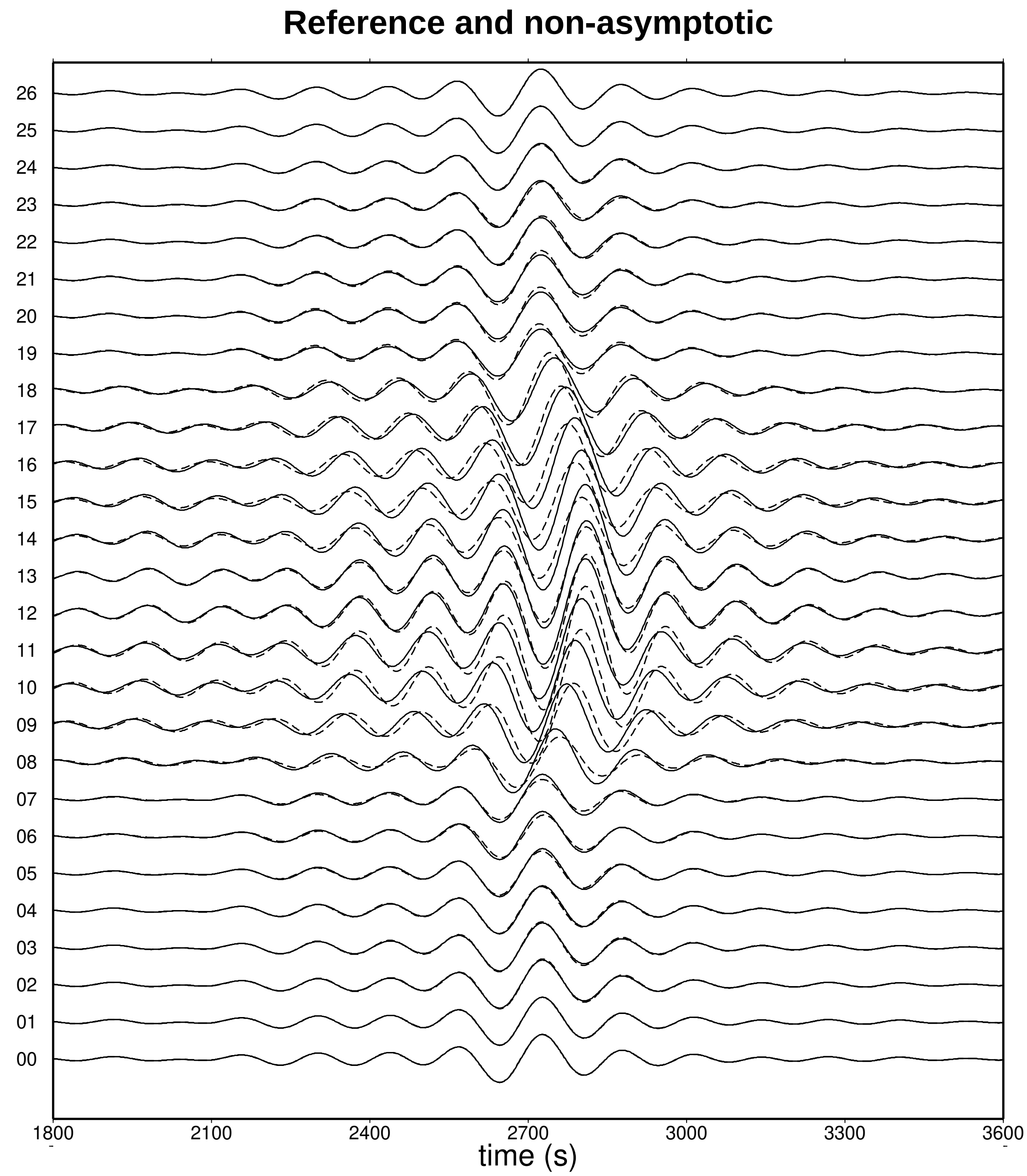

Figure 5.6. Non-asymptotic (solid lines) and reference (dashed lines) seismograms.

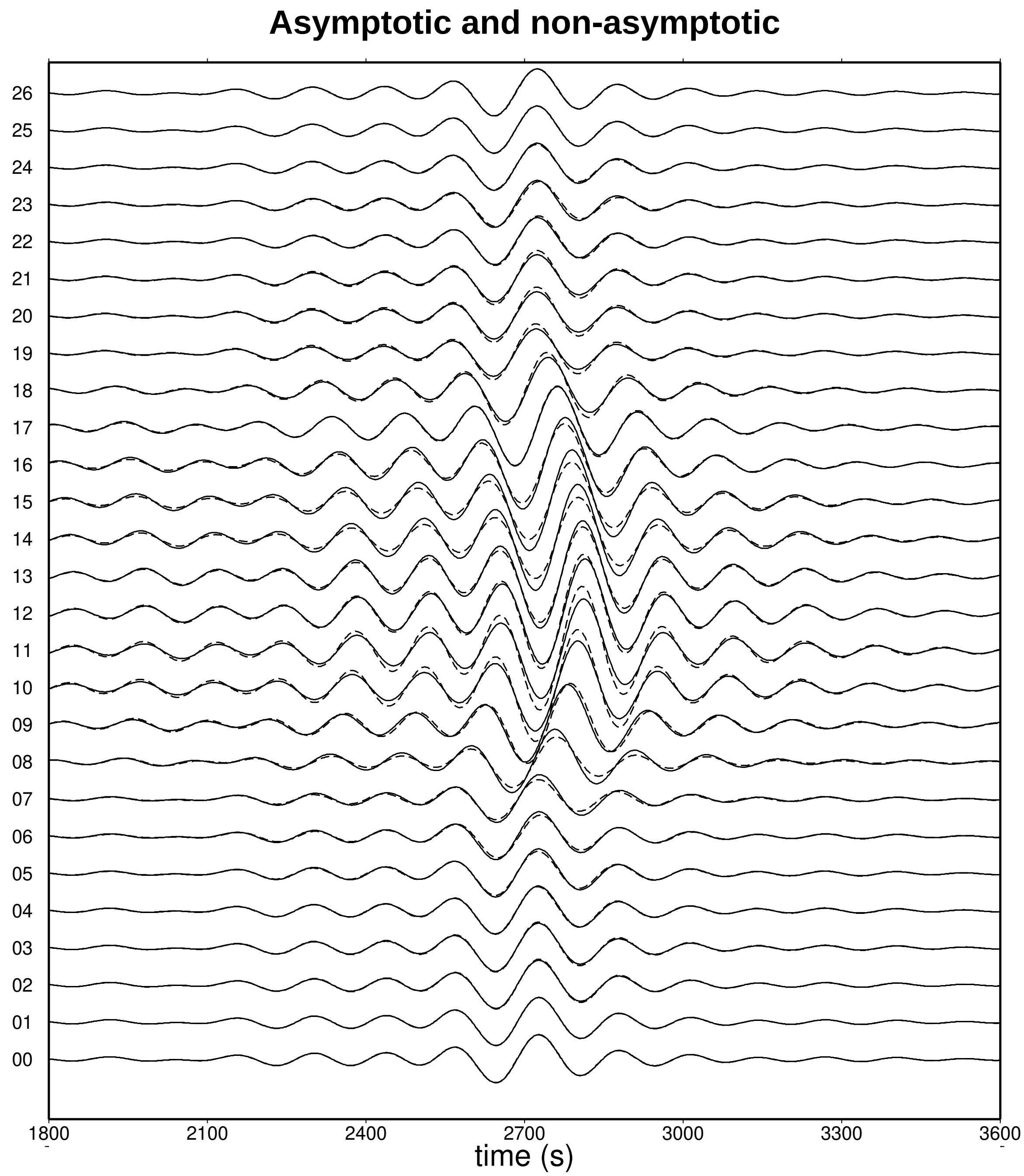

Figure 5.7. Non-asymptotic (solid lines) and asymptotic (dashed lines) seismograms (see figures 5.4 and 5.6).

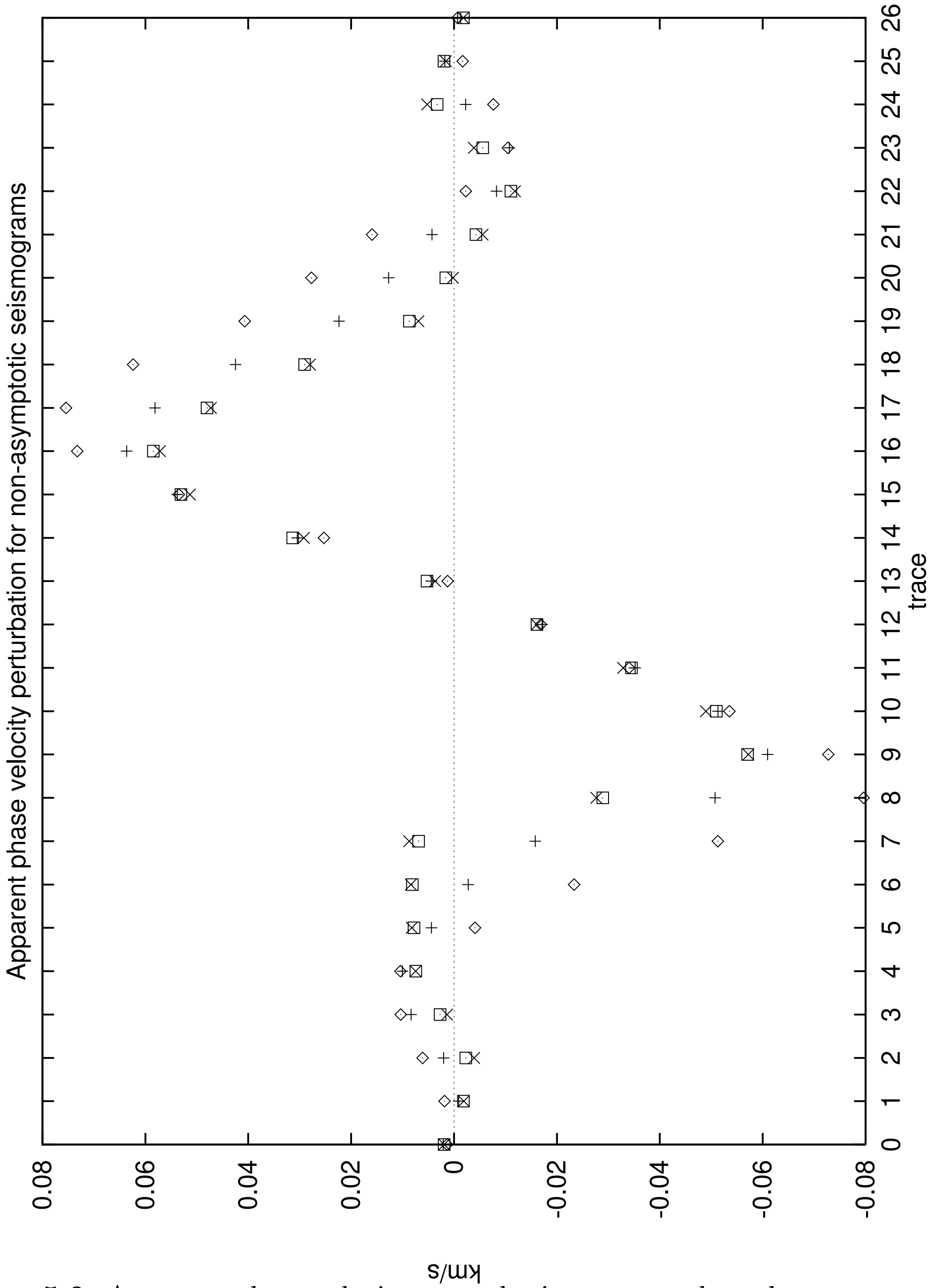

Figure 5.8. Apparent phase velocity perturbation measured on the non-asymptotic seismograms represented on figure (5.6) at frequencies 4 mHz (diamonds), 5 mHz (pluses), 6 mHz (squares) and 7mHz (crosses).

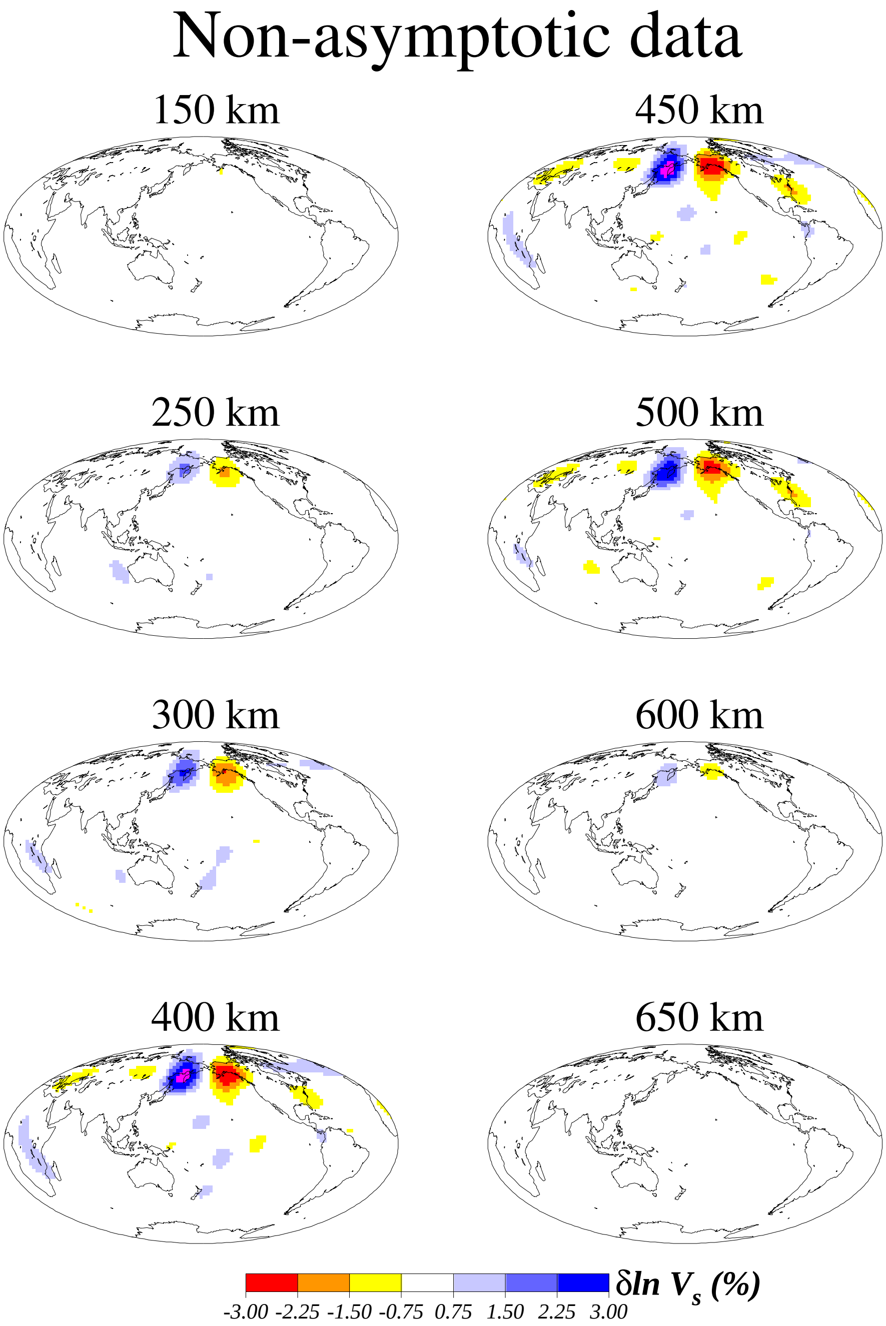

Figure 5.9. Output model obtained using non-asymptotic data. These synthetic data are used as input in the inversion scheme based on the asymptotic assumption ("non-circular test").

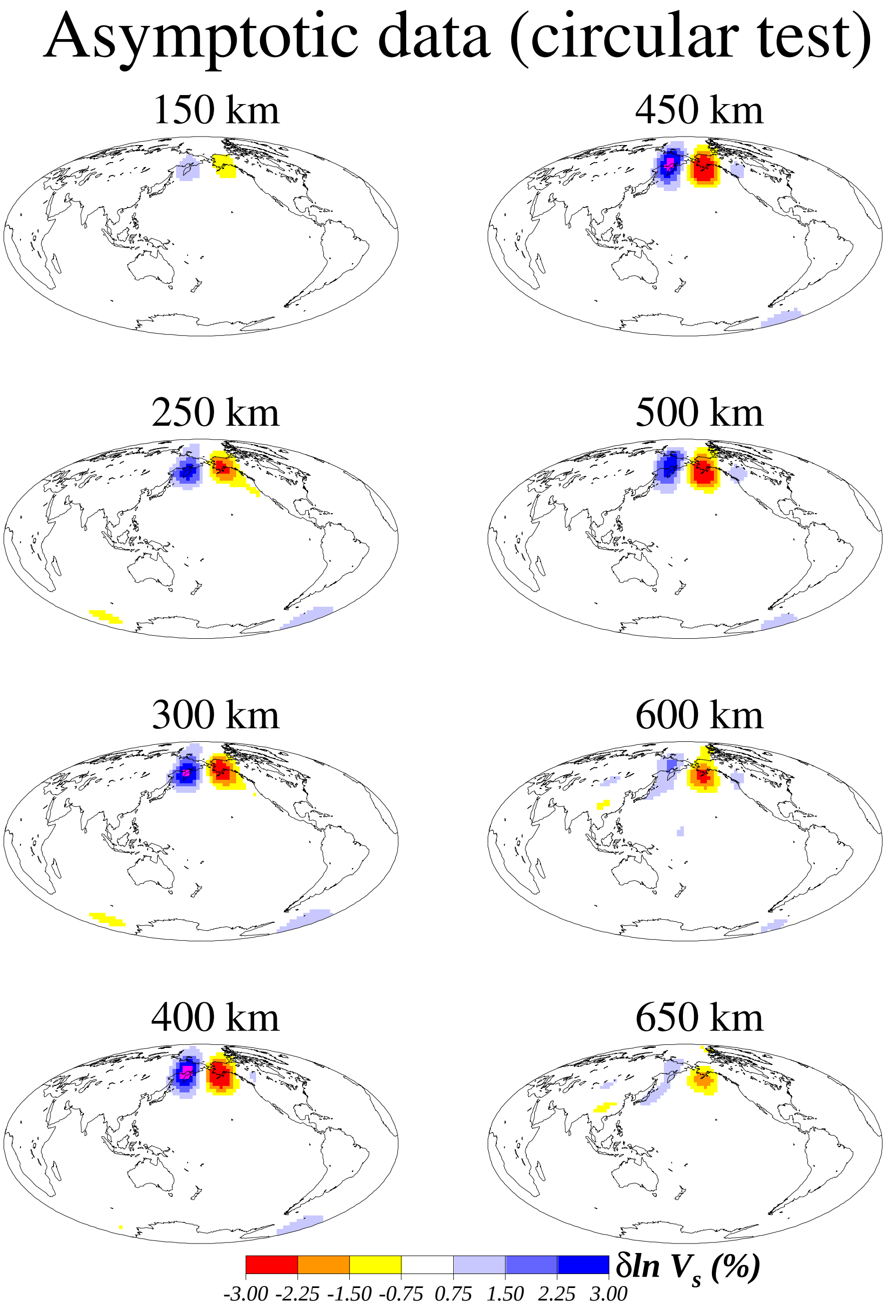

Figure 5.10. Output model obtained using asymptotic data. These synthetic data are used as input in the inversion scheme based on the same asymptotic assumption ("circular test").

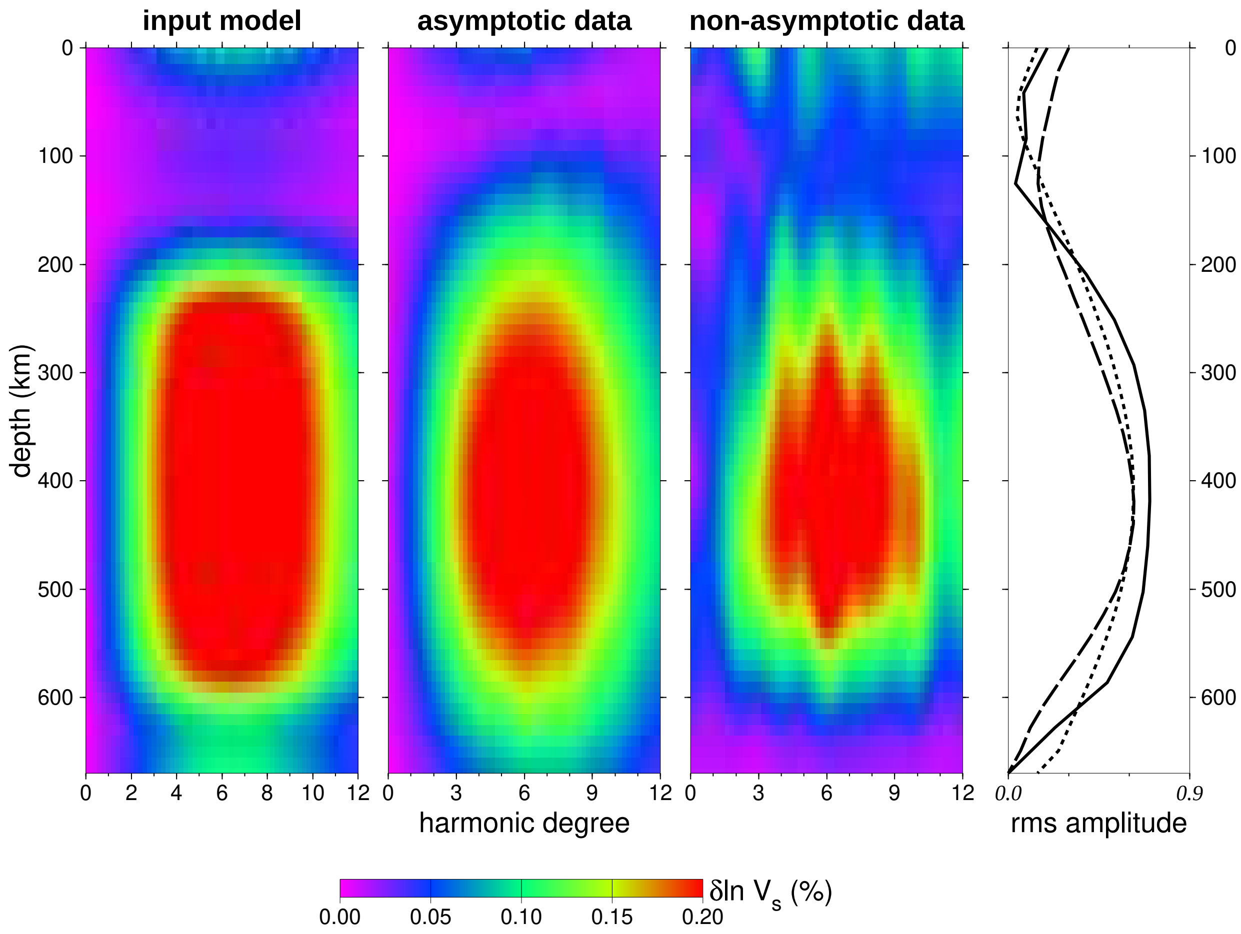

Figure 5.11. Spectral contents and rms profiles of the output model obtained using asymptotic data (dotted line for rms) and non-asymptotic data (dashed line for rms), compared to the input model (solid line for rms). Conventions are the same as for the figure (5.2).

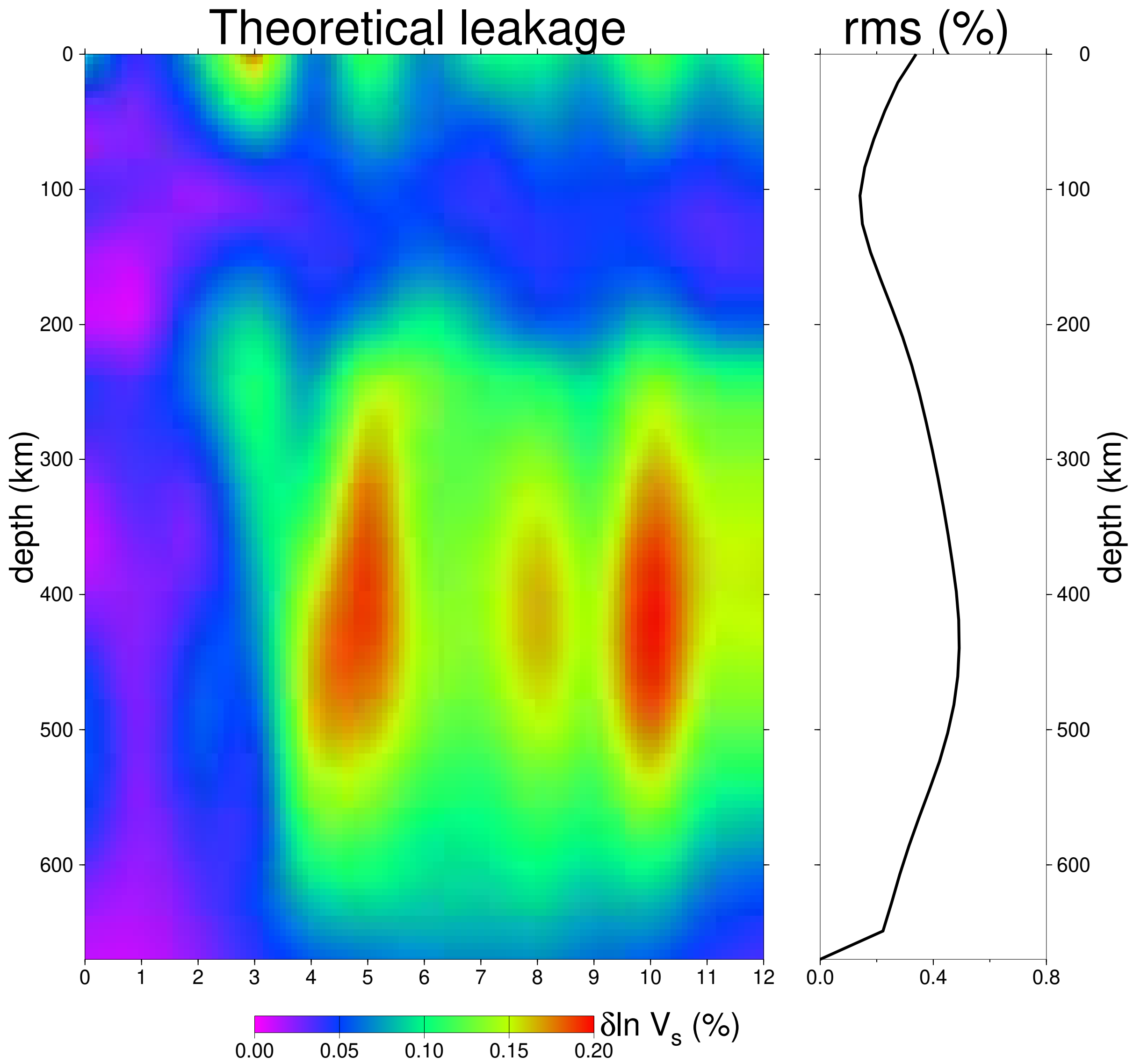

Figure 5.12. Spectral content and rms profile of the difference between the asymptotic and non-asymptotic output models.

Chapter 6

A 3D model of shear velocity in the mantle from the inversion of body, surface and higher mode waveforms.

Abstract

We present results from the inversion of a collection of handpicked transverse component body, surface and higher mode waveforms, for shear heterogeneity (V_{sh}) in the mantle. The waveforms are modeled using the nonlinear asymptotic coupling theory, the zeroth order asymptotic expansion of a Born seismogram computed by normal mode summation. We invert iteratively for mantle heterogeneity and for centroid moment tensors until convergence. Our model *SAW18B16* is parametrized laterally in spherical harmonics up to degree 18 and radially in 16 cubic b-splines, with knots spaced unevenly to reflect the data sampling with depth.

The power spectrum of the model is dominated by heterogenity in the upper and the lower boundary layer at low degrees: degrees 5 and 6 near the surface and degree 2 near the core-mantle boundary. The rest of the lower mantle is dominated by degree 3. We find significant heterogeneity up to spherical harmonic degree 18 in the transition zone and the uppermost part of the lower mantle. We also find that the dominant wavelength of the slow component of the velocity field increases with radius from the CMB to the bottom of the transition zone, suggesting a narrowing of upwellings during their ascension in the lower mantle.

With the exception of the African continent, the absence of broad fast anomalies under the continents deeper than 400 km suggests that continental keels may not significantly penetrate into the transition zone. This observation is consistent with the signature of the cratons as seen in the degree 5 peak in the spectrum of the fast component of the heterogeneity field.

Our model shows three broad low velocity zones extending continuously between the lowermost mantle and the surface, one originating under Africa and two distinct upwellings in the mid-Pacific. The image suggests a connection near the surface between the Pacific anomalies and the complex of ridges in the East Pacific, and between the African anomaly and the low-velocity zone in the Red Sea, the East African Rift and the Mid-Indian Ridge. These anomalies appear to ascend into the upper mantle without altering their shape near the 670 km discontinuity. Well isolated low velocity regions with amplitudes larger than 1.5% coincide at transition zone depths with the surface location of many Pacific hotspots,

including Hawaii, Tasmania, the Caroline Islands and the broad region bounded by Society Islands, the Cook Islands and Gambier. Among these, only the low velocity region beneath the Cook islands clearly extends vertically from the surface to the core-mantle boundary. Fast anomalies accumulate on the 670 km discontinuity under the Southern Kurile, Japan trench and Izu-Bonin arc, with little or no penetration into the lower mantle, in agreement with results from a variety of regional studies. Cross-sections through subduction zones such as Tonga-Kermadec, Java, the paleosubduction zone beneath North America, and the Peru-Chile trench show continuous fast structure penetrating into the lower mantle, with the depth of penetration fluctuating among regions.

The behavior of both fast and slow heterogeneity near 670 km thus suggests that the discontinuity does not act as a strong barrier to upgoing and downgoing flow between the upper and the lower mantle.

6.1 Introduction

Following pioneering work in the upper mantle by [*Woodhouse & Dziewonski*, 1984; *Nataf et al.*, 1986] and in the lower mantle by [*Dziewonski et al.*, 1977], 3D models of the whole mantle have been derived by research groups using different modeling techniques and a variety of datasets: among recent studies, [*Grand et al.*, 1997; *Grand*, 1994] computed travel time delays delays from body waveforms; [*Masters et al.*, 1996] combined absolute and differential travel times with phase velocity measurements of surface waves and normal mode; [*van der Hilst et al.*, 1997] used *ISC P* and *pP* travel time residuals with source parameters relocated by [*Engdahl et al.*, 1998] to derive a compressional velocity model; [*Vasco et al.*, 1994] used *P* and *S ISC* arrivals to constrain compressional and shear velocity structure in the mantle; [*Su et al.*, 1994; *Liu & Dziewonski*, 1994; *Liu & Dziewonski*, 1998] combined absolute and differential travel time measurements with surface and body waveform data modeled with a surface wave formalism; [*Li & Romanowicz*, 1996] derived a model exclusively from handpicked SH-waveforms by formulating the forward and inverse problem in a theoretical normal mode context valid both for body and surface waves.

Although there is a general consensus regarding the long wavelength components of these models, disagreements remain in the details. One of the causes of the discrepancies in the fine scale structure is the accuracy of the theoretical formalism used, the other the parametrization. The use of waveform data allows one to depart from the infinite frequency, ray-optic approximation that constitutes the theoretical foundation of 3D seismic velocity maps computed from travel time data (e.g. [*Vasco & Johnson*, 1998; *van der Hilst et al.*, 1997; *Liu & Dziewonski*, 1994; *Su et al.*, 1994]); the waveform approach also makes use of more information contained in the seismic signal and therefore considerably improves the sampling at depth in comparison with just travel time data, which are restricted to well-isolated phases on the seismogram.

The quality of tomographic images is not only related to the accuracy of the theoretical formalism, but can be improved by a judicious choice of parametrization. For example, [*Bijwaard et al.*, 1999] have attempted to achieve uniform resolution by locally varying the cell size of their model to minimize the difference in 'hit count' among cells. Such refinements are nevertheless precluded by the use of global basis functions and tomographers are increasingly abandoning their use in favor of functions with local support. In particular, several recent global models have been derived using cubic b-splines in the radial direction. [*Masters et al.*, 1996; *Su & Dziewonski*, 1996] used evenly spaced splines in their modeling, and [*Liu & Dziewonski*, 1998] modified this approach and distributed the spline knots of their models *S16U6L8* and *S16VB14* to reflect the data sampling at depth. Using the method derived by [*Wang & Dahlen*, 1995], [*Wang et al.*, 1998] derived global phase velocity maps using expansions in spherical splines in the lateral direction, and allowed the grid size to be smaller in regions of high coverage.

In a previous publication, [*Li & Romanowicz*, 1996] derived a degree 12 model of SH shear wave velocity parametrized radially in Legendre polynomials, constructed using waveforms of surface and body waves, modeled with the 'nonlinear asymptotic coupling theory' (*NACT*) formalism of [*Li & Romanowicz*, 1995]. We use their methodology to derive a higher degree model, adding overtone surface waveforms of the first and second orbit to the existing data set and increasing the collection of body waves and surface waves with more recent data. We therefore continue using a homogeneous dataset with all phase types fit with a consistent theoretical formalism. The present model is parametrized radially in cubic b-splines with knots spaced to reflect the distribution of rays at depth, a first step towards a fully locally parametrized whole mantle model.

6.2 Model characteristics

6.2.1 Data

Our model is fitted to handpicked transverse component waveforms for 738 events recorded during the period between 1977 and 1997 at 200 IRIS and GEOSCOPE network stations (figure 6.1). Our dataset consists of body waves, and first and second orbit fundamental and overtone surface wavetrains; (see Table 6.1). The body waveforms are tabulated in table 6.2.

Higher mode waveforms increase coverage in the transition zone and the upper part of the lower mantle [*Takeuchi & Saito*, 1972]. They have been modeled for this purpose in recent studies [*Stutzmann & Montagner*, 1994; *van Heijst & Woodhouse*, 1999] using techniques aiming at resolving the dispersion characteristics of each individual overtone [*Stutzmann & Montagner*, 1993; *van Heijst & Woodhouse*, 1997]. Complete time-domain waveforms have also been used (*e.g.* [*Woodhouse & Dziewonski*, 1984; *Tanimoto*, 1989; *Su et al.*, 1994]), but these approaches use only the phase information. In the present study, overtone data are also modeled in the time domain, but our formalism allows the modeling of amplitudes by including the effect of coupling across mode branches (see theory section below).

In figure 6.2, we show an example of body wave data windowing for a $M_w = 7.1$, 1996 Kurile Islands event recorded at station DRV in Antarctica. We compare the data low-pass filtered at 32 seconds (middle trace) with a synthetic computed in the spherically symmetric model *PREM* [*Dziewonski & Anderson*, 1981], corrected for ellipticity effects (bottom trace). The same record is plotted with a 16 second low-pass filter to facilitate phase identification and selection (top trace). Each relevant energy wavepacket in the seismic trace is picked individually. In this particular instance, the phases S_{diff}, SS, SSS & ScS_2 and S_4 were selected. We have shown in a recent publication that isolating the different energy wavepackets in a seismogram enhances the image at depth, and in particular that fitting the S_{diff} independently from the rest of the seismic trace considerably improves resolution in the lowermost mantle [*Mégnin & Romanowicz*, 1999a]. We follow the same philosophy with the surface waveforms by separating the fundamental modes from the overtones whenever possible, as amplitudes on long period seismograms are generally dominated by fundamental mode energy. Similarly, we separate the first orbit arrivals from the second orbit. This is particularly useful at short epicentral distances where the minor arc orbit can be considerably more energetic than the major arc. Another advantage of our waveform packet analysis is that phases arriving simultaneously but sampling different parts of the mantle can be accommodated, increasing the 3D structure resolution as compared to travel time datasets.

While events are evenly distributed between the Northern and Southern hemispheres, three out of four seismic stations are located in the Northern hemisphere. We thus expect images to be better resolved in the north than in the south, in particular in the lower mantle, which is sampled only by body waves. The second orbit surface waveforms in the upper mantle make up for the uneven distribution of stations, to some extent. In figure 6.3 (top), we show the coverage achieved by our fundamental surface wave collection. This is expressed as the logarithm of the number of one degree great circle segments in each $10^o \times 10^o$ cell (the resolution corresponding to degree 18), corrected for latitude. At the bottom of the figure, we show the same measure for the higher mode arrivals.

As the distribution of data in the 3D Earth is irregular, we use a weighting scheme to prevent images of the whole mantle from being controlled by the regions sampled by the most abundant travel paths. For each wavepacket, we compute a measure of redundancy with respect to all the other wavepackets in the dataset. We then assign to the wavepacket a weight inversely proportional to the square root of the redundancy estimate. Details of this procedure is given in [*Li & Romanowicz*, 1996, Appendix A].

6.2.2 Theory

The waveforms are modeled using 'nonlinear asymptotic coupling theory' (*NACT*) developed by [*Li & Romanowicz*, 1995]. The *NACT* formalism uses the Born approximation (*e.g.* [*Woodhouse*, 1983; *Tanimoto*, 1984]), with the coupling of the modes taken into account both along and across mode branches. It has been shown that across-branch coupling is necessary to model body waveforms (*e.g.* [*Li & Tanimoto*, 1993; *Marquering & Snieder*, 1995]). With *NACT*, the coupling along mode branches is taken asymptotically to order zero [*Romanowicz*, 1987; *Park*, 1987], which restricts the sensitivity of the synthetic waveforms to the structure along the great circle path.

6.2.3 Parametrization

The shear velocity model,we construct, *SAW18B16*, is expressed as perturbations from the spherically symmetric model *PREM* [*Dziewonski & Anderson*, 1981], parametrized laterally in spherical harmonics up to degree 18, and radially in 16 continuous cubic b-splines, with 6 spline knots in the upper mantle and 10 in the lower mantle:

$$\delta v_{sh}(r,\theta,\phi)/v_{sh}^{prem}(r) \;=\; \sum_{k=0}^{15}\sum_{s=0}^{18}\sum_{t=-s}^{s} {}_k a_s^t\, B_k(r) Y_s^t(\theta,\phi) \tag{6.1}$$

where $B_k(r)$ are cubic b-splines, defined in the appendix, and $Y_s^t(\theta,\phi)$ are fully normalized spherical harmonics as defined in [*Edmonds*, 1960]. The lateral resolution is about 1,100 km at the surface and 600 km in the lowermost mantle. The spline knots are spaced to reflect the radial resolution, varying smoothly from 100 km near the surface, to 300 km in the mid-mantle and 150 km in the lowermost mantle. Their distribution with depth is shown in figure 6.4. To avoid possible artefacts in transition zone images, we opted for a continuous parametrization across the 670 km discontinuity. Splitting the parametrization between upper and lower mantle presents the advantage of accommodating the difference in vertical resolution between the shallow and the deep parts of the mantle. However, it also introduces some level of decoupling as observed, for example, in the radial correlation functions, and may impact our analysis of continuity of structure across the 670 km discontinuity. Allowing the knot spacing to vary accomodates variability in radial resolution and does not bias transition zone images.

6.2.4 Inversion

The inverse problem is solved using a stochastic formalism (*e.g.* [*Jackson*, 1979; *Tarantola & Valette*, 1982]), and the finite-dimensional model is obtained by the recursive application of a Newton scheme to the Fréchet derivatives of the ℓ^2-norm objective function. A detailed description of the inversion procedure is given in [*Li & Romanowicz*, 1996].

SAW18B16 is derived by inverting iteratively for 3D velocity perturbations in the mantle, for moho depth perturbation from *ETOPO5*, and for perturbations to source parameters from those of the Harvard Harvard centroid moment tensor (*CMT*) catalog (hypocenter location, moment tensor and source time shift). Attenuation in the mantle is taken into account by using the radial attenuation model *QL6* [*Durek & Ekström*, 1996], which we hold fixed throughout all the inversion steps. We introduce the contribution to the waveforms from undulations of the free surface, bathymetry and moho depth, using the model *ETOPO5*. Higher frequency data is needed to constrain undulations in moho depth. In this study, we invert for moho topography only for the purpose of reducing the error resulting from contributions from 3D crustal variations, which are neglected here.

We use in the inversion of the data, the set of damping parameters constructed to recover the 3D spherical convection model *GEMLAB 1* [*Bunge et al.*, 1998] in a synthetic test. This model incorporates the effects of many parameters characteristic of Earth's dynamics, in particular two phase transitions, 20 % partial bottom heating, viscosity layering between the upper and the lower mantle, and the history of plate motions since the mid-Mesozoic. Using a simulated annealing algorithm [*Press et al.*, 1994], we compute the set of *a priori* constraints that minimize the ℓ^2 norm of the difference between the input model scaled to velocity perturbations and the inversion of a noise-free synthetic dataset. Details of this procedure is given in [*Mégnin & Romanowicz*, 1999b].

We conducted three rounds of inversion. Starting from the degree 12 model of [*Li & Romanowicz*, 1996], we inverted for 3D mantle heterogeneity using as initial moment tensors the results from [*Li & Romanowicz*, 1996] for the data prior to 1996, and from the *CMT* catalog for the more recent data. Holding that model fixed, we then performed an inversion for a new set of *CMT*s. Holding in turn the new set of sources fixed, we finally re-inverted for 3D mantle heterogeneity. For each round of inversion, several iterations (typically three) are performed until convergence. The improvement of the fit to the data resulting from the *CMT* inversions exceeds 10 percent. The residual variance of the final model with respect to each phase type is given in table 6.1.

6.3 Results

6.3.1 Overview

Two recent studies have shown that the mapping of errors due to the theoretical approximations involved with the use of the asymptotic formalism in the waveform modeling [*Clévédé et al.*, 1999] and the aliasing of short wavelength heterogeneity into long wavelength models [*Mégnin & Romanowicz*, 1999b] introduces a spurious low amplitude signal in the models, in particular at short wavelengths. We therefore 'enhance' the structure in our figures by setting to zero the heterogeneity whose amplitude has absolute value less than 0.2%, as we feel that, based on the above mentioned experiments, the signal below that level is unreliably resolved.

Figure 6.5 shows lateral sections of the model at mantle depths between 100 and 750 km. The largest amplitudes are at the shallowest depths. As expected, in the shallower sections have fast velocity anomalies under continents. At 100 km the anomaly in the East Pacific Rise is -6.3% and $+6.2\%$ in the North American Craton. We find, in agreement with [*van der Lee & Nolet*] very strong low velocity anomalies in the Western United States, extending to 300 km depth. The mid-ocean ridges in the East Pacific, mid-Atlantic and in the Indian ocean correspond to low velocities. The back-arc basins of the West Pacific are also associated with low velocity anomalies, which dominate the image in the uppermost mantle, concealing the onset of subduction.

Significant variations in the depth extent of the continental roots is observed. Bearing in mind that the radial resolution is on the order of 100 to 150 km at upper mantle depths, the fast anomaly beneath the Brazilian shield disappears below about 250 km, but extends to 400 km under North America, Eurasia and Australia. Continuous fast velocities are observed down to 500 km beneath Africa. The heterogeneity field at 650 km is largely dominated by fast velocities corresponding to subduction in the West Pacific and the South American continent, and most of it is still observed at 750 km.

The persistent signature of subduction is the most noticeable feature in the upper part of the lower mantle (figure 6.6, 850 km). Fast velocity anomalies with amplitudes above 1% are observed at 850 km beneath Tonga-Kermadec, Java, and the Marianas. They disappear beneath Japan and the Southern Kuriles but are strong in the Kamchatka region, in agreement with [*Ding & Grand*, 1994]. Fast velocities are also present under South America, and the fast anomaly associated with the Farallon paleosubduction is seen to migrate eastward with depth [*Grand et al.*, 1997; *van der Hilst et al.*, 1997].

We note the presence of a localized low velocity anomaly, extending from the top of the lower mantle to about 850 km with an amplitude of -1.5%, just west of the surface location of the Bowie hotspot, off the shore of British Columbia. This feature is further investigated below.

At 1,600 km, the fast velocity anomaly associated to subduction underneath South America has largely disappeared. In contrast, the Farallon plate continues its Eastward progression with depth, and is prominent below the Western Atlantic Ocean. Both these features are in agreement with the model of [*Grand*, 1994].

A large scale low velocity anomaly is observed under Africa, throughout the entire depth range of the lower mantle becoming more focused around 2,000 km. Anoher low velocity anomaly under the Central Pacific, also present throughout the lower mantle, becomes stronger around 2,000 km as well. In the lowermost mantle (2,800 km), the distribution of heterogeneity is dominated by a degree 2 pattern, consisting of two low velocity anomalies, one under Africa, one in the mid-Pacific, surrounded a fast velocity anomaly in the circum-Pacific (see figure 6.6 at 2,800 km and figure 6.15). This agrees with many other tomographic results (*e.g.* for the most recent ones [*Resovsky & Ritzwoller*, 1999; *Grand et al.*, 1997; *Li & Romanowicz*, 1996; *Masters et al.*, 1996; *Liu & Dziewonski*, 1994]). Peak amplitudes in the lowermost mantle are -3.5% under the mid-Pacific and $+2.5\%$ under the Gulf of Mexico.

In figure 6.7 (top), we show the lowermost mantle coverage, represented by the projection of the S_{diff} and sS_{diff} phases (horizontal lines) and the ScS, $sScS$ and ScS and $sScS$ multiples (dots). The disproportionate sampling between Northern and Southern hemisphere is directly related to the receiver distribution. The coverage density is shown at the bottom of the figure. This is measured by $\log(1+n)$ at the core-mantle boundary, where n is, for the diffracted phases, the number of one degree ray path segments in each $10° \times 10°$ degree cell corrected for latitude, and, for the reflected phases, the number of hit counts at the bounce points on the CMB. The sampling is best below the North Pacific, the Mid-Pacific and Asia and poorest in the South Atlantic and South of Australia.

6.3.2 East Pacific ridge complex

The image of the lowermost mantle under the Pacific is dominated by a large scale low velocity region. This anomaly splits radially into three distinct slow anomalies aligned almost linearly between the Northwest and the Southeast Pacific, up to about 2,000 km depth. This observation is in good agreement with the recent result of [*Resovsky & Ritzwoller*, 1999], obtained from normal mode measurements. In figure 6.8, we investigate the radial distribution of this complex anomaly. In particular, we assess its interaction in the uppermost mantle at the surface with the 'East Pacific ridge complex' (East Pacific Rise (*EPR*), Pacific-Antarctic Ridge (*PAR*) and Chile Ridge (*CR*)), by tracing six vertical cross sections in the region of the Pacific bounded by $45°N180°$ and $70°S300°$. The surface projections of the depth sections are represented by green great circle arcs, plotted on the lateral depth section at the top of the figure which shows the map at 2,800 km depth (the bottom of the mantle). The surface locations of hotspots are represented on the surface section by inverted yellow triangles related in size to the hotspot buoyancy flux observed at the surface [*Sleep*, 1990]. The projection of hotspots located at a distance less than 5° away from each great circle arc are also plotted on the cross-sections. The top of the plot includes the peak anomalies mentioned above in the Mid-Pacific and the Gulf of Mexico.

The cross section in figure 6.8 (A) is taken in the NE-SW direction, east of the negative anomaly peak in D", cutting across the surface locations of the Marquesas and the Tahiti hotspots. A continuous low velocity zone is observed throughout the lower mantle and extends laterally above the 670 km discontinuity at a depth of about 550 km, south of the Tahiti hotspot. This image suggests the presence of an upwelling originating at the core-mantle boundary and extending into the upper mantle where it 'pools' and connects, at the the Southern End, with the *PAR*. It also indicates that, in the East Pacific, the 670 km discontinuity does not act as a strong barrier to upgoing flow between lower and upper mantle. We refer to this low velocity region as '*PAC1*.'

Figure 6.8 (B) is taken in the E-W direction across the Nazca Plate and shows a continuous low velocity region extending from the surface location of the *EPR* with the top of *PAC1*.

This effect is also apparent in the lateral sections of figure 6.5 between 100km and 525 km, where the low velocity regions below the *EPR* migrates westward with depth. This feature is consistent on a global scale with fundamental spheroidal mode eigenfrequency shift measurements [*Romanowicz et al.*, 1987] that show a shift to the west of the heterogeneity field with depth. The cross section cuts across or near the surface location of the Samoa, Tahiti, Austral/Cooks islands, Gambier islands, Easter Island, and the San Felix hotspots and shows proximity between the upwelling and the four westernmost hotspots of the cross-section.

The section of figure 6.8 (C) is taken along the great circle between Hawaii and the Austral/Cooks Islands. A strong low velocity region, extending from about 1,600 km to 200 km and peaking in amplitude near 400 km is present underneath Hawaii. Here again, significant lateral extension of the negative anomaly is observed above the 670 km discontinuity. The slow anomaly at the Southern end of the cross-section corresponds to the Eastern part *PAC1* and extends vertically between the lowermost mantle and the Cook islands hotspot at the surface.

The cross section in figure 6.8 (D) is taken across the *CR* and the southwestern part of the *EPR*. In addition to a subhorizontal low velocity anomaly in the upper mantle connecting the *EPR* to *PAC1* to the West, a second continuous low velocity zone extends from the *CR* to the lowermost mantle almost vertically. We refer to this anomaly as '*PAC2*.'

In figure 6.8 (E), we show the latitudinal extent of *PAC2* by taking a North-South section across the Nazca plate. The dimensions and the amplitude of the anomaly are slightly smaller than those of *PAC1*.

A cross-section along the *EPR* is taken in figure 6.8 (F). The low velocity associated with the ridge is observed down to a depth of about 400 km. This is somewhat shallower than the results of [*Wielandt & Knopoff*, 1982] who find negative anomalies down to at least 450 km, but the difference is within the uncertainty resulting from the spline knot spacing at that depth and the wavelength of seismic waves.

Figure 6.9 shows three different isocontour levels corresponding to negative anomalies in *SAW18B16*. The plot shows only latitudes between 60°N and 60°S to avoid artefacts near the poles caused by the cylindrical projection. In the center of the bottom figure, the -1.25% isovelocity level shows a large scale low velocity zone spread horizontally throughout the mid-Pacific at lowermost mantle depth and extending vertically in the mid-Pacific. The low velocity domain in the mid-Pacific corresponds to *PAC1* and is reminiscent of the characteristic shape of a plume (*e.g.* [*Olson et al.*, 1993]), with a large scale base overlain by a narrow conduit topped in turn by a broad 'head'. The narrowing of the slow anomaly with radius is in agreement with the study of [*Bréger & Romanowicz*, 1998]. At the South Eastern End of the Pacific anomaly, the low velocity zone corresponds to *PAC2*. The middle figure shows the -1.0% isovelocity level. The two plumeheads are broader and the successive low velocity zones corresponding to *PAC2* suggest the occurence of intermittent upwellings. The scale length of this feature is nevertheless small and may not be well resolved. The -0.75% isocontour is plotted in the top figure where the two anomalies further extend in the vertical direction.

Although the cross sections show no systematic relationship between the Pacific upwellings and the surface location of hotspots, at least two Pacific hotspots are situated at the surface end of broad negative anomalies. The Cooks/Austral islands hotspot overlays a low velocity zone continuous between CMB and the surface, and Hawaii is situated at the northern end of an anomaly that extends from about 1,600 km to 200 km.
Figure 6.10 is a map view of the -2.47% isovelocity level at the upper mantle depths between the surface and 670 km. Because the projection is from above, depth information is not present on the figure, which displays radially integrated isocontours. The figure allows one to see correspondances between strong low velocity anomalies anywhere in the upper mantle with surface features. In addition to the ridges and back-arc basins observed at uppermost mantle depths in figure 6.5, slow features coincide with the surface location of many hotspots, in particular those that are distant enough from broader low velocity

anomalies, such as ridges. Figure 6.10 shows low velocity anomalies directly underneath Hawaii, the Caroline Islands, Tasmania, Cape Verde, and the region of the South Pacific around the Tahiti, the Gambier and the Austral/Cooks islands. Negative anomalies are also present beneath small hotspots such as the Crozet/Kerguelen region and near Trinidad/Arnold Seamount; these are sufficiently close to appear as one laterally averaged, broad low velocity anomaly.

Figure 6.11 shows the -1.5% isocontours in the Pacific, between 400 to 1,000 km depths. Assuming a temperature-velocity scaling of $\delta \ln V_s = -5 \times 10^{-5} \delta T$, this corresponds to an anomaly of 300K. We chose this depth range to avoid contamination from the mid-ocean ridges and to investigate the possibility of continuity of the anomalies between the upper and the lower mantle. The map view from the top shows correlation between the -1.5% isovelocity domains of the model and the surface location of Bowie (B), Hawaii (H), the Caroline islands (C), Tahiti/Society islands (S), Tasmania (T), the Austral/Cook islands (A) and Gambier (G). In the middle and bottom panels, the view is rotated to show the depth extent of the anomalies. The low velocity domains beneath Tasmania and Bowie appear rooted deeper than the others in the upper mantle, and, in the case of Bowie, to penetrate into the lower mantle. The latter observation is consistent with a regional study by [*Nataf & VanDecar*, 1993], who detected a low velocity region at 700 km depths, off of the coast of Canada.

6.3.3 African superswell

Figure 6.12 (top) shows a lateral section of upper mantle structure in Africa and the Indian Ocean, displaying a strong low velocity zone near the East African rift zone and the Red Sea and along the mid-Indian ridge. A low velocity zone separates the East African, West African and Congo cratons.

Figure 6.12 (A), shows a SW-NE cross-section across the continent. The slow domain under Africa extends vertically from the base of the mantle where it reaches a minimum velocity of -2.5%, into the upper mantle and is subsequently shifted to the NorthEast. The upper mantle image is consistent with the closure of the Tethys by the African continent throughout the Cretaceous: in the tomography, the upper part of the low velocity anomaly is offset in the direction of motion of the African plate. Figure 6.12 (B) shows an East-West cross-section. The low-velocity zone is deflected to the east by the Nubian plate where it connects with the mid-Indian ridge. The shape of this upwelling is shown in figure 6.9. It is a narrow conduit emerging from a broad base and penetrating the upper mantle without significantly altering its shape as it crosses 670 km. The margins and amplitude of this anomaly were investigated in a study by [*Ritsema et al.*, 1998], in which the amplitude and the shape of the anomaly was adjusted to satisfy S, SKS, $ScS - S$ and $S - SKS$ travel times. The cross-section (A) on the figure corresponds roughly to the great circle path in their figure 1. The shape of the anomaly in *SAW18B16* is in general agreement with their model M2, suggesting an upwelling shifting in the Northeast direction with increasing radius. Our model displays significantly lower heterogeneity, peaking at about 2% at the bottom of the mantle, and remainng constant at about 1% in the rest of the lower mantle. It is well known that model amplitudes resulting from inversions of data are damped, as a result of the penalty functions introduced to regularize seismic imaging.

So far, we have concentrated on the low velocity regions of the mantle. We now turn our focus to the the fast anomalies in our model.

6.3.4 Subduction under the Americas

Figure 6.13 (top) shows the Western part of the North and South American continents at 175 km depth, centered on the East Pacific Rise.

Figure 6.13 (A), shows a cross-section through the North American continent. In that figure, a fast velocity anomaly extends from the surface to D", in agreement with [*Grand et al.*, 1997; *Grand*, 1994], although our model does not show the same level of detail. Here again, the tomographic image suggests that the 670 km discontinuity does not significantly impact flow between upper and lower mantle. In D", both models display two high velocity anomalies, one at the base of the slab and the other west of it. The cross section in figure 6.13 (B) is taken across the Peru-Chile trench and shows a fast velocity anomaly penetrating into the lower mantle down to a depth of about 1,400 km. The model also shows a thickening of the slab in the lower mantle part of the model. Both this feature and the depth extent of the slab are consistent with the model of [*Grand*, 1994].

6.3.5 West Pacific subduction

The top of figure 6.14 shows the West Pacific and Indian Ocean regions at 100 km depth. At shallow depth, the heterogeneity is dominated by the signature of back-arc spreading. The low velocity zone in the South is associated with the SouthEast Indian Ridge, and the Indian and Australian continents appear as fast anomalies.

Figure 6.14 (A) is a cross section of the model across the southern Kurile Islands region, displaying a subhorizontal slab sinking to the 670 km discontinuity without entering the lower mantle. This observation is consistent with the V_p models derived from *ISC* data [*Fukao et al*, 1992; *van der Hilst et al.*, 1991] and from the waveform modeling study of [*Tajima & Grand*, 1998].
The cross-section of figure 6.14 (B) is taken across the Japan Trench. The slab appears to 'rest' horizontally on the discontinuity, in agreement with [*van der Hilst et al.*, 1991; *Fukao et al*, 1992]. The anomaly penetrates into the lower mantle at its Eastern end. The amplitude of this feature is nevertheless weak and may not be well resolved but it agrees qualitatively with the results of [*Tajima et al.*, 1998].
The cross-section of figure 6.14 (C) is taken across the Mariana Trench and indicates that the slab barely enters into the lower mantle. This result is surprising as it disagrees with several regional studies (*e.g.* [*van der Hilst & Seno*, 1993]) and may indicate poor resolution in this region.
In the region across the Solomon trench (figure 6.14 (D)), the slab rests on the discontinuity. This image is in stark contrast with the section across the Tonga-Kermadec region where the slab signature is seen to penetrate into the lower mantle (figure 6.14 (E)). Continuation of the Tonga slab into the lower mantle has been observed (*e.g.* [*Fischer et al.*, 1991]), and details of the structure of the slab across the 670 km discontinuity were mapped by [*van der Hilst*, 1995].

In figure 6.14 (F), we show a cross-section across the Java subduction zone. The image suggests the presence of slab in the deep mantle, in agreement with [*Fukao et al*, 1992]. Although this figure suggests that the slab reaches the CMB, the amplitudes below 1,500 km are low, indicating that the depth extent of this fast anomaly cannot be addressed reliably with the present model.

6.4 Spectral Analysis

In figure 6.15 (left), we show the spectral decomposition of *SAW18B16* at depth. The amplitudes of the model are shown as a function of wavelength (horizontal axis) and mantle depth (vertical axis). The image is dominated by the top and bottom boundary layers: the degree 5 & 6 tectonic signature in the uppermost mantle and a strong degree 2 component in D". To enhance the picture in the mid-mantle, the spectral heterogeneity map is normalized in figure 6.15 (center) by the rms amplitude at each depth (figure 6.15 (right)). Each mantle depth has a unique dominant wavelength: degree 5 in the uppermost mantle, degree 1 above the transition zone, degree 2 in the transition zone, the lower mantle is dominated by degrees 0, 3 and 2 and D" by degree 2. The depth range between 600-900 km is 'white', with significant heterogeneity up to degree 18.

Considering the thermal component of the heterogeneity field only, fast and slow anomalies should be related to downwellings and upwellings, respectively. To analyze their respective contribution to the spectrum of figure 6.15 separately, we split the model into the fast and the slow components of the velocity field. Since it is not possible to extract the positive and negative values directly from the spherical harmonic coefficients, we expand *SAW18B16* on two sets of grids, one corresponding to the 'fast' mantle and the other to the 'slow' mantle. Each grid is then interpolated on a spherical harmonic basis. We then compare the spectral signatures of the 'fast' and 'slow' components of mantle heterogeneity. This result is displayed in figure 6.16.

In the uppermost mantle, where the image is dominated by spherical harmonic degree 5, the spectral signature of tectonics corresponds primarily, in the case of the 'fast' anomalies, to the presence of the continents. The anomaly is seen strongly down to about 350 km depth and disappears below the 410 km discontinuity.

The spectral images in the transition zone suggest that the degree two pattern observed by [*Masters et al.*, 1982; *Souriau & Souriau*, 1983] corresponds to the fast component of the velocity field. In the 'slow' mantle, the transition zone spectrum is mostly white with weak peaks at degrees 3 and 4.

In the lower mantle, the spectrum of the fast heterogeneity peaks between degrees 2 and

3. In contrast, the signature of the slow heterogeneity field varies continuously from a degree 2 peak in the lowermost mantle to degree 7 under the 670 km discontinuity. The discrepancy between the two components of the velocity field may indicate that, while the length scale of fast anomalies remains constant in the bulk of the lower mantle, upwellings in the 'slow' lower mantle become narrower with radius. This is seen qualitatively in the isocontour maps of figure 6.9: the low velocity anomalies in the bottom of the mantle are overlain by narrow conduits, while the heterogeneity field that becomes more complicated with increasing radius.

6.5 Discussion

Two slow velocity regions, beneath Africa and the Pacific in the lower mantle, are present in every published model of the whole mantle (*e.g.* [*Liu & Dziewonski*, 1998; *Masters et al.*, 1996; *Grand*, 1994; *Su et al.*, 1994]). In this study, we show that the Pacific superplume consists in fact of two distinct upwellings, each displaying some level of interaction with the complex of ridges in the East Pacific at upper mantle depths. A low velocity anomaly '*PAC1*' is centered around $20°S160°W$, and continues vertically up to 500 km depth where it pools laterally and joins the Pacific-Antarctic Ridge to the south, and the East Pacific Rise to the east. *PAC1* continues its ascension vertically to the surface at its eastern end, where it coincides with the Austral/Cooks hotspot region. A secondary anomaly '*PAC2*' can be traced from the core-mantle boundary near $45°S80°W$ almost vertically to the Chile Ridge. The African upwelling appears to separate laterally beneath the thick African lithosphere to join the mid-Atlantic ridge to the West and the mid-Indian ridge to the East. The multiplicity of such interactions is not fortuitous: based on a study of the distribution of hotspots at plate boundaries, [*Weinstein & Olson*, 1989] demonstrated the high statistical significance of the presence of hotspots near divergent margins and hypothesized that it is the result of a plume capture effect caused by the upward flow in the vicinity of the spreading centers. This effect is also observed in convection simulations (*e.g.* [*Steinberger & O'Connell*, 1998]).

Low velocity domains coincide at upper mantle depths with the surface location of many hotspots. Plumes are nevertheless considered to be much finer features than can be resolved at degree 18. We believe that the probability that these features occur by chance in our model in these regions is very low, and the tomographic image probably represents a laterally smeared version of such anomalies.

A phase transition with a strongly negative Clapeyron slope is expected to slow down the progression of cold downwellings and hot upwellings due to the restoring force that opposes the boundary deflection. In tomographic images, such a barrier would manifest itself by lateral pooling of heterogeneity near the discontinuity. This is not observed in any of the slow anomalies of the present model nor in most regions of subduction, except in the Northwestern Pacific between the Southern Kuriles and the Izu-Bonin where the slab deflection has been hypothesized to be the result of the oceanward motion of the trench with age [*van der Hilst & Seno*, 1993]. Another seismological diagnostic of the slowing of flow across the mantle is the analysis of the correlation of the seismic velocity field with itself across the discontinuity [*Jordan et al.*, 1993]. In figure 6.17 (top), we plotted the radial correlation function for *SAW18B16* and compared it with that of a 3D spherical convection calculation including two phase transitions [*Bunge et al.*, 1998]. The convection model shows a strong 'pinching' of the correlation field at 670 km where the endothermic phase transition is imposed. We have shown in two recent studies [*Mégnin & Romanowicz*, 1999b; *Mégnin et al.*, 1997] that this feature would be resolved by tomography. Such a narrowing of the correlation band in the tomographic results is nevertheless not observed, further suggesting that the phase transition at 670 km does not significantly impede flow between upper and lower mantle.

Taking the degree 5 peak in the spectrum of the fast component of the heterogeneity field in the upper mantle as a proxy for the signature of continental roots, figure 6.16 (top) suggests that cratons are observed down to the 410 km discontinuity. The spectral image changes in the transition zone where it is dominated by degree 2, thus providing evidence that continents do not penetrate into the transition zone significantly. This result is reflected in the maps of figure 6.5 which, with the exception of the southern part of the African continent, do not show fast anomalies corrrelated with the continents below 400 km.

Acknowledgements:
We thank Raphaele Millot and Sean Ford for their help with the collection of data, Ludovic Bréger for body wave sampling code to derive figure 6.7 (top), and the staff of IRIS and GEOSCOPE networks for making the data available. We are indebted to Xiang-Dong Li for collecting most of the data and developing critical portions of the software used in this study. All figures were generated using GMT [*Wessel & Smith*, 1991], except figures 6.9, 6.10 and 6.11 which were constructed with VIS5D [*Hibbard & Santek*, 1990]. Thanks also to Phil Stark for a thorough lecture of the manuscript.

Appendix: Construction of the cubic b-splines

We construct the set of N cubic b-spline basis function $B_0(r)$ to $B_{N-1}(r)$ (*e.g.* [*De Boor*, 1978]), following the approach of [*Michelini & McEvilly*, 1991]. Their formalism was nevertheless developed for equidistant spline knots. For the purpose of this study, we generalize their approach to the case of arbitrarily spaced splines.

General case:

Cubic b-splines $B_k(r)$ whose knots are placed at a distance greater than two knots away from the edges ($2 \leq k \leq N-3$) are constructed as the sum of four cubic polynomials ${}_k\rho_j$ on the interval between r_{k-2} and r_{k+2}:

$$B_k(r) = \sum_{j=0}^{3} {}_k\rho_j(r) \tag{6.2}$$

where the polynomials are defined as:

$${}_k\rho_j(r) = a_j^k (r - r_j)^3 + b_j^k (r - r_j)^2 + c_j^k (r - r_j) + d_j^k \tag{6.3}$$

$$r_{k-2+j} < r < r_{k-1+j} \qquad {}_k\rho_j(r) = 0 \quad \text{elsewhere.} \tag{6.4}$$

The 16 coefficients a_j^k, b_j^k, c_j^k, and d_j^k are determined by imposing the following conditions:

- The spline function and its first and second derivatives vanish at the end points (6 conditions)
  ${}_k\rho_0(r_{k-2}) = {}_k\rho_0'(r_{k-2}) = {}_k\rho_0''(r_{k-2}) = 0$
  ${}_k\rho_0(r_{k+2}) = {}_k\rho_0'(r_{k+2}) = {}_k\rho_0''(r_{k+2}) = 0$

- Continuity of the spline and its first and second derivatives (9 conditions)
  ${}_k\rho_0(r_{k-1}) = {}_k\rho_1(r_{k-1})$; ${}_k\rho_1(r_k) = {}_k\rho_2(r_k)$; ${}_k\rho_2(r_{k+1}) = {}_k\rho_3(r_{k+1})$
  ${}_k\rho_0'(r_{k-1}) = {}_k\rho_1'(r_{k-1})$; ${}_k\rho_1'(r_k) = {}_k\rho_2'(r_k)$; ${}_k\rho_2'(r_{k+1}) = {}_k\rho_3'(r_{k+1})$

$$ {}_k\rho_0''(r_{k-1}) \;=\; {}_k\rho_1''(r_{k-1})\;;\; {}_k\rho_1'(r_k) \;=\; {}_k\rho_2''(r_k)\;;\; {}_k\rho_2'(r_{k+1}) \;=\; {}_k\rho_3''(r_{k+1}) $$

- Normalization condition:
  $\int_{r_{k-2}}^{r_{k+2}} B_k(r)dr = 1$

The solution of the 16x16 linear system yields the following values for the unknown coefficients:

$$
\begin{aligned}
a_0^k &= \frac{4}{h_0(h_0+h_1)(h_0+h_1+h_2)(h_0+h_1+h_2+h_3)} \\
b_0^k &= c_0^k \;=\; d_0^k \;=\; 0 \\
a_1^k &= \frac{-4(h_0^2+3h_0h_1+3h_1^2+2h_0h_2+4h_1h_2+h2^2+h_0h_3+2h_1h_3+h_2h_3)}{h_1(h_0+h_1)(h_1+h_2)(h_0+h_1+h_2)(h_1+h_2+h_3)(h_0+h_1+h_2+h_3)} \\
b_1^k &= \frac{12}{(h_0+h_1)(h_0+h_1+h_2)(h_0+h_1+h_2+h_3)} \\
c_1^k &= \frac{12h_0}{(h_0+h_1)(h_0+h_1+h_2)(h_0+h_1+h_2+h_3)} \\
d_1^k &= \frac{4h_0^2}{(h_0+h_1)(h_0+h_1+h_2)(h_0+h_1+h_2+h_3)} \\
a_2^k &= \frac{4(h_0h_1+h_1^2+2h_0h_2+4h_1h_2+3h_2^2+h_0h_3+2h_1h_3+3h_2h_3+h_3^2)}{h_2(h_1+h_2)(h_0+h_1+h_2)(h_2+h_3)(h_1+h_2+h_3)(h_0+h_1+h_2+h_3)} \\
b_2^k &= \frac{-12(h_0+2h_1+2h_2+h_3)}{(h_1+h_2)(h_0+h_1+h_2)(h_1+h_2+h_3)(h_0+h_1+h_2+h_3)} \\
c_2^k &= \frac{12(-h_0h_1-h_1^2+h_2^2+h_2h_3)}{(h_1+h_2)(h_0+h_1+h_2)(h_1+h_2+h_3)(h_0+h_1+h_2+h_3)} \\
d_2^k &= \frac{4(2h_0h_1h_2+2h_1^2h_2+h_0h_2^2+2h_1h_2^2+h_0h_1h_3+h_1^2h_3+h_0h_2h_3+2h_1h_2h_3)}{(h_1+h_2)(h_0+h_1+h_2)(h_1+h_2+h_3)(h_0+h_1+h_2+h_3)} \\
a_3^k &= \frac{-4}{h_3(h_2+h_3)(h_1+h_2+h_3)(h_0+h_1+h_2+h_3)} \\
b_3^k &= \frac{12}{(h_2+h_3)(h_1+h_2+h_3)(h_0+h_1+h_2+h_3)} \\
c_3^k &= \frac{-12h_3}{(h_2+h_3)(h_1+h_2+h_3)(h_0+h_1+h_2+h_3)} \\
d_3^k &= \frac{4h_3^2}{(h_2+h_3)(h_1+h_2+h_3)(h_0+h_1+h_2+h_3)}
\end{aligned}
$$

where, dropping the implicit index k for the h_i^k, we define the spacing between two adjacent knots $h_i \equiv r_{k+i-2} - r_{k+i-1}$.

Case k=1:

The second b-spline $B_1(r)$ is constructed with three cubic polynomials on the interval between r_0 and r_3:

$$B_1(r) = \sum_{j=0}^{2} {}_1\rho_j(r) \tag{6.5}$$

$$r_j < r < r_{j+1} \qquad {}_1\rho_j(r) = 0 \quad \text{elsewhere} \tag{6.6}$$

We impose the same normalization condition as for the general case. We also retain the continuity conditions for the right hand side but we relax the condition that the second derivative vanish on the left hand side to avoid the trivial solution. The nine coefficients obtained are as follows:

$$\begin{aligned}
a_0^1 &= \frac{-4(3h_0+2h_1+h_2)}{h_0(h_0+h_1)(h_0+h_1+h_2)(3h_0^2+4h_0h_1+h_1^2+2h_0h_2+h_1h_2)} \\
b_0^1 &= d_0^1 = 0 \\
c_0^1 &= \frac{12}{h_0(h_0+h_1)(h_0+h_1+h_2)(3h_0^2+4h_0h_1+h_1^2+2h_0h_2+h_1h_2)} \\
a_1^1 &= \frac{4(2h_0^2+6h_0h_1+3h_1^2+3h_0h_2+3h_+1h_2+h_2^2)}{h_1(h_0+h_1)(h_1+h_2)(h_0+h_1+h_2)} \\
b_1^1 &= \frac{-12(3h_0+2h_1+h_2)}{(h_0+h_1)(h_0+h_1+h_2)(3h_0^2+4h_0h_1+h_1^2+2h_0h_2+h_1h_2)} \\
c_1^1 &= \frac{12(-2h_0^2+h_1^2+h_1h_2)}{(h_0+h_1)(h_0+h_1+h_2)(3h_0^2+4h_0h_1+h_1^2+2h_0h_2+h_1h_2)} \\
d_1^1 &= \frac{4h_0(4h_0h_1+3h_1^2+2h_0h_2+3h_1h_2)}{(h_0+h_1)(h_0+h_1+h_2)(3h_0^2+4h_0h_1+h_1^2+2h_0h_2+h_1h_2)} \\
a_2^1 &= \frac{-4(2h_0+h_1)}{h_2(h_1+h_2)(h_0+h_1+h_2)(3h_0^2+4h_0h_1+h_1^2+2h_0h_2+h_1h_2)} \\
b_2^1 &= \frac{12(2h_0+h_1)}{(h_1+h_2)(h_0+h_1+h_2)(3h_0^2+4h_0h_1+h_1^2+2h_0h_2+h_1h_2)} \\
c_2^1 &= \frac{-12h_2(2h_0+h_1)}{(h_1+h_2)(h_0+h_1+h_2)(3h_0^2+4h_0h_1+h_1^2+2h_0h_2+h_1h_2)} \\
d_2^1 &= \frac{4h_2^2(2h_0+h_1)}{(h_1+h_2)(h_0+h_1+h_2)(3h_0^2+4h_0h_1+h_1^2+2h_0h_2+h_1h_2)}
\end{aligned}$$

Case k=N-2:

The penultimate b-spline $B_{N-2}(r)$ is constructed on the interval between r_{N-4} and r_{N-1}.

$$B_{(N-2)}(r) \; = \; \sum_{j=0}^{2} {}_{(N-2)}\rho_j(r) \tag{6.7}$$

$$r_{N+j-2} < r < r_{N+j-1} \qquad {}_{(N-2)}\rho_j(r) = \; 0 \quad \text{elsewhere} \tag{6.8}$$

We keep the same normalization and, interverting right hand side and left hand side, we use the continuity conditions as for the case k=1. The solution of the 9x9 system yields:

$$\begin{aligned}
a_0^{N-2} &= \frac{4(h_1+2h_2)}{h_0(h_0+h_1)(h_0+h_1+h_2)(h_0h_1+h_1^2+2h_0h_2+4h_1h_2+3h_2^2)} \\
b_0^{N-2} &= c_0^{N-2} \; = \; d_0^{N-2} \; = \; 0 \\
a_1^{N-2} &= \frac{-4(h_0^2+3h_0h_1+3h_1^2+3h_0h_2+6h_1h_2+2h_2^2)}{h_1(h_0+h_1)(h_1+h_2)(h_0h_1+h_1^2+2h_0h_2+4h_1h_2+3h_2^2)} \\
b_1^{N-2} &= \frac{12(h_1+2h_2)}{(h_0+h_1)(h_0+h_1+h_2)(h_0h_1+h_1^2+2h_0h_2+4h_1h_2+3h_2^2)} \\
c_1^{N-2} &= \frac{12h_0(h_1+2h_2)}{(h_0+h_1)(h_0+h_1+h_2)(h_0h_1+h_1^2+2h_0h_2+4h_1h_2+3h_2^2)} \\
d_1^{N-2} &= \frac{4h_0^2(h_1+2h_2)}{(h_0+h_1)(h_0+h_1+h_2)(h_0h_1+h_1^2+2h_0h_2+4h_1h_2+3h_2^2)} \\
a_2^{N-2} &= \frac{4(h_0+2h_1+3h_2)}{h_2(h_1+h_2)(h_0+h_1+h_2)(h_0h_1+h_1^2+2h_0h_2+4h_1h_2+3h_2^2)} \\
b_2^{N-2} &= \frac{-12(h_0+2h_1+3h_2)}{(h_1+h_2)(h_0+h_1+h_2)(h_0h_1+h_1^2+2h_0h_2+4h_1h_2+3h_2^2)} \\
c_2^{N-2} &= \frac{12(-h_0h_1-h_1^2+2h_2^2)}{(h_1+h_2)(h_0+h_1+h_2)(h_0h_1+h_1^2+2h_0h_2+4h_1h_2+3h_2^2)} \\
d_2^{N-2} &= \frac{4h_2(3h_0h_1+3h_1^2+2h_0h_2+4h_1h_2)}{(h_1+h_2)(h_0+h_1+h_2)(h_0h_1+h_1^2+2h_0h_2+4h_1h_2+3h_2^2)}
\end{aligned}$$

Case k=0:

The first b-spline $B_0(r)$ is constructed with two cubic polynomials defined on the interval between r_0 and r_2:

$$B_0(r) = \sum_{j=0}^{1} {}_0\rho_j(r) \tag{6.9}$$

$$r_j < r < r_{j+1} \qquad {}_0\rho_j(r) = 0 \quad \text{elsewhere} \tag{6.10}$$

We use the same conditions as for the case k=1 but have relaxed the condition that the first left hand-side derivative vanish to avoid the trivial solution. The solution of the 4x4 system yields:

$$\begin{aligned}
a_0^0 &= \frac{4}{h_0(h_0+h_1)(3h_0^2+3h_0h_1+h_1^2)} \\
b_0^0 &= 0 \\
c_0^0 &= \frac{-12}{3h_0^2+3h_0h_1+h_1^2} \\
d_0^0 &= \frac{4(2h_0+h_1)}{3h_0^2+3h_0h_1+h_1^2} \\
a_1^0 &= \frac{4}{h_1(h_0+h_1)(3h_0^2+3h_0h_1+h_1^2)} \\
b_1^0 &= \frac{12}{(h_0+h_1)(3h_0^2+3h_0h_1+h_1^2)} \\
c_1^0 &= \frac{-12h_1}{(h_0+h_1)(3h_0^2+3h_0h_1+h_1^2)} \\
d_1^0 &= \frac{4h_1^2}{(h_0+h_1)(3h_0^2+3h_0h_1+h_1^2)}
\end{aligned}$$

Case k=N-1:

The last b-spline, $B_{N-1}(r)$, is constructed with the two cubic polynomials on the interval between r_{N-3} and r_{N-1}:

$$B_{N-1}(r) = \sum_{j=0}^{1} {}_{(N-1)}\rho_j(r) \tag{6.11}$$

$$r_{N+j-3} < r < r_{N+j-2} \qquad {}_{(N-1)}\rho_j(r) = 0 \quad \text{elsewhere} \tag{6.12}$$

Interverting right hand side and left hand side, we keep the same normalization and continuity conditions as for the case k=0. The solution of the 4x4 system yields:

$$\begin{aligned}
a_0^{N-1} &= \frac{4}{h_0(h_0+h_1)(h_0^2+3h_0h_1+h_1^2)} \\
b_0^{N-1} &= c_0^{N-1} = d_0^{N-1} = 0 \\
a_1^{N-1} &= \frac{-4}{h_1(h_0+h_1)(h_0^2+3h_0h_1+h_1^2)} \\
b_1^{N-1} &= \frac{12}{(h_0+h_1)(h_0^2+3h_0h_1+h_1^2)} \\
c_1^{N-1} &= \frac{12h_0}{(h_0+h_1)(h_0^2+3h_0h_1+h_1^2)} \\
d_1^{N-1} &= \frac{4h_0^2}{(h_0+h_1)(h_0^2+3h_0h_1+h_1^2)}
\end{aligned}$$

Data type	Number of traces	Frequency band (s)	Variance
Body waveforms	11,286	300 - 180 - 37 - 31.4	.532
Surface waveforms	9,360	400.2 - 250.3 - 100.1 - 80	.404
Higher mode waveforms	1,440	400.2 - 250.3 - 100.1 - 80	.563

Table 6.1. Summary of the data used in this study. The frequency band is expressed in seconds and corresponds to the high-cut-off, high corner, low-corner, and low-cut-off periods respectively. A cosine taper is applied between the corner and cutoff frequencies. Residual variances with respect to model *SAW18B16* are given in the third column.

Body phase	Number of occurences
S & sS	5,865
SS & sSS	7,277
S_3 & sS_3	5,003
S_4 & sS_4	2,713
ScS & $sScS$	4,671
ScS_2 & $sScS_2$	3,423
ScS_3 & $sScS_3$	184
S_{diff} & sS_{diff}	1,220
Unidentified phases	941
Total	**31,084**

Table 6.2. Number of body wave phases used in this study.

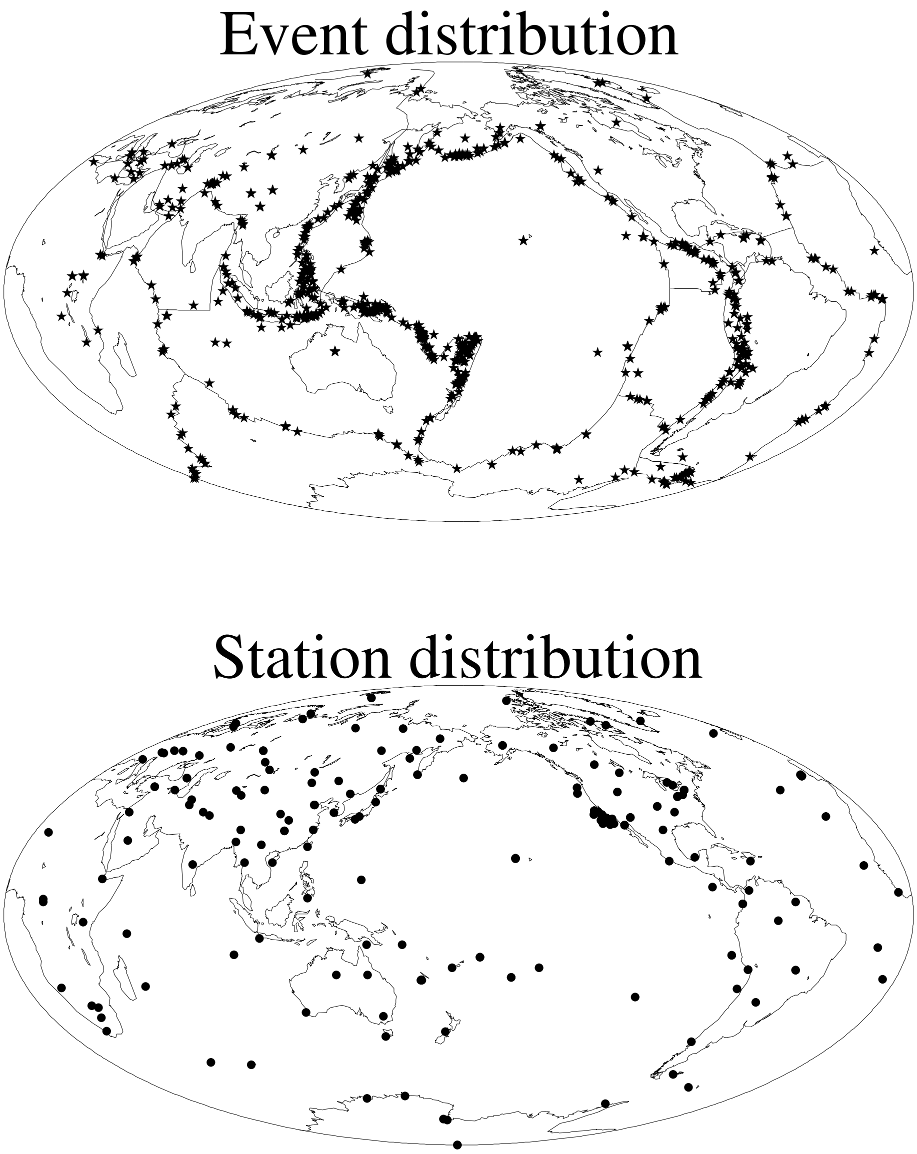

Figure 6.1. Top: Distribution of events used in this study. 347 in the Northern and 391 in the Southern hemisphere. Bottom: Distribution of IRIS & GEOSCOPE station locations. There are 148 in the Northern and 51 in the Southern hemisphere.

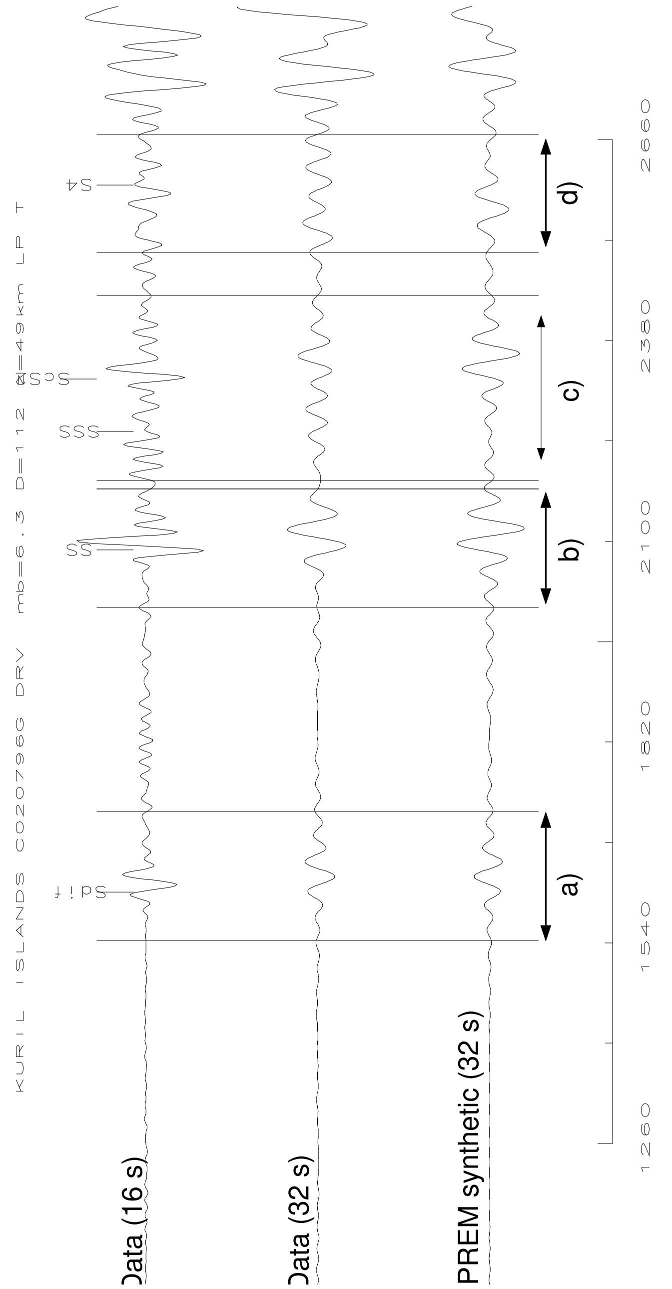

Figure 6.2. Data selection procedure for a February 1996, $M_w = 7.1$ event in the Kurile recorded at station DRV, Antarctica ($\Delta = 112^o$). Top trace: 16s deconvolved data. Middle trace: 32 s data. Bottom trace: PREM synthetic. Each body wavepacket is selected individually a) S_{diff} b) SS c) ScS_2 d) S_4.

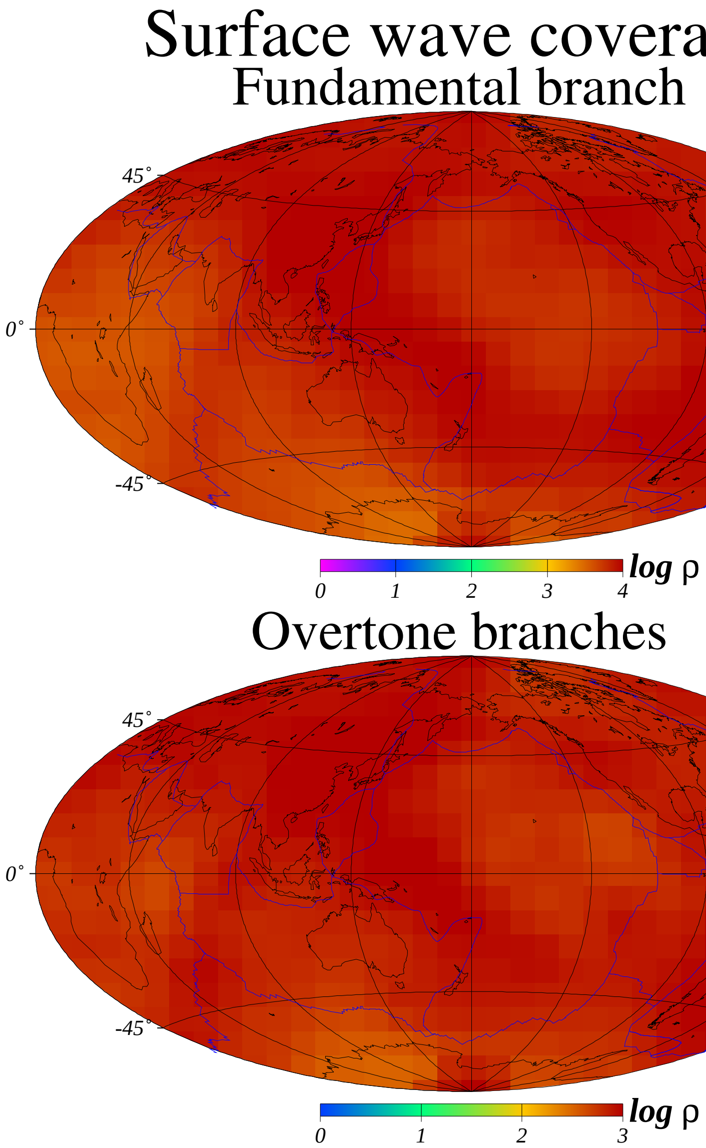

Figure 6.3. Top: Love wave density coverage, expressed as the logarithm of the number of 1 degree segments in each 10 by 10 degree cell (ρ). Bottom: Same as top, but for the higher mode phases.

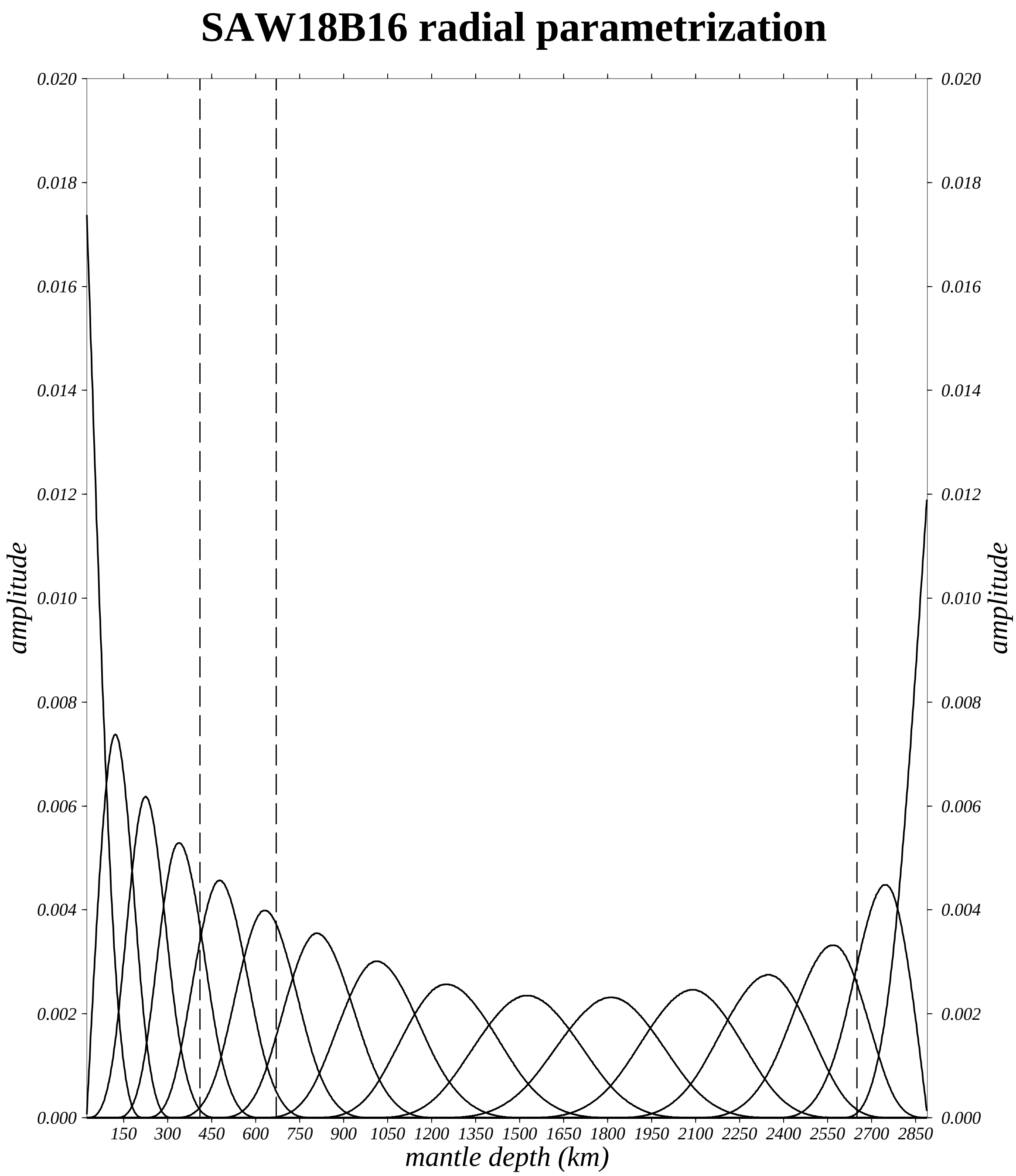

Figure 6.4. The 16 cubic b-splines that parametrize the model as a function of mantle depth. The splines are normalized to unit area.

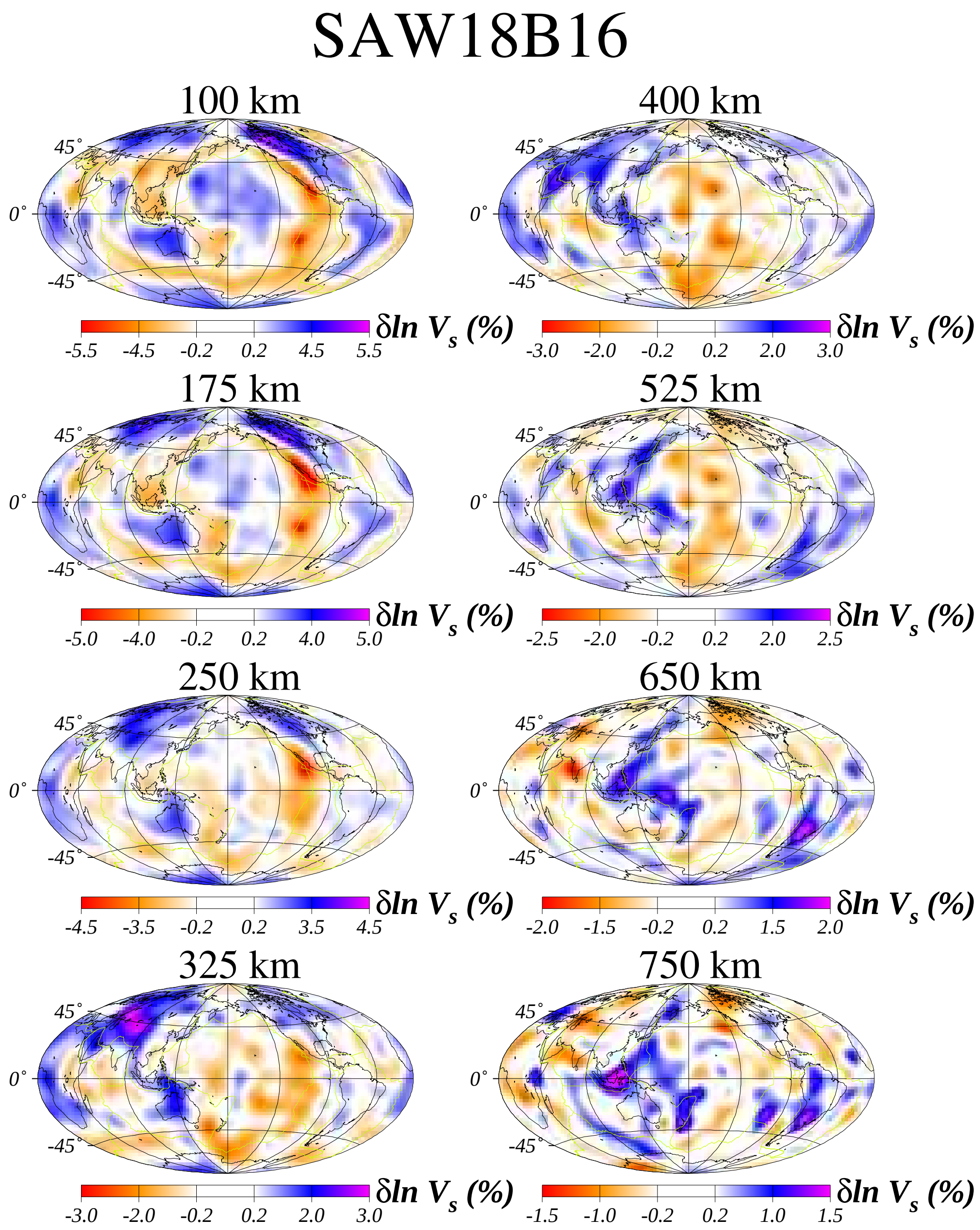

Figure 6.5. Upper mantle & 750 km depth sections for model *SAW18B16*.

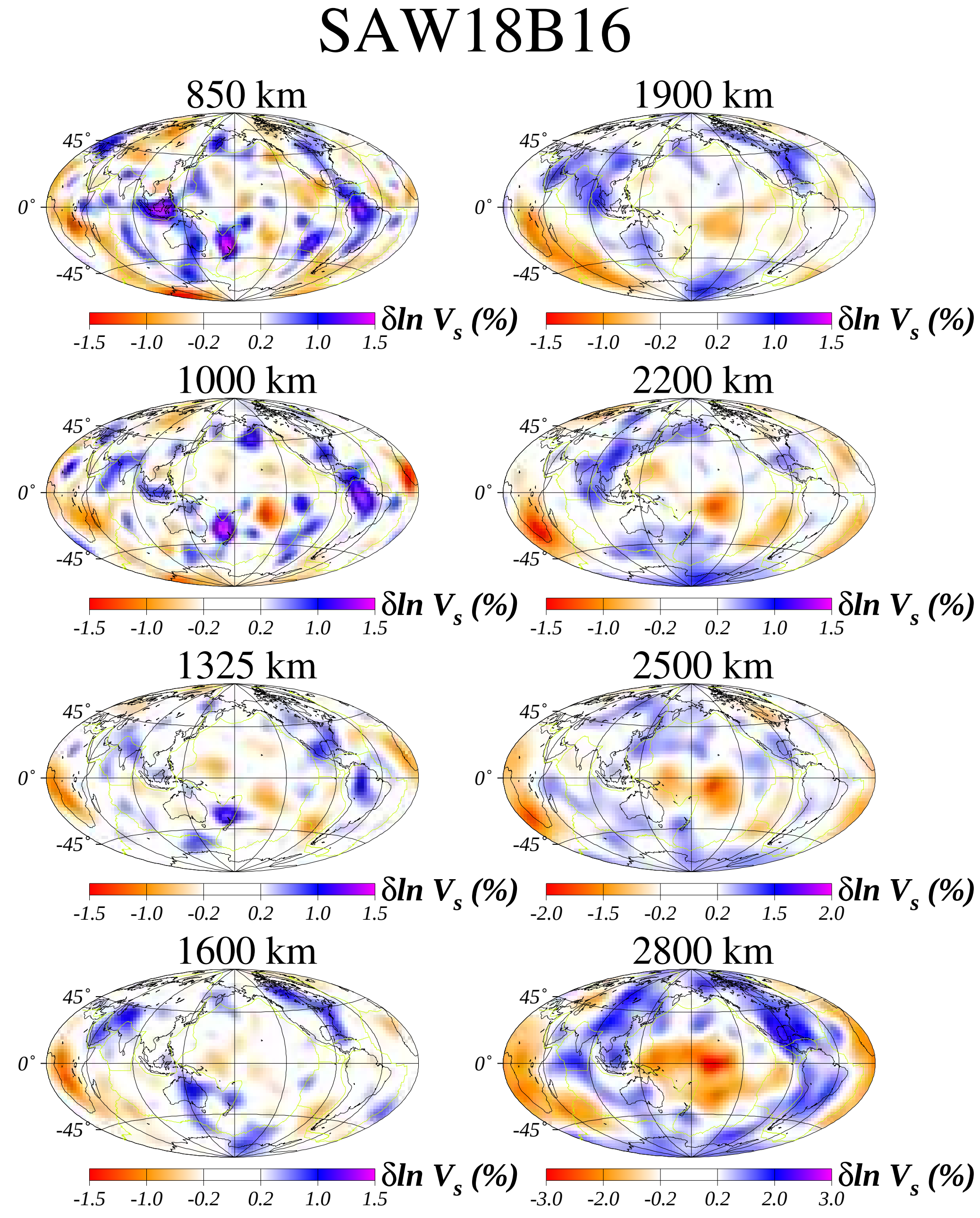

Figure 6.6. Lower mantle depth sections for model *SAW18B16*.

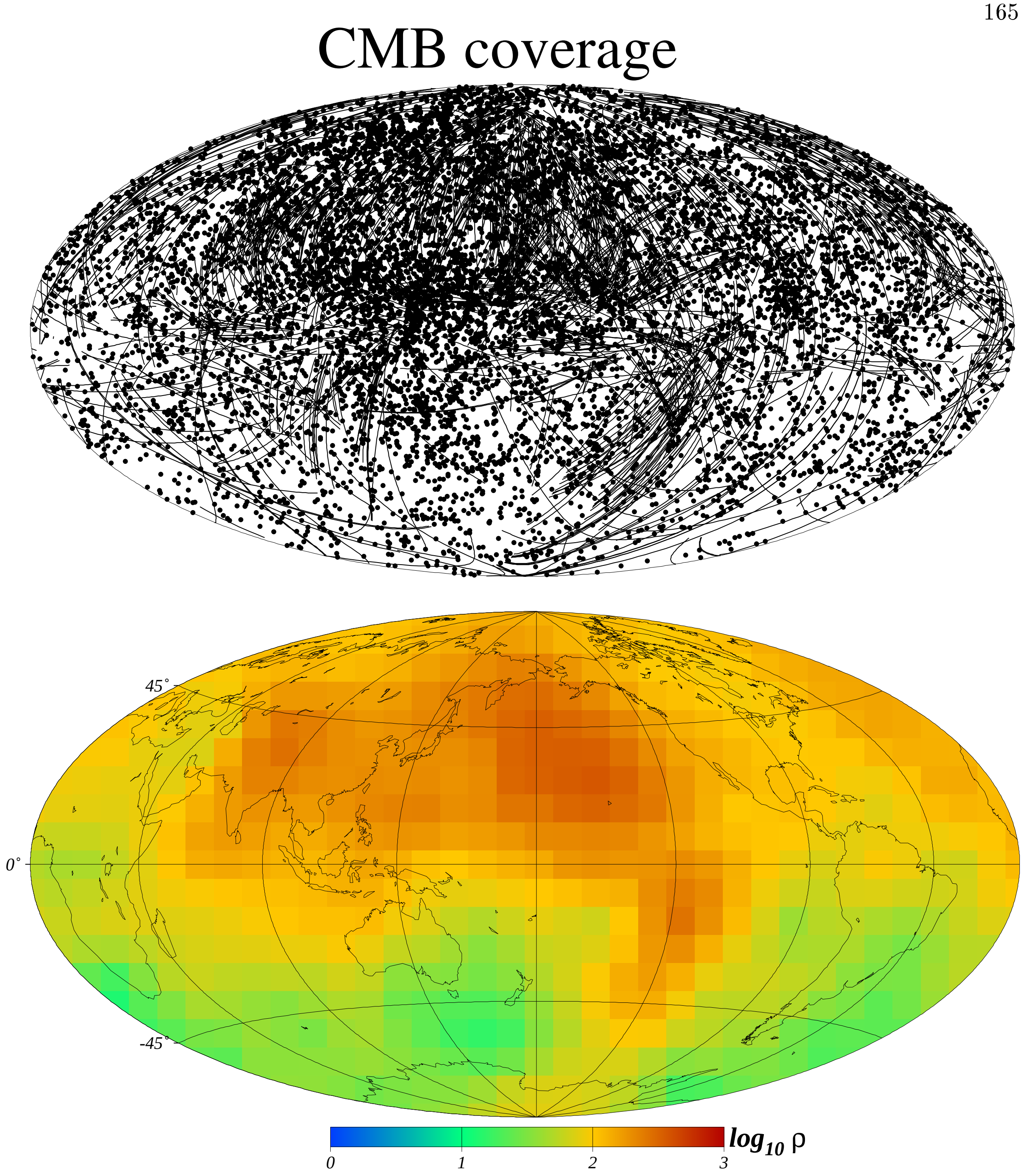

Figure 6.7. Top: Projection of rays at the CMB: $S_{\rm diff}$ and $sS_{\rm diff}$ (great circle arcs) and ScS, ScS_2 and ScS_3 and corresponding depth phases (points). Bottom: density coverage (as in Figure 6.3).

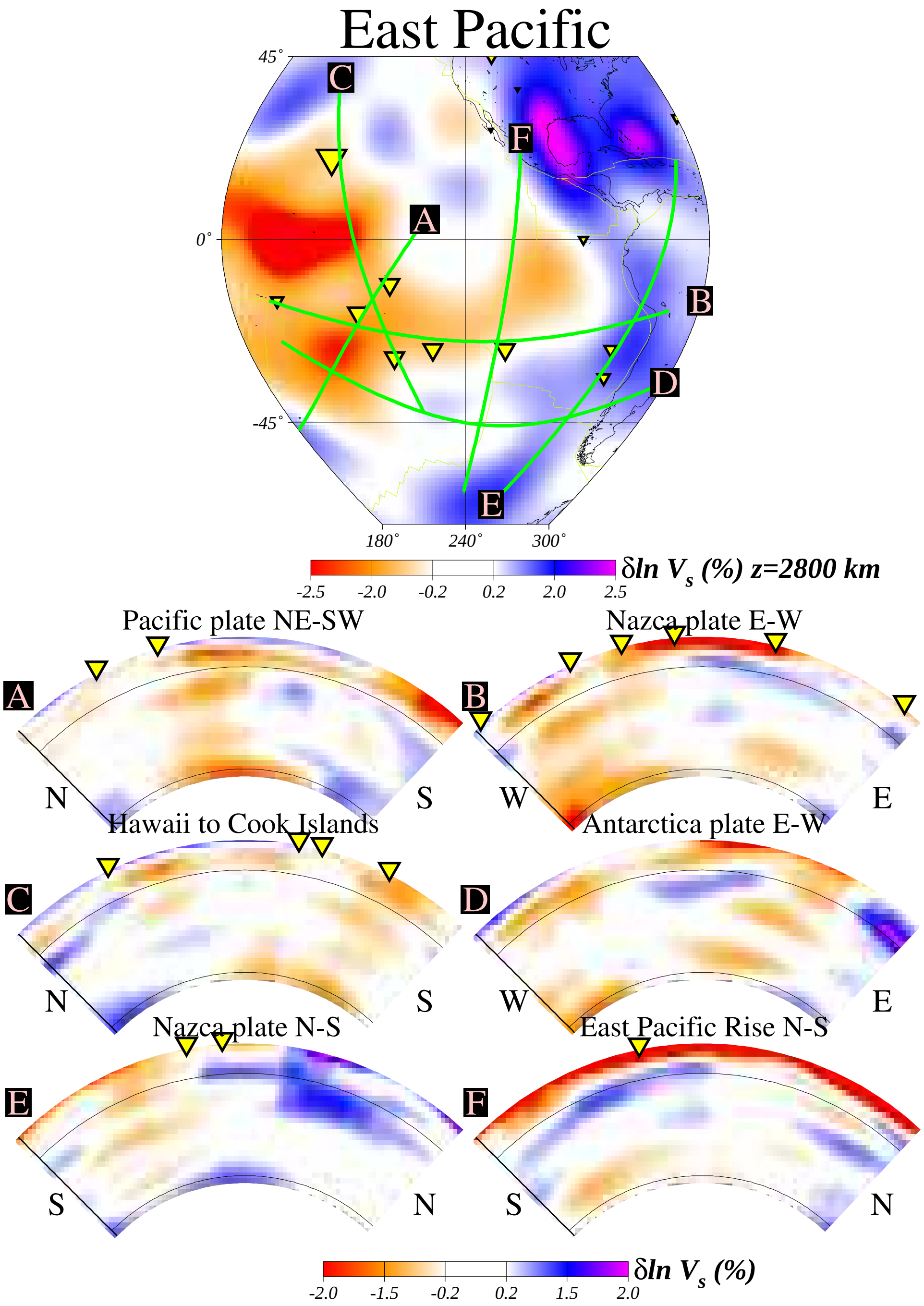

Figure 6.8. East and Central Pacific. Top: Lateral section about the East Pacific Rise at lowermost mantle depth. Cross-sections: horizontal lines are traced at 670 km and 2,650 km depth. A: Cocos plate, E-W section. B: Nazca Plate, E-W section. C: Antartica Plate, E-W section. D: Pacific Plate, N-S section. E: Nazca plate, N-S section. F: Along-ridge section: East Pacific Rise (N-S).

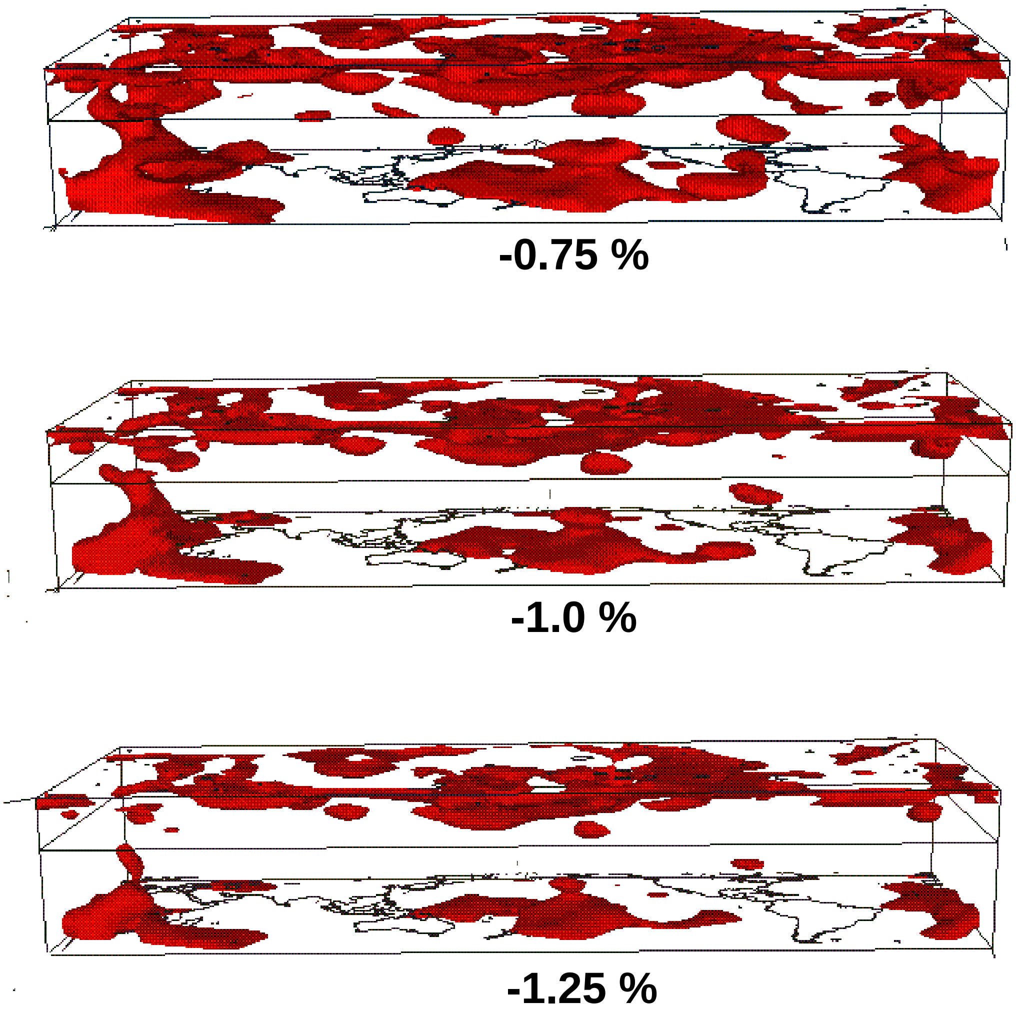

Figure 6.9. 3D isocontour maps. Bottom: $\partial \ln V_s = $-1.25%. Middle: $\partial \ln V_s = $-1.0%. Top: $\partial \ln V_s = $-0.75%

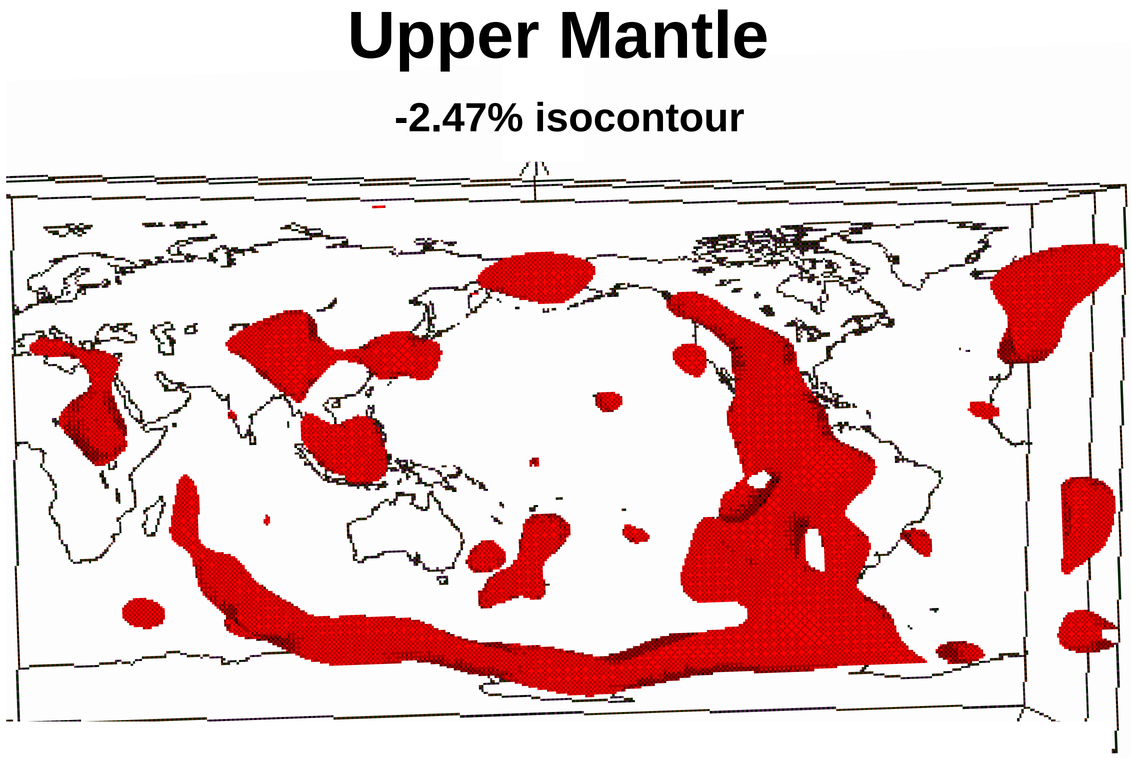

Figure 6.10. -2.5% isocontour map in the upper mantle.

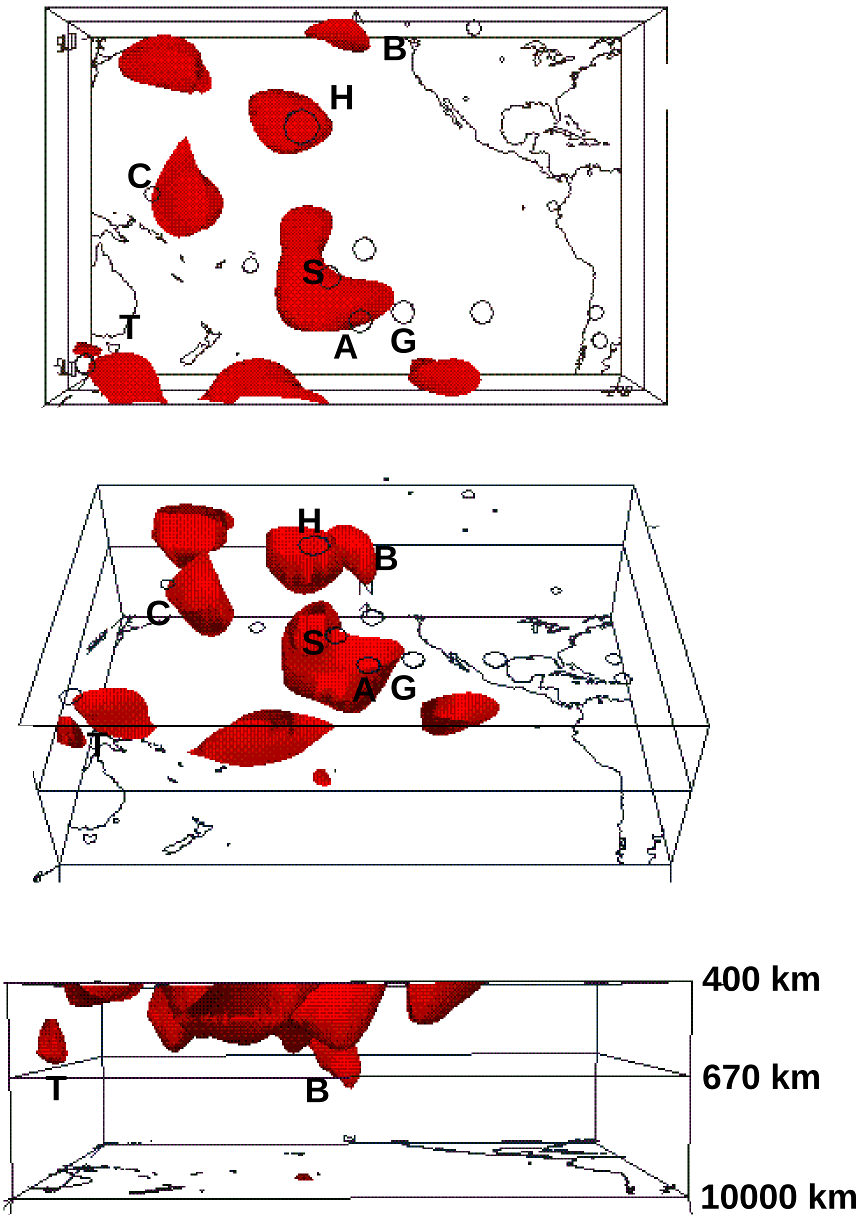

Figure 6.11. -1.5% isocontour map in the Pacific between 400 & 1,000 km depth. The hotspots are annotated on the map as: B: Bowie, H: Hawaii, C: Caroline islands, S: Society islands, A: Austral/Cooks islands, G: Gambier, T: Tasmania

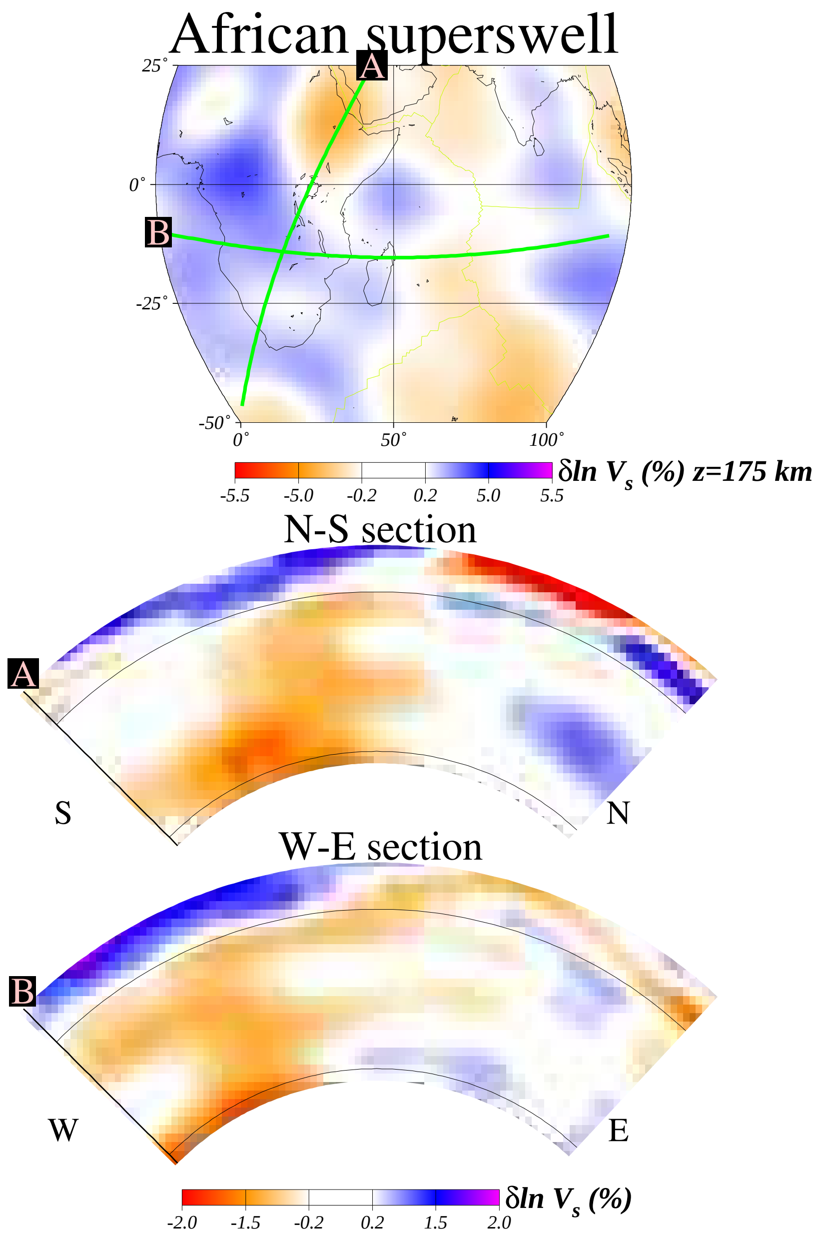

Figure 6.12. African superswell. Top: Lateral section at 100 km depth. A: North-South section. B: East-West section.

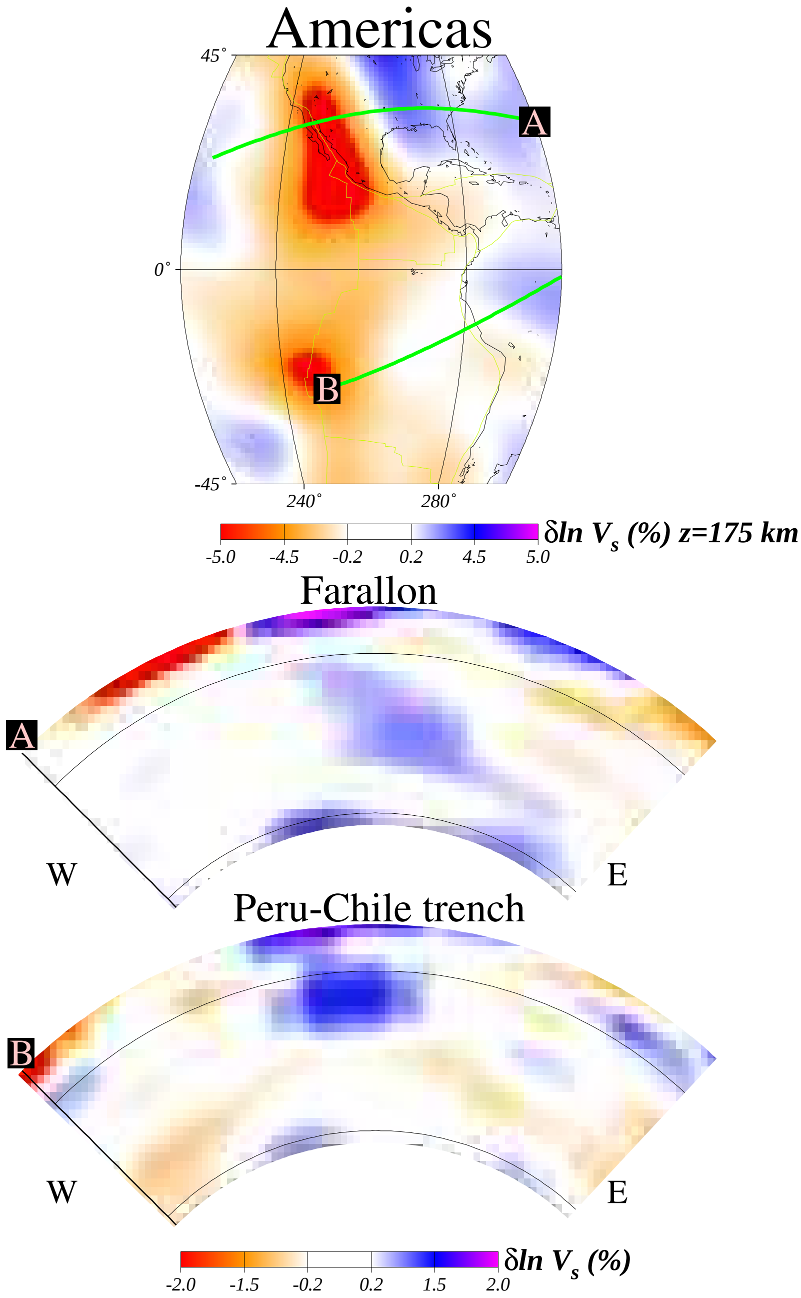

Figure 6.13. Subduction in the Americas. Top: Farallon section. Bottom: South American section.

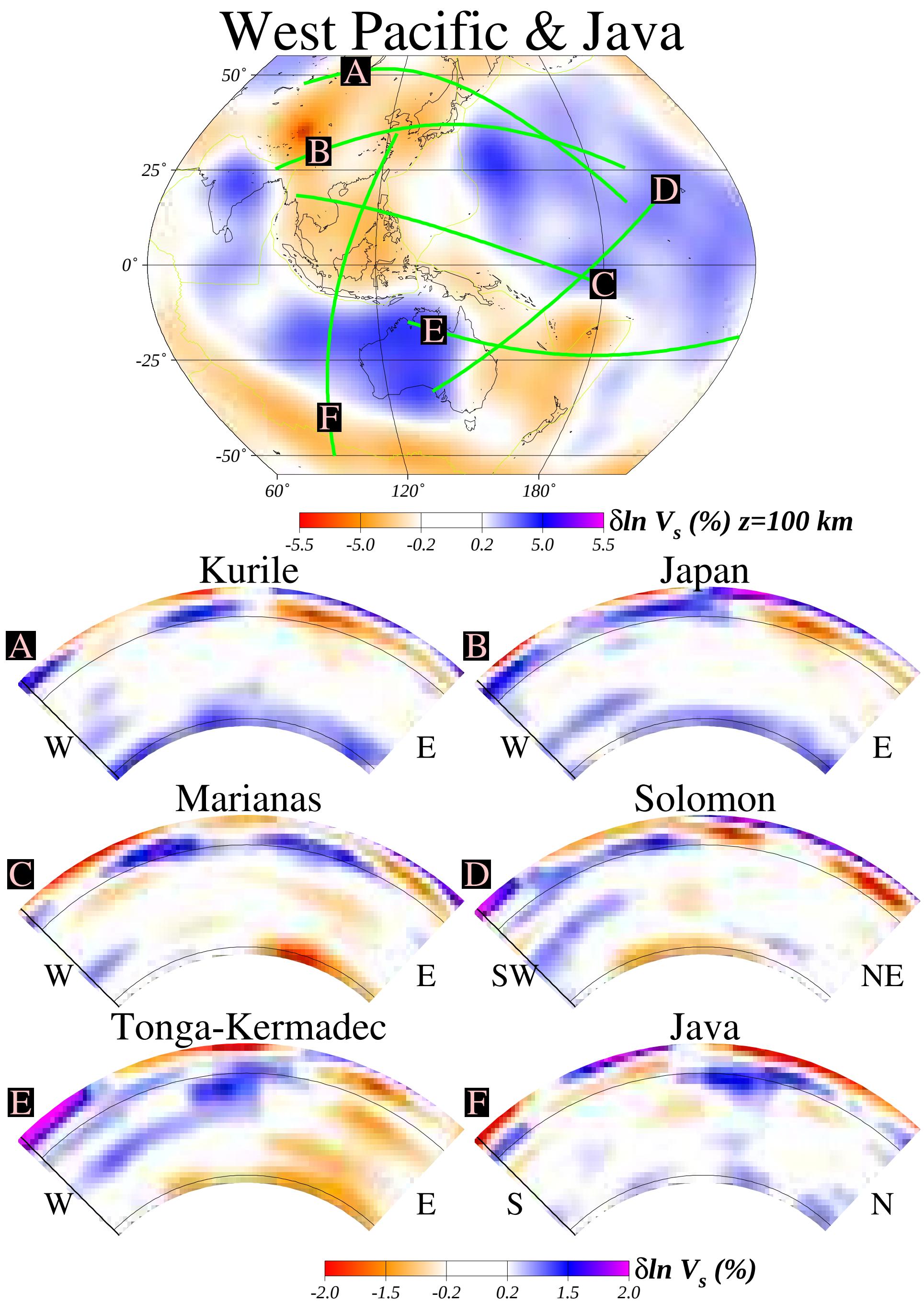

Figure 6.14. Subduction in the West Pacific & Java. Top: Lateral section at uppermost mantle depth. A: Kurile. B: Japan. C: Marianas. D: Solomon Islands. E: Tonga-Kermadec. F. Java.

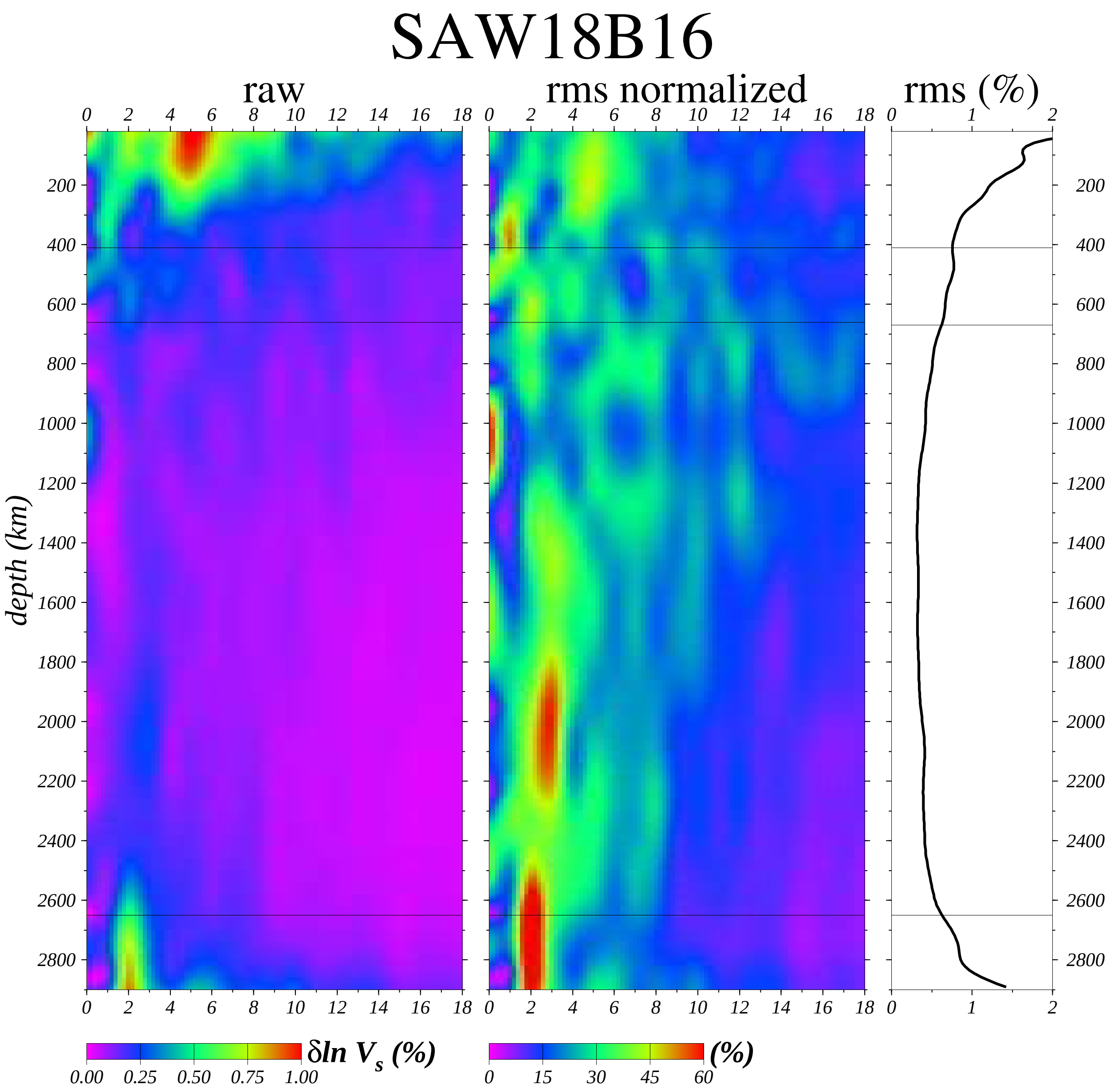

Figure 6.15. Spectral heterogeneity maps. Left - raw spectrum. Center - Same as left, but normalized by the rms at each depth. Right: rms amplitudes as function of depth.

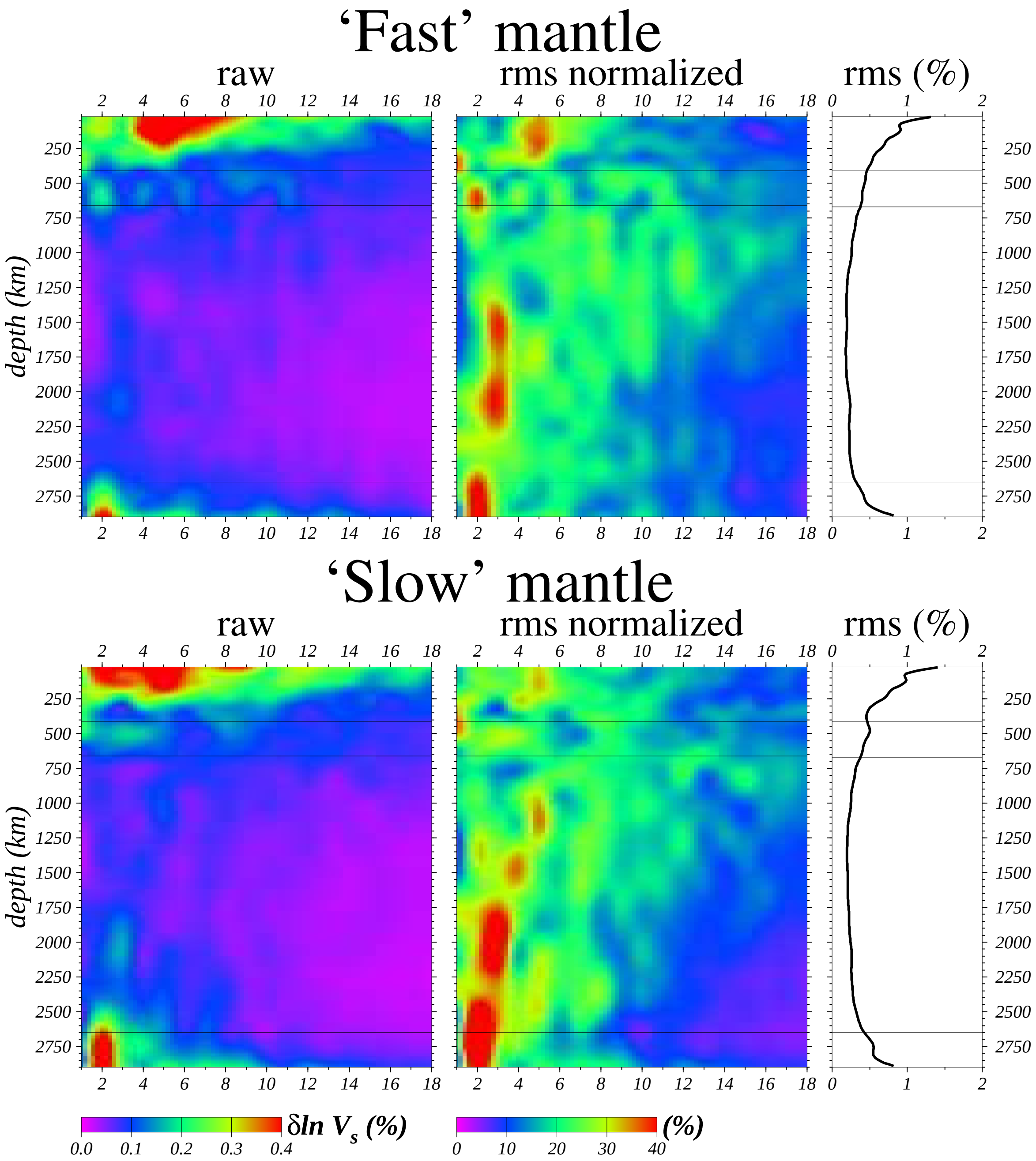

Figure 6.16. Spectral heterogeneity maps for the fast and slow components of the heterogeneity field in the model. The 'fast' mantle is plotted at the top and the 'slow' mantle at the bottom. Left, center and right, are as in figure 6.15.

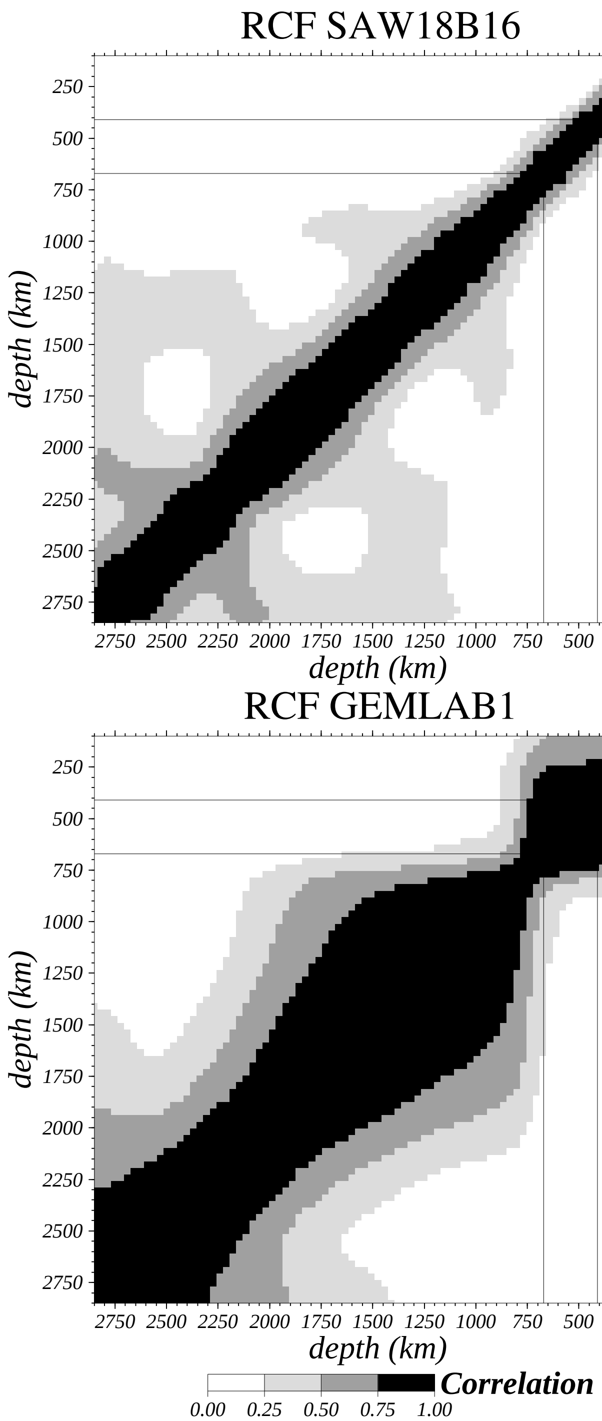

Figure 6.17. Top: Radial correlation function (RCF) of *SAW18B16*. Bottom: RCF of the convection model *GEMLAB1* [*Bunge et al.*, 1998].

General conclusion

We have developed a degree 18 model of V_{SH} heterogeneity in the mantle, using the time-domain modeling of fundamental and overtone surface wavetrains and body waveforms. Based on our model, we make the following inferences related to the structure of mantle:

- The slow anomaly near the core-mantle boundary under the Pacific separates into two distinct upwellings centered under the mid-Pacific and the Chile ridge.
- The large scale upwellings and mid-ocean ridges interact at the surface, presumably as a result of a capture effect by the upgoing current near divergent margins.
- Isolated low velocity regions of amplitude less than 1.5% are visible in the transition zone, beneath the location of most Pacific hotspots (Easter island a notable exception).

The spectral analysis of the model suggests the following features are characteristic of the mantle on a global scale:

- The lowermost mantle is dominated by a degree-two pattern, but heterogeneity is present at all wavelengths, at least up to degree 18.
- The fast component of the velocity field in the rest of the lower mantle is dominated by a degree 3 pattern, whereas the dominant wavelengths corresponding to slow velocities decrease with radius.
- The degree 2 pattern observed in the transition zone [*Masters et al.*, 1982; *Souriau & Souriau*, 1983] corresponds to fast velocities.
- The spectral signature of the continental roots is visible to a depth of 400 km.

Bibliography

Alsina, D., and R. Snieder, constraint on the velocity structure beneath the Tornquist-Tesseyre zone from beam forming analysis, *Geophys. J. Int.*, **126**, 205-218, 1996.

Alsina, D., R. L. Woodward and R. Snieder, Shear wave velocity structure in North America from large-scale waveform inversion of surface waves, *J. Geophys. Res.*, **101**, 15,969-15,986, 1996.

D. L. Anderson, Theory of the Earth, Blackwell Scientific Publications, 1989.

Bijwaard, H., W. Spakman & R. Engdahl, Closing the gap between regional and global travel time tomography, *J. Geophys. Res.*, in press, 1999.

Bréger, L., Romanowicz, B. and Vinnik, L. Test of tomographic models of D" using differential travel time data, *Geophys. Res. Lett.*, **25**, 5-8, 1998.

Bréger, L. and B. Romanowicz, Three dimensional structure at the base of the mantle beneath the Central Pacific, *Science*, **382**, 244-248, 1998.

Bunge, H.P., M.A. Richards, C. Lithgow-Bertelloni, J.R. Baumgardner, S. P. Grand and B. Romanowicz, Time scales and heterogeneous structure in geodynamic Earth models, *Science, 280, No 5360*, 91-95, 1998.

Bunge, H.P., M.A. Richards, and J.R. Baumgardner, A sensitivity study of 3-D spherical mantle convection at 10^8 Rayleigh number: Effects of depth-dependent viscosity, heating mode and an endothermic phase change, *J. Geophys. Res.*, **102**, 11,991-12,007, 1997.

Bunge, H.P., M.A. Richards, and J. R. Baumgardner, Effect of depth-dependent viscosity on the planform of mantle convection, *Nature*, **379**, 436-438, 1996.

Bunge, H.P. and M.A. Richards, The origin of long wavelength structure in mantle convection: effects of plate motions and viscosity stratification, *Geophys. Res. Lett.*, **23**, No 21, 2,987-2,990, 1996.

Busse, F.H. and J.A. Whitehead, Instabilities of convection rolls in a high Prandtl number fluid, *J. Fluid Mech.*, 47, 305-320, 1971.

Clayton, R.W. and R.P. Comer, A tomographic analysis of mantle heterogeneities from body wave travel time data, *EOS Trans. AGU* 64, p. 776 (abstract), 1983.

Clévédé, É., C. Mégnin, B. Romanowicz, and P. Lognonné, Seismic waveform modeling in a three-dimensional Earth: asymptotic and non-asymptotic approaches, submitted to *Phys. Earth planet. Inter.*, 1999.

Clévédé, É. and Lognonné, P. Fréchet derivatives of coupled seismograms with respect to an anelastic rotating Earth, *Geophys. J. Int.*, **124**, 456-482, 1996.

Clévédé, E., and P. Lognonné, Corrigendum to Fréchet derivatives of coupled seismograms with respect to an anelastic rotating Earth, *Geophys. J. Int.*, **126**, 903, 1996b.

Cummins, P. R., Takeuchi, N., and R. J. Geller, Computation of complete synthetic seismograms for laterally heterogeneous models using the Direct Solution Method, *Geophys. J. Int.*, **130**, 1-16, 1997.

Dahlen, F. A., Multiplet coupling and the calculation of synthetic seismograms, *Geophys. J. R. Astr. Soc.*, **91**, 241-254, 1987.

Davies, G.F., The role of the lithosphere in mantle convection, *J. Geophys. Res.*, **93**, 10,451-10,466, 1988.

De Boor, C., A practical guide to splines, Springer-Verlag, New-York, 1978.

Ding, X.Y. and S.P. Grand, Seismic structure of the deep Kurile subduction zone, *J. Geophys. Res.*, **99**, 23,767-23,786, 1994.

Durek, J.J. and G. Ekström, A radial model of anelasticity consistent with long period surface wave attenuation, *Bull. Seism. Soc. Am*, **86**, 144-158, 1996.

Dziewonski, A. M., Global seismic tomography of the mantle, *Reviews of Geophysics*, **33**, 419-423, 1995.

Dziewonski, A.M. and Anderson, D.L., Preliminary reference Earth model, *Phys. Earth planet. Inter.*, **25**, 297-356, 1981.

Dziewonski, A.M., B.H. Hager & R.J. O'Connell, Large scale heterogeneities in the lower mantle, *J. Geophys. Res.*, **82**, 1977.

Edmonds, A.R., Angular momentum in quantum mechanics, Princeton University Press, Princeton, New Jersey, 1960.

Engdahl, E.R., R.D. van der Hilst & Buland, R.P., Global teleseismic earthquake relocation with improved travel times and procedures for depth determination, *Bull. Seism. Soc. Am*, **88** No 3, 722-743, 1998.

Fetter, A.L. and J.D. Walecka, Theoretical mechanics of particles and continua, McGraw-Hill, 1980.

Fischer, K.M., K.C. Creager and T.H. Jordan, Mapping the Tonga slab, *J. Geophys. Res.*, **96**, 14,403-14,427, 1991.

Friederich, W., Wave-theoretical inversion of teleseismic surface waves in a regional network; phase-velocity maps and a three-dimensional upper-mantle shear-wave-velocity model for southern Germany, *Geophys. J. Int.* **132**, 203-225, 1998.

Friederich, W., E. Wielandt and S. Stange, Multiple forward scattering of surface waves - Comparison with an exact solution and Born single-scattering methods, *Geophys. J. Int.*, **112**, 264-275, 1993.

Fukao, Y., M. Obayashi, H. Inoue, M. Nenbai, Subducting slabs stagnant in the mantle transition zone, *J. Geophys. Res.*, **97**, 4,809-4,822, 1992.

Geller, R.J. and Takeuchi, N., 1995. A new method for computing highly accurate DSM synthetic seismograms, *Geophys. J. Int.*, **123**, 449-470.

Geller, R.J., and T. Hara, Two efficient algorithms for iterative linearized inversion of seismic waveform data, *Geophys. J. Int.*, **115**, 699-710, 1993.

Geller, R. J., Hara, T., and S. Tsuboi, On the equivalence of two methods for computing partial derivatives of seismic waveform, *Geophys. J. Int.*, **100**, 153-156, 1990.

Grand, S. P., R. D. van der Hilst and S. Widiyantoro, Global Seismic Tomography: A Snapshot of Convection in the Earth, *GSA Today*, **7**, No 4, 1-7, 1997.

Grand, S.P., Tomographic inversion for shear velocity beneath the North American plate, *J. Geophys. Res.*, **92**, 14,065-14,090, 1987.

Grand, S.P., Mantle shear structure beneath the Americas and surrounding oceans, *J. Geophys. Res.*, **99**, 11,591-11,621, 1994.

Gubbins, D. and J. Bloxham, Geomagnetic field analysis, III, Magnetic fields on the core-mantle boundary, *Geophys. J. R. Astr. Soc.*, **80**, 695-713, 1985.

Hager, B.H., R.W. Clayton, M.A. Richards, R.P. Comer and A.M. Dziewonski, Lower mantle heterogeneity, dynamic topography and the geoid, *Nature*, **313**, 541-545, 1985.

Hara, T., Tsuboi, S., and R. J. Geller, Inversion for laterally heterogeneous upper mantle S-wave velocity structure using iterative waveform inversion, *Geophys. J. Int.*, **115**, 667-698, 1993.

van Heijst, H.J. and J. Woodhouse, Global high resolution phase velocity distributions of overtone and fundamental-mode surface waves determined by mode branch stripping, *Geophys. J. Int.*, in press.

van Heijst, H.J. and J. Woodhouse, Measuring surface wave overtone phase velocities using a mode branch stripping technique, *Geophys. J. Int.*, **131**, 209-230, 1997.

Hibbard, W., and D. Santek, The Vis5D system for easy interactive visualization. Proc. Visualization '90, San Francisco, IEEE. 28-35, 1990.

van der Hilst, R.D. and H. Kárason, Compositional heterogeneity in the bottom 1,000 kilometers of Earth's mantle: toward a hybrid convection model, *Science*, **283**, 1,885-1,888, 1999.

van der Hilst, R.D., S. Widiyantoro and E.R. Engdahl, Evidence of deep mantle circulation from global tomography, *Nature*, **386**, 578-584, 1997.

van der Hilst, R.D., Complex morphology of subducted lithosphere in the mantle beneath the Tonga trench, *Nature*, **374**, 154-157, 1995.

van der Hilst, R.D. and T. Seno, Effects of relative plate motion on the deep structure and penetration depth of slabs below the Izu-Bonin and Mariana arcs, *Earth Planet. Sci. Lett.*, **120**, 395-407, 1993.

van der Hilst, R.D., E.R. Engdahl, W. Spakman and G. Nolet, Tomographic imaging of subducted lithosphere below northwest Pacific island arcs, *Nature*, **353**, 37-43, 1991.

Jackson, D. D., 1979. The use of a priori data to resolve non-uniqueness in linear inversion, *Geophys. J. R. Astr. Soc.*, **57**, 137-157.

Lévêque, J.J., Regional upper mantle S velocity models from phase velocities of great-circle Rayleigh waves, *Geophys. J. R. Astr. Soc.*, **63**, 23-43, 1980.

Johnson S., G. Masters, P.J. Tackley and G.A. Glatzmaier, How well can we resolve a convecting Earth with seismic data ? (abstract), *EOS Trans. AGU, 74*(43), Fall Meeting suppl.,80, 1993.

Jordan, T.H. A procedure for estimating lateral variations from low-frequency eigenspectra data, *Geophys. J. R. Astr. Soc.*, **52**, 441-455, 1978.

Jordan, T.H., P. Puster, G.A. Glatzmaier and P.J. Tackley, Comparisons between seismic earth structures and mantle flow models based on radial correlation functions, *Science*, **261**, 1,427-1,431, 1993.

Lerch, F.J., S.M. Klosko and G.B. Patel, A refined gravity model from LAGEOS (GEM-L2), *EOS Trans. AGU, 63*, (74) Fall Meeting suppl., p. 906, 1982.

Li, X.D. and B. Romanowicz, Global mantle shear-velocity model developed using nonlinear asymptotic coupling theory, *J. Geophys. Res.*, **101**, 22,245-22,272, 1996.

Li, X.D. and B. Romanowicz, Comparison of global waveform inversions with and without considering cross-branch modal coupling, *Geophys. J. Int.*, **121**, 695-709, 1995.

Li, X.D. and T. Tanimoto, Waveforms of long-period body waves in a slightly aspherical Earth model, *Geophys. J. R. Astr. Soc.*, **112**, 92-102, 1993.

Li, X.D., The asphericity of the earth from free oscillations, Ph.D. thesis, Harvard University, Cambridge, MA, 1990.

Liu, X.-F. and Dziewonski, A.M., Global analysis of shear wave velocity anomalies in the lower-most mantle, Gurnis M. editor, Core-mantle boundary region, American Geophysical Union, Washington, DC, 1998.

Liu, X.-F., The three-dimensional shear-wave velocity structure of the earth's lowermost mantle, Ph.D. thesis, Harvard University, Cambridge, MA, 1997.

Liu, X.-F. and Dziewonski, A.M. On the scale of heterogeneity in the lowermost mantle, *EOS Trans. AGU*, **78**, F17, 1997.

Liu, X.-F. and Dziewonski, A.M., Lowermost mantle shear wave velocity structure, *EOS Trans. AGU*, **75**, p. 663, 1994.

Lognonné, P., and É. Clévédé, Diffraction of long period Rayleigh waves by a slab: effects of mode coupling, *Geophys. Res. Lett.*, **24**, 1,035-1,038, 1997.

Lognonné, P., Normal modes and seismograms of an anelastic rotating Earth, *J. Geophys. Res.*, **96**, 20,309-20,319, 1991.

Lognonné, P., and B. Romanowicz, Modelling of coupled normal modes of the Earth: the spectral method, *Geophys. J. Int.*, **102**, 365-395, 1990.

Machetel, P., Short-wavelength lower mantle seismic velocity anomalies, *Geophys. Res. Lett.*, **17** No 8, 1145-1148, 1990.

Marquering, H., G. Nolet, and F.A. Dahlen, Three-dimensional waveform sensitivity kernels, *Geophys. J. Int.*, **132**, 521-534, 1998.

Marquering, H. & R. Snieder, Surface wave mode coupling for efficient forward modelling and inversion of body-wave phases, *Geophys. J. Int.*, **120**, 186-208, 1995.

Masters, G., S. Johnson, G. Laske, and H. Bolton, A shear-velocity model of the mantle, *Phil. Trans. R. Soc. London*, **354** 1,385-1,410, 1996.

Masters, G., T.H. Jordan, P.G. Silver and F. Gilbert, Aspherical Earth structure from fundamental spheroidal mode data,*Nature*, **298**, 609-613, 1982.

Mégnin, C. and B. Romanowicz, The effects of theoretical formalism and data selection scheme on mantle models derived from waveform tomography, *Geophys. J. Int.*, in press, 1999.

Mégnin, C. and B. Romanowicz, A comparison between tomographic and geodynamic models of the earth's mantle, submitted to Dynamics of Plate Motions, AGU monograph, van der Hilst editor, 1999.

Mégnin, C. and B. Romanowicz, A model of shear velocity in the mantle from the inversion of waveforms of body, surface and higher mode waveforms, in progress, 1999.

Mégnin, C., H.P. Bunge, B. Romanowicz and M.A. Richards, Imaging 3-D spherical convection models : What can seismic tomography tell us about mantle dynamics ?, *Geophys. Res. Lett.*, **24**, 1,299-1,303, 1997.

Mégnin, C. and B. Romanowicz, Improvements in waveform inversion techniques with applications to whole mantle structure, *EOS Trans. AGU* **78**, p. F460 (abstract), 1997.

Meier, T., S. Lebedev, G. Nolet and F. A. Dahlen, Diffraction tomography using multimode surface waves, *J. Geophys. Res.*, **102**, 8,255-8,267, 1997.

Michelena, R.J. & J.M. Harris, Tomography using natural pixels, *Geophysics*, **56**, 635-644, 1991.

Michelini, A. and T.V. McEvilly, Seismological studies at Parkfield. I. Simultaneous inversion for velocity structure and hypocenters using b-splines parametrization, *Bull. Seism. Soc. Am*, **81**, No 2, 524-552, 1991.

Mochizuki, E. Free oscillations and surface waves of an aspherical Earth, *Geophys. Res. Lett.*, **13**, 1478-1481, 1986.

Montagner, J.P. and B. Romanowicz, Degrees 2, 4, 6 inferred from seismic tomography, *Geophys. Res. Lett.*, **20** No 7, 631-634, 1993.

Nataf, H.-C. and Y. Ricard, 3SMAC: an a priori tomographic model of the upper mantle based on geophysical modeling, *Phys. Earth planet. Inter.*, **95**, 101-122, 1996.

Nataf, H.C. and J. VanDecar, Seismological detection of a mantle plume ?, *Nature*, **364**, 115-120, 1993.

Nataf, H.-C., I. Nakanishi & D.L. Anderson, Measurements of mantle wave velocities and inversion for lateral heterogeneities and anisotropy, *J. Geophys. Res.*, **91**, 7,261-7,307, 1986.

Okal, E, Regional dispersion of first-order overtone Rayleigh waves, *Geophys. J. R. Astr. Soc.*, **72** No 2, 461-481, 1983.

Olson, P., G. Schubert and C. Anderson, Structure of axisymmetric mantle plumes, *J. Geophys. Res.*, **98**, 6,829-6,844, 1993.

Park, J., Roughness constraints in surface wave tomography, *Geophys. Res. Lett.*, **16**, 1329-1332, 1989.

Park, J., The subspace projection method for constructing first-order coupled-mode long-period synthetic seismograms, *Geophys. J. Int.*, **101**, 111-124, 1990.

Park, J. Asymptotic coupled mode expressions for multiplet amplitude anomalies and frequency shifts on an aspherical Earth, *Geophys. J. R. Astr. Soc.*, **90**, 129-169, 1987.

Phinney, R.A. and R. Burridge, Representation of the elastic-gravitational excitation of a spherical earth model by generalized spherical harmonics, *Geophys. J. R. Astr. Soc.*, **34**, 451-487, 1973.

Pollitz, F., Surface wave scattering from sharp lateral discontinuities, *J. Geophys. Res.*, **99**, 21891-21909, 1994.

Press, W.H., S.A. Teukolsky, W.T. Vetterling and B.P. Flannery, Numerical Recipes in C, 2nd ed., Cambridge University Press, 1994.

Pulliam, R.J. and P.B. Stark, Confidence regions for mantle heterogeneity, *J. Geophys. Res.*, **99**, 6,931-6,943, 1994.

Resovsky, J. S. and M. H. Ritzwoller, A degree 8 mantle shear velocity model from normal mode observations below 3 mHz, *J. Geophys. Res.*, **104**, 993-1,014, 1999.

Ricard, Y., H.-C. Nataf and J.-P. Montagner, The three-dimensional seismological a priori model constrained: Confrontation with seismic data, *J. Geophys. Res.*, **101**, 8,457-8,472, 1996.

Ricard, Y., M. Richards, C. Lithgow-Bertelloni and Y. Le Stunff, A Geodynamic model of Mantle Density Heterogeneity, *J. Geophys. Res.*, **98**, 21,895-21,909, 1993.

Richards, M.A., B.H. Hager and N.H. Sleep, Dynamically supported geoid highs over hotspots: Observation and theory, *J. Geophys. Res., 93*, 7690-7708, 1988.

Ritsema, J., S. Ni, D.V. Helmberger and H.P. Crotwell, Evidence for strong shear velocity reductions and velocity gradients in the lower mantle beneath Africa, *Geophys. Res. Lett.*, **25** No 23, 4,245-4,248, 1998.

Ritzwoller, M. H., and E. M. Lavely, Three-dimensional seismic models of the Earth's mantle, *Reviews of Geophysics*, **33**, 1-66, 1995.

Romanowicz, B. Anelastic tomography: a new perspective on upper mantle thermal structure *Earth Planet. Sci. Lett.*, **128**, 113-121, 1994.

Romanowicz, B. The upper mantle degree two: constraints and inferences on attenuation tomographyfrom global mantle wave measurements, *J. Geophys. Res.*, **95**, 11,051-11,071, 1990.

Romanowicz, B. Multiplet-multiplet coupling due to lateral heterogeneity: asymptotic effects on the amplitude and frequency of Earth's normal modes, *Geophys. J. R. Astr. Soc.*, **90**, 75-100, 1987.

Romanowicz, B., G. Roult and T. Kohl, The upper mantle degree two pattern: constraints from GEOSCOPE fundamental spheroidal mode eigenfrequency and attenuation measurements, *Geophys. Res. Lett.*, **14**, No. 12, 1219-1222, 1987.

Romanowicz, B. and G. Roult, First order asymptotics for the eigenfrequencies of the Earth and application to the retreival of large-scale lateral variations of structure, *Geophys. J. R. Astr. Soc.*, **87**, 209-239, 1986.

Sleep, N.H., Hotspots and mantle plumes: some phenomenology, *J. Geophys. Res.*, **95**, 6,715-6,736, 1990.

Snieder, R., J. Beckers and F. Neele, The effect of small-scale structure on normal mode frequencies and global inversions, *J. Geophys. Res.*, **96**, 501-515, 1991.

Snieder, R., and B. Romanowicz, A new formalism for the effect of lateral heterogeneity on normal modes and surface waves, I, isotropic perturbations, perturbations of interfaces and gravitational perturbations, *Geophys. J. R. Astr. Soc.*, **92**, 207-221, 1988.

Snieder, R., and G. Nolet, Linearized scattering of surface waves on a spherical Earth, *Geophys. J. Int.*, **61**, 55-63, 1987.

Souriau, A. & M. Souriau, Test of tectonic models by great circle Rayleigh waves, *Geophys. J. R. Astr. Soc.*, **73**, 533-551, 1983.

Spakman, W., S. Stein, van der Hilst, R.D. and Wortel, R., Resolution experiments for NW Pacific subduction zone tomography, *Geophys. Res. Lett.*, **16** No 10, 1097-1100, 1989.

Stark, P.B. and D.I. Nikolaiev, Toward tubular tomography, *J. Geophys. Res.*, **98**, 8,095-8,106, 1993.

Steinberger, B. and O'Connell, R. J., Advection of plumes in mantle flow: implications for hotspot motion, mantle viscosity and plume distribution, *Geophys. J. Int.*, **132**, 412-434, 1998.

Stutzmann, E. and J.-P. Montagner, Tomography of the transition zone from the inversion of higher mode surface waves, *Phys. Earth planet. Inter.*, **86**, 99-115, 1994.

Stutzmann, E. and J.-P. Montagner, An inverse technique for retreiving higher mode phase velocity and mantle structure, *Geophys. J. Int.*, **113**, 669-683, 1993.

Su, W.J., and A.M. Dziewonski, Global tomographic inversion using b-splines, *Eos Trans. AGU*, **77**(46), Fall Meet. Suppl., 1996.

Su, W.J., R.L. Woodward, and A.M. Dziewonski, Degree 12 model of shear velocity in the mantle, *J. Geophys. Res.*, **99**, 6,945-6,980, 1994.

Su, W.-J. Woodward, R.L. and A. M. Dziewonski, Deep origin of mid-ocean-ridge seismic velocity anomalies, *Nature*, **360**, 149-152, 1992.

Su, W.-J. and A. M. Dziewonski, Predominance of long-wavelength heterogeneity in the mantle, *Nature*, **352**, 121-126, 1991.

Tackley, P.J., D.J. Stevenson, G.A. Glatzmaier and G. Schubert, Effects of multiple phase transitions in a three-dimensional spherical model of convection in Earth's mantle, *J. Geophys. Res.*, **99**, 15,877-15,901, 1994.

Tackley, P.J., D.J. Stevenson, G.A. Glatzmaier and G. Schubert, Effects of an endothermic phase transition at 670 km depth in a spherical model of convection in the Earth's mantle, *Nature*, **361**, 699-704, 1993.

Tajima, F., Y. Fukao, M. Obayashi and T. Sakurai, Evaluation of slab images in the northwestern pacific, *Earth Planets Space*, Vol 50, 953-964, 1998.

Tajima, F. & S.P. Grand, Variation of transition zone high-velocity anomalies and depression of 660 km discontinuity associated with subduction zones from the southern Kuriles to Izu-Bonin and Ryukyu, *J. Geophys. Res.*, **103**, 15,015-15,036, 1998.

Takeuchi, H. & M. Saito, Seismic surface waves, *Methods in computational physics*, **11**, 217-295, 1972.

Tanimoto, T. Formalism for travel time inversion with finite frequency effects, *Geophys. J. Int.* **121**, 103-110, 1995.

Tanimoto, T. Long wavelength S-wave velocity structure throughout the mantle *Geophys. J. Int.*, **100**, 327-336, 1990.

Tanimoto, T. The three-dimensional shear wave structure in the mantle by overtone waveform inversion–I. Radial seismogram inversion, *Geophys. J. R. Astr. Soc.*, **89**, 713-740, 1989.

Tanimoto, T. A simple derivation of the formula to calculate synthetic long-period seismograms in a heterogeneous earth by normal mode summation, *Geophys. J. R. Astr. Soc.*, **77**, 275-278, 1984.

Tarantola, A. and B. Valette, Generalized non-linear inverse problems solved using the least-squares criterion, *Rev. Geophys.*, **20**, 219-232, 1982.

Tromp, J., and F. A. Dahlen, Variational principles for surface wave propagation on a laterally heterogeneous Earth: 2. Frequency domain JWKB theory, *Geophys. J. Int.*, **109**, 599-619, 1992.

Tromp, J., and F. A. Dahlen, Maslov theory for surface wave propagation on a laterally heterogeneous Earth, *Geophys. J. Int.*, **115**, 512-528, 1993.

Um, J., Dahlen, F. A., and J. Park, Normal mode multiplet coupling along a dispersion branch, *Geophys. J. Int.*, **106**, 11-35, 1991.

van der Lee, S. and G. Nolet, Upper mantle S velocity structure of North America, *J. Geophys. Res.*, **102**, 22,815-22,838, 1997.

Vasco, D.W. and L.R. Johnson, Whole earth structure estimated from seismic arrival times, *J. Geophys. Res.*, **103**, 2,633-2,671, 1998.

Vasco, D.W., L.R. Johnson, R.J. Pulliam and P.S. Earle, Robust inversion of IASP91 travel time residuals for mantle P and S velocity structure, earthquake mislocations and station corrections, *J. Geophys. Res.*, **99**, 13,727-13,755, 1994.

Wang, Z., J. Tromp and G. Ekström, Global and regional surface-wave inversions; a spherical-spline parameterization, *Geophys. Res. Lett.*, **25** No. 2, 207-210, 1998.

Wang, Z. and F.A. Dahlen, Spherical spline parametrization of three-dimensional Earth models, *Geophys. Res. Lett.*, **22** No. 22, 3,099-3,102, 1995.

Wang, Z., and F.A. Dahlen, JWKB surface-wave seismograms on a laterally heterogeneous Earth, *Geophys. J. Int.*, **119**, 381-401, 1994.

Weinstein, S.A. P.L. Olson, The proximity of hotspots to convergent and divergent plate boundaries, *Geophys. Res. Lett.*, **16** No 5, 433-436, 1989.

Wessel, P. & W.H.F. Smith, New version of the Generic Mapping Tool released, *EOS Trans. AGU*, **72** 441, 445-446, 1991.

Wielandt, E. & L. Knopoff, Dispersion of very long period Rayleigh waves along the East Pacific Rise: evidence for S wave velocity anomalies to 450 km depth, *J. Geophys. Res.*, **87** No B10, 8,631-8,641, 1982.

Woodhouse, J.H., and Y.K. Wong, Amplitude, phase and path anomalies of mantle waves, *Geophys. J. R. Astr. Soc.*, **87**, 753-773, 1986.

Woodhouse, J.H. & A.M. Dziewonski, Mapping the upper mantle : Three dimensional modeling of Earth's structure by inversion of seismic waveforms, *J. Geophys. Res.*, **89**, 5,953-5,986, 1984.

Woodhouse, J.H. The joint inversion of seismic waveforms for lateral variations in Earth structure and eartquake source parameters, *Proc. 'Enrico Fermi' Int. Sch. Phys. LXXXV*, (eds Kanamori, H. & E. Boschi), 366-397, 1983.

Woodhouse, J.H. and T.P. Girnius, Surface waves and free oscillations in a regionalized earth model, *Geophys. J. R. Astr. Soc.*, **68**, 653-673, 1982.

Woodhouse, J.H. The coupling and attenuation of nearly resonnant multiplets in the earth's free oscillation spectrum, *Geophys. J. R. Astr. Soc.*, **61**, 261,283, 1980.

Zhang, Y.S. and T. Tanimoto, Ridges, hotspots and their interaction as observed in seismic velocity maps, *Nature*, **355**, 45-49, 1992.

Zhou, H.W. & R.W. Clayton, P and S wave travel-time inversions for subducting slabs under the island arcs of the northwest Pacific, *J. Geophys. Res.* **95**, 6,829-6,854, 1990.